



ROYAL INSTITUTE
OF TECHNOLOGY



Lukas Aichmayer

Solar Receiver Design and Verification for Small Scale Polygeneration Unit

Master Thesis

(Diplomarbeit)

Royal Institute of Technology Stockholm
Department of Energy Technology

Graz University of Technology
Institute for Thermal Turbomachinery and Machine Dynamics

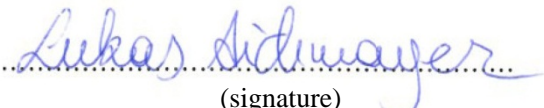
Dr. Björn Laumert, Royal Institute of Technology Stockholm
Ao.Univ.-Prof. DI Dr.techn. Wolfgang Sanz, Graz University of Technology

Graz, 2011

STATUTORY DECLARATION

I declare that I have authored this thesis independently, that I have not used other than the declared sources / resources and that I have explicitly marked all material which has been quoted either literally or by content from the used sources.

Graz, 27.11.2011


.....
(signature)

KURZFASSUNG

Angesichts des globalen Klimawandels zeigt solarthermische Stromproduktion großes Potential, um die globale Stromerzeugung von fossilen auf umweltfreundliche Energieträger umzustellen. Das Institut für Energietechnik an der Königlich Technischen Hochschule Stockholm trägt durch den Bau einer solarbetriebenen Polygenerationseinheit kleiner Leistung auf Basis einer extern gefeuerten Mikrogasturbine zu Forschung und Entwicklung solarthermischer Energieerzeugung bei.

Das Hauptaugenmerk dieser Arbeit lag auf Design, Analyse und Verifizierung eines Hochtemperatursolarreceivers zur Einbindung in die geplante Polygenerationseinheit. Die Herausforderung für das wesentliche Design stellten mittlere Bestrahlungsstärken von $5,5 \text{ MW/m}^2$ und Spitzenbestrahlungsstärken von 14 MW/m^2 am Brennfleck des Solarreceivers dar. Eine wärmetechnische Vorstudie hat hierbei gezeigt, dass volumetrische Receiver als einzige Receiverausführung sowohl den hohen Bestrahlungsstärken standhalten als auch im System integriert werden können.

Mit dieser gewählten volumetrischen Ausführung wurde ein grundlegendes Receivermodell mit Hilfe einer Mehrkriterienoptimierung, die auf evolutionären Algorithmen basiert, und eines numerischen Wärmetransfermodells ausgewertet. Die resultierenden Pareto-optimalen Lösungen zeigten einen Kompromiss zwischen Druckverlust im Receiver und Materialtemperaturen, speziell der Glasfenstertemperatur.

Auf Basis der vorangegangenen Analysen wurde eine Parameterstudie, evaluiert mit einer Nutzwertanalyse, um spezielle Aspekte des Ausgangsdesigns zu verbessern, durchgeführt. Von allen untersuchten Parametern hatte die Form des Absorbers den größten positiven Einfluss sowohl auf Materialtemperaturen als auch auf thermische Spannungen ohne dabei den Druckverlust signifikant zu erhöhen. Eine externe Kühlung des Glasfensters mit Umgebungsluft hat die Materialtemperatur, ohne den thermischen Wirkungsgrad bedeutend zu verschlechtern, positiv beeinflusst. Keramische Absorber wiesen im Gegensatz zu metallischen Absorbern bei hohen ungleichförmigen Bestrahlungsstärken eine bessere Eignung auf. Darüber hinaus wurde die mechanische Entkopplung des Glasfensters und des Absorbers von umgebenden Komponenten als überaus wichtig befunden, um unabhängige Expansion bei wechselnden Temperaturen zu ermöglichen und in weiterer Folge thermische Spannungen zu minimieren.

Zusammenfassend kann gesagt werden, ausgehend davon, dass in dieser Arbeit Designs mit Materialtemperaturen, thermischen Spannungen und Druckverlust unterhalb akzeptabler Limits gefunden wurden, volumetrische Solarreceiver für Polygenerationseinheiten kleiner Leistung realisierbar sind.

ABSTRACT

Against a backdrop of our world's changing climate solar thermal power generation shows great potential to move global energy production away from fossil fuels to non-polluting sources. The Department of Energy Technology at the Royal Institute of Technology Stockholm is contributing to the development and research of solar thermal power by building a solar driven small scale polygeneration unit based on an externally fired micro gas turbine.

This project focused on the design, analysis and verification of a high temperature solar receiver for integration into this planned solar polygeneration unit. Mean irradiance levels at the focal spot of the solar receiver of 5.5 MW/m^2 and peak levels of 14 MW/m^2 were identified as major design challenges. A preliminary heat transfer analysis found volumetric receivers to be the only applicable receiver type capable of withstanding these expected high irradiance levels.

With volumetric receivers selected as the receiver type, a basic volumetric receiver model was evaluated using a multi-objective optimization tool based on advanced evolutionist algorithms and a numerical heat transfer model. The results were a set of Pareto-optimal solutions showing a tradeoff between a pressure drop in the receiver and material temperature especially at the window of the receiver.

A parameter study was conducted based on the previous analysis to improve specific aspects of the initial design using a value of benefit analysis to evaluate the different designs. Of all the investigated receiver parameters, the absorber properties and shape had the biggest positive influence on material temperature and thermal stresses without significantly increasing the pressure drop. External cooling of the receiver window with ambient air was found to beneficially influence the window temperature without greatly decreasing the thermal efficiency. For non-uniform high irradiance levels ceramic absorber materials were found to be most suitable. Furthermore, mechanically decoupling the window and the absorber from their surrounding parts was found to be very important; enabling them to expand more or less independently with changing temperature minimizing thermal stresses.

It can be concluded, when properly designed, volumetric solar receivers for small scale solar polygeneration units are feasible as designs with material temperature, thermal stresses and pressure drop below acceptable limit were found within this work.

ACKNOWLEDGEMENT

I would like to thank Professor Torsten Fransson, head of the Department of Energy Technology at the Royal Institute of Technology for giving me the possibility to write my Master thesis at his department. The same gratitude goes to Professor Wolfgang Sanz, head of CFD and Cycle Optimisation Department at Graz University of Technology for supervising my work from Austria.

Gratitude is also extended to my supervisor Dr. Björn Laumert for his guidance and advice during this thesis. I would also like to extend my thanks to the PhD students Wujun Wang and James Spelling for their crucial support.

Last but not least, I must thank with all my heart my dear parents, Karl and Elfriede Aichmayer, who have given me love and support during these last years in Graz and Stockholm.

NOMENCLATURE

Abbreviations

CCA	Cross-Consistency Assessment
CPC	Compound Parabolic Concentrator
CSP	Concentrating Solar Power
CSR	Central Receiver System
DIAPR	Directly-Irradiated Annular Pressurized Receiver
DLR	German Aerospace Center (Deutsches Zentrum für Luft- und Raumfahrt)
DNI	Direct Nominal Irradiation
DOE	Department of Energy
DOM	Discrete Ordinate Method
DSG	Direct Steam Generation
GDP	Gross Domestic Product
HRSG	Heat Recovery Steam Generator
HTF	Heat Transfer Fluid
HTM	Heat Transfer Medium
IEA	International Energy Agency
IPCC	Intergovernmental Panel on Climate Change
KTH	Royal Institute of Technology (Kungliga Tekniska Högskolan)
LEC	Levelized Electricity Costs
LFR	Linear Fresnel Reflector
LTE	Local Thermal Equilibrium
LTNE	Local Thermal Non-Equilibrium
MOO	Multi Objective Optimizer
MU	Monetary Unit
NASA	National Aeronautics and Space Administration
NTU	Number of Transfer Units
PML	Profiled Multi-Layer
RANS	Reynolds-Averaged Navier-Stokes
REFOS	Receiver for Solar-Hybrid Gas turbine and CC Systems
RTE	Radiative Transfer Equation
SE	Systems Engineering
SiC	Silicon Carbide
SiSiC	Siliconized Silicon Carbide
SOLGATE	Solar hybrid gas turbine electric power system (EU-Project)
SOLHYCO	Solar hybrid cogeneration (EU-Project)

SOLUGAS	Solar Up-scale Gas Turbine System (EU-Project)
SPU	Solar Polygeneration Unit
U.S.	United States
UDF	User Defined Function
UDS	User Defined Scalar
UNFCCC	United Nations Framework Convention on Climate Change
VDI	The Association of German Engineers (Verein Deutscher Ingenieure)
WSTC	Water-Splitting Thermo-Chemical

Symbols

Symbol	Unit	Description	Symbol	Unit	Description
a	m	Cell size	α	-	Absorptivity
A	m ²	Area	α	1/m	Absorption coefficient
c ₀	m	Speed of light in vacuum	α_{sf}	1/m	Specific surface area
c _p	J/(kg·K)	Specific heat capacity	β	-	Scattering albedo
C _f	-	Inertial coefficient	δ	-	Light distribution factor
C	J/K	Heat capacity rate	ε	-	Heat exchanger effectiveness
d	m	Diameter	ε	-	Strain
d _h	M	Hydraulic diameter	ε_p	-	Porosity, emissivity
E ₁ , E ₂	-	Ergun constant	ξ	-	Friction factor
e	J/kg	Specific energy	ξ	-	Size parameter
E	MPa	Young's modulus	η	-	Efficiency
f	N/m ³	Body force	λ	m	Wave length
F	N	Force	μ	Pa·s	Dynamic viscosity
G	MPa	Shear modulus	ν	m ² /s	Dynamic viscosity
g	m/s ²	Gravitational constant	ν	-	Poisson's ratio
h, h _{sf}	W/(m ² ·K)	Heat transfer coefficient	Π	-	Pressure ratio
h _v	W/(m ³ ·K)	Volumetric heat transfer coefficient	ρ	kg/m ³	Density
h	J/kg	Specific Enthalpy	ρ	-	Reflectivity
h	Js	Universal Planck constant	σ	1/m	Scattering coefficient
k	J/K	Boltzmann constant	σ	W/(m ² ·K ⁴)	Stefan–Boltzmann constant
k	W/(m·K)	Thermal conductivity	σ	MPa	Strength
k	-	Extinction constant	σ	MPa	Stress
K	m	Absolut roughness	τ	-	Transmissivity
K	1/m	Extinction coefficient	τ	MPa	Shear stress
K	m ²	Specific permeability	Φ	m	Cell diameter
L	m	Length	Φ	-	Scattering phase function

Symbol	Unit	Description	Symbol	Unit	Description
\dot{m}	kg/s	Mass flow	Ω	sr	Solid angle
\dot{M}	kg/(m ² ·s)	Mass flux			
M_w	kg/kmol	the molecular weight			
n	-	Refractive index			
Nu	-	Nusselt number			
p	Pa	Pressure			
P	-	Reflection factor			
Pr	-	Prandtl number			
q	J/m ²	Heat flux			
Q	J	Heat			
r	m	Radius			
R	J/(kg·K)	Specific gas constant			
Re	-	Reynolds number			
s	m	Path length			
s''	W/m ³	Volumetric heat source			
S	-	Sutherland constant			
t	m	Wall thickness			
T	°C, K	Temperature			
u	m/s	Velocity			
u	-	Material utilization			
U	W/(m ² ·K)	Overall heat transfer coefficient			
x	m	Index variable			
Y	m	Index variable			
z	m	Index variable			

Subscripts

0	Initial	o	Outside
abs	Absorber	out	Outlet
amb	Ambient	p	Porous media
b	Blackbody	per	Permissible
c	Cavity	ref	Reference
c	Comparison	r	Radiative
conv	Convection	s	Solid
cr	Crushing	surf	Surface
el	Electrical	t	Transmitted
e	Effective	t	Turbulent
f	Fluid	T	Tube
f.d.	Fully developed	th	Thermal

h	Hydraulic	v	Volumetric, void
i	Inside	v	von Mises
i	Spatial index	w	Window
in	Inlet	λ	Spectrally
j	Spatial index	-	Leaving system
max	Maximal	+	Entering system
min	Minimal		

Radiometric definitions [1]

Symbol	Unit	Name	Description
Φ	W	Radiant power or radiant flux	Total power radiated by a source
Q	J	Radiant Energy	Total energy radiated by a source
I	W/sr	Radiant intensity	Power per unit solid angle
E	W/m ²	Irradiance or radiant flux density	Radiation power received by the unit area of the illuminated surface
M	W/m ²	Radiant emittance or radiant exitance	Radiation power emitted by the unit area
J	W/m ²	Radiosity	All radiant flux leaving the surface. Accounts for reflection, irradiance and emittance.

Reflectance, transmittance, absorptance, and emittance

ance endings indicate a value associated with a particular sample

Reflectivity, transmissivity, absorptivity, and emissivity

ivity endings indicate a generic value for a “pure” substance

Reflection, transmission, absorption, and emission

ion endings indicate a process

TABLE OF CONTENTS

1. Introduction and background.....	1
1.1 Concentrating solar power	1
1.2 Concentrating solar power systems.....	2
1.3 Objectives.....	5
1.4 Methodology and report structure.....	6
2. Literature review	8
2.1 Type of point focusing receivers.....	10
2.2 Operating pressure	11
2.3 Operating temperature.....	11
2.4 Heat transfer and heat transfer media.....	11
2.5 Absorber.....	12
2.5.1 Tubular receiver designs	12
2.5.2 Volumetric design.....	14
2.5.3 Heat pipe design	19
2.5.4 Solid particle design	21
3. Preliminary study	23
3.1 Situational analysis and boundary conditions	23
3.1.1 System layout.....	23
3.1.2 Fluid boundaries.....	25
3.1.3 Radiation boundaries.....	25
3.1.4 Summary of boundary conditions	29
3.2 Detailed objectives	29
3.3 Synthesis of solutions.....	30
3.4 Analysis of solutions	34
3.4.1 Tubular design.....	34
3.4.2 Volumetric design.....	37
3.4.3 Heat pipe design	46

3.5	Evaluation and decision	46
4.	Main study	48
4.1	Situation analysis	48
4.1.1	<i>Physical modeling</i>	48
4.1.2	<i>Numerical modeling</i>	68
4.1.3	<i>Verification</i>	71
4.1.4	<i>Optimization</i>	76
4.1.5	<i>Situation analysis results</i>	79
4.2	Re-design objectives	82
4.3	Synthesis of solutions.....	82
4.3.1	<i>Flow channel</i>	82
4.3.2	<i>Absorber</i>	83
4.3.3	<i>Window</i>	86
4.3.4	<i>Heat transfer fluid</i>	88
4.4	Analysis of solutions.....	89
4.4.1	<i>Modeling</i>	89
4.4.2	<i>Flow channel</i>	94
4.4.3	<i>Absorber</i>	96
4.4.4	<i>Window</i>	102
4.4.5	<i>Heat transfer fluid</i>	110
4.5	Evaluation and decision	110
4.5.1	<i>Value of benefit analysis</i>	110
4.5.2	<i>Values of benefit</i>	113
4.5.3	<i>Decision</i>	117
5.	Detailed study.....	118
5.1	Design analysis	118
5.1.1	<i>Parameter study</i>	118
5.1.2	<i>Evaluation and decision</i>	121
5.1.3	<i>Results and discussion</i>	122

5.2	Verification	123
5.2.1	<i>Modeling</i>	123
5.2.2	<i>Meshing</i>	125
5.2.3	<i>Results and discussion</i>	127
5.2.4	<i>Conclusion</i>	128
5.3	Prototype	128
5.3.1	<i>Materials</i>	128
5.3.2	<i>Drawings</i>	129
5.3.3	<i>Description</i>	129
6.	Conclusions	130
6.1	Summary of results	130
6.2	Analysis and interpretation	131
6.3	Remarks	132
6.4	Future work	132
7.	References	133
8.	Appendixes	140
8.1	Appendix A: Numerical model in MATLAB	141
8.1.1	<i>Receiver specifications</i>	141
8.1.2	<i>Numerical system solver</i>	143
8.2	Appendix B: User defined function in FLUENT	150
8.3	Appendix C: Receiver assembly	161

INDEX OF TABLES

<i>Table 3.1: Fluid boundary conditions</i>	25
<i>Table 3.2: Boundary conditions</i>	29
<i>Table 3.3: Morphological box for receiver design</i>	30
<i>Table 3.4: Simplified morphological box</i>	31
<i>Table 3.5: Cross-consistency assessment matrix</i>	32
<i>Table 3.6: Solution principles</i>	33
<i>Table 3.7: Nusselt number (on basis of [35])</i>	35
<i>Table 3.8: Boundary conditions for tubular receiver design</i>	36
<i>Table 3.9: Different models for the volumetric heat transfer coefficient</i>	41
<i>Table 3.10: Pressure drop models for foam absorber</i>	43
<i>Table 3.11: Pressure drop parameters for polygonal ducts</i>	44
<i>Table 3.12: Balance of arguments</i>	46
<i>Table 4.1: Different models for the extinction coefficient in open cell materials</i>	54
<i>Table 4.2: Ranges of measured and predicted extinction coefficients for cellular ceramics [79]</i>	54
<i>Table 4.3: Temperature stability of glass windows</i>	62
<i>Table 4.4: Additional parameters absorber materials</i>	67
<i>Table 4.5: Additional parameters window</i>	68
<i>Table 4.6: Key results</i>	74
<i>Table 4.7: Deviation from self-made numerical model</i>	75
<i>Table 4.8: Optical, thermodynamic, and resulting material requirements of absorber materials [81]</i> .	76
<i>Table 4.9: Objectives and parameters for optimization</i>	77
<i>Table 4.10: Situation analysis results</i>	80
<i>Table 4.11: Absorber material stresses and material utilization</i>	80
<i>Table 4.12: Absorber properties modifications 1</i>	85
<i>Table 4.13: Absorber properties modifications 2</i>	86
<i>Table 4.14: Window cooling</i>	88
<i>Table 4.15: Boundary conditions</i>	92
<i>Table 4.16: Matrix of criteria</i>	110
<i>Table 4.17: Weighting of sub criteria</i>	111

<i>Table 4.18: Target scale for value of benefit analysis.....</i>	<i>112</i>
<i>Table 4.19: Limits for target scale</i>	<i>113</i>
<i>Table 5.1: Final design parameters.....</i>	<i>121</i>
<i>Table 5.2: Main results.....</i>	<i>122</i>
<i>Table 5.3: Main FLUENT results.....</i>	<i>127</i>
<i>Table 5.4: Austenitic steel alloys.....</i>	<i>128</i>

INDEX OF FIGURES

<i>Figure 1.1: Potential regions for CSP [12]</i>	2
<i>Figure 1.2: Parabolic trough principle</i>	3
<i>Figure 1.3: Linear Fresnel reflector principle</i>	4
<i>Figure 1.4: Parabolic dish principle</i>	4
<i>Figure 1.5: Central receiver principle</i>	5
<i>Figure 1.6: Systems Engineering (SE) action model [24]</i>	6
<i>Figure 2.1: Classification of solar receivers – system view</i>	8
<i>Figure 2.2: Classification of solar receivers – component view</i>	9
<i>Figure 2.3: Classification of volumetric solar receivers</i>	9
<i>Figure 2.4: Solar receiver types</i>	10
<i>Figure 2.5: Convective heat losses of a cavity receiver [28]</i>	10
<i>Figure 2.6: Heat transfer mode</i>	12
<i>Figure 2.7: Absorption and heat transfer of tubular receivers (on basis of [26] and [30])</i>	12
<i>Figure 2.8: Existing tubular receiver designs</i>	13
<i>Figure 2.9: Recent tubular receivers designs</i>	13
<i>Figure 2.10: Absorption and heat transfer of volumetric receivers (on basis of [26] and [30])</i>	14
<i>Figure 2.11: Flow instability issues (on basis of [36])</i>	15
<i>Figure 2.12: Quadratic pressure drop versus HTF temperature (on basis of [36])</i>	16
<i>Figure 2.13: Open volumetric receivers</i>	17
<i>Figure 2.14: Closed (pressurized) volumetric receivers</i>	17
<i>Figure 2.15: Schematic representation of a heat pipe (on basis of [47])</i>	19
<i>Figure 2.16: Heat pipe receiver configuration [49]</i>	20
<i>Figure 2.17: Heat pipe receiver for Brayton cycle [51]</i>	21
<i>Figure 2.18: Solid particle receiver</i>	21
<i>Figure 2.19: Solid particle receiver layout for electricity generation (on basis of [57])</i>	22
<i>Figure 2.20: Solid particle receiver velocity vectors [58]</i>	22
<i>Figure 3.1: Micro gas turbine (COMPOWER)</i>	23
<i>Figure 3.2: KTH SPU schema</i>	24

<i>Figure 3.3: KTH SPU configurations</i>	24
<i>Figure 3.4: Mean irradiance for different number of lamps</i>	26
<i>Figure 3.5: Irradiance at focal plane in MW/m² (on basis of [44])</i>	27
<i>Figure 3.6: Spectral radiant intensity of a single lamp [45]</i>	28
<i>Figure 3.7: Solar spectral irradiance on top of the atmosphere and Earth's surface [46]</i>	28
<i>Figure 3.8: Graphical summary of solution principles</i>	33
<i>Figure 3.9: One dimensional heat transfer model for tubular receiver design</i>	34
<i>Figure 3.10: Pressure drop and wall temperature for tubular receiver design</i>	37
<i>Figure 3.11: Volumetric receiver design model</i>	38
<i>Figure 3.12: Foam parameters [63]</i>	40
<i>Figure 3.13: Honeycomb structure</i>	42
<i>Figure 3.14: Nusselt number for honeycomb structures [72]</i>	42
<i>Figure 3.15: Pressure drop and temperature for foam absorber</i>	44
<i>Figure 3.16: Pressure drop and temperature for honeycomb absorber</i>	45
<i>Figure 3.17: Fluid and absorber temperature</i>	45
<i>Figure 3.18: Enhanced cellular silicon carbide absorber [73]</i>	47
<i>Figure 4.1: Basic volumetric receiver design</i>	48
<i>Figure 4.2: Fluid flow simplifications</i>	49
<i>Figure 4.3: Irradiance attenuation within the porous medium</i>	53
<i>Figure 4.4: Spectral normal emittance of a cellular ceramic [79]</i>	55
<i>Figure 4.5: Change of intensity of a light beam passing through a glass plate [82]</i>	57
<i>Figure 4.6: Optical constants of fused silica (SiO₂ glass) [82]</i>	59
<i>Figure 4.7: Spectral extinction coefficient</i>	60
<i>Figure 4.8: Blackbody emittance [35]</i>	61
<i>Figure 4.9: Spectrally weighted absorptance, reflectance, and transmittance [88]</i>	61
<i>Figure 4.10: Radiation exchange between window and absorber surface</i>	63
<i>Figure 4.11: Heat exchanger model</i>	64
<i>Figure 4.12: Friction factor for the abrupt reduction of the cross sectional area (on basis of [47])</i>	66
<i>Figure 4.13: Numerical scheme layout</i>	69
<i>Figure 4.14: COMSOL analysis</i>	72

<i>Figure 4.15: Fluid and absorber solid temperature</i>	73
<i>Figure 4.16: Window temperature</i>	74
<i>Figure 4.17: Receiver optimization objectives</i>	77
<i>Figure 4.18: Receiver optimization parameters</i>	78
<i>Figure 4.19: Stresses within the window</i>	81
<i>Figure 4.20: Receiver modifications</i>	82
<i>Figure 4.21: Flow channel modifications</i>	83
<i>Figure 4.22: Absorber shape modifications</i>	84
<i>Figure 4.23: Absorber properties modifications 2</i>	86
<i>Figure 4.24: Window shape</i>	87
<i>Figure 4.25: Window cooling</i>	88
<i>Figure 4.26: Mesh in COMSOL</i>	93
<i>Figure 4.27: Flow channel modification (A) results</i>	95
<i>Figure 4.28: Absorber shape modification (B) results</i>	97
<i>Figure 4.29: Absorber properties modification 1 (C) results</i>	99
<i>Figure 4.30: Absorber properties modification 2 (D) results</i>	101
<i>Figure 4.31: Window shape modification (E) results</i>	103
<i>Figure 4.32: Window cooling outside (F) results</i>	105
<i>Figure 4.33: Fluid temperature before absorber (F)</i>	106
<i>Figure 4.34: Window cooling outside (F) efficiency</i>	107
<i>Figure 4.35: Window cooling inside (G) results</i>	108
<i>Figure 4.36: Window cooling inside (G) efficiency</i>	109
<i>Figure 4.37: Utility functions for value of benefit analysis</i>	113
<i>Figure 4.38: Value of benefit flow channel (A)</i>	113
<i>Figure 4.39: Value of benefit absorber modifications (B), (C), and (D)</i>	115
<i>Figure 4.40: Value of benefit window modifications (E), (F), and (G)</i>	116
<i>Figure 5.1: Receiver design</i>	118
<i>Figure 5.2: Chosen receiver design cell diameter variation</i>	119
<i>Figure 5.3: Temperature distribution and material stresses inside the absorber</i>	120
<i>Figure 5.4: Value of benefit</i>	121

<i>Figure 5.5: Mesh in ANSYS ICEM</i>	126
<i>Figure 5.6: Mesh quality</i>	126

1. INTRODUCTION AND BACKGROUND

Our world's climate is changing. Increases in global average air and ocean temperatures, widespread melting of snow and ice, and rising global average sea level are evidence for the warming of the earth's climate system [2]. Furthermore, the frequency and intensity of extreme events such as heat waves, droughts and floods are expected to increase as the earth's climate continues to change [2]. Some of these changes are already evident with increases in the frequency and intensity of heat waves and heavy precipitation events. There are also economic costs of climate change although impacts will vary regionally global mean losses could be 1 to 5 percent of GDP for 4°C of warming [3].

The release of greenhouse gas carbon dioxide into the atmosphere through burning fossil fuels is the largest known human induced contribution to climate change. Human impact on the climate since the start of the industrial era (around 1750) exceed predicted natural impacts due to any know natural processes [2]. In response to mentioned implications of anthropogenic climate change, an agreement was made at the United Nations Framework Convention on Climate Change (UNFCCC) to keep the increase in global temperature below 2°C [4]. This agreement, *The Copenhagen Account*, was noted by all conference participants but was not legally binding.

To achieve the 2°C Copenhagen Account goal and avoid the potentially devastating and costly consequences of human-induced climate change it is necessary to stabilize greenhouse gases at a level of no higher than 450 ppm CO₂ equivalents [5]. Therefore, the implementation of more ambitious goals than the ones agreed in the Copenhagen Account in would be necessary in the period to 2020 and much stronger action thereafter [5].

This is challenging given our world energy needs continue to increase. Emerging economies, led by China and India, are expected to drive the global energy demand even higher. Moreover, the International Energy Agency (IEA) expects that the global electricity demand continues to grow more strongly than other final forms of energy [5].

Solar thermal power generation shows great potential [6] and thus can be one system of many in the attempt to move the global energy production away from fossil fuels to non-polluting sources.

1.1 Concentrating solar power

As the name suggests, concentrating solar power (CSP) systems concentrate solar radiation to produce hot air or steam which can then be used to generate electricity in conventional power cycles. Today's CSP systems usually generate electricity in the range of 10kW up to several 100MW [6] [7] at levelized electricity costs (LEC) in the range of 10 to 20 cents€/kWh in Europe [8]. The United States Department of Energy suggest cost around 20 cents\$/kWh [10]. In the conventional electricity generation market, CSP systems compete with LEC of 3 to 4 cents€/kWh [8]. In the medium to long-term electricity generated using CSP technology is expected to become competitive at a slightly elevated price level as costs of fossil fuels and carbon emissions are expected to rise [8].

LEC is commonly used to compare different technologies for generating energy that might have different operating times, different investment costs, and/or different scales of operation.

Equation 1.1 shows the basic calculation of the LEC [9]. Total life cycle costs are based on a net present value calculation which includes initial investment costs, costs for operation and maintenance, as well as fuel costs. The total lifetime energy production includes all usable produced electricity.

$$LEC = \frac{\text{Total life cycle costs}}{\text{Total lifetime energy production}} \left(\frac{MU}{kWh} \right) \quad (1.1)$$

From an environmental point of view replacing fossil fuel based electricity generation with a CSP power plant can reduce CO₂ emissions by 200 to 300 kg per year and installed square meter of reflector surface [11].

Trieb F. [12] of the German Aerospace Center conducted a survey finding that the global technical CSP potential amounts to almost 3,000,000 TWh/a vastly exceeding the present world electricity consumption of 18,000 TWh/a. Potential regions for CSP power plants are presented in Figure 1.1. The main suitability criteria considered was a direct nominal radiation (DNI) higher than 2,000 kWh/m²/a [12].

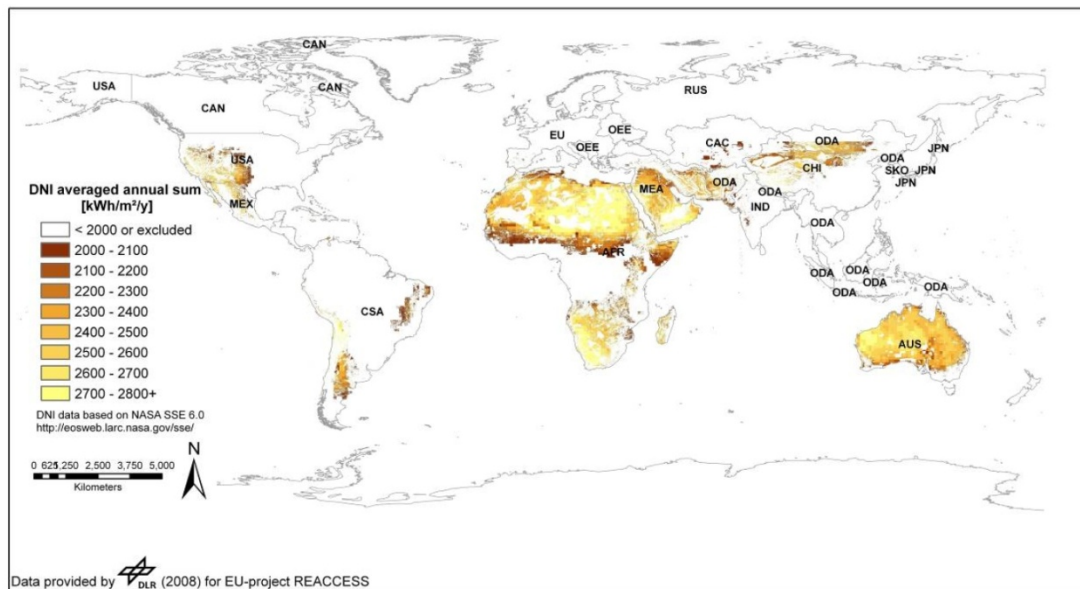


Figure 1.1: Potential regions for CSP [12]

The main advantage of CSP compared to other renewable sources of energy is the possibility of thermal storage [11]. CSP power plants also offer the possibility to easily operate in a hybrid mode, allowing supplementary co-firing for example with natural gas. As a result, CSP power plants have the potential to generate electricity at night and during periods of low solar irradiation due to clouds and other factors. This makes the technology suitable to provide both base load as well as peak load electricity [11].

1.2 Concentrating solar power systems

In this section the four main working principles of CSP power production are described. These can be divided into two different types: line focusing and point focusing.

Parabolic trough systems belong to the line focusing type. The parabolic shaped solar reflector concentrates the incoming solar radiation on to the linear receiver placed in the

trough's focal line. Today concentration ratios between 30 and 100 are realized [13] [14] [15]. In order to follow the sun over the course of the day the parabolic reflectors are equipped with a single-axis tracking system.

The receiver is another key component of the system. It consists of a steel pipe that is placed inside an evacuated glass tube in order to reduce convective heat losses. Additionally, the

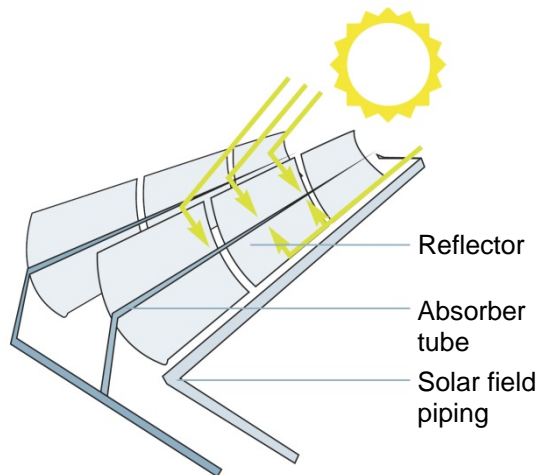


Figure 1.2: Parabolic trough principle (on basis of [6])

steel tubes are coated with a solar selective coating to improve the absorptance of the concentrated solar radiation over a broad spectral range and furthermore reduce the thermal radiation heat losses to the environment. Typical selective coatings provide a thermal emittance lower than 7 percent and a solar absorptance higher than 96 percent [16].

Within the steel tube a heat transfer fluid (HTF), usually thermal synthetic oil, is heated up and then used to generate high-pressure superheated steam. The maximum operating

temperature of the system is limited by the synthetic oil to around 400°C. Alternatively, the thermal synthetic oil can be replaced by water in a so called direct steam generation (DSG) system allowing higher operating temperatures. However, the direct evaporating system presents problems with heat transfer and density change in the two phase fluid flow. Independent of the steam generation the steam is subsequently converted to electricity in conventional power cycles.

Parabolic trough systems are considered to be the most proven and mature of the CSP technologies [11] [18]. The first power plant based on parabolic trough system design was built in 1984 and continues to operate to the present day. A survey conducted by the German Aerospace Center described the technology as commercially available with high levels of experience and reliability [18].

Linear Fresnel reflector (LFR) systems are similar to parabolic trough systems but demonstrate numerous potential advantages [17]. LFR systems consist of an array of nearly-flat reflectors that concentrate the incoming solar radiation on to an inverted linear receiver (Figure 1.3). A secondary concentrator or reconcentrator is placed on top of the receiver to compensate for inaccurate solar tracking and increase the effective absorber area.

Additionally, the planar reflectors reduce wind loads significantly allowing the reflector width per absorber tube to be increased, leading to theoretically higher concentration ratios and higher possible fluid temperatures. LFR systems are also more economical as they use less expensive planar mirrors rather than parabolic trough reflectors. Furthermore, the absorber tubes are stationary which eliminates the need for flexible high pressure fluid joints.

In contrast to parabolic trough systems LFR systems abandon the concept of evacuated glass tubes, a fact that should further decrease the investment cost. However, the convective heat losses which are almost eliminated in the parabolic trough system are become more significant. LFR systems are also more space efficient. As the reflectors are placed equidistant above the ground shading effects are minimized. These advantages of LFR systems result in a cost reduction of the solar field of 50 percent compared to parabolic trough systems [17].

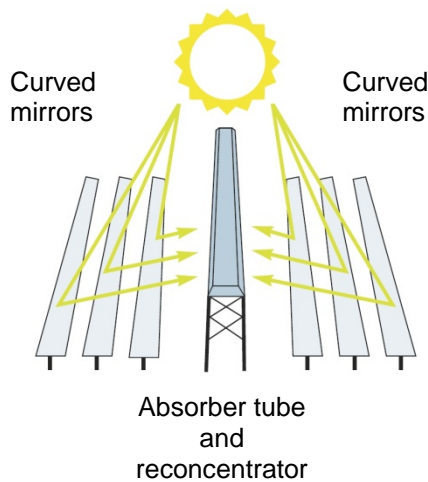


Figure 1.3: Linear Fresnel reflector principle
(on basis of [6])

Within the absorber tubes water is directly evaporated and subsequently converted to electricity in a conventional power cycle.

From a maturity point of view this technology is quite new. The German Aerospace Center study rates the technology as pre-commercial, the experience as low and the reliability as unknown [18].

Dish systems are of the point focusing type. The dish-shaped solar reflector concentrates the incoming solar radiation on to the receiver placed in the dish's focal point. Today concentration ratios are usually above 2000 [19] and reflector areas between 50 to 150 square meters [20] although reflector areas of 400 and 500 square meters have also been proven to work effectively [21].

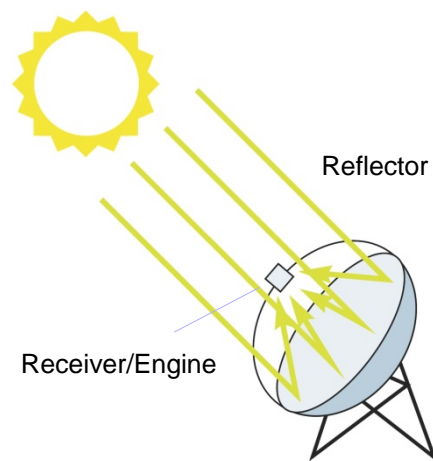


Figure 1.4: Parabolic dish principle
(on basis of [6])

In order to follow the sun over the course of the day the dish system is equipped with a two-axis tracking system. The concentrated radiation is absorbed by a liquid or gaseous HTF at operating temperatures of around 750°C [11]. The HTF is then used to generate electricity in one of the following power cycles.

- Conventional and Organic Rankine cycle
- Open and closed Brayton cycle
- Stirling cycle

Solar dish systems are characterized by their modularity, autonomous operation and inherent hybrid capability. They can be used as small stand-

alone off-grid units, grouped together for small grid-connected power plants and clustered to large grid-connected dish parks. Additionally, solar dish systems demonstrated the highest solar-to-electric conversion efficiency of around 30 percent of all CSP technologies and therefore having the potential to become the least expensive source of renewable energy [19].

Current dish systems with a Stirling engine usually generate an electric output of about 25kW_e and systems using a Brayton cycle usually generate about 30kW_e. Smaller dish systems with 5 to 10kW_e have also been shown [19].

The German Aerospace Center [18] rates the experience with the technology as moderate and the reliability as high.

Central receiver systems (CSR) are of the point focusing type. They consist of a circular array of hundreds to thousands of sun tracking mirrors called heliostats which concentrate the incoming solar radiation at the central receiver located on the top a centrally positioned tower

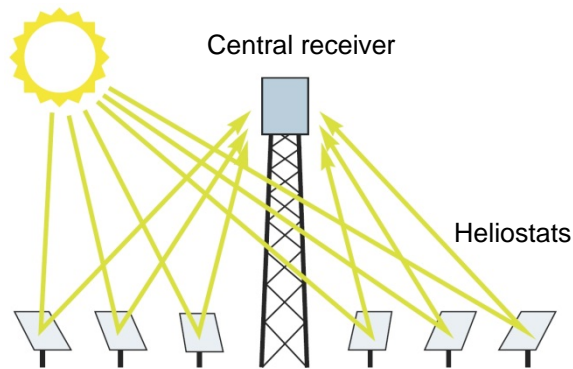


Figure 1.5: Central receiver principle
(on basis of [6])

(Figure 1.5). Concentration ratios for central receiver systems are usually lower than those measured for solar dish systems and are in the range of 500 to 1500 [20] while reflector areas per heliostat commonly in the range of 50 to 150 square meters [23]. The concentrated radiation is absorbed by a HTF that is then used to produce steam that subsequently generates electricity in conventional power cycles. Alternatively, air can be heated within the central receiver and fed directly into a gas turbine.

The current state of today's receiver seems to limit the operating temperature to about 1000°C [31] which subsequently imposes lower gas turbine efficiencies since these components are designed for higher turbine inlet temperatures.

Current central receiver systems are suited to electrical power outputs of 30 to 400 MW_e. Usually, these systems utilize thermal storage to increase the capacity factor from around 25 percent without storage to around 65 percent with storage capabilities [22]. Today there appears to be a trend towards operating solar central receiver systems in a hybrid mode to reduce the financial risk. Fossil fuel based co-firing can be used to both enable the operation of the power plant during low insolation or at nights as well as increasing the operating temperatures.

The German Aerospace Center rates the current level of experience with central receiver technology as moderate and the reliability as moderate [18]

1.3 Objectives

The solar power group within the Energy Department of the Royal Institute of Technology (KTH) Stockholm is currently working on the design and construction of a test rig for a solar driven small scale polygeneration unit. One of the main purposes of the test rig will be to test different solar receivers and their implementation into the polygeneration unit.

The objective of this MSc Thesis work is to design, analyze and verify a solar receiver for the integration into the planned solar polygeneration unit (SPU). Besides generating relatively high receiver outlet temperatures the receiver must be designed to allow the testing of different absorber materials.

First, conceptual layouts of solar receivers for the test rig will be created. Computational fluid dynamics (CFD) and finite element analysis (FEA) tools will then be used to analyze the thermodynamics and mechanical integrity of the receiver designs.

Finally, drawings will be made of a potential solar receiver for integration into the test rig.

1.4 Methodology and report structure

The methodology used in this thesis is based on the Systems Engineering (SE) concept [24] and the VDI-Richtlinie 2221 [25]. Figure 1.6 shows the SE action model which describes how to approach a complex project.

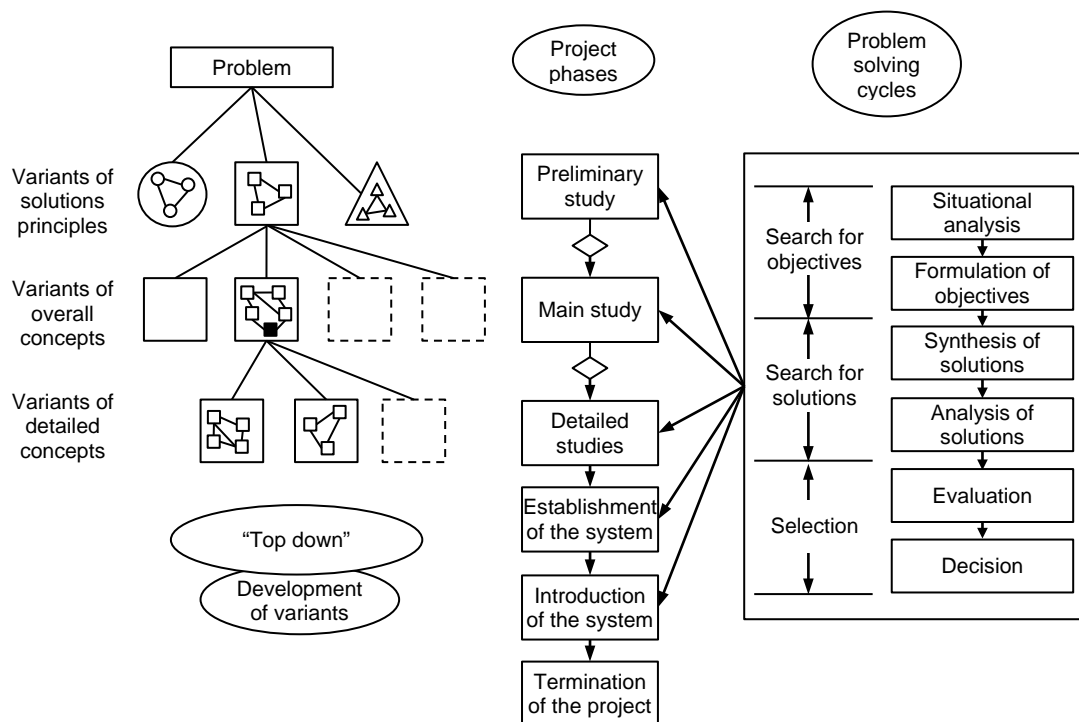


**Figure 1.6: Systems Engineering (SE) action model [24]
Top down approach (left), project phases and problem solving cycle (right)**

A brief introduction and background of concentrated solar power has been given in this section.

Section 2 presents a literature review of different receiver designs that have been discussed, tested and/or commercialized in the past.

In section 3 a preliminary study is conducted discussing variants of solution principles based on the SE top down approach and the project solving cycle as shown in Figure 1.6. Moreover, the study includes a situation analysis of the planned solar polygeneration unit at KTH determining boundary conditions, limitations, and requirement. The main goal of the preliminary study is to find a solar receiver concept that is worth further investigations.

Section 4 presents the main parameter study to find the most feasible receiver design for the solar polygeneration unit. A situation analysis using a relatively simple heat transfer model and a multi objective optimizer provides the initial design parameters for the parameter study. The main analysis is conducted using two dimension rotational symmetric models.

Section 5 presents a more detailed study of the chosen receiver design. Moreover, the previous models are verified using a more complex three dimensional model.

Section 6 presents the main results of the detailed study and a conclusion. Furthermore, possible future work is discussed.

2. LITERATURE REVIEW

As discussed in section 1, concentrated solar power plants are either of the line focusing or point focusing type. Since the planned solar polygeneration unit at KTH is a point focusing system this literature review will be limited to solar receivers suitable for this application.

Figure 2.1 and Figure 2.2 give an overview of possible solar receivers and suggest a possible classification system based upon both a system and component view.

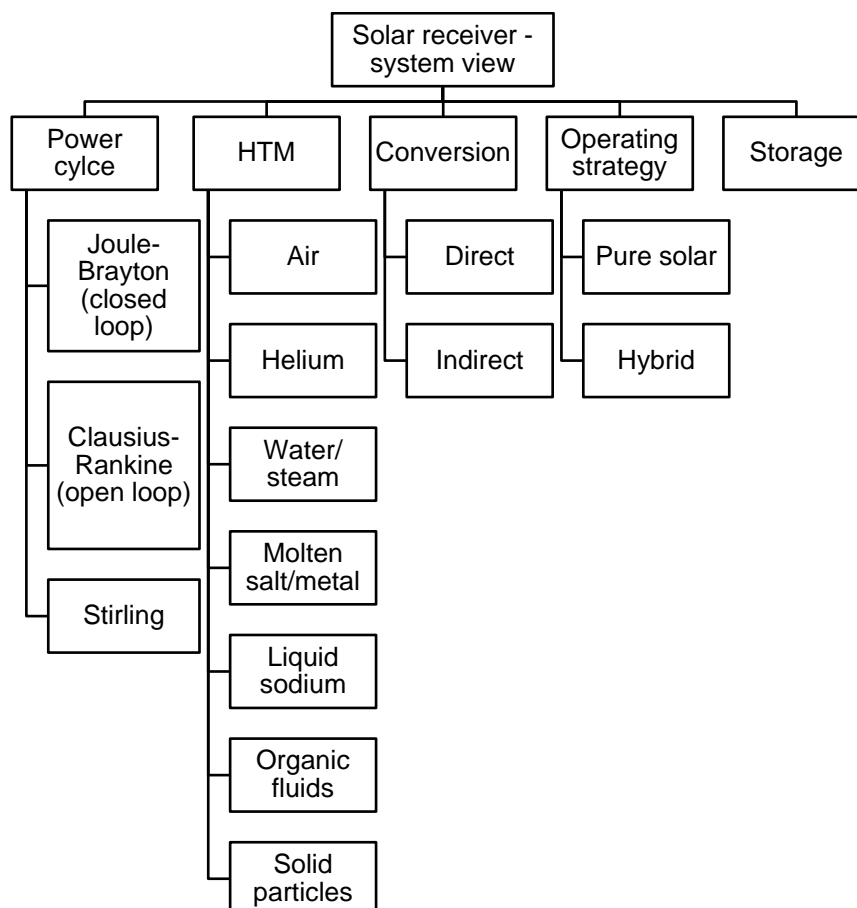


Figure 2.1: Classification of solar receivers – system view

When the CSP plant system is looked at as a whole a multitude of different system configurations are possible. The power cycle forms the basis for the whole system. A wide variety of heat transfer media (HTM) can be used to generate electricity directly or detoured to heat exchangers to heat up the working fluid of the power cycle. Moreover, different operation strategies and storage possibilities are available.

From a component point of view multiple configurations are possible as well. Solar receiver can be distinguished by their type, their operating pressure and operating temperature. As already presented in the system view the way of heat transfer and HTM used can also be used for classification. Moreover, different absorbers can be used in solar receivers.

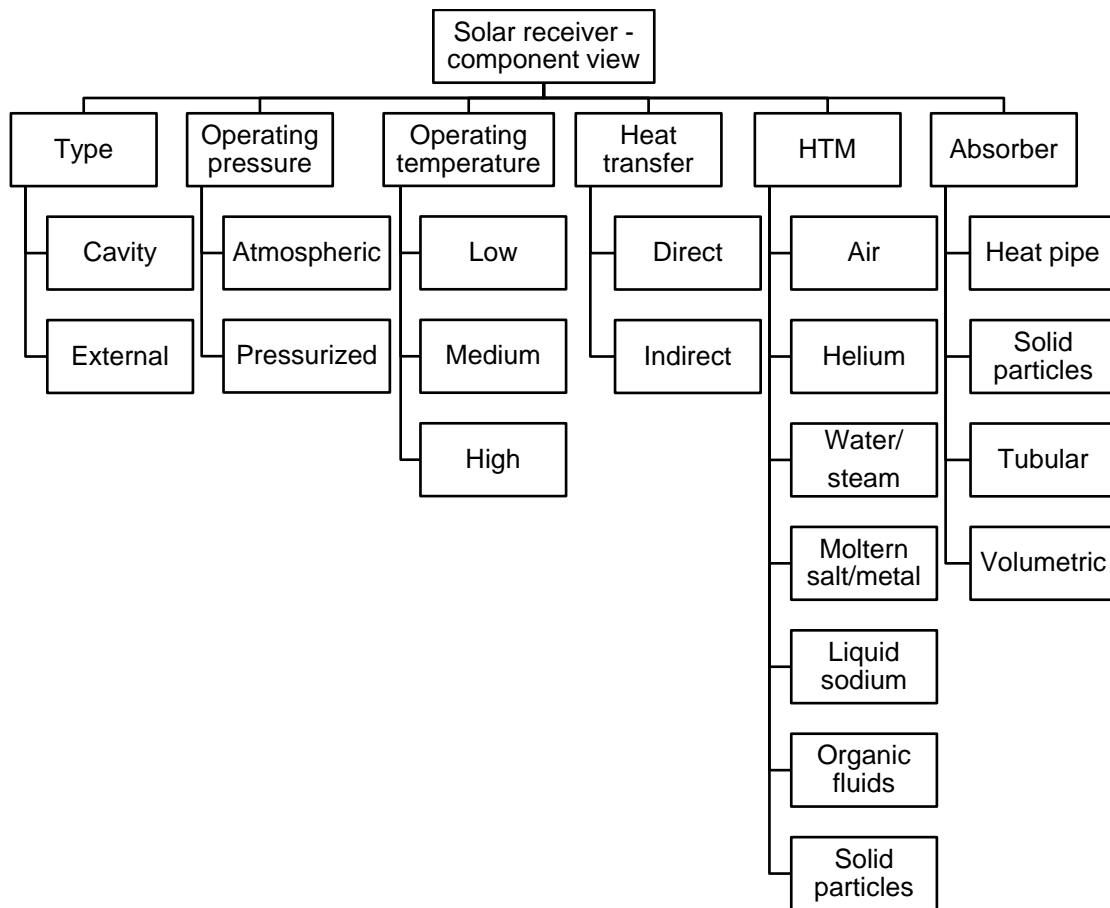


Figure 2.2: Classification of solar receivers – component view

A more detailed classification of volumetric receivers is shown in Figure 2.3.

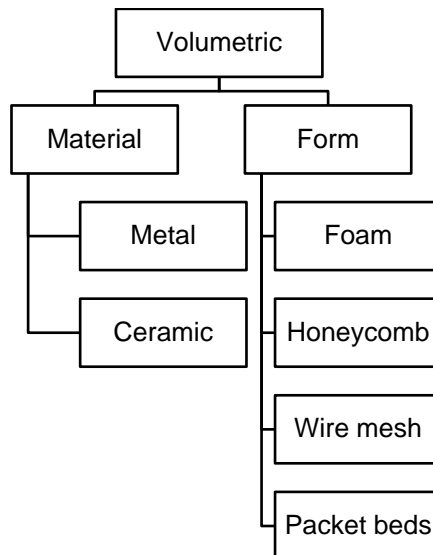
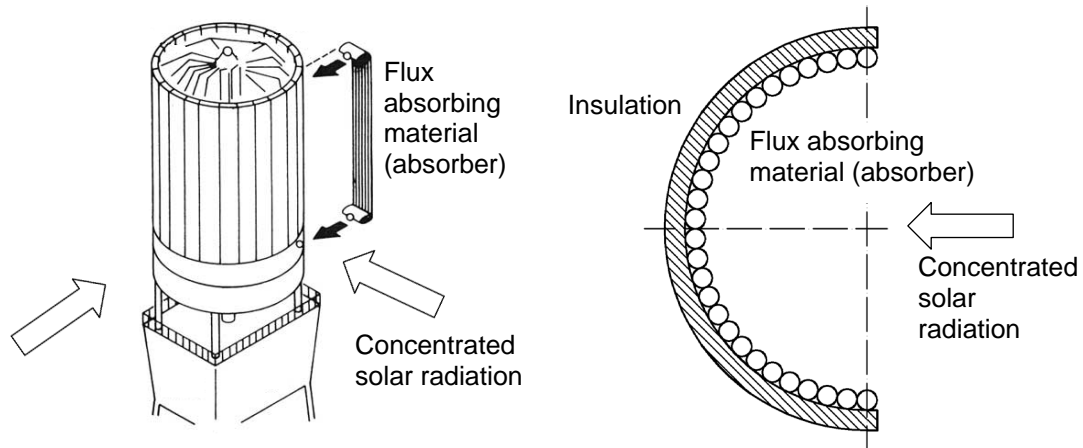


Figure 2.3: Classification of volumetric solar receivers

While the optimal configuration of the system is subject of current research, the component view has greater relevance for this work. Therefore, the following sections discuss receiver characteristics from the component point of view.

2.1 Type of point focusing receivers

There are two main types of point focusing solar receiver: external and cavity, which are differentiated from one another by the location of the absorbing material. Figure 2.4 shows both types – on the left side the external type and on the right side the cavity type.



*Figure 2.4: Solar receiver types
“Solar One” external solar receiver (left, on basis of [27]) and cavity receiver (right)*

While the external receiver type is characterized by the flux absorbing material (absorbers) being located on the exterior of the receiver, the cavity type is characterized by the flux absorbing material being located within a cavity. The heat losses of external receivers are mainly determined by its surface area. Attempts to reduce this area are limited by the maximum operating temperature of the absorber and thus by the heat removal capacity of the HTF. The better the heat removal capacity of the HTF, the lower the absorber temperature, which means receiver size and heat losses can be reduced. For example, the absorber area can be cut in half if a HTF of water/steam is replaced by sodium due to its superior heat transfer capabilities [27].

The cavity receiver type on the other hand, reduces convective and radiative heat losses to the environment by placing the absorber inside a cavity. In principle, the cavity design itself is enough to reduce the convective heat losses. However, the placement of the cavity receiver influences the efficiency significantly.

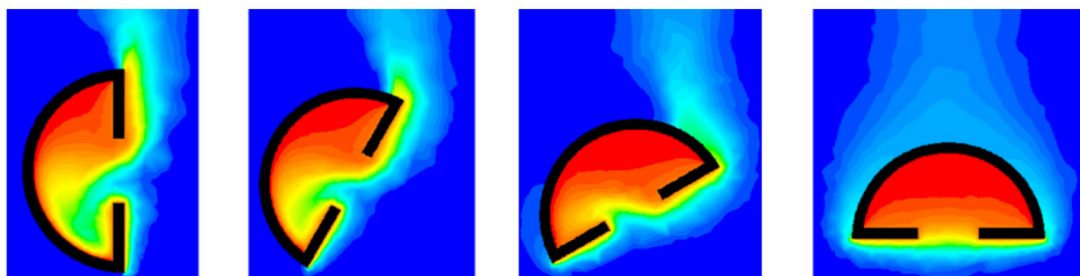


Figure 2.5: Convective heat losses of a cavity receiver [28]

Figure 2.5 shows convective heat losses for a cavity receiver type where blue represents low temperatures and red high temperatures. Clearly, horizontal placement of the cavity

minimizes convective heat losses although this configuration may make it difficult to mount the receiver.

Concerning radiative losses the cavity has distinct advantages over the external receiver. Losses due to reflection of impinging concentrated solar radiation can be significantly reduced and in some cases they become so low that they are even negligible [29]. Thermal radiation losses in the infrared-band can also be greatly reduced.

The advantage of the external receiver type with an absorber arrangement of 360° is that it allows concentrated solar radiation to impinge from all sides whereas the acceptance angle of the cavity type is limited to around 60 to 120° depending on the design [27]. In order to increase the acceptance angle multiple cavities can be placed adjacent to each other.

2.2 Operating pressure

Two different receiver operation modes can be distinguished depending on the system layout; operation under ambient pressure and pressurized operation. The pressure in the pressurized operation ranges from a few bar in a micro gas turbine cycle to around 20 to 25bar in a conventional gas turbine cycle.

2.3 Operating temperature

The operating temperature of the receiver is also determined by the system layout. Low temperature receivers operate at fluid outlet temperatures up to 550°C , medium temperature receivers operate up to 800°C , and high temperature receivers above 800°C [31].

The operating temperature highly influences the type of absorber and materials that can be used. This will be further discussed in section 2.5.

2.4 Heat transfer and heat transfer media

There are two different principles of heat transfer in a solar power plant. On the one hand there is the direct heat transfer shown in Figure 2.6 on the left. The energy of the concentrated solar radiation is transferred by the receiver directly to the working fluid of the power cycle. On the other hand there is the indirect heat transfer shown in Figure 2.6 on the right. In this case, the energy of the concentrated solar radiation is transferred to a HTM in the receiver. In a subsequent step the hot HTM fluid is used to heat up the working fluid of the power cycle.

The most common used HTMs are fluids like air, water/steam, helium, molten salt/metal and liquid sodium [22]. Every HTF has its own advantages, e.g. liquid sodium offers better heat transfer capabilities compared to water/steam as discussed in section 2.1. Other systems use solid particle HTMs which are subsequently used to heat up the working fluid of the power cycle.

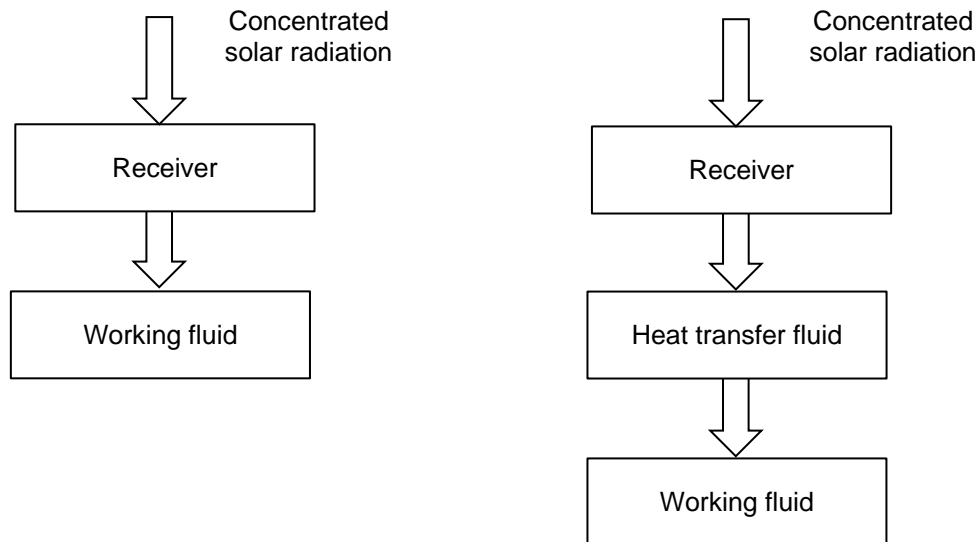


*Figure 2.6: Heat transfer mode
Direct heat transfer (left), indirect heat transfer (right)*

2.5 Absorber

In CSP plants the absorber has the task to absorb the impinging concentrated solar radiation and transfer the absorbed heat to the HTF. Early days of receiver development and research the main focus was on tubular designs and later the development of volumetric receiver designs began [26].

2.5.1 Tubular receiver designs

In tubular receiver designs concentrated solar radiation is absorbed by a bundle of tubes able of withstanding high temperatures. The energy is then transferred to the HTF flowing within the tube. Figure 2.7 shows the basic principle. It can be seen that the solid temperature of the tube is always greater than the fluid temperature limiting the maximum operating temperature.

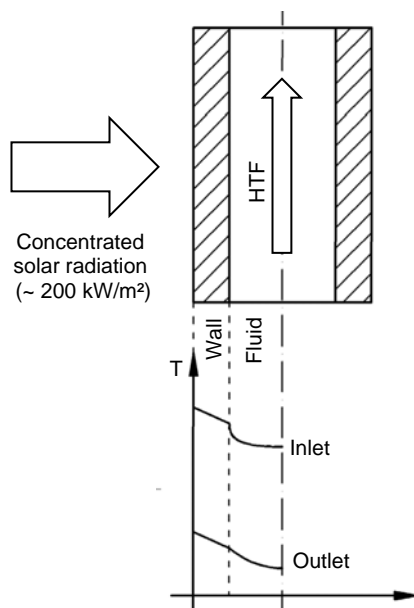


Figure 2.7: Absorption and heat transfer of tubular receivers (on basis of [26] and [30])

On the other hand tubular designs have the advantage that the HTF fluid can easily be pressurized and the only pressure limit is the yield strength of the tubes.

Usually, tubular receiver designs have heat loss problems to the ambient due to reflection, thermal radiation and convection losses. In order to minimize reflection losses the tubes are commonly covered with solar selective coating to increase the solar absorptance. However, the solar flux remains limited to about 200 kW/m² [26]. Ambient heat losses can also be reduced by placing the tubular absorber within a cavity as described in section 2.1.

Figure 2.8 shows already existing and tested tubular solar receivers. On the left, the

SOLGATE low temperature receiver is displayed. According to the SOLGATE report [31] tubular solar receivers for receiver fluid outlet temperatures below 550°C considerably reduce the overall cost compared to volumetric receivers (see also section 2.5.2).

One of the first central receivers ever built, the Solar One external receiver, is presented on the right-hand side of Figure 2.8. Solar One was operated between 1982 and 1988 in Nevada in the USA with a nominal power output of 10MW_e, direct evaporation of water within the receiver, and electricity generation in a conventional Rankine cycle [22]. For a long time it was the world’s largest solar power tower plant demonstrating the feasibility of large-scale power production of such systems until the PS10 plant was built 2007 in Spain.

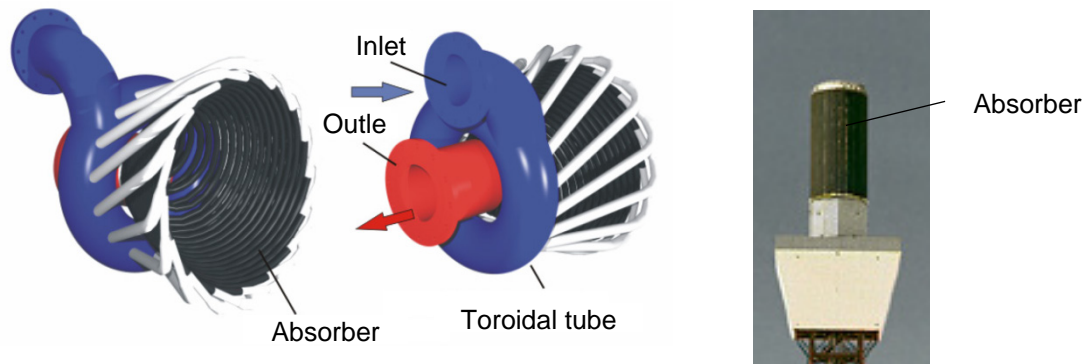


Figure 2.8: Existing tubular receiver designs
SOLGATE low temp. tubular receiver (left, [31]), Solar One tubular receiver (right [32])

Figure 2.9 shows recent tubular receiver design developments. On the left the SOLar HYbrid power and COgeneration plants (SOLHYCO) tubular cavity design is presented [33]. This system is based on a 100 kW micro turbine and the receiver works at a fluid outlet temperature of around 800°C with the possibility to operate on varying contributions of solar power input and fuel.

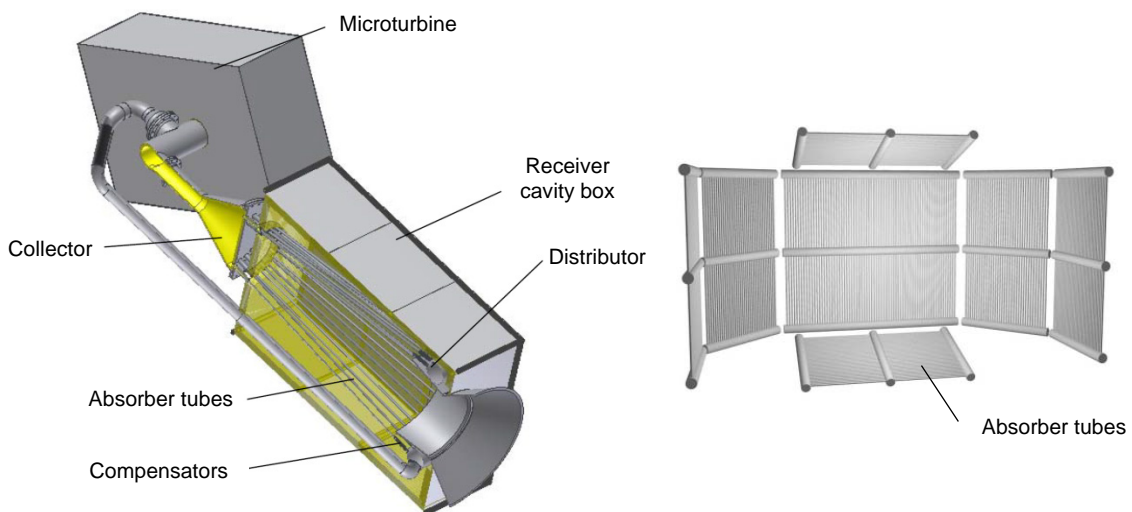


Figure 2.9: Recent tubular receivers designs
SOLHYCO tubular cavity receiver (left, [33]), SOLUGAS tubular cavity receiver (right, [34])

The main improvement of the SOLHYCO receiver is reported to be a novel absorber tube design based on profiled multi-layer (PML) tubes. The concept relies on absorber tubes that are built of multiple layers in this case an outer layer of heat resistant steel-alloys and an inner

layer of heat conductive copper. This causes the heat transfer from the irradiated absorber wall to the HTF to increase, reducing the circumferential temperature differences within the tubes and hence improving the durability. Due to manufacturing problems the PML tubes were not tested during the project period between 2006 and 2010.

The right side of Figure 2.9 presents the Solar Up-scale Gas Turbine System (SOLUGAS) tubular cavity design based on a solar pre-heated Brayton topping cycle and a subsequent Rankine bottoming cycle [34]. The receiver consists of several tubular receiver panels and is used to pre-heat the pressurized HTF which is air up to 650°C before it enters the combustion chamber of a commercial 4.6MW_e gas turbine. Due to the relatively low temperatures conventional material can be used for the absorber tubes.

2.5.2 Volumetric design

Volumetric receiver designs are based on absorber materials consisting of a multitude of porous interlocking shapes such as knit-wire packs, foam, honeycomb structures, packed beds and others with a specific porosity. The absorber material occupies a volume inside the receiver and is irradiated by concentrated solar radiation. The absorber material absorbs the energy in the depth of the structure thus heating up. This effect causes one of the biggest advantages of volumetric solar receivers namely the increase of the heat transfer area and the consequent reduction of local flux density at the absorber surface. The HTF, which commonly is air, passes through the volume at the same time the solar energy is transferred via forced convection from the absorber material to the HTF.

Radiative heating of the HTF due to the effects of absorption and scattering of the impinging concentrated solar radiation inside the HTF are very small compared to the convective heat transfer and usually negligible according to Incropera et al. [35]. Figure 2.10 shows the basic principle including the volumetric effect that causes the temperature of the irradiated surface

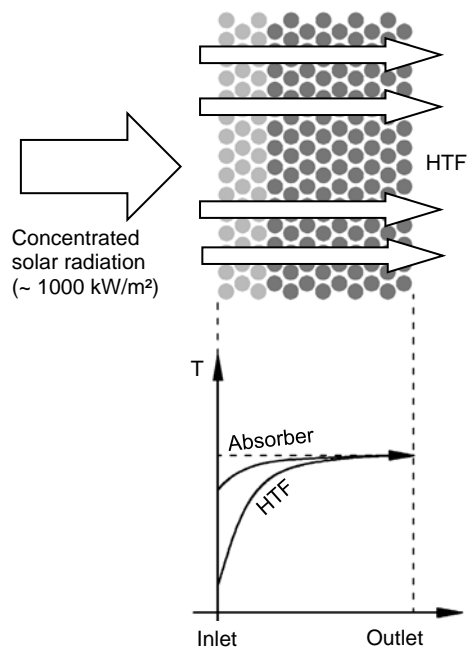


Figure 2.10: Absorption and heat transfer of volumetric receivers (on basis of [26] and [30])

to be lower than the outlet temperature [26] causing decrease re-radiation losses.

Concerning the choice of material for the absorber due to relatively high temperatures metals or ceramics seem to be appropriate. According to Ávila-Marín [26] volumetric receivers with metallic absorber are able to produce fluid outlet temperatures from 800°C to 1000°C, receivers with siliconized silicon carbide (SiSiC) ceramic absorbers temperatures of 1200°C, and receivers with silicon carbide (SiC) absorbers temperatures of 1500°C.

The main advantage of volumetric receivers compared to tubular ones is the ability to absorb relatively high solar flux, operate at high temperatures while still being compact [29].

2.5.2.a Flow stability

An important issue of volumetric receivers is flow stability. Figure 2.11 shows the basic relationship between solar flux and flow speed according to Becker et al. [36]. It can be seen that local high solar flux leads to low mass flow and local low solar flux leads to high mass flow. The main reason for this behavior is the temperature dependency of the dynamic viscosity of the HTF, in the case of volumetric receivers mostly air.

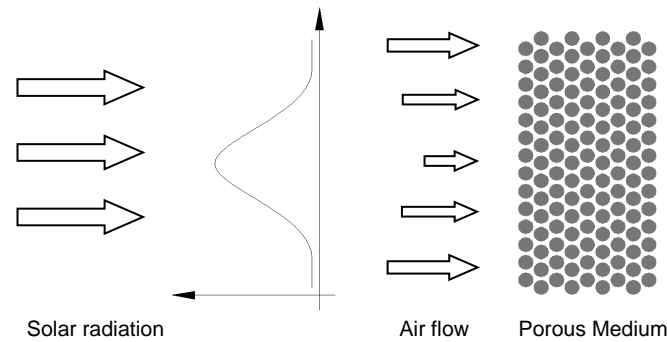


Figure 2.11: Flow instability issues (on basis of [36])

Becker et al. [36] state that theoretical approaches of Kribus et al. [37] and others as well as numerical simulations agree fairly well with experiments and general tendencies could be shown. Apparently, the pressure loss characteristics of the porous media have the most important influence on flow instability. If the pressure drop within the porous media depends linearly on the flow velocity (Darcy flow) instabilities can occur, whereas if there is a solely quadratic dependency (Forchheimer flow) instabilities do not occur.

Furthermore, Becker et al. [36] propose a simple mathematical model based on the Darcy-Forchheimer equation that describes the pressure loss within a porous media as a function of the superficial fluid flow velocity. The pressure loss is described by

$$-\frac{dp}{dx} = \frac{\mu}{K} \cdot u + \frac{\rho_f \cdot C_f}{\sqrt{K}} \cdot u^2 \quad \left(\frac{Pa}{m}\right) \quad (2.1)$$

where p stands for pressure, x is the index variable in flow direction, K the specific permeability, C_f the inertial coefficient, μ the dynamic viscosity and, ρ the density of the HTF and u the superficial fluid velocity. The specific permeability and inertial coefficient are properties of the absorber material and will be discussed later in more detail.

Generally, the way to increase the fluid outlet temperature of the receiver at a constant solar flux is to decrease the mass flow which also leads to a decreased pressure loss. If the flow is unstable more than one mass flow is possible for one specific pressure drop. Figure 2.12 on the left shows what happens to the quadratic pressure drop for different solar fluxes when there is a solely linear dependence on the flow velocity, that is when $C_f=0$. If for one and the same pressure drop more than one fluid outlet temperature and therefore connected mass flows are possible, instability occurs. That means that for one and the same solar flux parts of the absorber can have a low mass flow and others a high mass flow and thus different temperatures. This may lead to local overheating and to absorber failures such as melting or cracking. It can also be seen that instabilities only occur above a certain solar flux level.

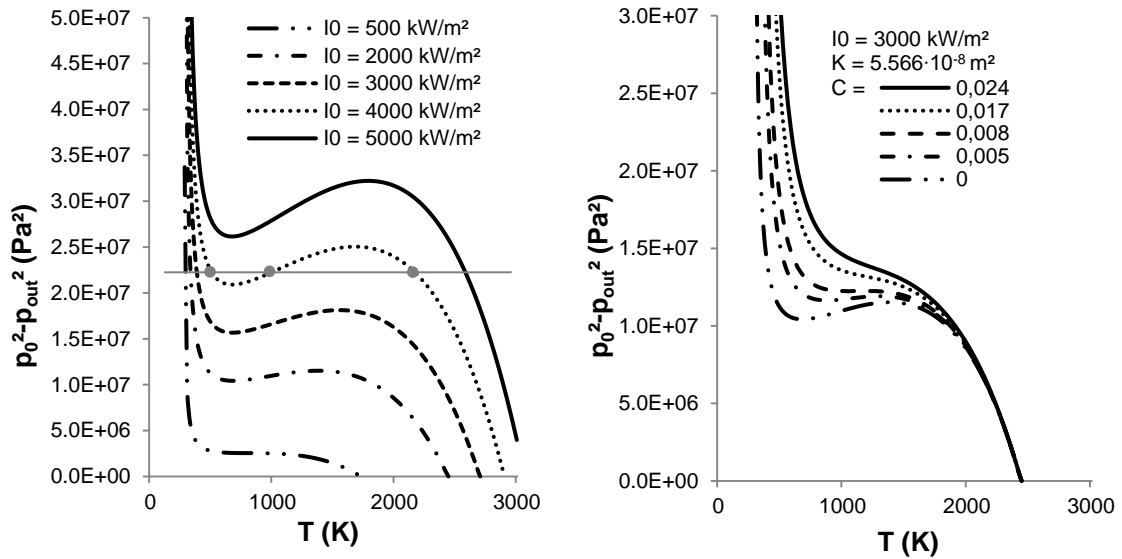


Figure 2.12: Quadratic pressure drop versus HTF temperature (on basis of [36]) for different solar fluxes (left), for different inertial coefficients C_f (right) (material for graphs: SiC foam, porosity 0.9, cell diameter 2mm)

Figure 2.12 on the right shows what happens to the quadratic pressure drop when there is also a quadratic dependence on the flow velocity, that is when $C_f > 0$. Changing the pressure drop characteristic of the absorber causes significant changes. The higher the inertial coefficient C_f gets the more unlikely it is for instabilities to occur. Becker et al. [36] suggest a critical product of the inertial coefficient and the square root of specific permeability above which instabilities are not expected.

$$C_f \cdot \sqrt{K} = 1.94 \cdot 10^{-6} \quad (m) \quad (2.2)$$

2.5.2.b Open volumetric receiver

As described in section 2.2 volumetric receivers can work either at ambient pressure or pressurized. Receivers operating at ambient pressure are usually called open volumetric receivers and ones operating at elevated pressure levels closed (or pressurized) volumetric receivers.

Figure 2.13 on the left shows the operating principle of open volumetric receivers based on the High Temperature Receiver (HiTRec I) [26]. Concentrated solar radiation is absorbed by a ceramic honeycomb absorber heating it up. Ambient air is sucked into the receivers acting as the HTF. In order to improve the receiver efficiency open volumetric receivers system often implement an air return system. The “cold” air leaving the system is first used for cooling the receiver structure and then fed into the system again in front of the absorber in order to reuse the enthalpy. The HiTRec I was not equipped with such an air return system but successor projects (HiTRec II, SOLAIR 200, SOLAIR 3000) were [26]. Air return ration of around 50 percent are commonly used [26].

On the right of Figure 2.13 the assembly of multiple open volumetric receivers on top of a solar power tower is shown.

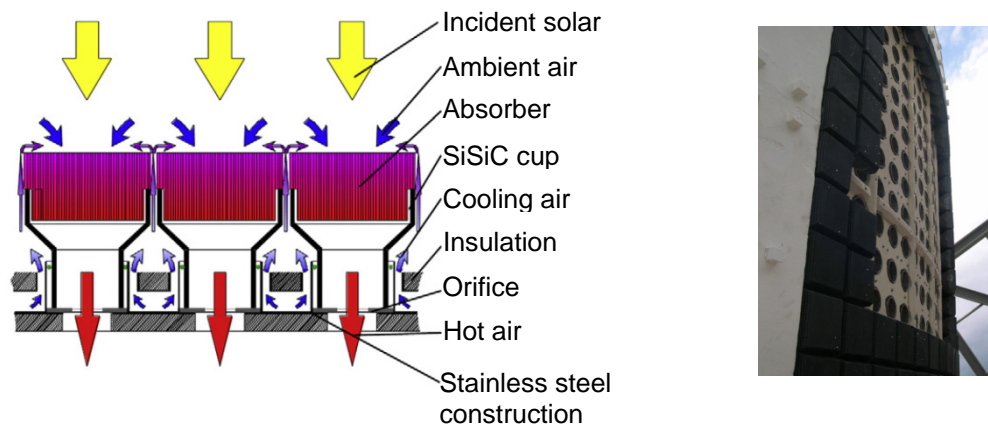


Figure 2.13: Open volumetric receivers
HiTRec I (left, [26] on basis of [38]) and SOLAIR 3000 assembly (right, [26])

Usually, the hot air is used to produce superheated steam and subsequently generate electricity in a conventional Rankine cycle. Right now the above mentioned technology is at a pre-commercial state. 2009 the first demonstration plant using SOLAIR 3000 technology started its operation in, Germany [26].

2.5.2.c Closed volumetric receiver

The second type of volumetric receivers is the closed volumetric receiver that is usually pressurized. These receivers rely on a transparent window to enable high-pressure operation, minimize reflection losses, re-radiation and convection losses. Figure 2.14 shows the working principle of two closed volumetric receivers. On the left the Directly-Irradiated Annular Pressurized Receiver (DIAPR) that is based on porcupine absorbers made of high temperature ceramics is shown. On the right a Receiver for Solar-Hybrid Gasturbine and CC Systems (REFOS) with a metallic or ceramic absorber is shown.

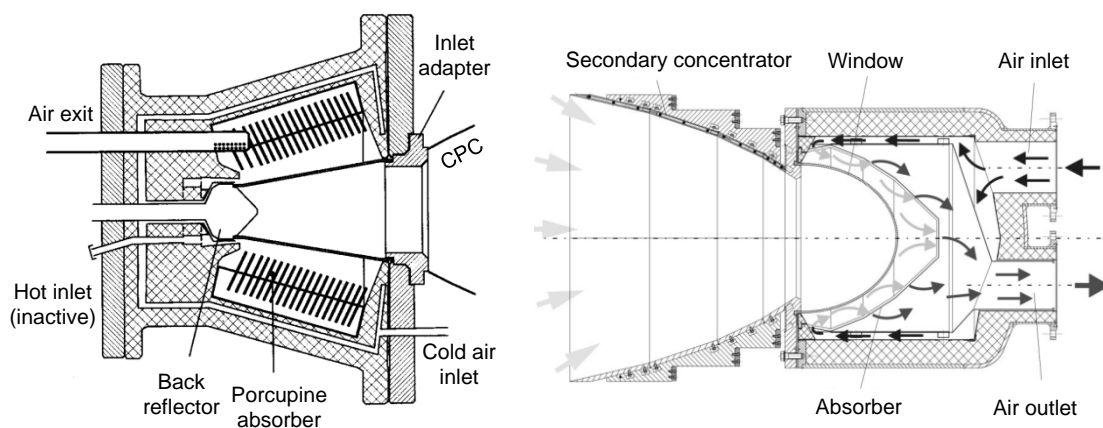


Figure 2.14: Closed (pressurized) volumetric receivers
DIAPR receiver (left, [39]), REFOS receiver (right, [41])

The operating principle of the closed volumetric receivers is similar to open volumetric receivers. One difference is the use of secondary concentrators in order to focus the solar radiation on the absorber and shield the surrounding receiver structure. As mentioned before closed volumetric receivers are equipped with a transparent window through which the

concentrated solar radiation has to pass through before impinging on the absorber and heating it up. The HTF (air) is not ambient air but pressurized air entering the receiver at the “air inlet”. It is then heated up by the hot absorber and leaves the receiver at the “air outlet/exit”. It can then be used in a solar only cycle directly as fuel for a conventional gas turbine or in a hybrid cycle as preheated air entering the combustion chamber of a gas turbine cycle.

According to Ávila-Marín [26] a lot of research has been done in the past 20 years that demonstrated that transparent windows pose difficult design problems. The main difficulties are related to “*limitations in size and specific requirements in optical properties, mechanical strength, high variable working temperature, stress-free installation and sealing and cooling capability*” [26].

The first mentioned volumetric receiver, the DIAPR receiver, was developed by the Israeli Weizmann Institute of Science. The main components are the secondary compound parabolic concentrator (CPC) to increase the solar flux even more and to protect the receiver structure, the frustum-like pressure window that could withstand a pressure of 50 bar, and the porcupine volumetric absorber.

Karni et al. [29] already showed 1997 that experimentally their DIAPR was able to work at pressures of 10 to 30 bar and solar radiation flux of up to 10 MW/m², while producing HTF outlet temperature of up to 1300°C. Further testing proved that the design was able to operate at pressures of 17 to 20 bar and solar fluxes between 3.6 and 5.3 MW/ m² while creating HTF outlet temperatures of 1200°C for an extended time period of around 250 hours [39]. In these tests hundreds of heating and cooling cycles were passed through without noticeable local hot spots neither on the absorber nor on the window. The lack of hot spots and the fact the porcupines are mechanically independent allowing each element to expand as the temperature varies avoiding thermal stresses no failures appeared. The receiver efficiency was estimated to be between 70 and 90 percent during the tests. Worth mentioning are also the reflectivity losses of the glass window which were found to be less than one percent using ray tracing calculations [29]. Concluding, Kribus et al. [39] state that the DIAPR theoretically was able to produce HTF outlet temperatures of 1400°C without compromising the components’ thermal limits.

Recently, an Israeli company called Aora built a solar tower power demonstration plant using the above mention DIAPR technology in the Arava desert in southern Israel. The plant is based on a single receiver module and generates 100 kW_e and additionally 170 kW_{th} [40].

The second mentioned volumetric receiver, the REFOS receiver, was developed in the REFOS project starting 1996 and was also used within the SOLGATE project starting 2001. The main components are the secondary compound parabolic concentrator (CPC) to increase the solar flux even more and to protect the receiver structure, the doomed quartz glass window that could withstand a pressure of 19.5 bar and additionally providing reduced reflectivity losses compared to a flat window, and the volumetric metallic wire mesh absorber.

In the REFOS project the receiver was supposed to absorb 350 kW_{th} of concentrated solar radiation at a solar flux of around 1000 kW/m² per module producing air outlet temperatures of 800°C at a pressure of 15 bar and an efficiency of 80 percent [41]. Tests showed that air

outlet temperatures of 815°C were possible even though the efficiency was not as high as expected due to poor performance of the secondary concentrator [41].

Although, the tests have been quite short compared to lifetime requirements first signs of degradation of the quartz window were revealed ([42] as cited in [26]).

Within the SOLGATE project the REFOS receiver was used as a medium and high temperature receiver. For the medium temperature application the metallic wire mesh absorber was maintained while the absorber in the high temperature receiver was replaced by a highly porous ceramic foam absorber [31]. From the previous REFOS project problems with the quartz window were known and therefore an active multiple air jet window cooling was installed. In a test in spring 2003 air outlet temperatures of 960°C were reached before a problem in the gas turbine caused the test to stop. The active window cooling seemed to work keeping the window temperature well below the acceptable limit of 800°C [43].

Concluding, volumetric absorbers seem to have both major advantages and disadvantages which have to be considered for the specific application.

2.5.3 Heat pipe design

Another way of absorbing concentrated solar radiation and transferring it to the HTF is by using heat pipes.

Figure 2.15 shows the basic working principle of a heat pipe. According to Bienert [49] the main components are a sealed container, a wick, and a suitable working fluid that is in equilibrium with its own vapor i.e. saturation condition. When heat is applied to the evaporator the local temperature raises slightly causing some of the fluid to evaporate. Furthermore, the temperature difference causes a change in vapor pressure due to the saturation condition. Consequently, vapor flows to the cooler part of the heat pipe namely the condenser where it releases its latent heat and liquefies again. The liquid is then pumped back through the wick because of capillarity effects. It is favorable to place the heat pipe vertically with the evaporator below the condenser in order to let gravity forces assist the pumping.

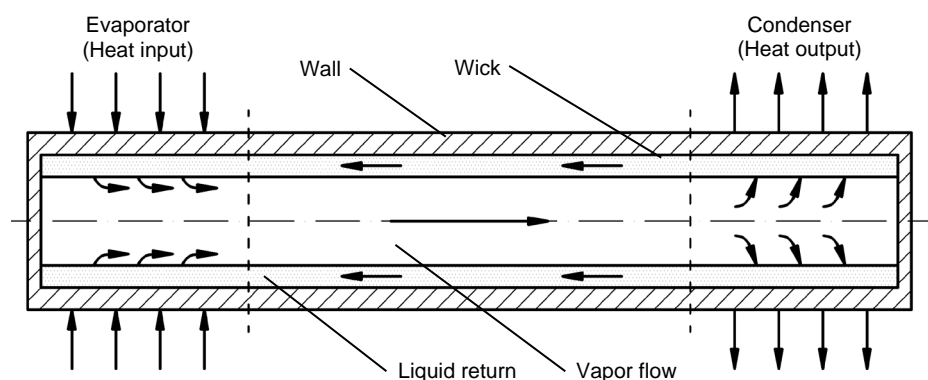


Figure 2.15: Schematic representation of a heat pipe (on basis of [47])

The first use of heat pipe solar receivers was in the aerospace applications. Later in the 1970s the use of heat pipes receivers for concentrated solar power plant emerged. Bienert [49] presents the main advantages and disadvantages as well as examples of heat pipe solar receivers using pure liquid alkali metals. This working fluid is chosen as it appears to be the most suitable in the temperature range of interest of 400-1000°C.

The main advantages are

- nearly loss free flux transformation from the high solar flux to the lower heat flux on the gas system side,
- high temperature capabilities (500-1000°C),
- low pressure stresses in high temperature component as the heat pipe works at nearly ambient pressure,
- low pressure drop on the gas side due to large design flexibilities,
- uniform circumferential temperature distribution due to extremely high heat transfer capabilities of the working fluid, as well as
- redundancy due to multitude of heat pipes per receiver.

The main disadvantages on the other hand are

- limited receiver outlet temperatures of 900°C because of temperature limits of the metallic heat pipe material,
- the lower operating limit of 400°C below which liquid metal heat pipes do not function,
- an evaporator flux limit of around 1 MW/m², and
- a slight orientation sensitivity.

Figure 2.16 shows a heat pipe receiver configuration developed for the U.S. DOE used in a Brayton cycle with an electrical power output of 10 MW_{el}. The heat pipes are mounted on panels inside a cavity. Concentrated solar power impinges on the heat pipes which transfer the energy nearly isothermal to the finned condenser section and subsequently to the HFT.

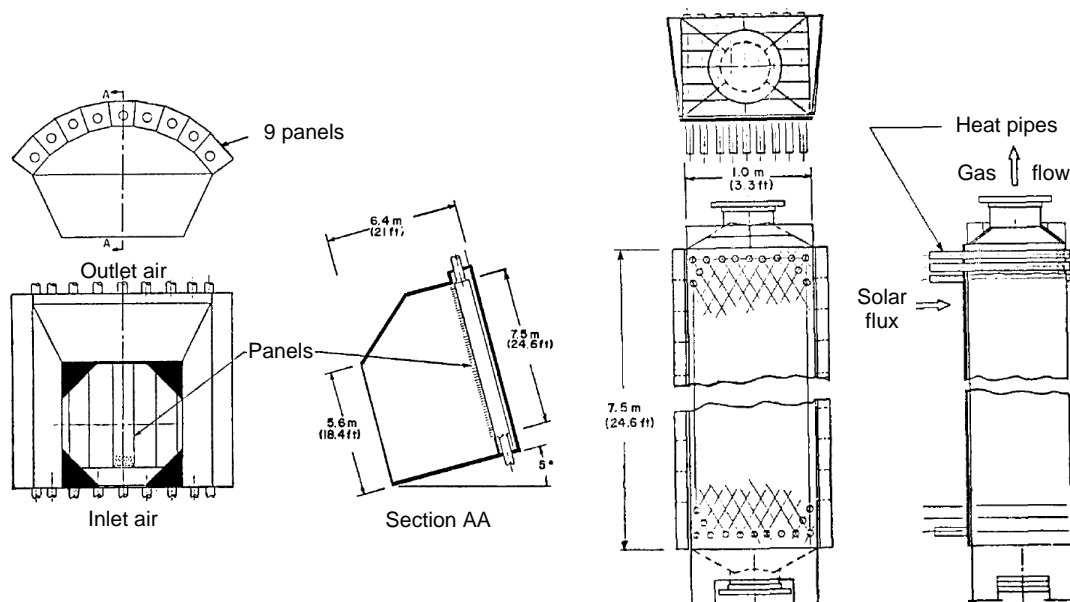


**Figure 2.16: Heat pipe receiver configuration [49]
Cavity receiver configuration (left), panel configuration (right)**

A heat pipe receiver of the National Aeronautics and Space Administration (NASA) for space applications is shown in Figure 2.17. The operating principle is similar to the above mentioned solar receiver. Solar radiation impinges on the heat pipes in the receiver portion which transfer the energy to the plate fin heat exchanger and subsequently to the working

fluid. The main difference can be seen in the thermal storage device portion. There, a multitude of canisters of phase change material (PCM) surround the heat pipe providing thermal energy storage.

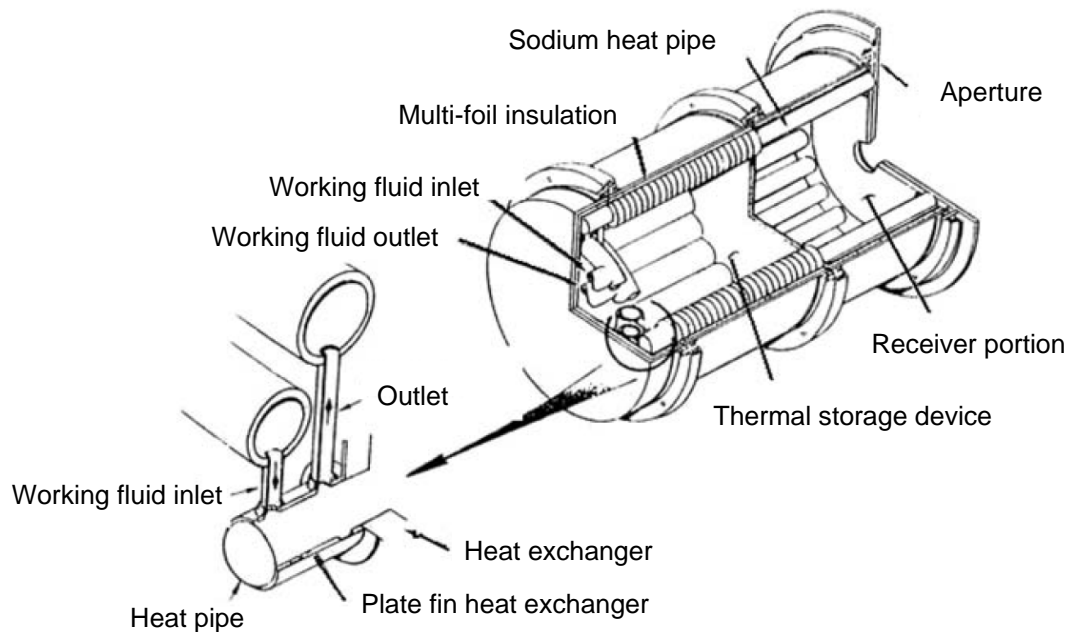


Figure 2.17: Heat pipe receiver for Brayton cycle [51]

A few more applications of heat pipe solar receiver can be found in literature especially for parabolic dish concentrators working with Stirling engines [52]. As the objective of this thesis is to design a solar receiver using a Brayton cycle designs working with Stirling engines are not discussed further.

2.5.4 Solid particle design

The last way of absorbing concentrated solar radiation presented in this chapter is by using solid particles. Figure 2.18 shows the concept, a drawing and a picture of a solid particle receiver that is currently being tested by Sandia National Laboratories for the U.S. DOE [54].

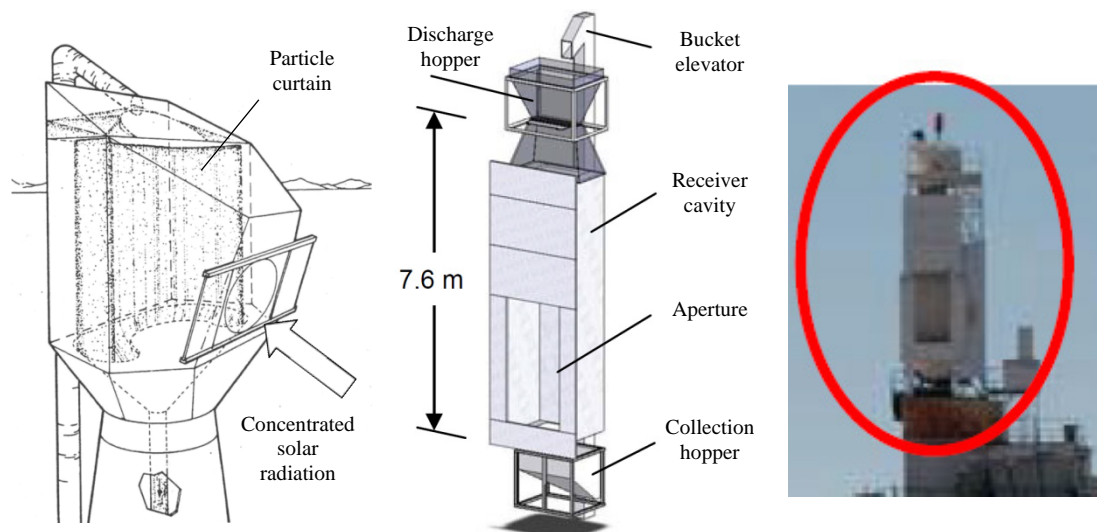


Figure 2.18: Solid particle receiver Concept (left, [53]), drawing (middle, [54]), picture (right, [54])

The concept is based on a curtain of falling solid ceramic particles that directly absorbs the concentrated solar radiation and are heated to temperatures in excess of 1000°C [55]. The differentiation between absorber and heat transfer medium is ambiguous. That is the reason why solid particles were also mentioned as a heat transfer medium previously.

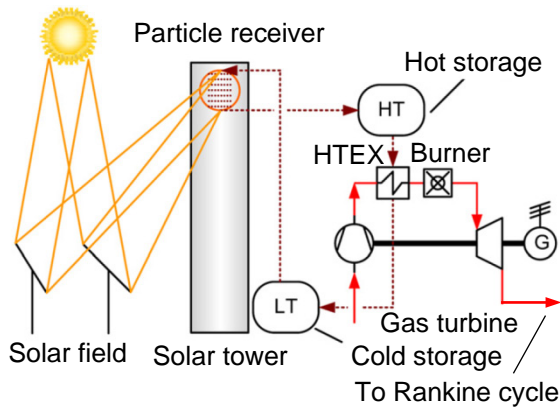


Figure 2.19: Solid particle receiver layout for electricity generation (on basis of [57])

The main application of solid particle receivers is as a heat source for chemical processes especially for solar-driven water-splitting thermo-chemical (WSTC) cycles for hydrogen producing rather than electricity generation [55] [56]. However, DLR is currently assessing a particle receiver system for electricity generation shown in Figure 2.19 [57]. Particles are pumped from the cold storage tank at 360°C to the particle receiver where they are heated up to 1000°C and

subsequently stored within the hot storage. The hot particles are used for preheating air up to 950°C before entering the burner of an open Brayton cycle. The heat transfer between the particles and the pressurized air happens in special direct contact heat exchanger that is equipped with an internal lock system for pressure balance and filters. The heat exchanger is not described in more detail. After the leaving the turbine the exhaust gases are used in a HRSG to produce steam for a subsequent Rankine cycle.

The main problems of solid particle receivers are losses due convection and wind effects. Several studies have been conducted trying to prevent these losses by an aerowindow right outside the aperture (i.a. [58], [59]). Figure 2.20 shows improvement on the air velocity vectors of a solid particle receiver when an aerowindow protects the cavity.

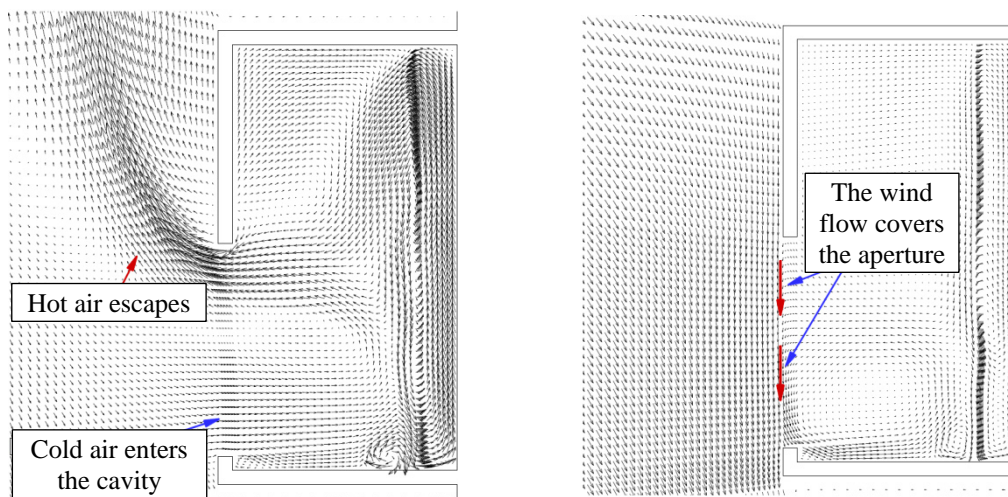


Figure 2.20: Solid particle receiver velocity vectors [58] Without aerowindow (left), with aerowindow (right)

3. PRELIMINARY STUDY

The goal of this preliminary study is to find a solar receiver concept for further investigation in the main study.

The approach to this study is based on the problem solving cycle of the systems engineering concept as described in the methodology. It recommends searching for objectives first, then searching for different variants of solution principles and finally selecting a promising principle for further analysis.

3.1 Situational analysis and boundary conditions

In order to formulate objectives a clear picture of the prevailing situation is necessary. Therefore, this section is dedicated to discuss the boundary conditions, limitations, and requirements for the solar receiver for KTH's SPU.

3.1.1 System layout

Basis of the SPU is an externally fired micro gas turbine system. Figure 3.1 shows a picture of the micro gas turbine as well as its current system layout. Air at ambient conditions ($p_{amb} \approx 1\text{bar}$, $T_{amb} \approx 20^\circ\text{C}$) is compressed in a radial compressor (C) with a pressure ratio π_c of about 3, heated up in the recuperator (heat exchanger) and expanded in the micro gas turbine (T). Right now the only energy source is natural gas that is combusted within the burner (B). The air needed for combustion is provided by a small blower delivering a mass flow of around 0.01 kg/s. The hot gases are subsequently mixed with the exhaust air of the micro gas turbine to reduce the temperature to acceptable limits and fed into the recuperator to heat up the incoming air. The recuperator is currently limited to a maximum operating temperature of 650°C but will be replaced within this year to sustain temperatures of 780°C .

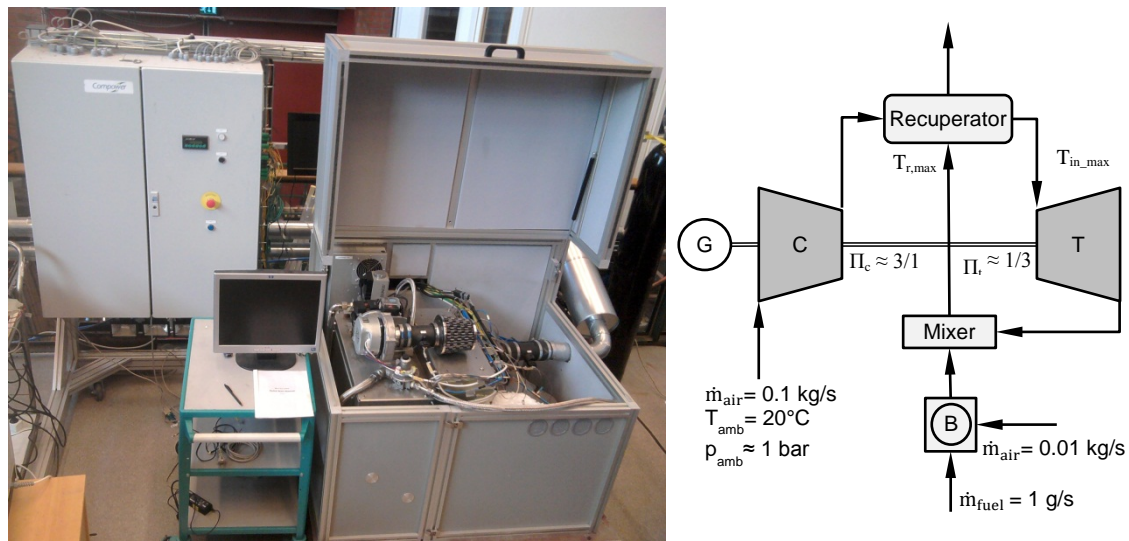


Figure 3.1: Micro gas turbine (COMPOWER)

The main reason to heat up the incoming air in a recuperator and not as usual in a combustion chamber between compressor and turbine is the fact that the unit is intended for testing polygeneration applications. Thus, allowing the combustion of a variety of different fuels without the risk of turbine fouling because the turbine always operates with pure air

Tests have been performed showing that the system currently works at a fuel-to-electricity efficiency of 18.46 percent generating 4.615 kW_{el}.

The basic schema of KTH's SPU at its first development stage is shown in Figure 3.2. The main source of energy is light radiation provided by high power lamps substituting solar radiation. The radiation is then concentrated by the parabolic dish reflector onto the solar receiver.

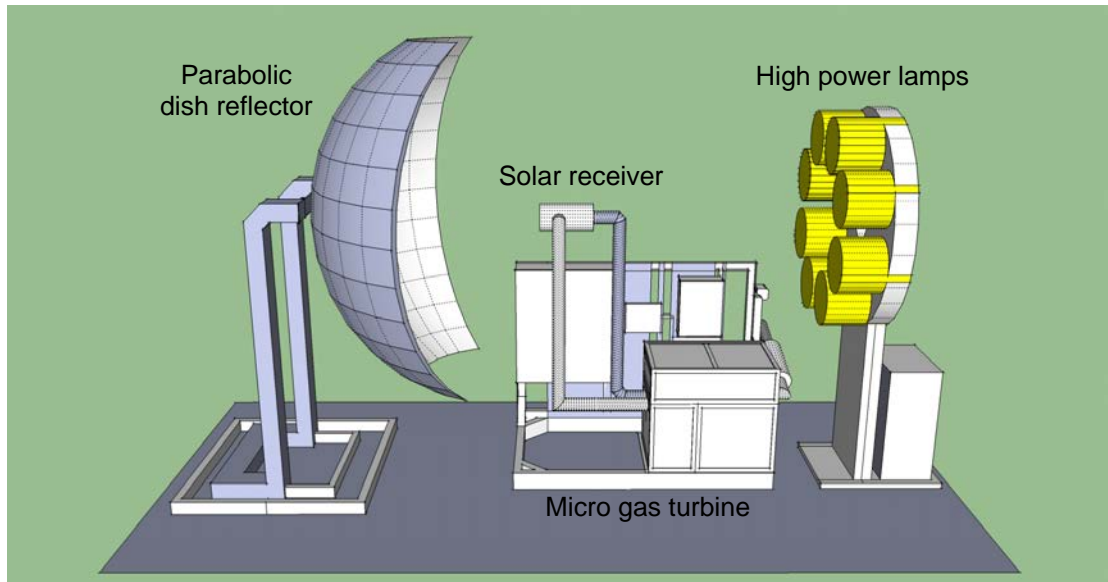


Figure 3.2: KTH SPU schema

For solar receiver testing two different configurations have been proposed which are shown in Figure 3.3. In the first configuration shown on the left the receiver is placed in front of the turbine. The solar receiver operates at inlet temperatures of around 500°C and a pressure of 3 bar while allowing receiver outlet temperatures up to the maximum turbine inlet temperatures of 900°C.

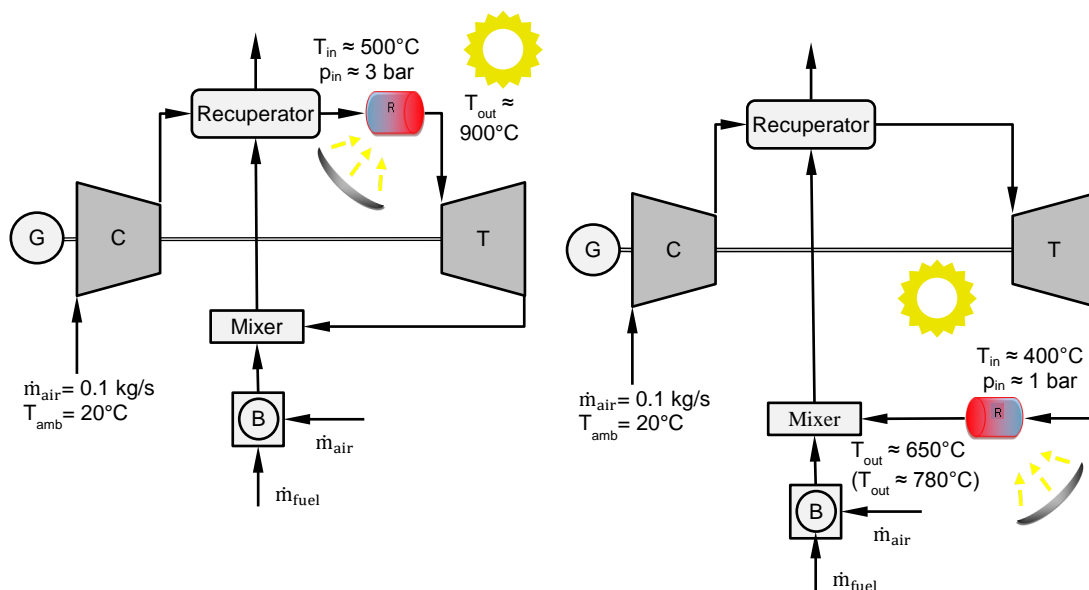


Figure 3.3: KTH SPU configurations

Configuration 1: solar receiver before turbine (left), configuration 2: solar receiver after turbine (right)

In the second configuration shown on the right the receiver is placed after of the turbine. The solar receiver operates at inlet temperatures of around 400°C which corresponds to the turbine outlet temperature and a pressure of 1 bar. The main difference to configuration one is that the maximum receiver outlet temperature is limited to the material limits of the recuperator of 650°C respectively 780°C. By using a mixer a temperature decrease is possible even though it might not be much as the air mass flow of the burner is limited to about 0.01 kg/s by the blower.

Theoretically, both configurations can be operated in a solar only as well as in a hybrid mode where the burner and mixer are used to increase the air temperature before the recuperator.

Because configuration one is unfavorable due to integration problems of the solar receiver into the system first tests will be very likely performed using configuration two.

3.1.2 Fluid boundaries

Based on the two different SPU configurations Table 3.1 outlines the fluid boundary conditions of the solar receiver.

Table 3.1: Fluid boundary conditions

Configuration	1	2
Working fluid	Air	
Inlet pressure (bar)	3	1
Inlet temperature (°C)	500	400
Outlet temperature (°C)	900	800
HTF mass flow (kg/s)	0.1	

3.1.3 Radiation boundaries

Another crucial boundary condition is the irradiance level to which the solar receiver is exposed. Since the design and construction of the unit is still in progress the real irradiance level cannot be determined experimentally but can only be estimated.

With the assumption that all radiant losses can be described by a parabolic dish reflector efficiency the radiant power in the focal spot can be calculated by

$$\bar{\Phi} = n \cdot P_{el} \cdot \eta_{el-light} \cdot \eta_{dish} \quad (W) \quad (3.1)$$

where $\bar{\Phi}$ stands for the mean radiant power, n is the number of lamps used, P_{el} the electrical power demand of one lamp, $\eta_{el-light}$ the electricity-to-light efficiency of the lamps, and η_{dish} the efficiency of the parabolic dish reflector. The parabolic dish reflector efficiency accounts for losses to due inaccurate concentration of the radiation besides the intended focal point and losses due to heating of the reflector itself and consequently causing radiative and convective heat losses. Losses due to blocking of the radiation because of objects in the path between the lamps and the reflector, in that case the absorber are not considered. Moreover, for further calculations the focal spot is considered to be perfectly circular and the radiant power outside the focal point of the reflector is considered to be zero.

Thus, the mean irradiance \bar{E}_0 in the focal point can be calculated by

$$\bar{E}_0 = \frac{\bar{\Phi}}{A} = \frac{4 \cdot \bar{\Phi}}{d_{focal_spot}^2 \cdot \pi} \quad \left(\frac{W}{m^2}\right) \quad (3.2)$$

where $\bar{\Phi}$ is the above mentioned mean radiant power, and A and d the area and the diameter of the focal spot respectively.

The lamps used in the rig are based on short arc xenon lamps purchased from the Chinese company NOYE. Their nominal electrical power consumption is 7 kW and an electricity-to-light efficiency 90 percent [45]. Based on consultations with KTH personnel and preliminary calculations of them the reflector efficiency is estimated to be 85%. Furthermore, the focal spot is considered to be circular with a diameter of 10 cm.

Figure 3.4 shows the mean irradiance as a function of the number of lamps based on the above mentioned parameter.

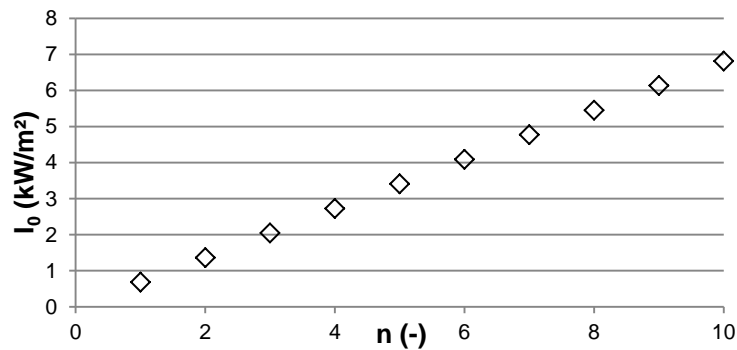


Figure 3.4: Mean irradiance for different number of lamps

Preliminary calculations considering losses of the receiver with an overall receiver efficiency of 90 percent indicate that an air mass flow of 0.1 kg/s and a temperature rise from 400°C to 800°C seven lamps are required. Due to rather huge uncertainties in the assumptions the rig is designed to be equipped with 8 lamps resulting in a mean irradiance of 5.455 MW/m².

In reality, the radial distribution of the irradiance will not be uniform. Experiments at the solar laboratory of the Swiss Federal Institute of Technology (ETH) Zürich whose laboratory is similar the one KTH is building have shown that the irradiation at the focal plane will be highly non uniform [44]. Figure 3.5 on the left shows the idealized two dimensional irradiance map at the focal plane and on the right an idealized one dimensional irradiance graph. The dashed line represents the experiments at ETH whereas the solid line represents an exponential approximation with the same mean irradiance.

The reason why the test data has been idealized concerning the circumferential dependence of the irradiance is the fact that the test rig at KTH is not built yet and nobody knows exactly how the irradiance distribution will look like in reality and calculations are simplified a lot.

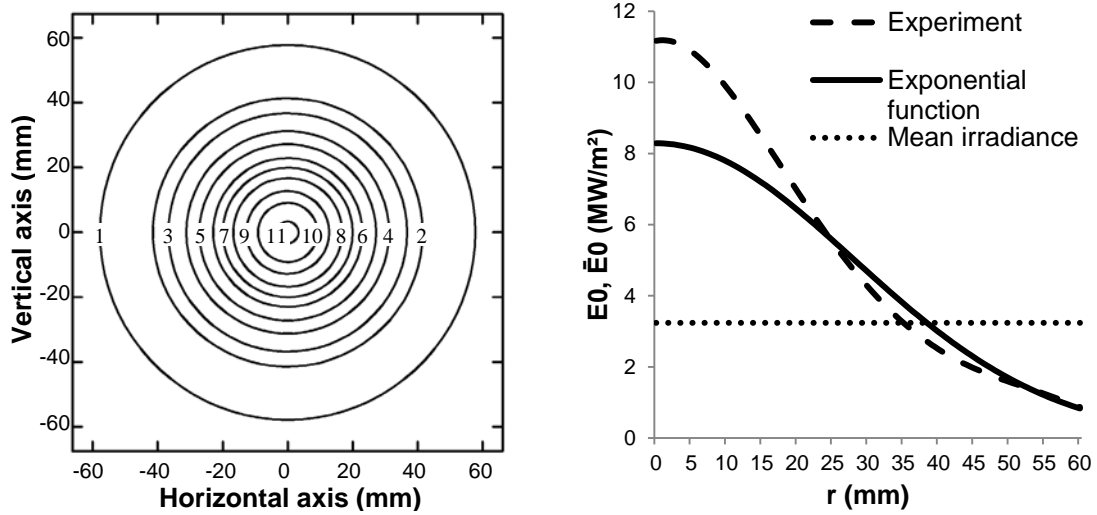


Figure 3.5: Irradiance at focal plane in MW/m² (on basis of [44])
Idealized irradiance map (left), idealized radial irradiance (right)

An exponential approximation of the test data was chosen due to simplicity considerations for following calculations compared to a polynomial approximation. The following correlation to describes the radial irradiance distribution at the focal plane

$$E_0(r) = \hat{E}_0 \cdot e^{(\ln(\delta) \cdot (\frac{r}{R})^2)} = \hat{E}_0 \cdot \delta^{(\frac{r}{R})^2} \quad \left(\frac{W}{m^2}\right) \quad (3.3)$$

where E_0 stands for the irradiance, \hat{E}_0 is the peak irradiance in the middle of the focal point ($r=0$), δ a new defined irradiance distribution factor, r the radial index variable, and R the diameter of the focal spot. The irradiance distribution factor is defined as the ratio of the irradiance at the outer border of the focal spot ($r=R$) and the irradiance at the middle of the focal spot ($r=0$).

$$\delta = \frac{E_0(r = R)}{E_0(r = 0)} \quad (-) \quad (3.4)$$

Since the irradiance distribution is rotationally symmetric the mean irradiance \bar{E}_0 can be calculated by

$$\bar{E}_0 = \frac{1}{A} \iint E_0(r) \cdot dA = \frac{1}{R^2 \pi} \int_{r=0}^R E_0(r) \cdot 2r\pi \cdot dr \quad \left(\frac{W}{m^2}\right) \quad (3.5)$$

Inserting equation 3.3 in equation 3.5 the peak irradiance for a given mean irradiance follows.

$$\hat{E}_0 = \frac{\bar{E}_0 \cdot \ln(\delta)}{(\delta - 1)} \quad \left(\frac{W}{m^2}\right) \quad (3.6)$$

Using the method of least squares the irradiance distribution factor for a best approximation can be found to be 0.04. Unfortunately, this factor leads to extremely high peak values in the middle of the focal spot especially at higher mean irradiances. Therefore, one of the objectives in the design and construction of the KTH test laboratory has to be a reduction of the radial difference in irradiance. This suggestion has already been passed on and will be considered and therefore for further calculations an irradiance distribution factor of 0.1 will

be used. In Figure 3.5 on the right the exponential approximation using the before mentioned distribution factor can be seen as the solid line.

For future assessments spectral irradiance distribution is of interest as well. The spectral distribution of a single lamp is shown in Figure 3.6.

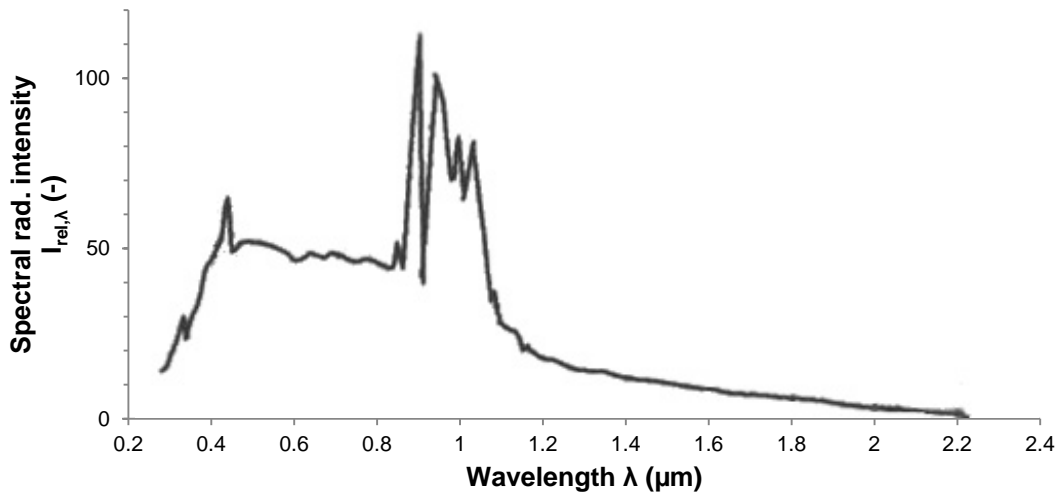


Figure 3.6: Spectral radiant intensity of a single lamp [45]

Assuming that the spectral distribution does not change from the lamps to the receiver, every lamp produces the same spectral distribution and the superposition is perfect the receiver is exposed to the same spectral distribution.

In order to make qualitative predictions of the feasibility of tested solar receivers the test results inside the solar laboratory using artificial sun light need to be related to real solar irradiance. Figure 3.7 shows the solar spectral irradiance at the top of Earth's atmosphere and the surface. Comparing it to the previous figure it can clearly be seen that there is a difference especially in the infrared range between 800 and 1100 nm.

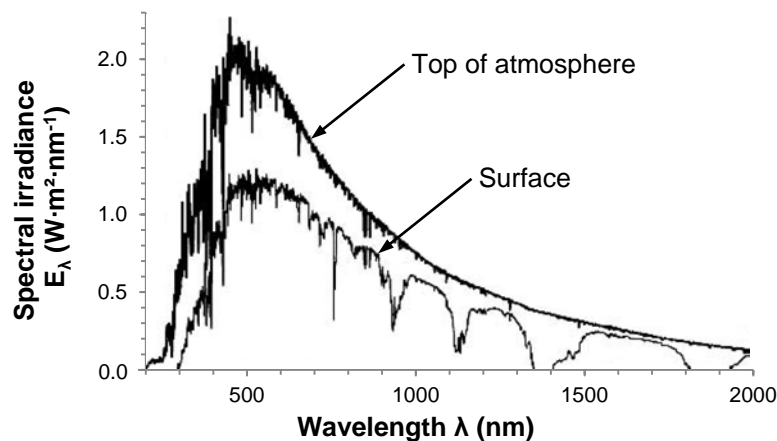


Figure 3.7: Solar spectral irradiance on top of the atmosphere and Earth's surface [46]

Nonetheless, these comparisons exceed the scope of this thesis. It is just important to keep in mind that all the following calculations are based on the conditions only found in the laboratory.

3.1.4 Summary of boundary conditions

Table 3.2 shows a summary of the expected boundary conditions of solar receiver for both SPU configurations.

Table 3.2: Boundary conditions

Configuration	1	2
Working fluid	Air	
Fluid inlet pressure p_{in} (bar)	3	1
Fluid inlet temperature $T_{f,in}$ (°C)	500	400
Fluid outlet temperature $T_{f,out}$ (°C)	900	800
HTF mass flow \dot{m} (kg/s)	0.1	
Mean irradiance \bar{E}_0 (MW/m ²)	5.455	
Peak irradiance \hat{E}_0 (MW/m ²)	13.956	
Irradiance distribution	$E_0(r) = \hat{E}_0 \cdot \delta\left(\frac{r}{R}\right)^2$ (3.7)	
Irradiance distribution factor δ	0.1	
Focal spot diameter R (mm)	50	

3.2 Detailed objectives

After finishing the situational analysis the next step is to determine detailed objectives for the preliminary study. The objectives are based on the overall objectives presented in section 1 but aligned with the findings of the situational analysis and therefore more specific.

In order to reduce the complexity of this preliminary study the main focus is on the absorber and not the whole receiver. The following objectives have to be met within this preliminary study.

- For the two different layout configurations presented before the receiver must be able to heat the working fluid to the required outlet temperature. Table 3.1 outlined the heating requirements for both configurations.
- The pressure drop of the receiver especially in the absorber must be kept as low as possible as the receiver operates within a Brayton cycle that is very sensitive to pressure drops. Preliminary economic calculations at the Energy Department suggest that a pressure drop of less than 4 percent within the receiver is required for a reasonable operation of a solar power plant with a Brayton cycle. Nevertheless, consultation with Anders Malmquist who is responsible for the micro gas turbine system showed that the pressure drop should not exceed 10 percent of the inlet pressure.
- The solar receiver and especially the absorber must be able to withstand mean irradiance levels up to 5.5 MW/m² and peak radiation levels in excess of that. Furthermore, the receiver must be designed to work with a circular focal spot as small as 10 cm in diameter
- Material temperatures and stresses within the absorber must not exceed limits of commercially available materials.

- The receiver should be designed in a way that allows testing of different absorber materials and the design should not add unnecessary complexity to the system.

3.3 Synthesis of solutions

The task of the synthesis section is to find different variants of solution principles that are able to meet the previous defined objectives. The main reason for trying to find different variants is to avoid the trap of choosing the first variant that comes to one's mind although it might not be the best or most suitable variant for the particular problem.

According to Wohinz [60] one way to structure the search for different variants of solutions is the morphological analysis that was created by Zwicky F. Based on the literature review done before Table 3.3 shows the parameters and their relevant "values" or appearances creating the morphological box. This morphological box contains 1728 possible configurations which can be calculated as the product of the number of appearances of each parameter ($2 \cdot 2 \cdot 3 \cdot 2 \cdot 6 \cdot 3 \cdot 4$).

Table 3.3: Morphological box for receiver design

Parameter	Appearance of the parameters					
Type	External	Cavity				
Pressure of HTM	Atmospheric	Pressurized				
Operating temperature	Low	Medium	High			
Heat transfer	Direct	Indirect				
Heat transfer medium	Air	Water/steam	Helium	Molten salt/metal	Liquid sodium	Solid particles
Working fluid	Air	Water/steam	Helium			
Absorber	Tubular	Volumetric	Heat pipe	Solid particles		

Before thinking of different solution variants it is wise to apply the objectives and boundary conditions to the morphological box to reduce the complexity. Wohinz [60] mentions that one should keep in mind that even non-optimal appearances of parameters can yield to excellent overall solutions due to particular advantages of combinations. Nevertheless, it does not make any sense to consider solutions that are not within the scope of this thesis.

Due to the requirement of receiver outlet temperatures of 800 and 900°C respectively the operating temperature can be considered to be high. Thus, the values low and medium from the parameter operating temperature can be eliminated.

Considering the objective that the receiver system should not add unnecessary complexity to the overall system an indirect heat transfer does not seem very suitable. At the moment the system already relies on one gas to gas heat exchanger. Having a receiver system with an indirect heat transfer would impose another heat exchanger. When pursuing this thought it is obvious that a solid particle receiver system is not suitable either. The only way to transfer the energy stored within the solid particles is with the help of a heat exchanger. Hence, the

application of a solid particle receiver will be abandoned as well. A heat pipe receiver in the narrow sense works with an indirect heat transfer as well although it does not require an extra heat exchanger in the system. Therefore, a heat pipe receiver is considered as a possible solution.

Concerning the working medium of the power cycle the circumstances are clear. The system is an open Brayton cycle operating with air. Therefore, the only appearance of the parameter working fluid that remains is air.

All this considerations simplify the upper morphological box and reduce the possible configuration from 1728 to 144. The result can be seen in Table 3.4.

Table 3.4: Simplified morphological box

Parameter	Appearance of the parameters					
Type	External	Cavity				
Pressure of HTM	Atmospheric	Pressurized				
Operating temperature	High					
Heat transfer	Direct	Indirect				
Heat transfer medium	Air	Water/steam	Helium	Molten salt/metal	Liquid sodium	Solid particles
Working fluid	Air					
Absorber	Tubular	Volumetric	Heat pipe			

According to Ritchey [61] the next step in the morphological analysis process is the reduction of the formally possible configurations to a smaller set of internally consistent configurations. Zwicky called this process the principle of contradiction and reduction whereas Ritchey [61] calls it cross-consistency assessment (CCA). The reason why the CCA is applied to reduce the numbers of configurations is simple. *“While the number of configurations in a morphological field grows exponentially with each new parameter, the number of pair-wise relationships between conditions grows only as a quadratic polynomial - or, more specifically, proportional to the triangular number series.”* [61]

Table 3.5: Cross-consistency assessment matrix

		Type		Pressure		Temp.	HT		HTM						Working fluid	Absorber		
		External	Internal	Atmospheric	Pressurized	High	Direct	Indirect	Air	Water/steam	Helium	Molten salt/metal	Liquid sodium	Solid particles	Air	Tubular	Volumetric	Heat pipe
Type	External	0																
	Internal	-	0															
Pressure	Atmospheric	+	+	0														
	Pressurized	+	+	-	0													
Temperature	High	+	+	+	+	0												
HT	Direct	+	+	/	+	+	0											
	Indirect	+	+	+	+		-	0										
HTM	Air	+	+	+	+	+	+	+	0									
	Water/steam	+	+	/	+	+	+	+	-	0								
	Helium	+	+	+	+	+	+	+	-	-	0							
	Molten salt/metal	+	+	+	/	/	/	+	-	-	-	0						
	Liquid sodium	+	+	+	/	/	/	+	-	-	-	-	0					
	Solid particles	+	+	+	/	+	/	+	-	-	-	-	-	0				
Working fluid	Air	+	+	+	+	+	+	+	+	/	/	+	+	+	0			
Absorber	Tubular	+	+	+	+	/	+	+	+	+	+	+	+	/	+	0		
	Volumetric	+	+	+	+	+	+	+	+	+	+	/	/	/	+	-	0	
	Heat pipe	+	+	+	+	/	+	+	/	/	/	+	+	/	+	-	-	0
		+	Relation possible															
		-	Logical contradiction															
		/	Empirical constraint (relationship highly improbable)															
		0	Relation with itself															




Based on the morphological analysis Table 3.6 shows the most promising solution principles for both SPU configuration described in section 3.1.

The first set of solution principles is based on a tubular receiver design. The only difference between the two configurations is that pressure level of the HTM. Since both configurations are based on a direct heat transfer the HTM and the working fluid are the same. In one configuration the receiver works at a pressure level close to the atmospheric pressure and the other configuration the HTM is pressurized within the receiver.

The second set of solution principles is based on a volumetric receiver design. Again, the only difference between the configurations lies in the pressure levels. The configuration where the pressure level of the HTM (= working fluid) is close to the atmospheric pressure is similar to an open volumetric receiver design. Whereas, the configuration where the HTM (= working fluid) is pressurized the design is similar to a closed volumetric receiver.

Table 3.6: Solution principles

Tubular				Volumetric				Heat pipe			
Parameter	Appearance of the parameters			Parameter	Appearance of the parameters			Parameter	Appearance of the parameters		
Type	External	Cavity		Type	External	Cavity		Type	External	Cavity	
Pressure of HTM	Atmospheric	Pressurized		Pressure of HTM	Atmospheric	Pressurized		Pressure of HTM	Atmospheric	Pressurized	
Operating temperature	High			Operating temperature	High			Operating temperature	High		
Heat transfer	Direct	Indirect		Heat transfer	Direct	Indirect		Heat transfer	Direct	Indirect	
Heat transfer medium	Air	Molten salt/metal	Etc.	Heat transfer medium	Air	Molten salt/metal	Etc.	Heat transfer medium	Air	Molten salt/metal	Etc.
Working fluid	Air			Working fluid	Air			Working fluid	Air		
Absorber	Tubular	Volumetric	Heat pipe	Absorber	Tubular	Volumetric	Heat pipe	Absorber	Tubular	Volumetric	Heat pipe

	Solar polygeneration unit configuration 1	$p_{in} = 3 \text{ bar}$	$T_{out} = 900^\circ\text{C}$
	Solar polygeneration unit configuration 2	$p_{in} = 1 \text{ bar}$	$T_{out} = 800^\circ\text{C}$
	Solar polygeneration unit configuration 1 & 2		

The final set of solution principles is based on a heat pipe receiver design with an inherited indirect heat transfer. Since the pressure is related to the HTM only one configuration exists. Although, the working fluid is pressurized in one SPU configuration the HTM within the heat pipe is not affected.

Figure 3.8 shows a graphic summary of the four different solution principles of this preliminary study.

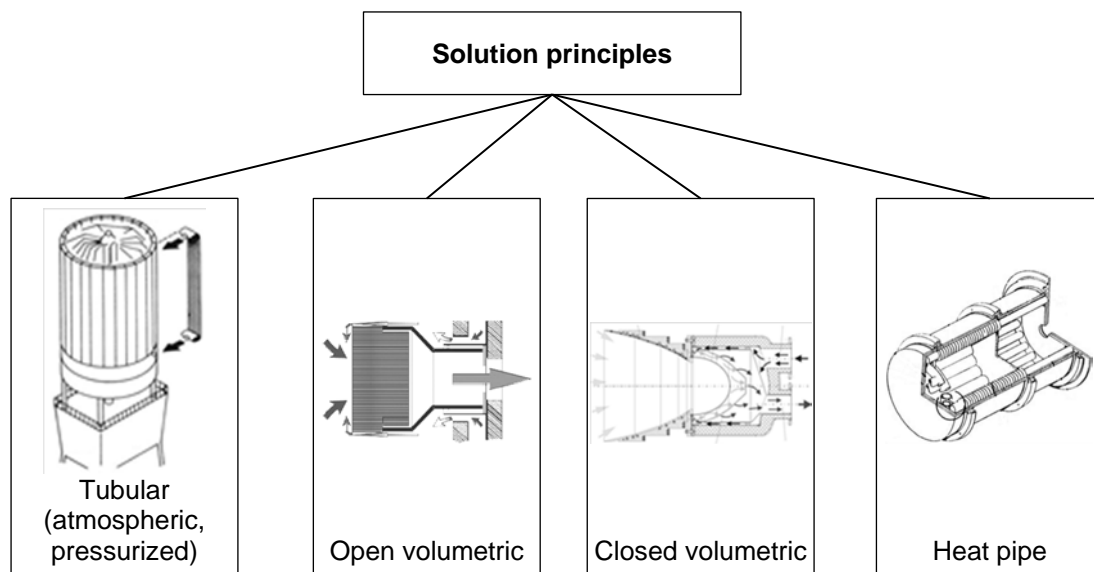


Figure 3.8: Graphical summary of solution principles (on basis of [27], [26], [41], and [51])

3.4 Analysis of solutions

The goal of this section is to analyze the different solution principles and provide a sound basis for the subsequent evaluation and decision.

3.4.1 Tubular design

In this first analysis the material temperatures of the absorber as well as the pressure drop within the absorber are investigated. The reason therefore is that if the absorber cannot withstand the solar radiation while providing an acceptable pressure drop the whole concept is not worth further studies.

To simplify the analysis a one dimensional heat transfer model for a tube of the length $L=1\text{m}$ is chosen and shown in Figure 3.9. Furthermore, this analysis investigates an ideal scenario based on the hypothesis that if the tubular absorber cannot withstand this ideal scenario conditions there is no way that is able to withstand real world conditions.

First and foremost, the irradiance distribution is considered to be uniform around the perimeter assuming that the surrounding structure distributes the incoming solar radiation perfectly. In a real world scenario the irradiance distribution will be highly non-uniform.

Second, the temperature of the fluid inside the tube is considered to remain constant over the whole length of the tube. This leads to the best heat removal possible. Along with the temperature all fluid properties are considered to be constant.

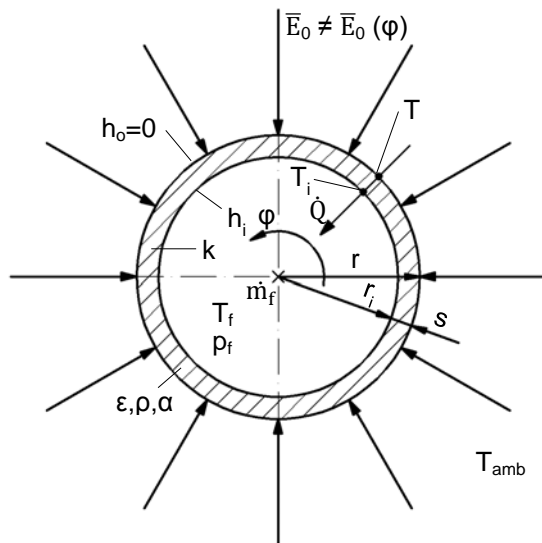


Figure 3.9: One dimensional heat transfer model for tubular receiver design

selective coating mentioned in section 1.2 and therefore the absorptivity and emissivity are 96 percent and 7 percent respectively.

For further simplifications all fluid properties except the density and kinematic viscosity are considered to be independent of the pressure. The density is calculated according to the ideal gas law based on the density at the corresponding temperature and a pressure of one bar. The kinematic viscosity is calculated as the ratio of the dynamic viscosity and the density.

Concerning the thermal properties of the tube simplifications are made as well. The thermal conductivity of the tube is assumed to be infinitely high which means that the tube does not oppose any resistance to the heat transfer. Moreover, the wall thickness of the tube is assumed to be very small compared to the inner diameter so it can be neglected. Thus, the irradiance absorbing surface on the outside equals the convective heat transfer surface on the inside yielding to the best heat transfer from radiation to fluid possible.

Assumptions for the radiative properties of the tube have to be made as well. It is assumed that the tube is covered with solar

The wall temperature of the tube can be calculated using a thermal resistance network model as

$$0 = E_0 \cdot A_o \cdot (1 - \rho_t) - h_o \cdot A_o - UA \cdot (T_o - T_f) - \varepsilon_t \cdot \delta \cdot A_o \cdot (T_o^4 - T_{amb}^4) \quad (W) \quad (3.8)$$

where \bar{E}_0 is the mean irradiance impinging on the tube, A_o the outer wall surface, ρ_t the radiative reflectivity, h_o is the outer convective heat transfer coefficient, UA the overall heat transfer coefficient between the outer wall and the fluid, T_o , T_f and T_{amb} the outer wall, the fluid and ambient temperature respectively, ε_t the radiative emissivity, and δ the Stefan–Boltzmann constant. Since the influence of natural convection on the outside of the tube is small in comparison to the forced convection inside the tube and natural convection is neglected. Thus, the heat transfer coefficient on the outside h_o becomes zero.

The correlation between reflectivity and absorptivity on the outside of the tube is given by

$$\rho + \alpha + \tau = 1 \quad (-) \quad (3.9)$$

where ρ is the reflectivity, α the absorptivity and τ the transmissivity which is equals to zero for opaque materials.

The previous mentioned overall heat transfer coefficient can be calculated by

$$\frac{1}{UA} = \frac{1}{h_i \cdot A_i} + \frac{\ln(r_o/r_i)}{2 \cdot \pi \cdot k \cdot L} \quad \left(\frac{K}{W}\right) \quad (3.10)$$

where h_i is the internal convective heat transfer coefficient, A_i the inner wall surface, r_o and r_i the outer and inner diameter respectively, k the thermal conductivity of the tube, and L the length of the tube.

The internal convective heat transfer coefficient can be calculated as

$$h = \frac{Nu \cdot d}{k_f} \quad \left(\frac{W}{m^2 \cdot K}\right) \quad (3.11)$$

where k_f is the thermal conductivity of the fluid, Nu the Nusselt number, and d the characteristic length, in the case of an internal flow in a circular tube the inner diameter.

With the assumption that the flow inside the tube is both hydrodynamically and thermally developed Table 3.7 outlines how the Nusselt number can be calculated. The correlation depends on both the flow condition and the boundary conditions.

Table 3.7: Nusselt number (on basis of [35])

Flow condition	Boundary condition	
	Constant wall temperature	Uniform surface heat flux
Laminar flow (Re<2300)	$Nu = 3.66$ (3.12)	$Nu = 4.36$ (3.13)
Turbulent flow (Re≥2300)	$Nu = 0.023 \cdot Re_D^{4/5} \cdot Pr^{1/3}$ (3.14)	

In this analysis for laminar flow conditions the Nusselt number is calculated according to equation 3.13 as the irradiance and therefore the heat flux are uniform.

The pressure drop within the absorber tubes is defined by

$$\Delta p = \xi \cdot \frac{L}{d_i} \cdot \frac{\rho \cdot u_i^2}{2} \quad (Pa) \quad (3.15)$$

where ξ is the friction factor, L and d_i the length and inner diameter of the tube respectively, ρ and u_i the density and mean velocity inside the tube. According to the Association of German Engineers [47] all fluid properties and velocity should be obtained with the mean temperature and mean pressure.

For laminar flows ($Re < 2300$) the friction factor is defined by

$$\xi = \frac{64}{Re} \quad (-) \quad (3.16)$$

where Re the Reynolds number is calculated by

$$Re = \frac{u_i \cdot d_i}{\nu} = \frac{u_i \cdot \rho \cdot d_i}{\mu} \quad (-) \quad (3.17)$$

where ν and μ are the kinematic and dynamic viscosity respectively.

For turbulent flows ($Re \geq 2300$) the friction factor is also depended on the roughness of the inner wall. According to Nikuradse, Prandtl, v. Kármán, Moddy, Colebrook et al. (as cited in [47]) the friction factor can be calculated by

$$\frac{1}{\sqrt{\xi}} = -2 \cdot \lg \left[\frac{2.51}{Re \cdot \sqrt{\xi}} + \frac{K/d_i}{3.71} \right] \quad (-) \quad (3.18)$$

where K is the absolute roughness. For an ideal scenario the absolute roughness is assumed to be zero.

Table 3.8 outlines the boundary conditions for the configurations presented in section 3.1, the first with an inlet pressure of 1 bar and the second with an inlet pressure of 3 bar.

Table 3.8: Boundary conditions for tubular receiver design

Configuration	1	2
Inlet pressure (bar)	3	1
Inlet temperature (°C)	500	400
Mean radiation (MW/m ²)	5.5	
Mass flow (kg/s)	0.1	

The results of the calculation for inner tube diameters from 1 to 100 mm can be seen in Figure 3.10. For both inlet configurations (1 and 3 bar) the wall temperature of the tube for the corresponding radii is the same. This is due to the fact that the Reynolds number did not change due to the simplifications made and the heat transfer coefficient did not alter because the flow condition remained constant within the considered range of tube diameters.

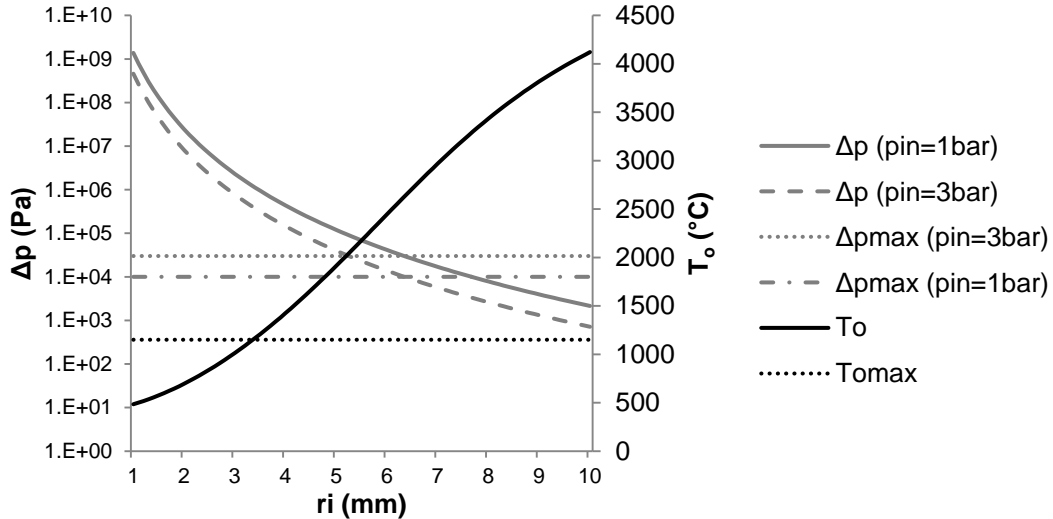


Figure 3.10: Pressure drop and wall temperature for tubular receiver design

For each radius the pressure drop was calculated for a tube that's outer wall surface is equivalent to the area of the focal spot. Thus, the length of the tube increases for smaller radii explaining the exponential growth of the pressure drop.

As discussed in the objectives the maximal tolerable pressure drop within the whole receiver is limited to 10 percent of the inlet pressure. With the assumption that the entire pressure drop occurs in the absorber the maximal pressure drop corresponds to 0.1 and 0.3 bar respectively.

The maximum material temperature was chosen to be 1150°C. This corresponds to the maximum service temperature of Outokumpu's high temperature austenitic stainless steel alloy 353 MA in dry air [62]. This steel alloy matches the high temperature requirements very good. Additionally, it is very good weldable which is very valuable for the design of a prototype.

Concluding it can be said that for the given boundary conditions no tubular receiver designs was found where both the pressure drop and the maximum material temperature are below acceptable limits.

3.4.2 Volumetric design

According to the literature review the most common materials for volumetric receivers are foams and honeycomb structures both out of metal and ceramic. Therefore, this analysis of volumetric receiver focuses on these two absorber materials.

The goal of this analysis is the same as the previous. The material temperatures of the absorber as well as the pressure drop within the absorber have to be below the maximum allowable values for the concept to be worth further investigations.

A one dimensional heat transfer model for a cylindrical volumetric absorber is chosen and shown in Figure 3.11. A uniform solar radiation impinges on the absorber surface and is fully absorbed by the absorber in its depth heating up the material. At the same time a uniform fluid flow with the inlet temperature $T_{f,i}$ passes through the absorber and is heated up to the outlet temperature $T_{f,o}$.

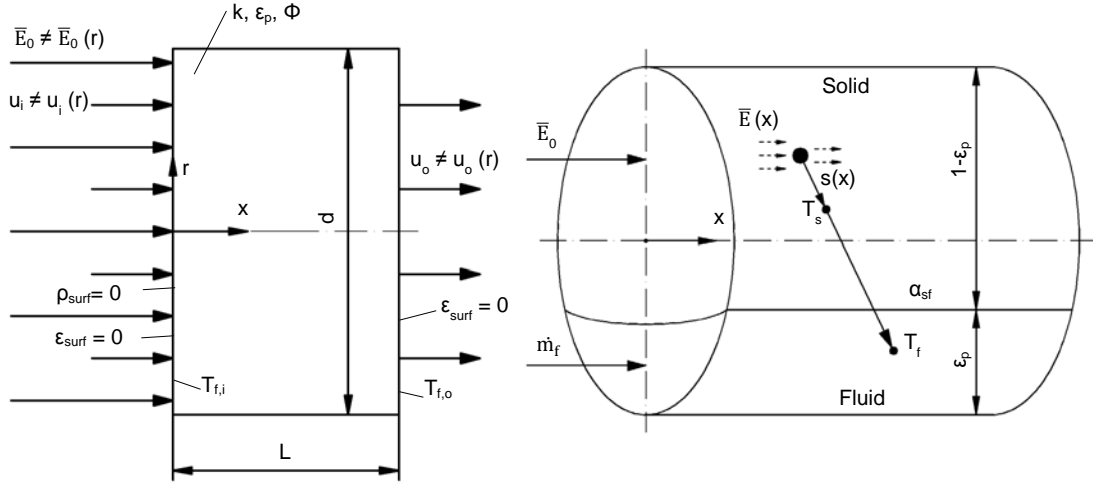


Figure 3.11: Volumetric receiver design model
Layout (left), heat transfer model (right)

In order to make a first assessment of this concept a couple of simplification and assumptions are made.

First and foremost, the absorber temperature is considered to be constant over the length. This is due to the fact that the actual absorption of the solar radiation within the absorber is unknown. Becker [36] states that when looking at long absorbers the temperature of the material along the length can be well approximated by the outlet temperature, which implies a constant absorber temperature. Although, this analysis is not only focused on long absorbers the assumption of constant absorber temperature seems to be more appropriate than the assumption of constant heat flux. This hypothesis is backed up by the Figure 2.10 which shows a quantitative temperature distribution along the length of an absorber.

Second, material properties are assumed to be spatially constant. Furthermore, radiative heat transfer is neglected except, the absorption of solar radiation by the absorber material. Radiative heat transfer is neglected at the boundaries the ambient. Thus, both the reflectivity and the emissivity at the boundaries are considered to be zero.

To calculate the solid and fluid temperatures the local thermal nonequilibrium (LTNE) has to be applied. In contrast to the local thermal equilibrium the difference between the volume-averaged fluid and solid temperature is not negligible. According to Ghafir and Lauriat [48] the LTNE has to be used because among the condition for the LTE are relatively slow motion and the absence of volumetric heating of one material but not the other. For a high temperature solar receiver these two conditions are clearly not fulfilled. It has to be mentioned that although the LTNE is considered at the pore level, the LTE is considered at the macroscopic scale. The solid and fluid temperatures can be calculated using the energy equation for the solid and fluid respectively.

$$k_{se} \frac{d^2 T_s}{dx^2} - h_v (T_s - T_f) + s_s''(x) = \rho_s c_{ps} (1 - \varepsilon_p) \frac{dT_s}{d\tau} \quad \left(\frac{W}{m^3} \right) \quad (3.19)$$

$$k_{fe} \frac{d^2 T_f}{dx^2} + h_v (T_s - T_f) + s_f''(x) = \rho_f c_{pf} u_f \frac{dT_f}{dx} + \rho_f c_{pf} \varepsilon_p \frac{dT_f}{d\tau} \quad \left(\frac{W}{m^3} \right) \quad (3.20)$$

Here, k_{se} and k_{fe} are the effective thermal conductivity of the solid and fluid respectively, T_s and T_f the solid and fluid temperature respectively, x the index variable in flow direction, h_v the volumetric heat transfer coefficient, s_s'' and s_f'' the heat source in the solid and fluid per unit total volume respectively, ε_p the porosity, ρ_s and ρ_f the density of the solid and fluid respectively, c_{ps} and c_{pf} the specific heat capacity of the solid and fluid respectively, u_f the superficial fluid velocity, and τ the time.

Taking into account radiation losses from the front of the absorber and assuming zero flux at the end of the absorber, the boundary conditions for the solid phase can be written

$$k_{se} \left. \frac{dT_s}{dx} \right|_{x=0} = -\varepsilon_{surf} \cdot \sigma \cdot (T_s^4(0) - T_{amb}^4) \quad \left(\frac{W}{m^2} \right) \quad (3.21)$$

$$k_{se} \left. \frac{dT_s}{dx} \right|_{x=L} = 0 \quad \left(\frac{W}{m^2} \right) \quad (3.22)$$

where ε_{surf} is the radiative emissivity at the surface, σ the Stefan–Boltzmann constant, T_s , T_f and T_{amb} the solid, fluid and ambient temperature respectively.

According to Ghafir and Lauriat [48] the effective conductivities can be calculated as

$$k_{se} = (1 - \varepsilon_p) \cdot k_s \quad \left(\frac{W}{mK} \right) \quad (3.23)$$

$$k_{fe} = \varepsilon_p \cdot k_f \quad \left(\frac{W}{mK} \right) \quad (3.24)$$

where k_s and k_f are the solid and fluid thermal conductivity, respectively.

With the assumption of total absorption of the impinging solar radiation within the absorber, no reflection of the impinging solar radiation at the surface and no radiation losses at the surface to the ambient the fluid outlet temperature can be calculated by a heat balance.

$$\bar{E}_0 \cdot A_0 = \dot{m} \cdot [h(T_{f,out}) - h(T_{f,in})] \quad (W) \quad (3.25)$$

Here, \bar{E}_0 is the mean irradiance impinging on the surface, A_0 the front absorber surface, and h the enthalpy of the fluid at the inlet and outlet temperature $T_{f,in}$ and $T_{f,out}$ respectively.

Using the energy equation for the solid with the assumptions of steady state conditions, negligible conductivity of the solid, that the entire solar radiation is absorbed by the solid and none by the fluid, and constant wall (absorber) temperature the solid temperature T_s can be calculated by

$$\bar{E}_0 \cdot A_0 + \bar{h}_v \cdot V \cdot \frac{(T_{f,out} - T_{f,in})}{\ln \left(\frac{T_s - T_{f,in}}{T_s - T_{f,out}} \right)} = 0 \quad (W) \quad (3.26)$$

where \bar{h}_v is the mean volumetric heat transfer coefficient, V the total volume of the receiver, and T_f the fluid temperature.

Using the energy equation for the fluid with the assumptions of steady state conditions, negligible conductivity of the fluid, and no absorption of solar radiation by the fluid as stated before the fluid temperature $T_f(x)$ along the length of the absorber can be calculated by

$$\frac{T_s - T_f(x)}{T_s - T_{f,in}} = \exp\left(-\frac{A \cdot x}{\dot{m} \cdot c_{pf}} \cdot \left[\frac{1}{x} \int_0^x h_v(x) \cdot dx\right]\right) \quad (-) \quad (3.27)$$

where x is the index variable along the absorber, $T_{f,in}$ the fluid inlet temperature to the absorber, and A the cross sectional area. For a constant volumetric heat transfer coefficient the square bracket reduces to said constant volumetric heat transfer coefficient h_v .

In order to calculate the volumetric heat transfer coefficient the absorber material has to be specified. For foam materials one way to define the structure was presented by Lacroix et al. [63]. They state that a structure of a foam material is defined its porosity ε_p which is the ratio of the volume of the void space and the total volume, and the cell diameter Φ . Figure 3.12 on the left shows a model of the foam cell and on the right an optical picture a SiC foam. The white dotted circle indicates the (dodecahedral) cell diameter Φ .

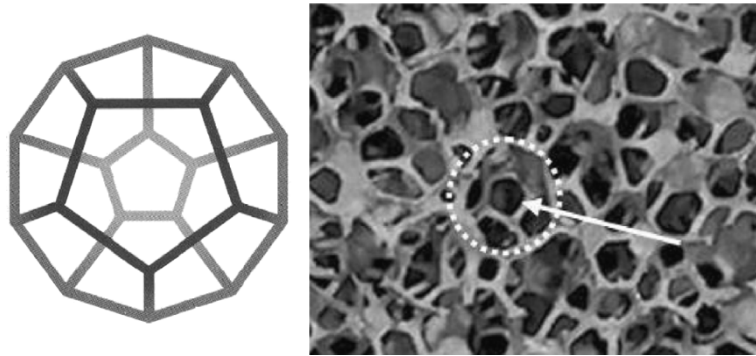


*Figure 3.12: Foam parameters [63]
Model of foam cell (left), picture of SiC foam (right)*

For this first analysis a foam that Lacroix et al. [63] used in their experiments is chosen. It has a porosity of 90 percent and a cell diameter of 2mm.

Another important parameter of foam materials is the mean particle diameter. It is also required to calculate the volumetric heat transfer coefficient. According to Lacroix et al. [63] it can be calculated by

$$d_p = \frac{1.5}{2.3} \cdot \frac{\Phi \cdot \left[\frac{4}{3\pi}(1-\varepsilon_p)\right]^{1/2}}{1 - [1 - \varepsilon_p]^{1/2}} \quad (m) \quad (3.28)$$

where d_p stands for the mean particle diameter, Φ is the cell diameter, and ε_p the porosity.

According to Xu et al. [64] and Alazmi and Vafai [65] the volumetric heat transfer coefficient is constant over the length of the porous medium and can be calculated using four different models. Table 3.9 gives an overview of the different models.

Table 3.9: Different models for the volumetric heat transfer coefficient

	$h_{sf} = \bar{h}_{sf}$	α_{sf}	Source
1	$\frac{k_f \cdot (2 + 1.1 \cdot Pr^{1/3} \cdot Re_d^{0.6})}{d_p}$ (3.29)	$\frac{6 \cdot (1 - \varepsilon_p)}{d_p}$ (3.30)	Vafai and Amiri see [65]
2	$0.004 \cdot \left(\frac{d_v}{d_p}\right) \cdot \left(\frac{k_f}{d_p}\right) \cdot Pr^{0.33} \cdot Re_d^{1.35}, Re_d < 75$ (3.31) $1.064 \cdot \left(\frac{k_f}{d_p}\right) \cdot Pr^{0.33} \cdot Re_d^{0.59}, Re_d > 350$ (3.33)	$\frac{20.346(1 - \varepsilon_p) \cdot \varepsilon_p^2}{d_p}$ (3.32)	Hwang et al. [66]
3	$\left[\frac{d_p \cdot \varepsilon_p}{0.25555 \cdot Pr^{1/3} \cdot Re_d^{2/3} \cdot k_f} + \frac{d_p}{10 \cdot k_s} \right]^{-1}$ (3.34)	$\frac{6 \cdot (1 - \varepsilon_p)}{d_p}$ (3.35)	Dixon and Creswell [67]
4	$[(1.18Re_d^{0.58})^4 + (0.23Re_h^{0.75})^4]^{1/4} / (d_p k_f)$ (3.36)	$\frac{6 \cdot (1 - \varepsilon_p)}{d_p}$ (3.37)	Achenbach [68]

Here, h_{sf} is the interfacial convective heat transfer coefficient, α_{sf} the specific surface area per unit volume, Re_d the Reynolds number, Pr the Prandlt number, d_p the mean particle diameter, d_v the average void diameter defined as $d_v = \frac{4\varepsilon_p}{\alpha_{sf}}$, k_f and k_s the thermal conductivity of the fluid and the solid respectively, and Re_h another definition of the Reynolds number as $Re_h = \frac{Re_d}{1 - \varepsilon_p}$.

The Reynolds number is defined by

$$Re_d = \frac{u_0 \cdot d_p}{\nu} \quad (-) \quad (3.38)$$

where u_0 is the superficial or Darcian velocity, and ν the kinematic viscosity.

The volumetric heat transfer can then be calculated as

$$h_v = h_{sf} \cdot \alpha_{sf} \quad \left(\frac{W}{m^3 \cdot K} \right) \quad (3.39)$$

Xu et al. [64] compared these models for the convective heat transfer with experimental data from Fend et al. [69] and came to the conclusion that model number 1 from Hwang et al. [66] matches the experimental data best. Thus, this model is used for further analysis.

Honeycomb structures on the other hand are defined by their cell size and wall thickness shown in Figure 3.17. Usually, the cell size is not denoted but the cells per square inch (CPSI).

For this analysis a ceramic honeycomb structure from the Chinajinti [70] was chosen. The main parameters are 600 CPSI, a wall thickness of 0.15mm and a maximum operating temperature greater than 1370°C.

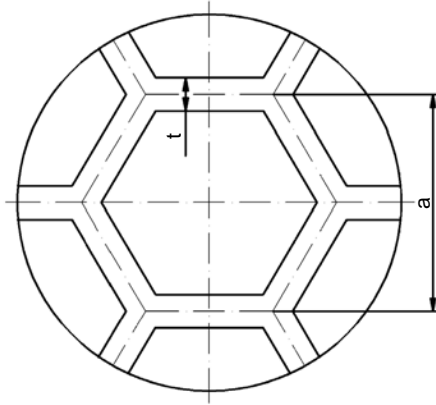


Figure 3.13: Honeycomb structure

The following equations present the correlations for the main honeycomb parameters; the cell size a , the specific surface area per unit volume α_{sf} , and the porosity ε_p .

$$a = \sqrt{\frac{2}{\sqrt{3} \cdot CPSI}} \cdot 2.54 \cdot 10^{-2} \frac{m}{inch} \quad (m) \quad (3.40)$$

$$\alpha_{sf} = 4 \cdot \frac{a - t}{a^2} \quad \left(\frac{1}{m}\right) \quad (3.41)$$

$$\varepsilon_p = \frac{(a - t)^2}{a^2} \quad (-) \quad (3.42)$$

For the assumption of constant wall temperature and laminar flow the Nusselt number for the honeycomb structure can be gathered from Figure 3.14. The assumption of laminar flow is very often true for honeycomb structures [72]. For a best case scenario it is assumed that the absorber is small enough that the entire heat transfer happens in the entrance region where the flow is not yet thermally developed. Thus, a mean Nusselt number of 9 is chosen.

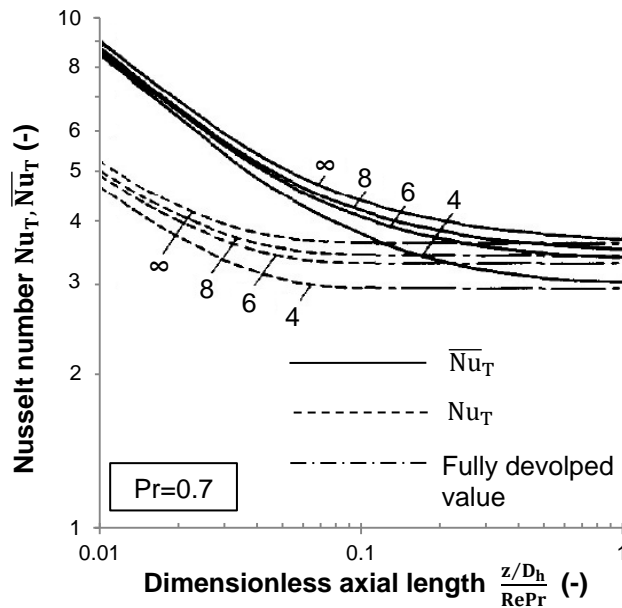


Figure 3.14: Nusselt number for honeycomb structures [72]

Concerning the pressure loss at least two different models for foam structures exist. Nevertheless, both of them are based on the Darcy-Forchheimer equation described in section 2.5.2. Table 3.10 outlines the pressure drop models of Bai [71] and Becker et al. [36].

Table 3.10: Pressure drop models for foam absorber

Quadratic pressure drop	Source
$\frac{p_{in}^2 - p_{out}^2}{2} = (a_1 \dot{M} + a_2 \dot{M}^2) \cdot L \quad (3.43)$	Bai [71]
$a_1 = \frac{R}{K} \frac{2\mu_{ref}(T_r + S)}{T_{ref}^{1.5}(T_{f,o} - T_{f,i})} \left[\frac{1}{5} (T_{f,o}^{2.5} - T_{f,i}^{2.5}) - \frac{S}{3} (T_{f,o}^{1.5} - T_{f,i}^{1.5}) + B^2 (\sqrt{T_{f,o}} - \sqrt{T_{f,i}}) - S^{2.5} \arctan \left(\frac{\sqrt{S}(\sqrt{T_{f,o}} - \sqrt{T_{f,i}})}{S + \sqrt{T_{f,o}T_{f,i}}} \right) \right] \quad (3.44)$	
$a_2 = \frac{C_f R (T_{f,o} - T_{f,i})}{\sqrt{K}} \quad (3.45)$	
$\frac{p_{in}^2 - p_{out}^2}{2} = \left(R \cdot \frac{\mu_r}{K \cdot T_r^{0.7}} T_{f,o}^{1.7} \cdot \dot{M} + \frac{R \cdot T_{f,o}}{C_f} \cdot \dot{M}^2 \right) \cdot L \quad (3.46)$	Becker et al. [36]

Here, p denotes pressure, L the length of the absorber, \dot{M} the mass flux (mass flow per unit area), R the specific gas constant (for air R=287 J/(kg K)), K the specific permeability, C_f the inertia coefficient, μ and μ_{ref} the dynamic viscosity of the fluid at the fluid temperature and the reference temperature respectively, T_f and T_{ref} the fluid temperature and the fluid reference temperature respectively, and S the Sutherland constant (for air S=110.4). Both models show similar results. Since the model of Bai [71] is the more recent one it is chosen for further investigations.

According to Kaviany [75] the specific permeability and the inertia coefficient can be calculated using the modified Ergun equation.

$$K = \frac{d_p^2}{E_1} \frac{\varepsilon_p^3}{(1 - \varepsilon_p)^2} \quad (\text{m}^2) \quad (3.47)$$

$$C_f = \frac{E_2}{\sqrt{E_1} \cdot \varepsilon_p^{3/2}} \quad (-) \quad (3.48)$$

Here, E_1 and E_2 are the Ergun constants, d_p the particle diameter, and ε_p the porosity. For packed beds the standard Ergun constants are 150 and 1.75. Concerning ceramic foam Lacroix et al. [63] conducted an investigation with these standard constants and found good agreement with experimental data. Therefore, for this analysis the standard Ergun constants are used as well.

According to Asako et al. [72] the pressure drop within the honeycomb structure can be calculated by

$$\frac{p_{in} - p(x)}{(\rho \cdot \bar{u}^2)/2} = (fRe)_{f.d.} \cdot \left(\frac{4x}{D_h \cdot Re} \right) + K(x) \quad (-) \quad (3.49)$$

where x is the index variable along the absorber, ρ the fluid density, \bar{u} the physical fluid velocity which is the ratio of the superficial fluid velocity and the porosity, $(f Re)_{f.d.}$ the friction factor for the hydrodynamically fully developed region, D_h the hydraulic diameter, Re the Reynolds number, and $K(x)$ the incremental pressure drop due to entrance effects.

Table 3.11 shows the parameters for the pressure drop calculation for polygonal ducts. For honeycomb structures the row with 6 vertices is important.

Table 3.11: Pressure drop parameters for polygonal ducts

n	$(f Re)_{f.d.}$	$K(\infty)$
4	14.167	1.445
6	15.065	1.324
8	15.381	1.292
∞	15.925	1.253

Here, n is the number of vertices, $(f Re)_{f.d.}$ friction factor for the hydrodynamically fully developed region, $K(\infty)$ the total incremental pressure drop due to the entrance effects for large x . Since no values for incremental pressure drop due to the entrance were found in this analysis the values for the total pressure drop are used.

The boundary conditions as well as the pressure drop limits are the same as in the previous analysis. The maximum material temperature for both the foam and honeycomb structure was chosen to be 1500°C [80].

Figure 3.15 and Figure 3.16 show the absorber temperature as well as the pressure drop within the absorber as a function of the absorber length L for the foam and honeycomb structure respectively.

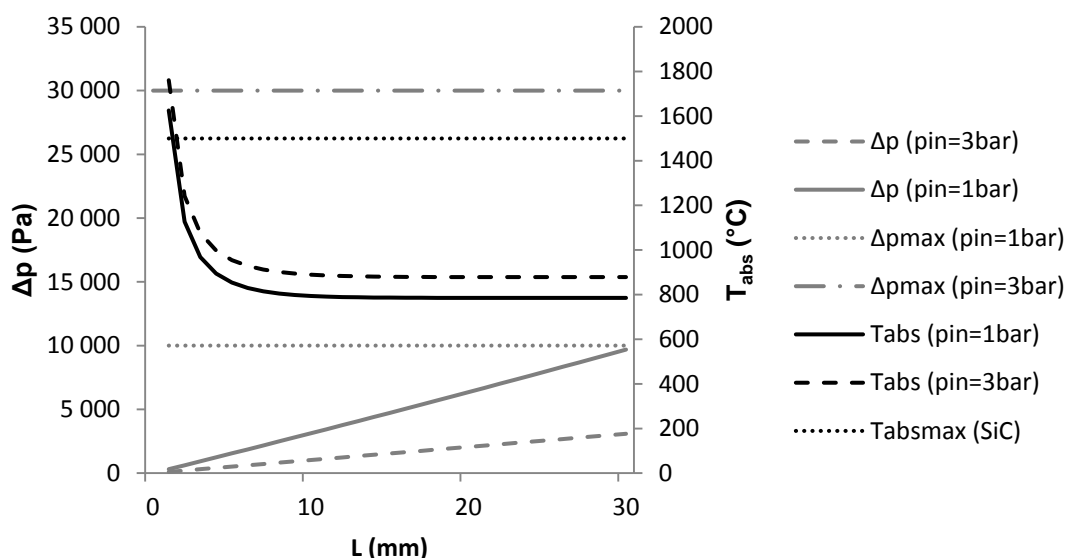


Figure 3.15: Pressure drop and temperature for foam absorber

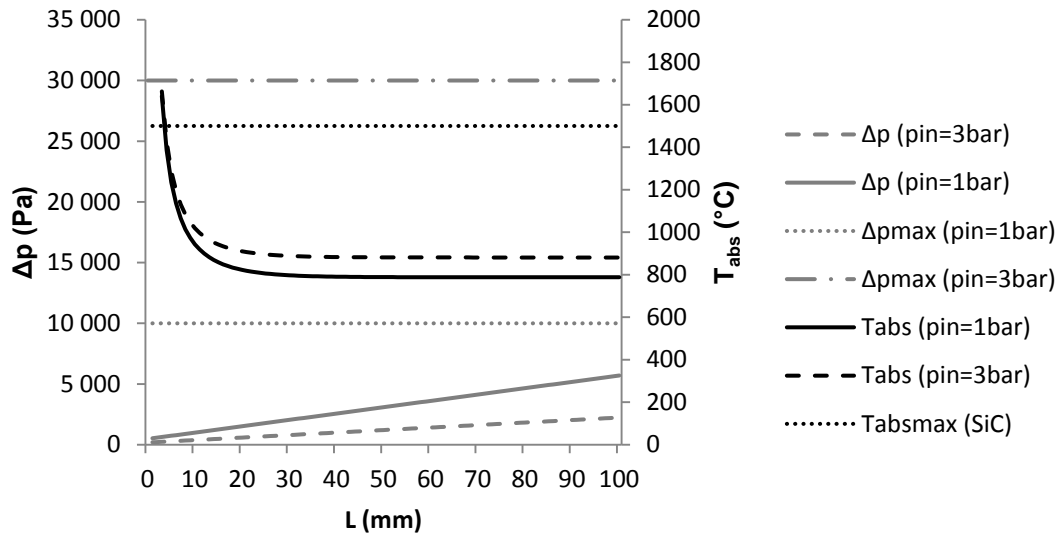


Figure 3.16: Pressure drop and temperature for honeycomb absorber

It can be seen that for both foam and honeycomb absorbers designs are possible where both the pressure drop and the maximum material temperature are below acceptable limits. The pressurized configuration provides slightly higher material temperatures than the atmospheric configuration due to a smaller heat transfer coefficient because of smaller fluid flow velocities. In turn lower fluid flow velocities result in a lower pressure drop of the pressurized configuration.

For long absorber lengths the solid temperatures of foam and honeycomb absorbers reach the same values. The pressure drop on the other hand is different. Honeycomb absorbers are clearly favorable from a pressure drop point of view.

Finally, Figure 3.17 shows the fluid and absorber temperature over the length of the absorber for a specific length L of 10mm.

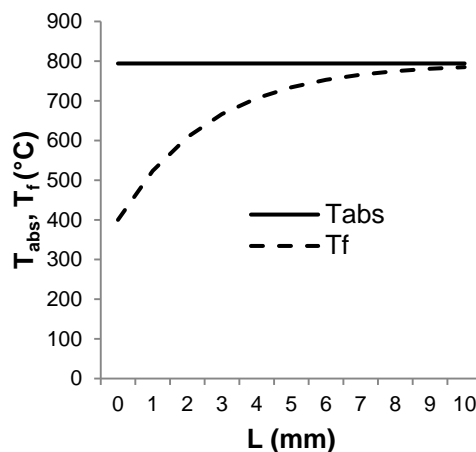


Figure 3.17: Fluid and absorber temperature

3.4.3 Heat pipe design

In this section the heat pipe receiver design is analyzed to see whether this concept is worth further investigations. The analysis is based on the literature review presented in section 2.

Bienert [49] claims that theoretically heat pipe receivers can withstand irradiance levels up to 10 MW/m² but a practical limit seems to be around 1 MW/m². Furthermore, heat pipe designs that are able of providing fluid outlet temperatures up to 900°C use liquid alkali metals as HTFs which have a lower operating limit of 400°C.

Both the practical irradiance limit of 1 MW/m² and the lower operating limit of 400°C make the heat pipe design unattractive for the use in the SPU.

3.5 Evaluation and decision

The evaluation and decision are based on the performance of the receiver designs at an irradiance level of 5.5 MW/m² analyzed in the previous section. The designs must be able to withstand this irradiance level i.e. the material temperature must not exceed the maximum material temperature. At the same time the pressure drop within the receiver must not exceed the previous defined limits.

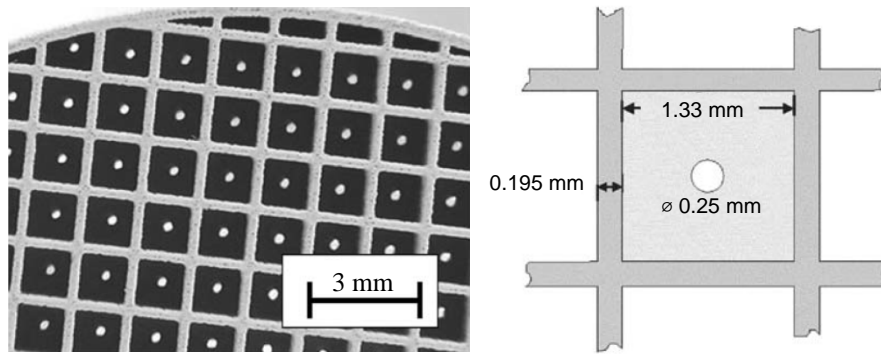
In order to structure the evaluation a balance of arguments is made and presented in Table 3.12.

Table 3.12: Balance of arguments

Design	Advantages	Disadvantages
Tubular	Simple design	Material temperatures too high for acceptable pressure drop and vice versa
Volumetric ↳ foam	Acceptable material temperatures and pressure drop at the same time Quadratic pressure drop	Higher pressure drop than honeycomb structures
Volumetric ↳ honeycomb	Acceptable material temperatures and pressure drop at the same time	Linear pressure drop
Heat pipe	Theoretically low pressure drop	Unsuitable for given irradiance

The balance of arguments suggests that the volumetric receiver design is the most suitable for the application within the SPU. Tubular designs are not suitable because no design was found where both the pressure drop and the maximum material temperature were below acceptable limits. Foam absorbers have the advantage of a quadratic pressure drop which makes it less vulnerable for flow instabilities than the honeycomb absorber with its linear pressure drop characteristic. On the other hand honeycomb structures yields a significant lower pressure drop compared to foam absorbers. Heat pipe receiver designs are not able to withstand the high expected irradiance levels.

Fend et al. [73] present a possibility to improve the pressure loss characteristic of cellular absorbers such as honeycomb structures.



**Figure 3.18: Enhanced cellular silicon carbide absorber [73]
Sample manufactured by Bauer R&D (left), detailed drawing of a single channel (right)**

Figure 3.18 shows the enhanced cellular silicon carbide absorber. In each channel a plane of 270 μm thickness perpendicular to the channel direction is placed with a small hole of 250 μm diameter. This additional plane leads to a more quadratic pressure drop characteristic. The problem is that this structure cannot be manufactured by common extrusion techniques but has to be manufactured using rapid prototyping processes. Thus, it is not commercially available.

Therefore, the main study will be performed on a volumetric receiver design with a ceramic or metallic foam absorber.

4. MAIN STUDY

In this section a more detailed analysis of the previously chosen volumetric receiver design with a foam absorber is conducted. The approach to this analysis is similar to the approach in the preliminary study.

First, the current situation is analyzed and objectives are formulated. On that basis a variety of solutions is searched for and analyzed. Finally, the results are evaluated and the most promising design is chosen for a detailed analysis.

4.1 Situation analysis

In this situational analysis a basic closed volumetric receiver design shown in Figure 4.1 is analyzed. The goal is to get an idea of the temperatures, pressure losses and thermal stresses of the design. Based on these findings re-design objectives for the main study are formulated.

First, the physical modeling of the main receiver components is described. On that basis a numerical model is created. This is then used in a multi objective optimization process to obtain specifications for the basic design instead of guessing them. Based on these specifications the design is analyzed in more detail to obtain temperatures, pressure losses and thermal stresses of the design.

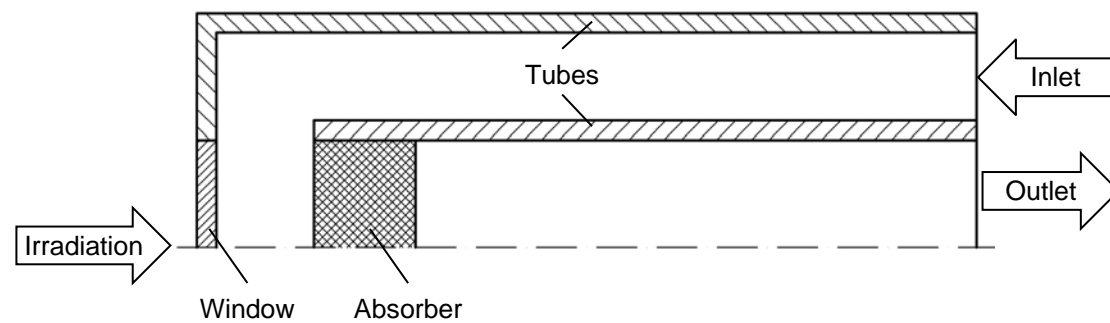


Figure 4.1: Basic volumetric receiver design

The working principle of the design is fairly easy. The cold HTF enters the receiver in the outer tube. On its way to the absorber it is heated slightly by the hot HTF leaving the receiver. Simultaneously, concentrated solar radiation passes through the window and impinges on the absorber. The irradiation is absorbed by the absorber in its depth heating it up. The HTF that passes through the hot absorber is heated up and leaves the receiver at the outlet.

4.1.1 Physical modeling

In this section the physical modeling of the main receiver components is described. Although, it would be favorable to consider the physics in its full complexity it would exceed the scope of this thesis. Therefore, a couple of simplifications and assumptions have to be made.

4.1.1.a Heat transfer

For the convective heat transfer between the fluid and the window and the convective heat

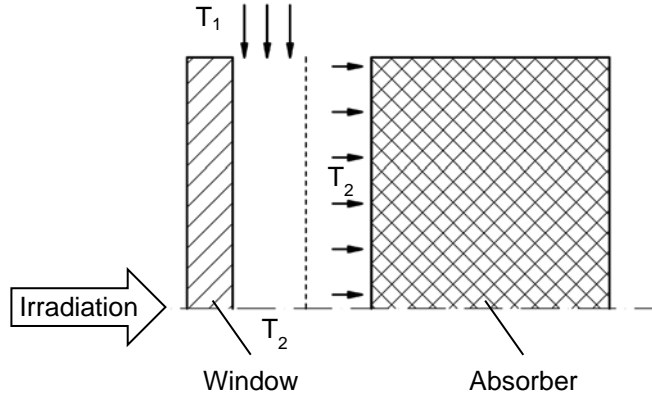


Figure 4.2: Fluid flow simplifications

transfer between the fluid and the absorber simplifications

concerning the fluid flow and heat transfer need to be made.

Figure 4.2 illustrates said simplifications concerning the fluid flow. It is assumed that the flow entering the cavity between the absorber and the window has a uniform velocity distribution.

The convective heat transfer between the fluid and the window is considered according the

model of forced convection across a flat plate with the same area and the characteristic length of the window radius. Furthermore, the flow is considered to enter the cavity with a uniform temperature distribution T_1 and after the convective heat transfer with the window it is considered to have a uniform equivalent temperature T_2 . Then the fluid enters the absorber with said equivalent temperature T_2 and a uniform velocity distribution. The convective heat transfer on the outside of the window is considered according the model of free convection across a vertical flat plate. The heat transfer in the first part of the receiver is modeled according to heat exchanger theory and is described later in section 4.1.1.f. Other heat losses to the ambient than from the window are neglected. That means the outer tube is considered to be perfectly insulated.

As far as the temperature distribution within the window and absorber is concerned a more detailed model is chosen. In the preliminary study the temperature was considered to be spatially constant. In order to increase the accuracy the temperatures are calculated by a 2 dimensional rotationsymmetric model.

For this 2 dimensional rotationsymmetric model the energy equations for the window, and for the solid and fluid within the absorber and can be written as

$$k_w \left(\frac{d^2 T_w}{dx^2} + \frac{d^2 T_w}{dr^2} + \frac{dT_w}{r \cdot dr} \right) + s_w''(x, r) = \rho_w c_{pw} \frac{dT_w}{d\tau} \quad \left(\frac{W}{m^3} \right) \quad (4.1)$$

$$(k_{se} + k_r) \left(\frac{d^2 T_s}{dx^2} + \frac{d^2 T_s}{dr^2} + \frac{dT_s}{r \cdot dr} \right) - h_v \cdot (T_s - T_f) + s_s''(x, r) = \rho_s c_{ps} (1 - \varepsilon_p) \frac{dT_s}{d\tau} \quad \left(\frac{W}{m^3} \right) \quad (4.2)$$

$$k_{fe} \left(\frac{d^2 T_f}{dx^2} + \frac{d^2 T_f}{dr^2} + \frac{dT_f}{r \cdot dr} \right) + h_v \cdot (T_s - T_f) + s_f''(x, r) = \rho_f c_{pf} u_f \frac{dT_f}{dx} + \rho_f c_{pf} \varepsilon_p \frac{dT_f}{d\tau} \quad \left(\frac{W}{m^3} \right) \quad (4.3)$$

where, k_w is the thermal conductivity of the window, k_{se} and k_{fe} the effective thermal conductivity of the solid and fluid respectively, k_r the radiative conductivity within the solid, T_w , T_s and T_f the window, solid and fluid temperature respectively, x the axial index variable

in flow direction, r the radial index variable perpendicular to the flow direction, h_v the volumetric heat transfer coefficient, s_w'' , s_s'' and s_f'' the heat source in the window, the solid and fluid per unit total volume respectively, ε_p the porosity, ρ_w , ρ_s and ρ_f the density of the window, the solid and fluid respectively, c_{pw} , c_{ps} and c_{pf} the specific heat capacity of the window, the solid and fluid respectively, u_f the superficial fluid velocity, and τ the time.

For the reason of simplicity a few assumptions are made. First, the conductivity of the fluid is considered to be negligible for both the radial and axial direction. Secondly, the fluid flow is considered to be solely axial i.e. no mass transfer in the radial direction.

The volumetric heat transfer coefficient used to couple the fluid and solid energy equation has already been discussed in the preliminary study in section 3. An analysis conducted by Xu et al. [64] showed that the model form Hwang et al. [66] matches experimental data best. The volumetric heat transfer can therefore be calculated as

$$h_v = h_{sf} \cdot \alpha_{sf} \quad \left(\frac{W}{m^3 \cdot K} \right) \quad (4.4)$$

where h_{sf} is the interfacial convective heat transfer coefficient and α_{sf} the specific surface area per unit volume. For Reynolds numbers below 75 the interfacial convective heat transfer coefficient is defined as

$$h_{sf} = 0.004 \cdot \left(\frac{d_v}{d_p} \right) \cdot \left(\frac{k_f}{d_p} \right) \cdot Pr^{0.33} \cdot Re_d^{1.35} \quad \left(\frac{W}{m^2} \right) \quad (4.5)$$

whereas for Reynolds numbers above 350 it is defined as

$$h_{sf} = 1.064 \cdot \left(\frac{k_f}{d_p} \right) \cdot Pr^{0.33} \cdot Re_d^{0.59} \quad \left(\frac{W}{m^2} \right) \quad (4.6)$$

where Re_d is the Reynolds number, Pr the Prandtl number, d_p the mean particle diameter, d_v the average void diameter defined as $d_v = \frac{4\varepsilon_p}{\alpha_{sf}}$, k_f and k_s the thermal conductivity of the fluid and the solid respectively. Between these Reynolds numbers the interfacial convective heat transfer coefficient needs to be linearly interpolated. The specific surface area per unit volume for this model can be calculated by the following equation.

$$\alpha_{sf} = \frac{20.346(1 - \varepsilon_p) \cdot \varepsilon_p^2}{d_p} \quad \left(\frac{1}{m} \right) \quad (4.7)$$

The Reynolds number is defined as

$$Re_d = \frac{u_0 \cdot d_p}{\nu} \quad (-) \quad (4.8)$$

where u_0 is the superficial or Darcian velocity, and ν the kinematic viscosity.

For the window and the solid in the axial direction the following boundary conditions can be written that are similar to the ones of the preliminary study.

$$k_w \left. \frac{dT_w}{dx} \right|_{x_w=0} = -h_f \cdot (T_w(0) - T_{amb}) - \varepsilon_{surf,w} \cdot \sigma \cdot (T_w^4(0) - T_{amb}^4) \quad \left(\frac{W}{m^2} \right) \quad (4.9)$$

$$k_w \left. \frac{dT_w}{dx} \right|_{x_w=L_w} = -h \cdot (T_w(L) - T_{f,c}) + (\dot{q}_{s \rightarrow w} - \dot{q}_t) \quad \left(\frac{W}{m^2} \right) \quad (4.10)$$

$$k_{se} \left. \frac{dT_s}{dx} \right|_{x=0} = -\dot{q}_{s \rightarrow w} \quad \left(\frac{W}{m^2} \right) \quad (4.11)$$

$$k_{se} \left. \frac{dT_s}{dx} \right|_{x=L} = 0 \quad \left(\frac{W}{m^2} \right) \quad (4.12)$$

Here, h and h_f are the convective heat transfer coefficient on the inside and outside of the window respectively, $T_{f,c}$ the fluid temperature inside the cavity that is far enough away for not being influenced by the convective heat transfer, $T_w(0)$ and $T_w(L)$ the window temperature at the inside and outside respectively, and T_{amb} the ambient temperature. The term $\dot{q}_{s \rightarrow w}$ accounts for the radiation exchange between the front of the absorber and the glass window whereas the term \dot{q}_t accounts for the thermal radiation transmitted through the window.

The boundary conditions for the radial direction are simple. Since the model is rotationsymmetric the radial temperature gradient in the center is zero. With the assumption of perfect insulation at the outer boundary ($r=R$) that gradient becomes zero as well.

$$k_w \left. \frac{dT_w}{dr} \right|_{r=R} = k_w \left. \frac{dT_w}{dr} \right|_{r=R} = 0 \quad \left(\frac{W}{m^2} \right) \quad (4.13)$$

$$k_{se} \left. \frac{dT_s}{dr} \right|_{r=0} = k_{se} \left. \frac{dT_s}{dr} \right|_{r=R} = 0 \quad \left(\frac{W}{m^2} \right) \quad (4.14)$$

4.1.1.b Radiation treatment absorber

Radiation treatment within the porous absorber is essential for the modeling as it influences the absorption of light radiation and thus the temperature distribution.

Howell [74] states that there are two common approaches to treat radiative transfer in porous media. Furthermore, he claims that for most applications the fluid within the porous media can be assumed to be transparent to radiation especially if the fluid is a gas. Kaviany [75] calls the two approaches direct simulation and continuum treatment.

In the direct simulation approach the radiative heat transfer is modeled among discrete structural elements. For this approach the structure of the medium needs to be well defined. Moreover, additional information about the radiative properties of the solid elements is required. Often this information is not available. If the effects of dependent scattering become significant the problem gets even more difficult. Dependent scattering appears if the elements of the porous media are so closely spaced that the radiation from one element is affected by the radiation of neighboring elements.

In the second approach, the continuum treatment, the porous medium is treated as a continuum as the name suggests. According to Howell [74] the decision whether the continuum treatment can be used depends on two factors. The first factor is the dimensionless bed size (L/d) where L is the minimum bed dimension and d the particle diameter d_p .

The second factor is the size parameter defined as

$$\xi = \frac{\pi d_p}{\lambda} \quad (-) \quad (4.15)$$

where d_p is the particle diameter and λ the important wavelength in the radiative transfer.

For most applications the continuum treatment can be used if the dimensionless bed size exceeds $(L/d) \geq \sim 10$ and the size parameter $\xi \geq \sim 5$ [74]. If these criteria are fulfilled the effective radiative properties can be measured by averaging over the pore structures.

For this analysis the important wavelengths for solar radiation and thermal radiation of solids around 1000°C are below 100µm. For expected absorber materials with porosities around 90 percent and a cell diameter around 2mm both criteria are fulfilled.

Furthermore, Howell [74] mentions that if the continuum treatment is applicable the propagation of radiative intensity through the medium can be described by the standard radiative transfer equation (RTE).

$$\frac{dI_\lambda(\Omega)}{k_\lambda \cdot ds} = I_{s,\lambda}(\Omega) - I_\lambda(\Omega) \quad \left(\frac{W}{sr \cdot m} \right) \quad (4.16)$$

Here, I_λ denotes the spectral intensity, Ω the solid angle, k_λ the spectral attenuation or extinction coefficient, s the path length, and $I_{s,\lambda}$ the source function.

The spectral extinction coefficient can be calculated as

$$K_\lambda = (\alpha_\lambda + \sigma_{s\lambda}) \quad \left(\frac{1}{m^2} \right) \quad (4.17)$$

where α_λ and $\sigma_{s\lambda}$ are the spectral absorption and spectral scattering coefficient.

The source function consists of two terms. The first accounts for contribution to the intensity by emission of the medium. The second accounts for contribution to the intensity by intensity traveling other directions and then scattered into directions within the solid angle Ω .

$$I_{s,\lambda}(\Omega) = (1 - \beta_\lambda) \cdot I_{\lambda b} + \beta_\lambda \int_{\Omega_i=0}^{4\pi} I_\lambda(\Omega_i) \cdot \phi(\Omega_i, \Omega) \cdot d\Omega_i \quad \left(\frac{W}{sr \cdot m} \right) \quad (4.18)$$

Here, β_λ is the single scattering albedo of the medium defined as $\beta_\lambda = \sigma_\lambda/k_\lambda$. It is a measure for the fraction of extinction that is due to scattering. ϕ is the scattering phase function that describes the intensity scattered from the solid angle Ω into the solid angle Ω_i .

Because the radiative heat exchange distance within the porous medium is relatively short the assumption can be made that scattering effects are not significant. This means that radiation scattered from one element is absorber within a short distance from another element. Thus, the source function becomes zero and the RTE simplifies. Moreover, the spectral dependence is neglected as it the model would become too complex otherwise.

With these two assumptions the source function becomes zero and the RTE simplifies. The intensity distribution can then be calculated as

$$I(s) = I_0 \cdot e^{-Ks} \quad \left(\frac{W}{sr}\right) \quad (4.19)$$

where I_0 is the initial intensity, K the total extinction coefficient and s path length. With the further assumption of parallel irradiance the irradiance distribution within the porous medium becomes

$$E(x) = E_0 \cdot e^{-Kx} \quad \left(\frac{W}{m^2}\right) \quad (4.20)$$

where E denotes irradiance, E_0 is the initial irradiance impinging at the front surface, ρ_{surf} the reflectivity of the front surface, K the total extinction coefficient, and x the index variable along the porous medium. Figure 4.3 shows qualitatively the attenuation within the porous medium.

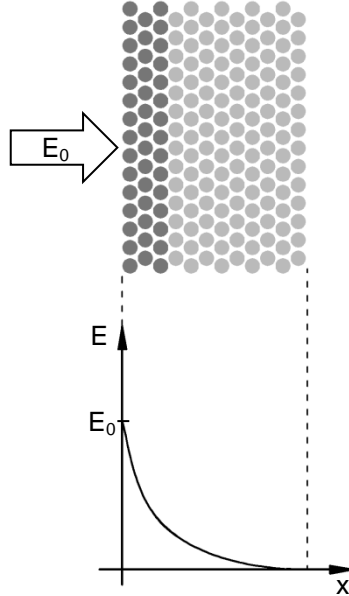


Figure 4.3: Irradiance attenuation within the porous medium

With the assumption that any reduction in the irradiance is due to absorption by the solid absorber the following equation shows the local heat source per unit volume.

$$s''(x) = -\frac{dE}{dx} = E_0 \cdot K \cdot e^{-Kx} \quad \left(\frac{W}{m^3}\right) \quad (4.21)$$

Taking into account the radial distribution of the irradiation the local heat source per unit volume can be expressed as

$$s''(x, r) = -\frac{dE}{dx} = \hat{E}_{00} \cdot \tau_w \cdot K \cdot e^{(\ln(\delta)\left(\frac{r}{R}\right)^2 - Kx)} \quad \left(\frac{W}{m^3}\right) \quad (4.22)$$

where \hat{E}_{00} is the peak irradiance in the middle of the focal point ($r=0$) impinging on the window front surface ($x=0$), τ_w the transmissivity of the window, δ a previously defined irradiance distribution factor, r and x the radial and axial index variable respectively, R the outer diameter of the absorber, and K the extinction coefficient of the absorber.

Howell [74] claims that open cell materials such as foams can be treated according to the continuum approach and that independent scattering should not be an issue. Furthermore, he presents a literature review of contemporary models describing the extinction coefficient in open cell materials. In Table 4.1 the different models are summarized.

Table 4.1: Different models for the extinction coefficient in open cell materials

	K (1/m)	Materials	Condition	Wave length	Source
1	$K = \frac{3}{\phi}(1 - \varepsilon)$ (4.23)	PSZ	$\phi > 0.6$ mm		Hsu and Howell [76]
2	$K = \frac{\varphi}{\phi}(1 - \varepsilon)$ (4.24) $a = (2 - \varepsilon)\frac{3}{2\phi}(1 - \varepsilon)$ (4.25) $\sigma_s = \varepsilon\frac{3}{2\phi}(1 - \varepsilon)$ (4.26)	PS ZrO ₂ : $\varphi=4.4$ SiC: $\varphi=4.8$		400 - 500nm	Hendricks and Howell [77]
3	$K = \frac{3}{\phi}(1 - \varepsilon)$ (4.27)	Mullite, SiC, cordierite, yttria-zirconium-alumina	1200 – 1400 K		Mital [78]

Here d_p is the mean particle diameter, Φ the cell diameter, and ε the porosity.

Fu et al. [79] compared three of the above mentioned models with their own measurements. The results of their study are shown in Table 4.2.

Table 4.2: Ranges of measured and predicted extinction coefficients for cellular ceramics [79]

	Pores per centimeter (PPC)			
	4	8	12	26
Hale and Bohn ($\lambda = 0.488 \mu\text{m}$) (Alumina)	900 - 1000	1100 – 1200	1100 – 1300	2400 - 2600
Hendricks and Howell [77] ($\lambda = 0.4 - 5 \mu\text{m}$) (PSZ) (OB SiC)	570 - 800 500 - 550	940 – 1100 600 – 840		2000 - 3630 1150 - 2600
Mital et al (YZA, mullite, SiC, cordierite, cordierite LS 2)	105 - 125	202 - 225		
Fu et al. [79] (Based on $\varepsilon_p=0.85$)	419 – 479	837 – 958	1257 - 1437	2733 - 3113

It can be seen that the correlations of Hale and Bohn as well as the one from Hendricks and Howell [77] have good agreement with the experimental data. The predictions of Hendricks and Howell [77] agree best for high porosities i.e. few pores per centimeter. Thus, this correlation is used for further analyses because high porosities are expected.

Unfortunately, no correlations for metallic foam were found. Therefore, it is assumed that the correlations valid for ceramics foams are valid for metallic foams as well.

Another important radiative property of the absorber is its emissivity. Because the structure of the absorber is complex the calculation of the emissivity is not trivial. Fu et al. [79] conducted an investigation concerning said emissivity.

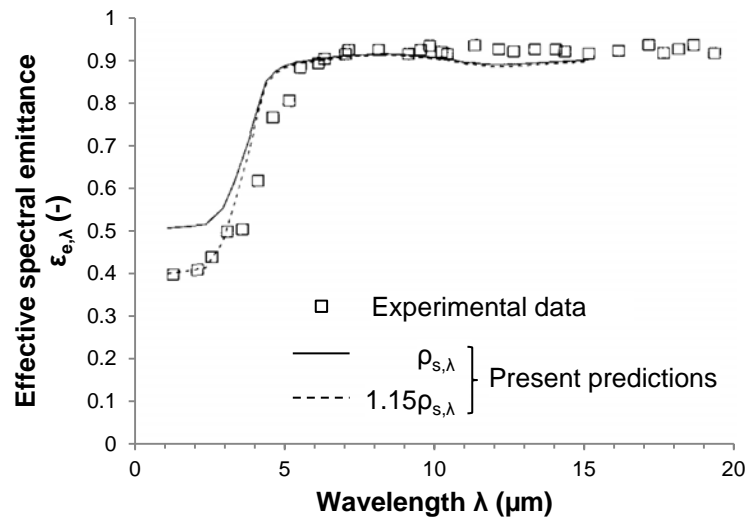


Figure 4.4: Spectral normal emittance of a cellular ceramic [79] ($\epsilon_p=0.85, 12 \text{ PPC}$)

Figure 4.4 shows the spectral emittance for a cellular ceramic with a porosity of 85 percent and 12 pores per centimeter. Although this specimen corresponds to a cell diameter of approximate 1mm it is the best figure found. For further calculations a constant emittance over the spectral range is assumed. Based on the figure above it is approximated to be 80 percent. Here, the same problem as for the extinction coefficient is present. No correlation of experimental data for the emittance of metallic foam was found. Thus, the same assumption as before is made and the emittance of ceramic and metallic foam is considered to be the same.

According to Howell [74] the radiative conductivity for an optically thick medium can be estimated by

$$k_r = \frac{16 \cdot \sigma \cdot T_s^3}{3 \cdot K} \quad \left(\frac{W}{m^2}\right) \quad (4.28)$$

where σ is the Stefan-Boltzmann constant, T_s the temperature of the solid, and K the radiative extinction coefficient. This estimation can be made if the optical thickness

$$\tau = K \cdot L \gg 1 \quad (-) \quad (4.29)$$

where L is the smallest dimension in the medium. With an extinction coefficient in the order of magnitude of 100 and a cell diameter in the order of magnitude of one millimeter this condition is not fulfilled. Nevertheless, this radiative conductivity is used since it is the only way to consider the radiative transport within the absorber with a reasonable effort.

4.1.1.c Solid mechanics absorber

In this section the mechanical properties of absorber are discussed that are needed for solid mechanics calculations. Ashby [92] and Gibson and Ashby [93] present correlations for the scaling of cellular solids' properties such as foam.

An important parameter used for the scaling is the relative density defined as

$$\rho = \frac{\tilde{\rho}}{\rho_s} = 1 - \varepsilon_p \quad (-) \quad (4.30)$$

where $\tilde{\rho}$ is the density of the foam, ρ_s the density of the solid of which the foam is made, and ε_p the porosity.

According to Gibson and Ashby [93] the Young's modulus \tilde{E} , the shear modulus \tilde{G} , the Poisson's ratio $\tilde{\nu}$, and the bulk modulus \tilde{K} of the foam can be expressed as

$$\frac{\tilde{E}}{E_s} \approx \rho^2 \quad (-) \quad (4.31)$$

$$\frac{\tilde{G}}{E_s} \approx \frac{3}{8}\rho^2 \quad (-) \quad (4.32)$$

$$\tilde{\nu} \approx \frac{1}{3} \quad (-) \quad (4.33)$$

$$\frac{\tilde{K}}{E_s} \approx \frac{1}{9}\rho \quad (-) \quad (4.34)$$

where E_s is the Young's modulus of the material the foam is made of.

In ductile materials the collapse is dominated by bending behavior i.e. that the foam collapses by plastic bending of the cell edges. The stress at which plastic strain starts can be expressed as

$$\frac{\tilde{\sigma}_{pl}}{\sigma_{\gamma,s}} \approx 0.3\rho^{3/2} \quad (-) \quad (4.35)$$

where $\sigma_{\gamma,s}$ is the yield strength of the solid of which the foam is made of. It is also called plateau stress because the deformation happens at almost constant stress.

Elastomeric foams do not collapse by bending but by buckling. The stress at which plastic buckling begins can be expressed by the following equation.

$$\frac{\tilde{\sigma}_{el}}{E_s} \approx 0.05\rho^2 \quad (-) \quad (4.36)$$

Brittle materials as ceramic foam collapse due to cell wall fracture. The crushing stress can be expressed as

$$\frac{\tilde{\sigma}_{cr}}{\sigma_{cr,s}} = 0.2\rho^{3/2} \quad (-) \quad (4.37)$$

where $\sigma_{cr,s}$ is the modulus of rupture of a strut.

The linear thermal expansion coefficient on the other hand does not scale between the solid material and an open cell material i.e. it remains the same.

In order to see whether the internal stresses are acceptable or not comparison stresses have to be calculated.

For ductile materials such as steel a comparison stress according to von Mises can be calculated by

$$\sigma_{c,v}^2 = \sigma_x^2 + \sigma_y^2 + \sigma_z^2 - \sigma_x\sigma_y - \sigma_x\sigma_z - \sigma_y\sigma_z + 3(\tau_{xy}^2 + \tau_{xz}^2 + \tau_{yz}^2) \quad (Pa^2) \quad (4.38)$$

$$\sigma_{c,v}^2 = \frac{1}{2}[(\sigma_I - \sigma_{II})^2 + (\sigma_{II} - \sigma_{III})^2 + (\sigma_{III} - \sigma_I)^2] \quad (Pa^2) \quad (4.39)$$

where σ_x , σ_y , and σ_z are the normal stresses in the x, y, and z direction, where τ_x , τ_y , and τ_z are the shear stresses in the x, y, and z direction, and σ_I , σ_{II} , and σ_{III} the principal stresses.

For brittle material such as ceramic another theory for calculating the comparison stress needs to be applied. The maximum stress theory according to Rankine is based on the hypothesis that the material will fail due to the maximal principal stress is suitable for these materials. The comparison stress can be calculated as

$$\sigma_{c,p} = \max(\sigma_I; \sigma_{II}; \sigma_{III}) \quad (Pa) \quad (4.40)$$

where σ_I , σ_{II} , and σ_{III} are the principal stresses.

For ceramic foam materials compressive stress is equally bad as tensile stress. The comparison stress can therefore be expressed by the following equation.

$$\sigma_{c,p} = \max(|\sigma_I|; |\sigma_{II}|; |\sigma_{III}|) \quad (Pa) \quad (4.41)$$

4.1.1.d Radiation treatment window

This section presents the radiation treatment within the glass window since the basic receiver design is pressurized a window is needed. A preliminary analysis shows that the most suitable materials for the window are fused silica or quartz glass as relatively high temperatures are expected.

In order to describe the radiation behavior in the glass window the change of intensity of a light beam passing through a glass plate has to be looked at.

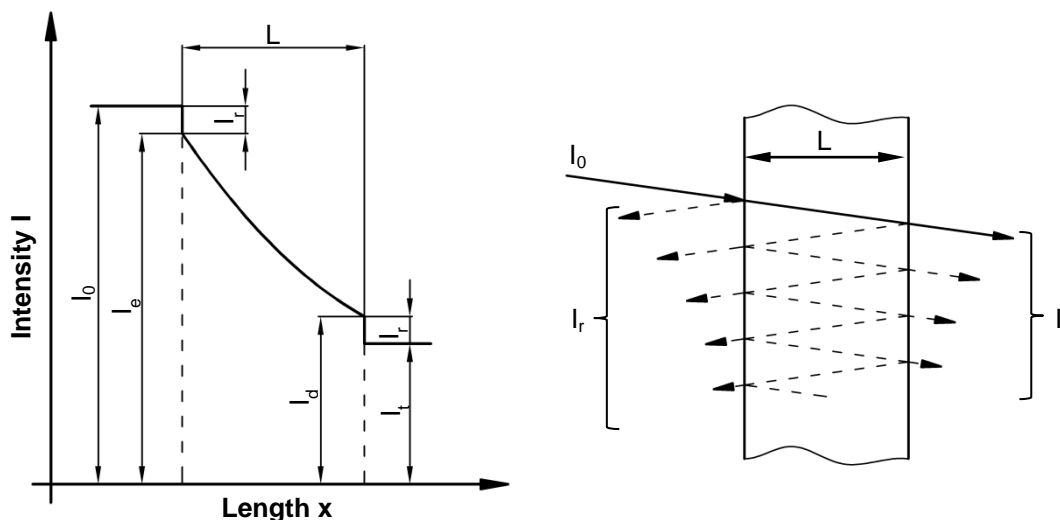


Figure 4.5: Change of intensity of a light beam passing through a glass plate [82]
One beam (left), multiple reflections (right)

Figure 4.5 on the left shows the change of intensity for a single beam where I_0 is the incident intensity, I_r the reflected intensity, I_e the entrance intensity, I_d the exit intensity, I_t the transmitted intensity, and L the plate thickness. On the right multiple reflections within the glass plate are presented.

The following equations if not otherwise mentioned are based on Bach and Neuroth [82]. For a two reflections, one at the inlet and outlet boundary respectively, the transmitted intensity can be calculated as

$$I_t = I_0 \cdot (1 - r)^2 \cdot e^{-K \cdot L} \quad \left(\frac{W}{sr}\right) \quad (4.42)$$

where K is the extinction coefficient per unit length and r is reflectivity.

As described in equation 4.17 the extinction coefficient can be calculated as the sum of the absorption and scattering coefficient. It is also related to the complex index of refraction. According to Bennet [83] the complex refractive index is defined as

$$\tilde{n} = n - ik \quad (-) \quad (4.43)$$

where n is the refractive index, and k the extinction constant. He also states the correlation between the extinction constant and the extinction coefficient as

$$K = \frac{4\pi k}{\lambda_0} \quad \left(\frac{1}{m}\right) \quad (4.44)$$

where K is the extinction coefficient, k the extinction constant, and λ_0 the wavelength in vacuum.

For a dielectric material with the refractive index n the reflectivity is shown in the following equation.

$$r = \left(\frac{n - 1}{n + 1}\right)^2 \quad (-) \quad (4.45)$$

When taking into account multiple reflections the transmission across the glass plate can be calculated as

$$\tau = \frac{I_t}{I_0} = P \cdot \tau_i \quad (-) \quad (4.46)$$

where τ_i is the internal transmission

$$\tau_i = \frac{I_d}{I_e} = e^{-K \cdot L} \quad (-) \quad (4.47)$$

and P the “reflection factor”. It can be approximated by

$$P \approx \frac{(1 - r)^2}{1 - r^2} = \frac{2n}{n^2 + 1} \quad (-) \quad (4.48)$$

while making an error in the range of 10^{-2} to 10^{-3} depending on the reflectivity and the internal transmission [82].

For multiple reflections the absorption α within the glass plate can be calculated as

$$\alpha = \frac{I_a}{I_0} = (1 - r) \cdot \sum_{i=0}^{\infty} r^i \cdot (e^{-i \cdot K \cdot L} - e^{-(i+1) \cdot K \cdot L}) \quad (-) \quad (4.49)$$

where I_a is the absorbed intensity within the glass plate. However, the absorption can be very good approximated accounting for only one reflection on the inside, i.e. the reflection is passing through the glass plate in the opposite direction once, by the following equation.

$$\alpha \approx (1 - r)(1 - e^{-K \cdot L}) + (1 - r)r(e^{-K \cdot L} - e^{-2 \cdot K \cdot L}) \quad (-) \quad (4.50)$$

For fused silica glass Bach and Neuroth [82] present typical optical properties shown in Figure 4.6. According to Heraeus [86] the optical properties of fused silica and quartz glass are very similar. Therefore, the optical calculations are based on fused silica and it is assumed that they are valid for quartz glass as well.

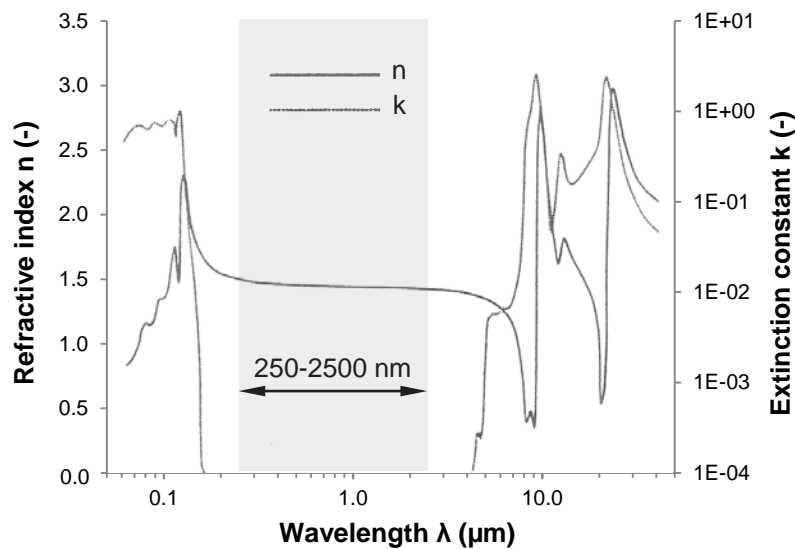


Figure 4.6: Optical constants of fused silica (SiO_2 glass) [82]

The interesting spectrum of wavelengths for the impinging solar radiation onto the glass window is determined by the spectral irradiance of the light source within the solar lab and the sunlight respectively. Both show a similar range of 250 to 2500 nm (cp. Figure 3.6 and Figure 3.7). Within this spectral range the refractive index and the absorption constant can be considered as constant. For the refractive index a value of 1.5 is considered that is also the value the glass manufacturer Schott specifies for their silica glass [87].

For the wavelength of interest the extinction constant cannot be determined from Figure 4.6. The only statement that can be made is that the extinction constant is lower than 10^{-4} . Unfortunately, the source mentioned (Philipp [84]) does not provide data for this wavelength either. However, Kitamura et al. [85] present another summary for the optical constants of silica glass. According to their paper the extinction constant in for wavelengths between 250 and 2500 nm is almost constant at a value of 10^{-7} . As described in equation 4.47 the extinction coefficient is not only dependent on the extinction constant but also on the wavelength. Figure 4.7 shows both the spectral and the mean extinction coefficient for the before mentioned wavelength.

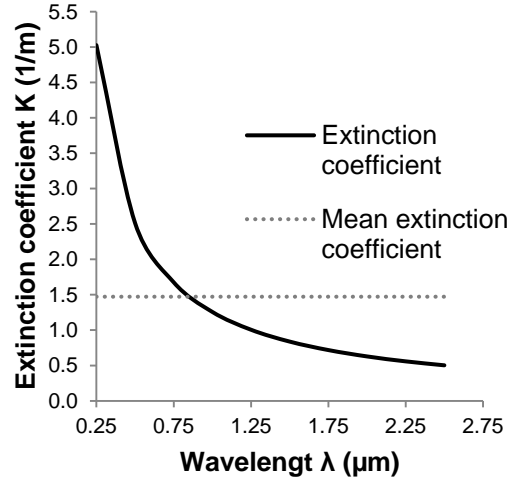


Figure 4.7: Spectral extinction coefficient

Based on the idealized calculations, a glass plate of 5mm in thickness, and a mean extinction coefficient of 1.48 the transmittance, absorptance, and reflectance are 91.43, 0.73, and 7.84 percent respectively.

The thermal radiation of the hot absorber to the glass window happens at higher wavelengths than the solar radiation. The emittance of the sun can be approximated by a blackbody radiator at 5800K. The hot solid absorber on the other hand emits thermal radiation at temperatures around 1000°C. Figure 4.8 on the left shows the spectral emittance of a blackbody radiator at 5800 and 1300 K respectively.

The radiant blackbody spectral emittance is calculated according to Planks law as

$$M(\lambda, T) = \frac{2\pi hc_0^2}{\lambda^5 \left[e^{\left(\frac{hc_0}{\lambda kT}\right)} - 1 \right]} \quad \left(\frac{W}{m^3}\right) \quad (4.51)$$

where $h = 6.626 \cdot 10^{-34}$ Js and $k = 1.381 \cdot 10^{-23}$ J/K are the universal Planck and Boltzmann constant respectively, $c_0 = 2.999 \cdot 10^8$ m/s is the speed of light in vacuum, and T is the absolute temperature of the blackbody.

Figure 4.8 on the right shows the fraction of the total emission in the spectral band from 0 to λ as a function of λT . It is defined by the following equation.

$$F_{(0 \rightarrow \lambda)} = \frac{\int_0^\lambda M_{\lambda,b} d\lambda}{\int_0^\infty M_{\lambda,b} d\lambda} \quad (-) \quad (4.52)$$

For a blackbody radiator at 1300K the fraction above a wavelength of 2500nm is about 65 percent. For a blackbody radiator of 5800K the fraction above a wavelength of 2500nm is only around 3 percent. Moreover, the absorption constant shown in Figure 4.6 increases significantly above a wavelength of 3000nm. Therefore thermal radiation has to be treated in a different way than solar radiation.

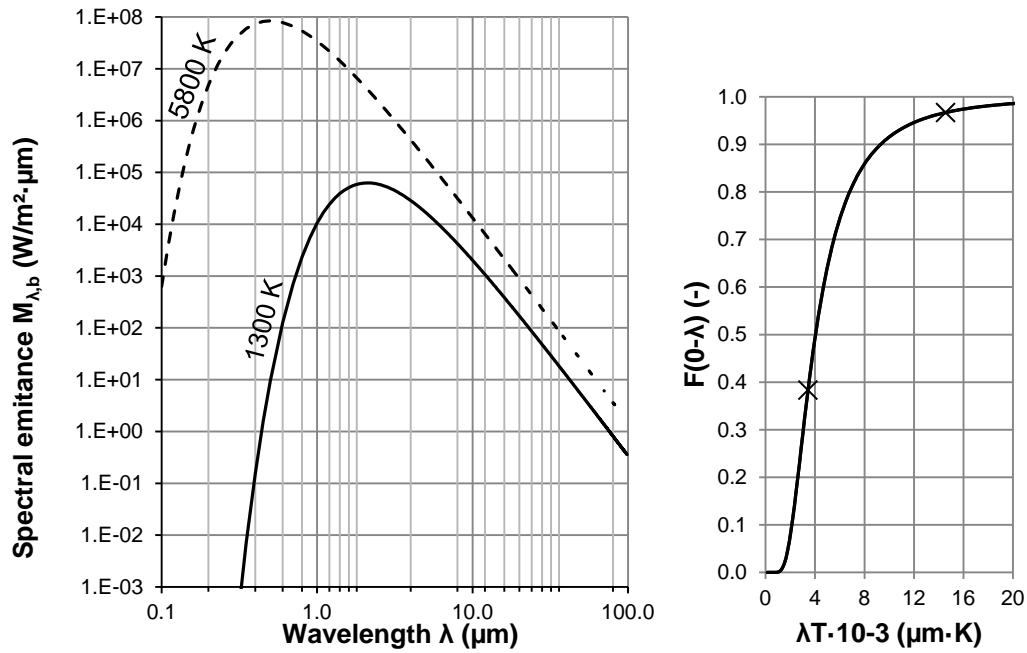


Figure 4.8: Blackbody emittance [35]
Spectral emissive power (left), fraction of the total emission in the spectral band from 0 to λ as a function of λT (right)

Röger et al. [88] present optical properties of fused silica glass based on more detailed calculations. The main difference is that the optical properties are spectrally weighted with respect to the dominant radiation. Figure 4.9 shows the weighted optical properties of a 5mm thick specimen of fused silica. The left column presents the optical properties weighted with the spectrum of the impinging solar radiation. The right column presents the optical properties weighted according to a blackbody spectrum at 1100°C.

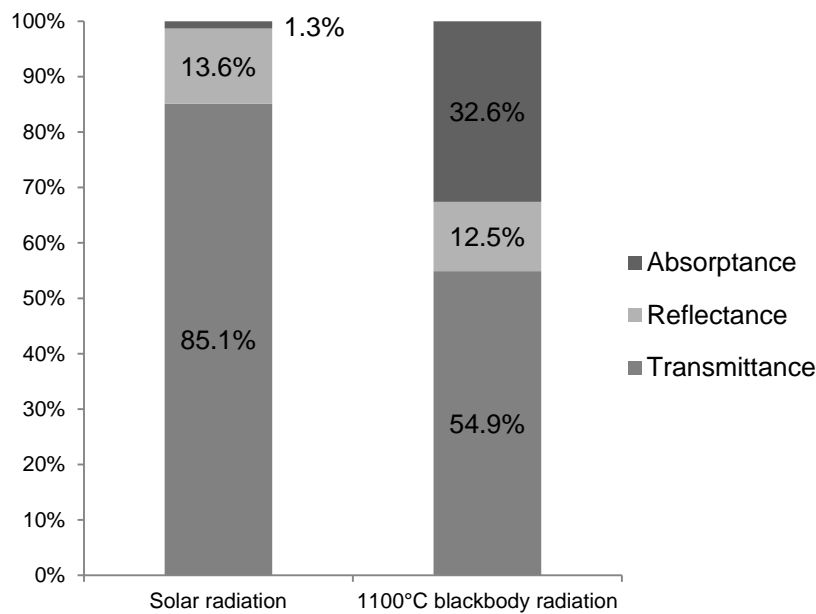


Figure 4.9: Spectrally weighted absorptance, reflectance, and transmittance [88]
Solar spectrum weighting (UV) (left), 1100°C blackbody spectrum weighting (IR) (right)

The transmittance and the reflectance for the solar radiation presented by Röger et al. [88] show good agreement with the values calculated before. In contrast, the absorptance is almost twice as high. Since the optical properties presented by Röger et al. [88] are based on more detailed calculations and define a more unfavorable scenario they are chosen for further investigations. Furthermore, by Röger et al. [88] claim that infrared-reflective solar transparent coatings on the inside of the fused silica window can significantly reduce the glass temperature. Research on this topic is still going on and it is not market-ready yet. Thus, the possibility of coating the glass window is not considered in this situation analysis.

Due to the fact that the radiation attenuation within the window is relatively small the assumption of an axially constant heat source can be made. For the solar radiation the heat source can be expressed as

$$s''_{UV}(r) = -\frac{dE}{dx} = \frac{\hat{E}_{00} \cdot \alpha_{UV}}{s_w} \cdot e^{(\ln(\delta)(\frac{r}{R})^2)} = \frac{\hat{E}_{00} \cdot \alpha_{UV}}{s_w} \cdot \delta^{(\frac{r}{R})^2} \quad \left(\frac{W}{m^3}\right) \quad (4.53)$$

where \hat{E}_{00} is the peak irradiance in the middle of the focal point ($r=0$) impinging on the window front surface ($x=0$), $E(r)$ the thermal irradiation as a function of the radius, α_{UV} the absorptance of the solar of the window respectively, and s_w the thickness of the window.

Because elevated temperatures of the window are expected Table 4.3 shows the maximal working temperatures for high temperature glass.

Table 4.3: Temperature stability of glass windows

Type	Max. continuous working temperature (°C)	Max. short-term working temperature (°C)	Manufacturer
Electrically fused quartz	1160	1300	Heraeus [86]
Flame fused quartz	1110	1250	Heraeus [86]
Fused silica	950 / 930	1200 / 1180	Heraeus [86] / Schott [87]

However, Röger et al. [88] claim for fused silica glass the maximal acceptable temperature for enduring and safe operation is considered to be 800°C especially if the receiver design is pressurized to 15 bar as the REFOS receiver in the SOLGATE project.

4.1.1.e Surface-to-surface radiation modeling

This section covers the radiation heat exchange between the absorber surface and the window. Because the window is relatively thin and the heat source is considered constant in axial direction the temperature in this axial direction is considered constant as well.

Figure 4.10 shows the model used for calculating the radiation transfer between the two surfaces. It is assumed that solar radiation is neither reflected nor absorbed at the front surface of the absorber solar radiation at the boundary is not of importance and therefore not sketched in Figure 4.10. With a further assumption that the thermal radiation impinging on the absorber surface does not penetrate the absorber volume due to its large wavelength the absorber can be treated as an opaque material with respect to thermal radiation.

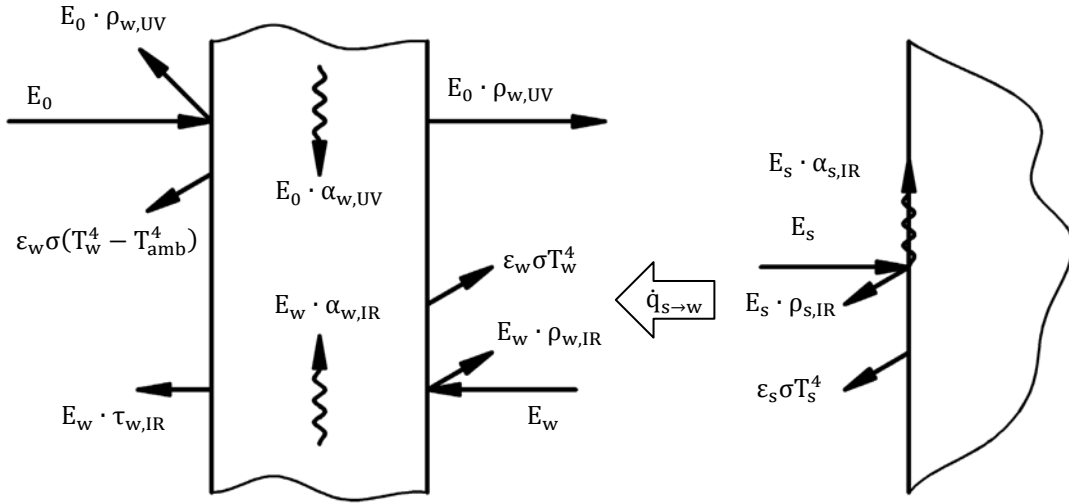


Figure 4.10: Radiation exchange between window and absorber surface

An opaque material is characterized by a transmissivity $\tau = 0$ and therefore the following equation simplifies.

$$\rho_{IR} + \alpha_{IR} + \tau_{IR} = 1 \quad (-) \quad (4.54)$$

The reflectivity is then defined as

$$\rho_{IR} = 1 - \alpha_{IR} \quad (-) \quad (4.55)$$

where the absorptivity α can be approximated with sufficient accuracy by the emissivity ε .

The total radiation exchange between the two surfaces can then be calculated as

$$\dot{Q}_{s \rightarrow w} = \frac{\sigma \cdot \left(T_s^4 - \frac{\varepsilon_{w,IR}}{1 - \rho_{w,IR}} T_w^4 \right)}{\frac{(1 - \varepsilon_s)}{A_s \varepsilon_s} + \frac{1}{A_w F_{s \rightarrow w}} + \frac{\rho_{w,IR}}{A_w (1 - \rho_{w,IR})}} \quad (W) \quad (4.56)$$

where ε is the emissivity, ρ_{IR} the reflectivity, A the surface area, and $F_{s \rightarrow w}$ the view factor between the two surfaces. Because the equation above considers the entire heat flux to be absorbed the transmitted part has to be accounted for separately. The next equation shows the irradiation that impinges at the window surface.

$$E_w = \frac{\varepsilon_{w,IR} \sigma T_w^4 + \frac{\dot{Q}_{s \rightarrow w}}{A_w}}{(1 - \rho_{w,IR})} \quad \left(\frac{W}{m^2} \right) \quad (4.57)$$

Knowing the irradiation the transmitted part can be expressed as

$$\dot{q}_t = \tau_{w,IR} \cdot E_w = \tau_{w,IR} \cdot \frac{\varepsilon_{w,IR} \sigma T_w^4 + \frac{\dot{Q}_{s \rightarrow w}}{A_w}}{(1 - \rho_{w,IR})} \quad \left(\frac{W}{m^2} \right) \quad (4.58)$$

where $\tau_{w,IR}$ is the transmissivity of the window for thermal radiation.

The view factor $F_{s \rightarrow w}$ is defined as the fraction of radiation that leaves the surface s that is intercepted by the surface w . Considering the radiative heat transfer between the annular

surfaces of every control volume at the boundary would require a more detailed analysis. Therefore, it is assumed that the distance between the two surfaces is sufficiently small enough that all radiation emitted by one annular surface is intercepted by the adjacent annular surface and none by the neighboring surfaces. Thus, the view factor for the radiation heat exchange between the absorber and window surface is one.

4.1.1.f Heat exchanger modeling

As mentioned previously the first part of the receiver is very similar to a heat exchanger. Thus, the heat transfer within this part is calculated according to heat exchanger theory namely the number of transfer units (NTU) method. It assumes perfect insulation on the outside and i.e. no heat transfer to the ambient. Figure 4.11 shows the basic model. If not otherwise mentioned the following equations are based on Incropera et al. [35].

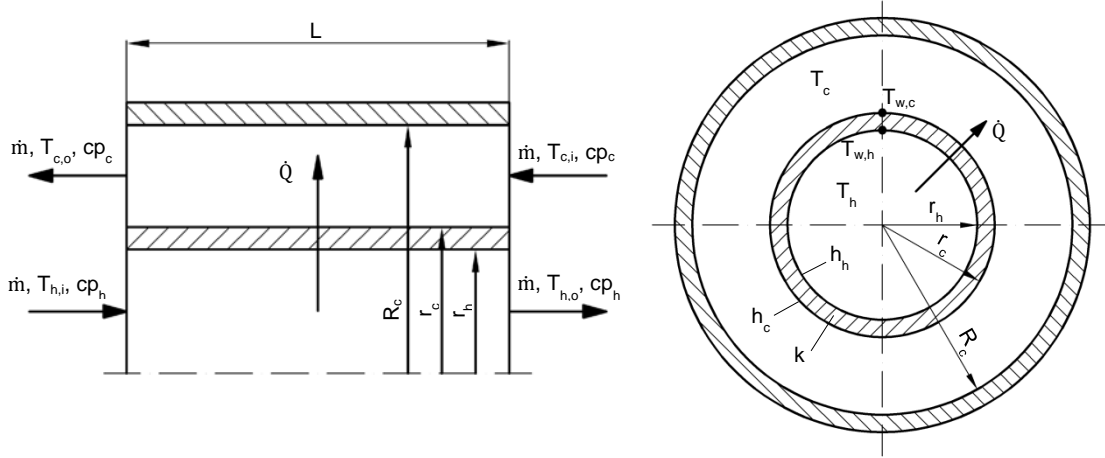


Figure 4.11: Heat exchanger model

The actual transferred energy is the product of the maximal transferrable energy and the heat exchanger effectiveness ε .

$$\dot{Q} = \varepsilon \cdot \dot{Q}_{max} \quad (W) \quad (4.59)$$

The maximal transferrable energy can be calculated as

$$\dot{Q}_{max} = C_{min} \cdot (T_{h,i} - T_{c,i}) \quad (W) \quad (4.60)$$

where C_{min} is the minimal heat capacity rate which is the product of the mass flow and the specific heat capacity and $T_{h,i}$ and $T_{c,i}$ the fluid inlet temperature at the hot and cold side respectively. The actual heat transfer rate is defined by the following equation.

$$\dot{Q} = C_h \cdot (T_{h,i} - T_{h,o}) = C_c \cdot (T_{c,o} - T_{c,i}) \quad (W) \quad (4.61)$$

The above mentioned heat exchanger effectiveness is a function of the number of transfer units (NTU) and the heat capacity ratio C_r . For a counterflow heat exchanger and a heat capacity ratio smaller than one the effectiveness can be calculated as

$$\varepsilon = \frac{1 - \exp[-NTU \cdot (1 - C_r)]}{1 - C_r \cdot \exp[-NTU \cdot (1 - C_r)]} \quad (-) \quad (4.62)$$

whereas for a heat capacity ratio equal to one the correlation simplifies and the effectiveness can be calculated by the following equation.

$$\varepsilon = \frac{NTU}{1 - NTU} \quad (-) \quad (4.63)$$

The number of transferred units is defined as

$$NTU = \frac{UA}{C_{min}} \quad (-) \quad (4.64)$$

where U is the overall heat transfer coefficient and A the heat transfer area. The heat capacity ratio can be calculated as

$$C_r = \frac{C_{min}}{C_{max}} \quad (-) \quad (4.65)$$

and the overall heat transfer coefficient as

$$\frac{1}{UA} = \frac{1}{h_h \cdot 2\pi r_h \cdot L} + \frac{\ln(r_c/r_h)}{2\pi kL} + \frac{1}{h_c \cdot 2\pi r_c \cdot L} \quad \left(\frac{K}{W}\right) \quad (4.66)$$

where h_c and h_h are the convective heat transfer coefficient of the cold and hot side respectively, r_c and r_h the radius of the cold and hot side respectively, L the length of the heat exchanger, and k the conductive heat transfer coefficient of the tube between the two fluids. The convective heat transfer is calculated according to equation 3.11 with the Nusselt number defined in Table 3.7.

4.1.1.g Pressure drop

The pressure drop in the receiver is calculated as the sum of pressure drops due to different effects as

$$\Delta p = \Delta p_{t,in} + \Delta p_{t,out} + 2\Delta p_D + \Delta p_{c,in} + \Delta p_{c,out} + \Delta p_{abs} \quad (Pa) \quad (4.67)$$

where $\Delta p_{t,in}$ and $\Delta p_{t,out}$ is the pressure drop in the inflow and outflow tube of the receiver respectively, Δp_D the pressure drop due to the deviation of the flow by 90°, $\Delta p_{c,in}$ and $\Delta p_{c,out}$ the pressure drop due to change of the cross sectional area at the inlet and outlet of the cavity between absorber and window, and Δp_{abs} the pressure drop across the absorber. If not otherwise mentioned the following equations are based on the Association of German Engineers [47].

The pressure in the inflow and outflow of the receiver is calculated by

$$\Delta p_t = \xi_t \cdot \frac{L_t}{d_h} \cdot \frac{\rho \cdot u_t^2}{2} \quad (Pa) \quad (4.68)$$

where ξ_t is the friction factor, L_t and d_h the length and hydraulic diameter of the tube respectively, ρ and u_t the density and mean velocity inside the tube. For laminar flow the friction factor is calculated according to equation 3.16 and for turbulent flow according to equation 3.18.

The pressure drop across the cavity between the window and absorber is approximated by superposing pressure drop correlations designed for fluid flow in conduits. Even though this approach is not accurate it gives a fairly good estimation.

The first effect considered across the cavity is the pressure drop due to deviation of the flow by

$$\Delta p_D = \xi_D \cdot \frac{\rho \cdot u^2}{2} \quad (Pa) \quad (4.69)$$

where ξ_D is the friction factor for flow deviation. For a deviation of 90° the friction factor can be approximated as 1.2 [47]. As the flow is deviated by 180° the pressure drop is doubled.

The second effect considered is the pressure drop due to the change of cross sectional area at the inlet and outlet of the cavity. Depending on the distance between the window and absorber the flow experiences a reduction or enlargement of the cross sectional area. If it the cross sectional area reduces the pressure drop is calculated by

$$\Delta p_R = \xi_R \cdot \frac{\rho \cdot u_2^2}{2} \quad (Pa) \quad (4.70)$$

where ξ_D is the friction factor for reduction of the cross sectional area and u_2 the fluid velocity after the reduction. The friction factor is determined according to Figure 4.12.

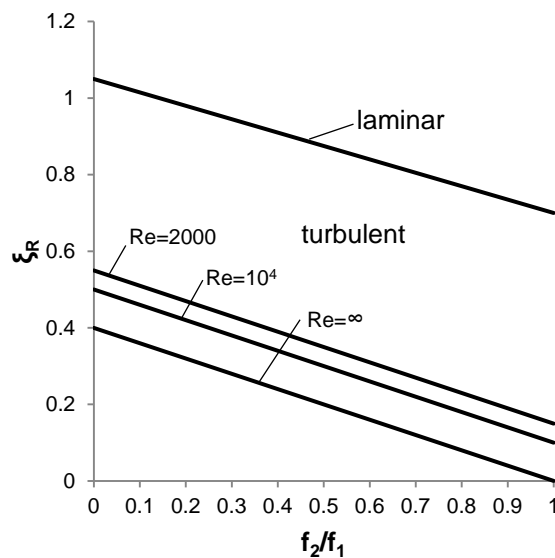


Figure 4.12: Friction factor for the abrupt reduction of the cross sectional area (on basis of [47])

Here, Re is the Reynolds number of the fluid after the reduction, f_1 and f_2 the cross sectional area before and after the reduction respectively. For Reynolds numbers between the illustrated the friction factor is linearly interpolated. The line denoting laminar flow is assumed to have a Reynolds number of zero whereas the line denoting an infinite Reynolds number is approximated by a Reynolds number of 10^{10} .

If it the cross sectional area enlarges the pressure drop is calculated by

$$\Delta p_E = \xi_E \cdot \frac{\rho \cdot u_1^2}{2} \quad (Pa) \quad (4.71)$$

where ξ_E is the friction factor for enlargement of the cross sectional area and u_1 the fluid velocity before the enlargement. The friction factor is calculated according to

$$\xi_E = \left(1 - \frac{f_1}{f_2}\right) \quad (-) \quad (4.72)$$

where f_1 and f_2 are the cross sectional area before and after the enlargement respectively.

The pressure drop across the absorber has already been discusses in the preliminary study in section 3.4.2 and the model presented by Bai [71] chosen. Therefore, the pressure drop across the absorber is calculated according to equation 3.43.

4.1.1.h Additional parameters

Table 4.4 shows additional parameter for both metallic and ceramic absorber materials at elevated temperatures in the order of magnitude of 1000°C. Most of the parameters are temperature dependent but for the sake of simplicity they are approximated as constant values.

Table 4.4: Additional parameters absorber materials

Parameter	Metal (353 MA)	Ceramic (SiC)
	Outokumpu [62]	Somiya and Inomata [80]
Thermal conductivity k	23 W/(m·K)	120 W/(m·K)
Linear thermal expansion coefficient α	$18 \cdot 10^{-6} \text{ K}^{-1}$	$4.3 \cdot 10^{-6} \text{ K}^{-1}$
Tensile strength	82 MPa	-
Bending strength σ	-	620 MPa
Poisson's ratio ν	0.24	0.16
Young's modulus	130 GPa	420 GPa

The reason why these two materials are chosen is simple. Outokumpu's 353 MA is an austenitic steel alloy with the highest service temperature found. It is able to withstand material temperatures up to 1150°C. Silicon carbide (SiC) is chosen because it is a commonly used material in solar receiver besides SiSiC. Moreover, it can withstand material temperatures up to 1500°C.

Further parameters of the glass window that are needed in this analysis are shown in Table 4.5. They are almost the same for all three types of glass. Simplifications and assumption made to gain these values are discussed below.

Table 4.5: Additional parameters window

Parameter	Value	References
Total normal emissivity ε	0.8	Tanaka et al. [89], Smith [90]
Thermal conductivity k	2 W/(m·K)	Heraeus [86], Schott [87]
Linear thermal expansion coefficient α	$0.5 \cdot 10^{-6} \text{ K}^{-1}$	Heraeus [86], Schott [87]
Bending strength σ	67 / 80–100 MPa	Heraeus [86] / Schott [87]
Poisson's ratio ν	0.17	Heraeus [86], Schott [87]
Young's modulus	72 GPa	Heraeus [86], Schott [87]

The total normal emissivity which is an important radiative property seems to be temperature depended. Tanaka et al. [89] and Smith [90] present experimental data for said emissivity. For temperatures up to 900°C they suggest that the emissivity does not change much. Since the temperature of the glass window is not expected to exceed 900°C a constant value is considered.

Because this analysis considers radial thermal conduction within the glass window the thermal conductivity is needed as well. According to the glass manufacturers Heraeus [86] and Schott [87] the thermal conductivity of fused silica is temperature depended. However, in the temperature range of interest between 400 and 950°C it can be approximated by a constant value.

In order to be able to consider thermally induced stresses the linear thermal expansion coefficient is needed. According to the glass manufacturers Heraeus [86] and Schott [87] this coefficient is again temperature dependent but way less than the thermal conductivity. Thus, the linear expansion coefficient can be approximated by a constant value as well.

For mechanical integrity calculations the bending strength of the window is of importance. According to Schott [87] it varies slightly with temperature and reaches a minimum of 80 MPa at the maximum working temperature of 930°C whereas according to Heraeus [86] the minimum bending strength is 67 MPa at the maximum working temperature of 950°C.

The remaining parameters are either not temperature dependent or no detailed specifications are given.

4.1.2 Numerical modeling

In order to solve the coupled differential equation for the absorber presented in section 3.4.2 the absorber is divided into a series of finite sections for which the equations can be solved. A number of finite differences methods can be chosen from to approximate the spatial derivatives to create algebraic equations that are easier to solve than the full differential equation.

Since this analysis is conducted at steady state conditions no numerical instabilities are expected. Thus an explicit scheme is chosen because it is easier to implement than an implicit scheme.

Under the condition of equidistant finite differences the first spatial derivative can be calculated using an explicit first-order upwind scheme. The application of a directional

scheme is possible because the fluid flow does not change its direction during the calculation. The error of the approximation is in the order of magnitude of the spacing.

$$\left. \frac{dT}{dx} \right|_i = \frac{T_i - T_{(i-1)}}{\Delta x} + O(\Delta x) \quad \left(\frac{K}{m} \right) \quad (4.73)$$

$$\left. \frac{dT}{dr} \right|_j = \frac{T_j - T_{(j-1)}}{\Delta r} + O(\Delta r) \quad \left(\frac{K}{m} \right) \quad (4.74)$$

The second spatial derivative is calculated by an explicit second-order central schema with an error in order of magnitude of the square of the spacing.

$$\left. \frac{d^2T}{dx^2} \right|_i = \frac{T_{(i+1)} - 2T_i + T_{(i-1)}}{\Delta x^2} + O(\Delta x^2) \quad \left(\frac{K^2}{m^2} \right) \quad (4.75)$$

$$\left. \frac{d^2T}{dr^2} \right|_j = \frac{T_{(j+1)} - 2T_j + T_{(j-1)}}{\Delta r^2} + O(\Delta r^2) \quad \left(\frac{K^2}{m^2} \right) \quad (4.76)$$

By substituting the derivatives in the previous mentioned differential equations a finite difference model for the absorber can be obtained.

Figure 4.13 shows the positions of the different temperature values needed for the evaluation of the different equations at the particular nodes.

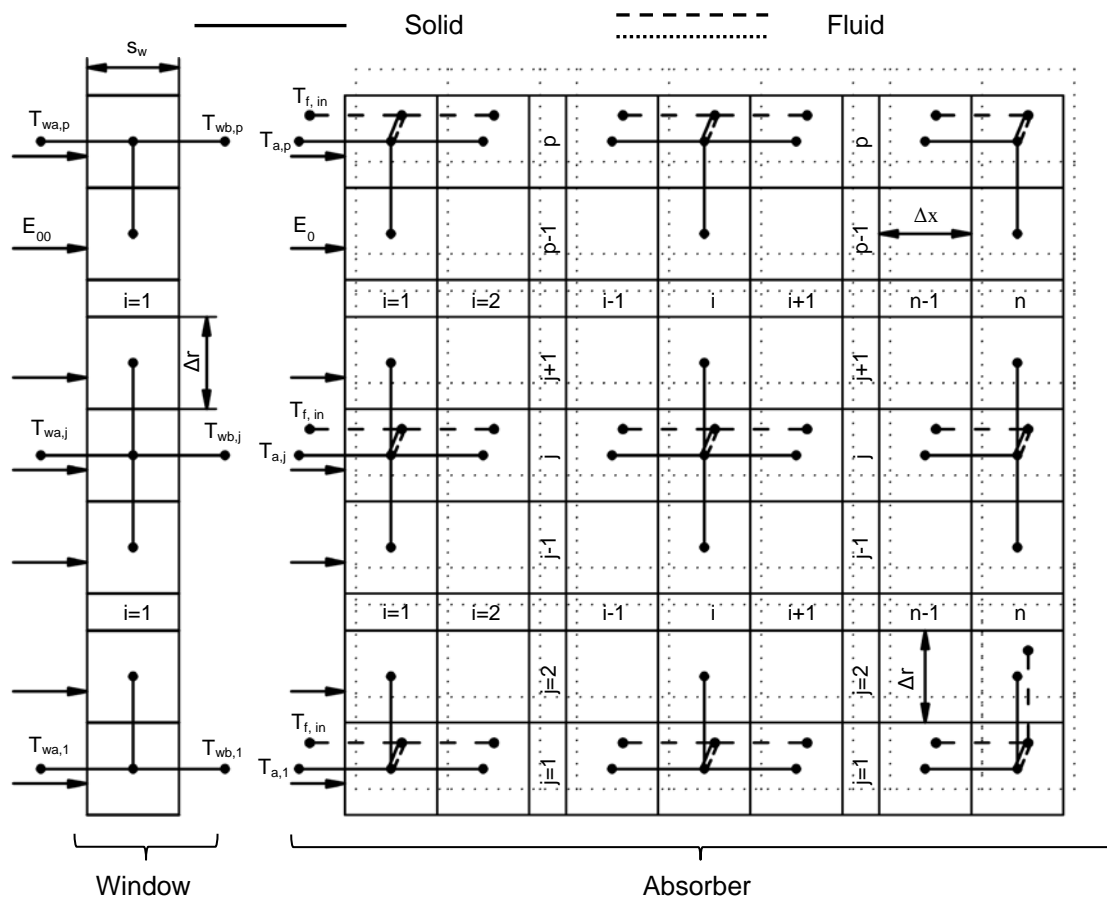


Figure 4.13: Numerical scheme layout

The heat source per unit volume due to radiation absorption within the absorber can be expressed as

$$\begin{aligned}
s''_{i,j} &= \frac{\int_{b_i^-}^{b_i^+} \int_{b_j^-}^{b_j^+} s''(r, x) \cdot 2r\pi \cdot dr \cdot dx}{\Delta x \cdot A_{ij}} \\
&= \frac{R^2}{(1-2j) \cdot \Delta r^2 \Delta x} \cdot \frac{\hat{E}_0}{\ln(\delta)} \\
&\quad \cdot \left[\delta^{\left(\frac{(j-1)\Delta r}{R}\right)^2} - \delta^{\left(\frac{j\Delta r}{R}\right)^2} \right] \cdot [e^{-k(i-1)\Delta x} - e^{-ki\Delta x}]
\end{aligned} \tag{4.77}$$

where $b_i^+ = i\Delta x$ and $b_i^- = (i-1)\Delta x$ are the position of the upwind and downwind boundary of the axial node i , $b_j^+ = j\Delta r$ and $b_j^- = (j-1)\Delta r$ are the position of the upwind and downwind boundary of the radial node j , and A_{ij} the cross sectional area of the CV j .

The heat source per unit volume due to radiation absorption within the window can be expressed as

$$\begin{aligned}
s''_j(r) &= \frac{\int_{b_j^-}^{b_j^+} s''(r, x) \cdot 2r\pi \cdot dr}{A_j} \\
&= \frac{R^2}{(1-2j) \cdot \Delta r^2 s_w} \cdot \frac{\alpha_{UV} \cdot \hat{E}_0}{\ln(\delta)} \cdot \left[\delta^{\left(\frac{(j-1)\Delta r}{R}\right)^2} - \delta^{\left(\frac{j\Delta r}{R}\right)^2} \right]
\end{aligned} \tag{4.78}$$

where $b_j^+ = j\Delta r$ and $b_j^- = (j-1)\Delta r$ are the position of the upwind and downwind boundary of the radial node j , and A_j the cross sectional area of the CV j .

For the HTF passing through the absorber and a central radial node j the following discrete equations can be written for the first axial node, for a central axial node i , and for the last axial node n respectively

$$\dot{M}_f c_{pf} \cdot T_{f,in} - \dot{M}_f c_{pf} \cdot T_{f,1,j} + h_v \Delta x \cdot (T_{s,1,j} - T_{f,1,j}) = 0 \tag{4.79}$$

$$\dot{M}_f c_{pf} \cdot T_{f,(i-1),j} - \dot{M}_f c_{pf} \cdot T_{f,i,j} + h_v \Delta x \cdot (T_{s,i,j} - T_{f,i,j}) = 0 \tag{4.80}$$

$$\dot{M}_f c_{pf} \cdot T_{f,(n-1),j} - \dot{M}_f c_{pf} \cdot T_{f,n,j} + h_v \Delta x \cdot (T_{s,n,j} - T_{f,n,j}) = 0 \tag{4.81}$$

where \dot{M}_f denotes the fluid mass flow per unit area. Since the equations do not change in radial direction they are not mentioned explicitly.

For the solid and a central radial node j the following discrete equations can be written for the first axial node, for a central axial node i , and for the last axial node n respectively

$$\begin{aligned}
&k_{se} \cdot \left(\frac{T_{s,a,j} - 2T_{s,1,j} + T_{s,2,j}}{\Delta x^2} \right. \\
&\quad \left. + \frac{T_{s,1,(j-1)} - 2T_{s,1,j} + T_{s,1,(j+1)}}{\Delta r^2} + \frac{T_{s,1,j} - T_{s,1,(j-1)}}{\left(j + \frac{1}{2}\right)\Delta r \cdot \Delta r} \right) \\
&\quad - h_v \cdot (T_{s,1,j} - T_{f,1,j}) + s''_{1,j} = 0
\end{aligned} \tag{4.82}$$

$$k_{se} \cdot \left(\frac{T_{s,(i-1),j} - 2T_{s,i,j} + T_{s,(i+1),j}}{\Delta x^2} + \frac{T_{s,1,(j-1)} - 2T_{s,1,j} + T_{s,(j+1)}}{\Delta r^2} + \frac{T_{s,i,j} - T_{s,i,(j-1)}}{(j + \frac{1}{2})\Delta r \cdot \Delta r} \right) \left(\frac{W}{m^3} \right) \quad (4.83)$$

$$- h_v \cdot (T_{s,i,j} - T_{f,i,j}) + s''_{i,j} = 0$$

$$k_{se} \cdot \left(\frac{T_{s,(n-1),j} - 2T_{s,n,j} + T_{s,b,j}}{\Delta x^2} + \frac{T_{s,(n-1),j} - 2T_{s,n,j} + T_{s,b,j}}{\Delta r} + \frac{T_{s,(n-1),j} - T_{s,(n-1),(j-1)}}{(j + \frac{1}{2})\Delta r \cdot \Delta r} \right) \left(\frac{W}{m^3} \right) \quad (4.84)$$

$$- h_v \cdot (T_{s,n,j} - T_{f,n,j}) + s''_{n,j} = 0$$

where T_a and T_b denote fictive temperatures before the inlet and after the outlet respectively to account for the boundary conditions.

For the window in the axial direction the following discrete boundary conditions can be written for a general radial node j and for the only node 1 at the downwind and upwind boundary respectively.

$$k_w \frac{dT_w}{dx} \Big|_{1^-,j} = -h_f \cdot (T_{w,j} - T_{amb}) - \varepsilon_{surf,w} \cdot \sigma \cdot (T_{w,j}^4 - T_{amb}^4) \left(\frac{W}{m^2} \right) \quad (4.85)$$

$$k_w \frac{dT_w}{dx} \Big|_{1^+,j} = -h \cdot (T_w - T_{f,c}) + \dot{q}_{s \rightarrow w,j} - \dot{q}_{t,j} \left(\frac{W}{m^2} \right) \quad (4.86)$$

For the solid in the axial direction and a general radial node j the following discrete boundary conditions can be written for the first node and for the last node n respectively.

$$k_{se} \frac{dT_s}{dx} \Big|_{1,j} \approx k_{se} \frac{T_{s,a,j} - T_{s,1,j}}{\Delta x} = -\dot{q}_{s \rightarrow w,j} \left(\frac{W}{m^2} \right) \quad (4.87)$$

$$k_{se} \frac{dT_s}{dx} \Big|_{n,j} \approx k_{se} \frac{T_{s,n,j} - T_{s,b,j}}{\Delta x} = 0 \left(\frac{W}{m^2} \right) \quad (4.88)$$

For the solid in the radial direction and a general axial node i the following discrete boundary conditions can be written for the first node and for the last node p respectively.

$$\frac{dT_s}{dr} \Big|_{i,1} = 0 \left(\frac{W}{m^2} \right) \quad (4.89)$$

$$\frac{dT_s}{dr} \Big|_{i,p} = 0 \left(\frac{W}{m^2} \right) \quad (4.90)$$

The implementation of the numerical model in MATLAB, especially solving the system of equations, can be seen in Appendix A: Numerical model in MATLAB.

4.1.3 Verification

Before using the numerical model in the optimization process it needs to be verified. Therefore, two models are created using the Multiphysics Modeling and Simulation Software COMSOL. The design parameters used for the verification are based on the Pareto-optimal solutions chosen in the optimization presented in section 4.1.4.

The first model is a simplified model and used to verify the solid and fluid temperatures within the absorber and the solid temperature of the window. The most important simplification made is the assumption that the fluid that enters the absorber has radially a totally uniform velocity and temperature distribution. The convective heat transfer between fluid and window is modeled according to the model of forced convection across a flat plate as in the self-made numerical model. Moreover, the temperature distribution within the window is considered axially constant.

The second model is a more detailed model that considers the non-uniform fluid flow within the receiver. The model is used to verify the pressure drop of the whole receiver. A detailed description of the model is given in the main study in section 4.4.1.

Figure 4.14 presents the fluid temperature and velocity arrows as well as the solid temperature of the window and the tubes for the two COMSOL models.

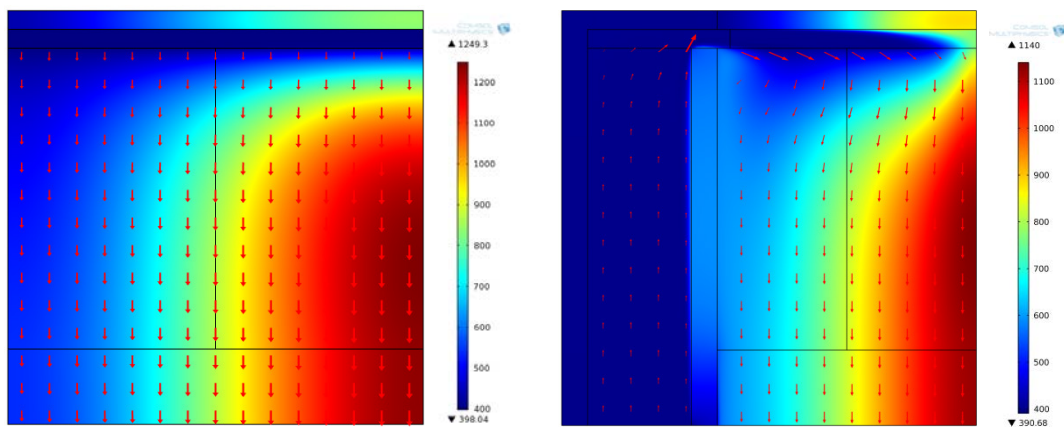
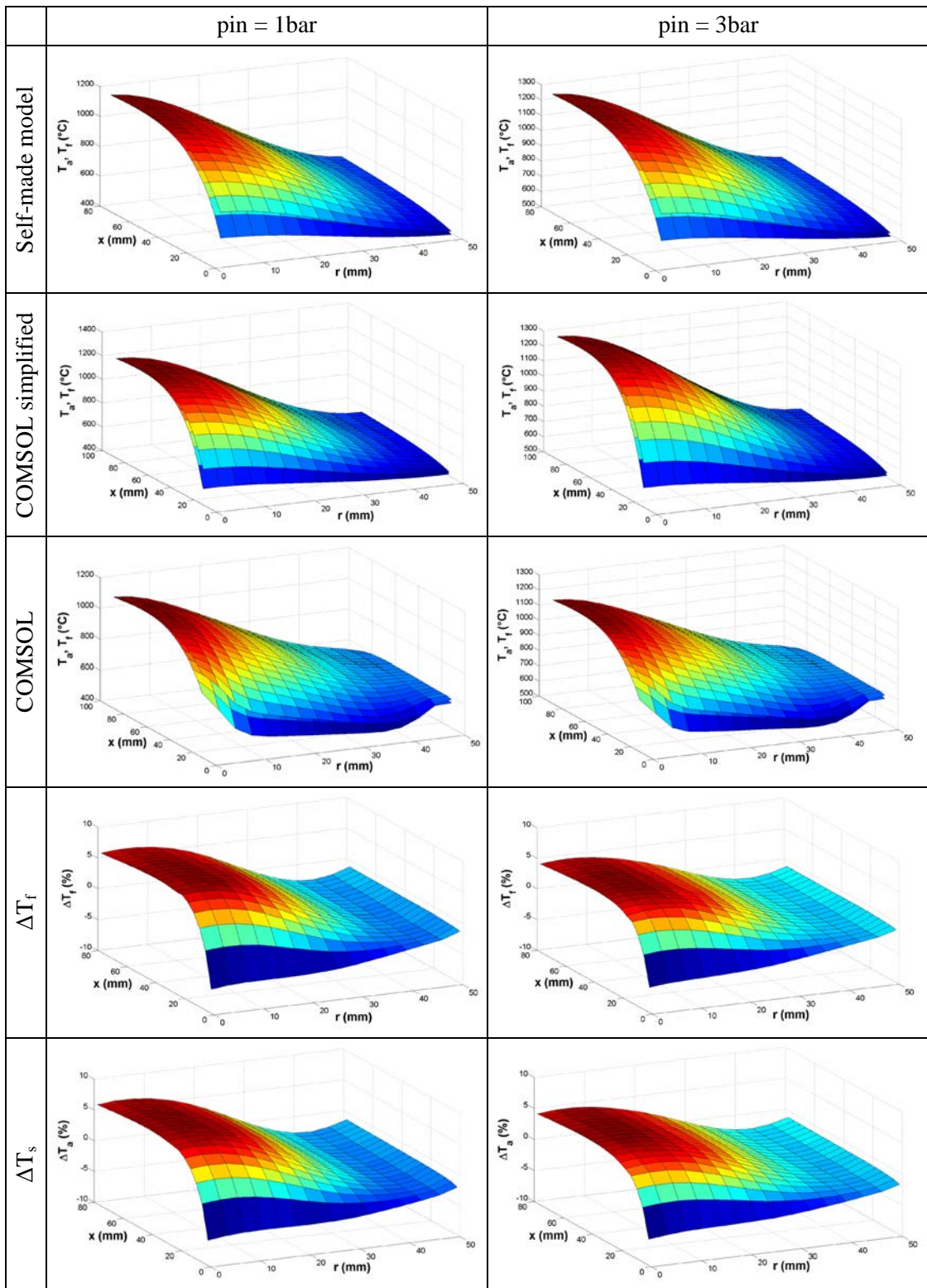


Figure 4.14: COMSOL analysis
Simplified (left), full (right)

Figure 4.15 summarizes the results of the self-made numerical model and the two COMSOL models. The first row shows the fluid and solid temperature within the absorber based on the self-made numerical model with a spatial resolution of 15x20 control volumes. The second and third row present the solid and fluid temperature within the absorber of the simplified and full COMSOL model.

In the fourth and fifth row the error in percent between the self-made numerical model and the simplified COMSOL model is presented. The fourth row shows the difference of the fluid temperature within the absorber. The fifth row shows the difference of the solid temperature within the absorber.

For both cases the error is smaller than ± 7.5 percent which is sufficiently small. The reason for the error is the different spatial resolution and the simplified radiation treatment. The self-made numerical model has a spatial resolution of 20x15 control volumes within the absorber that leads to a mesh element size of around 4mm. The model within the commercial software has a much higher resolution with a mesh element size of approximately 0.5mm.



**Figure 4.15: Fluid and absorber solid temperature
pin = 1 bar (left), pin = 3bar (right)**

Comparing the temperature distribution of the simplified and full COMSOL model shows a rather big difference because of the different fluid flow treatment. This outlines the importance of considering the fluid flow in its full complexity in following analyses.

The window temperature is another important result of this analysis. Figure 4.16 shows the radial distribution of the window surface temperature of the self-made numerical model and the two COMSOL models.

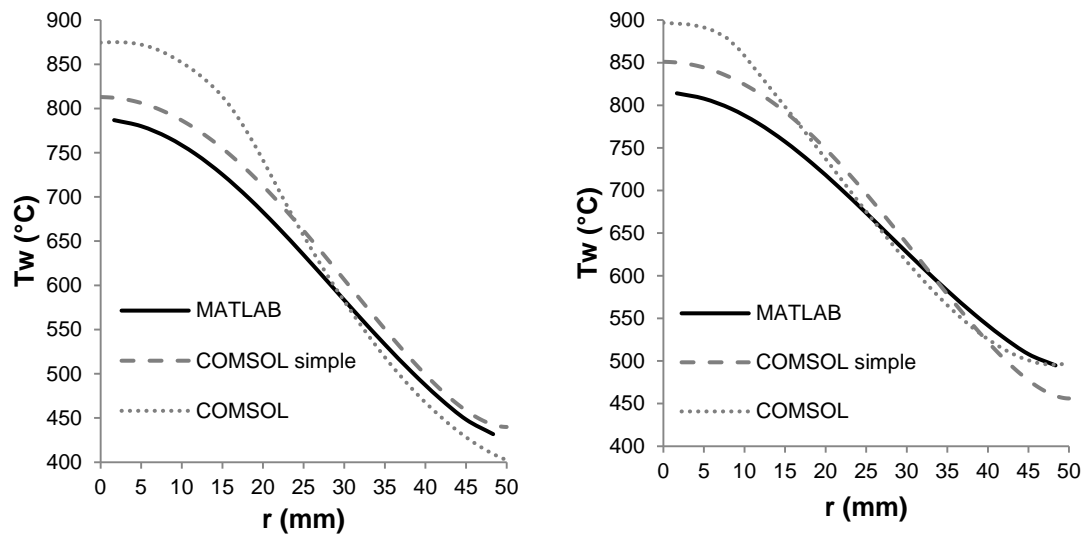


Figure 4.16: Window temperature $p_{in} = 1$ bar (left), $p_{in} = 3$ bar (right)

The agreement of the self-made numerical model and the simplified COMSOL model is relatively good. The difference is most likely due to the different treatment of the radiation heat exchange between the absorber and the window surface. Moreover, it can be seen that the more complex model that considers the non-uniformity of the fluid flow differs significantly leading to window temperatures of almost 900°C.

Table 4.6: Key results

Config.	Result	Model			
		Theoretically	MATLAB	COMSOL simplified	COMSOL
$p_{in} = 1$ bar	$T_{f,out}$ (°C)	734.25	728.12	725.21	726.21
	$T_{w,max}$ (°C)	-	786.86	826.05	868.42
	$T_{abs,max}$ (°C)	-	1151.40	1252.37	1143.45
	$\Delta p = \frac{p_{in} - p_{out}}{p_{in}}$ (%)	-	10.60	7.58	11.77
$p_{in} = 3$ bar	$T_{f,out}$ (°C)	828.13	821.23	818.58	819.36
	$T_{w,max}$ (°C)	-	814.09	851.01	896.8
	$T_{abs,max}$ (°C)	-	1246.70	1323.46	1196.23
	$\Delta p = \frac{p_{in} - p_{out}}{p_{in}}$ (%)	-	1.27	1.03	1.85

Table 4.6 shows the key results of the different models. The theoretical values are calculated using a simple heat balance accounting only for reflection losses at the window.

For the COMSOL models the temperature and mass flux at the outlet of the receiver are no longer uniform. For the comparison an equivalent temperature \bar{T} has to be calculated. In general it can be expressed implicitly in the following equation.

$$\iint_A \dot{M} \cdot \left(\int_{T_i}^{\bar{T}} c_p(T) \cdot dT \right) \cdot dA = 0 \quad (W) \quad (4.91)$$

Here, T_i and \dot{M} are the fluid temperature and mass flux at a specific point at the surface respectively, c_p is the specific heat capacity as a function of the temperature, and A the cross sectional area.

With the assumption of constant specific heat capacity the equivalent temperature can be expressed as

$$\bar{T} = \frac{\oint_A T \cdot \dot{M} \cdot dA}{\oint_A \dot{M} \cdot dA} = \frac{\oint_A T \cdot \dot{M} \cdot dA}{\dot{m}} \quad (K) \quad (4.92)$$

which is call mass averaging.

Table 4.7 summarizes the deviations of the key results of the two COMSOL models from the self-made model.

Table 4.7: Deviation from self-made numerical model

	$p_{in} = 1\text{bar}$		$p_{in} = 3\text{bar}$	
	COMSOL simplified	COMSOL	COMSOL simplified	COMSOL
$\Delta T_{f,out} = \frac{T_{f,out}}{T_{f,ref}} (\%)$	-0.29	-0.19	-0.24	-0.17
$\Delta T_{f,abs} = \text{extremum} \left(\frac{T_f(r,z) - T_{f,ref}(r,z)}{T_{f,ref}(r,z)} \right) (\%)$	7.14	21.39	-5.90	14.64
$\Delta T_{f,abs} = \text{extremum} \left(\frac{T_f(r,z) - T_{f,ref}(r,z)}{T_{f,ref}(r,z)} \right) (\%)$	7.04	15.58	-5.86	13.82
$\Delta T_{w,max} = \frac{T_{w,max} - T_{w,ref}}{T_{w,ref}} (\%)$	3.70	7.70	3.40	7.61
$\Delta p = \frac{\Delta p - \Delta p_{ref}}{\Delta p_{ref}} (\%)$	-28.49	10.04	-18.90	45.67

As mentioned before the simplified COMSOL model is used to verify the temperatures of the self-made numerical model whereas the full COMSOL model is used to verify the pressure drop. The comparison between the self-made model and the full COMSOL model is important as well as it provides information of the overall quality of the self-made model.

The difference of the receiver fluid outlet temperature is negligible. As far as the fluid and solid temperature within the absorber are concerned the maximal difference between the self-made numerical model and the simplified COMSOL model is smaller than 7.5 percent which is sufficiently small. Compared to the full COMSOL model that considers the non-uniform fluid flow the maximal difference is smaller than 25 percent which is relatively good as well.

For both SPU configurations and both COMSOL models the difference of the maximum window temperature is smaller than 8 percent. The difference to the simplified COMSOL model is even below 4 percent.

The maximal pressure drop difference depends heavily on the SPU configuration. For the atmospheric configuration the maximal deviation between the self-made model and the full

COMSOL model is about 10 percent. For the pressurized configuration the maximal difference is in the range of 50 percent. Considering the simplicity of the pressure drop model deviations of 10 and 50 percent respectively are still acceptable. However, the most important fact is that the model gives consistent results within each configuration.

4.1.4 Optimization

In this section the numerical model is used to identify the optimal receiver design that will be the basis for further analyses. Since more than one objective and multiple parameters are expected a multi objective, multi parameter optimization is present. To solve this problem a Multi Objective Optimizer (MOO) developed in the Industrial Energy Systems Laboratory at École Polytechnique Fédérale de Lausanne is used [94]. This optimizer is based on an advanced evolutionist algorithm and implemented in MATLAB.

4.1.4.a Objectives and parameters

The literature review showed that for closed volumetric receivers the window temperatures is important. Therefore, the window temperature is chosen as one objective for the optimization that needs to be minimized.

Since the receiver is working within a Brayton cycle the pressure drop in the whole receiver is crucial as well. The pressure drop is therefore chosen as the second objective for the optimization that needs to be minimized as well.

The first parameter considered for optimization is the cavity height H which is the distance between the absorbers surface and the window. A decrease of this distance increases the convective heat transfer between the window and the fluid leading to a smaller window temperature. However, at the same time this decrease increases the pressure drop.

The next set of parameters is linked to the absorber. Fendt et al. [81] present optical, thermodynamic, and resulting material requirements for absorber materials shown in Table 4.8.

Table 4.8: Optical, thermodynamic, and resulting material requirements of absorber materials [81]

Optical/thermodynamic requirements	Material requirements
High absorption	Dark Color
Optical extinction	High porosity
Heat transfer surface	High cell density
High flux	Temperature resistance
Radial heat transport	Thermal conductivity
High permeability	3D structure

For a fixed material the main parameters influencing these requirements are the cell diameter Φ and the porosity ϵ_p presented in section 3. The influence of these two parameters on the objectives is not trivial. Especially, with the additional condition that at least 99 percent of the impinging radiation needs to be absorber within the absorber. This is necessary because radiation passing the absorber will be absorbed by other parts of the receiver that are not design for that purpose leading to possible overheating and failure of the system.

The minimal needed absorber length can be expressed by

$$L = -\frac{\ln(1 - \alpha)}{K} \quad (\text{m}) \quad (4.93)$$

where α is the required absorption and K the extinction coefficient of the absorber. An increase of the porosity should lead to an axially more evenly distributed heat source and thus lower peak temperatures. At the same time the increase of porosity increases the needed length of the absorber what in turn increases the pressure drop. For the variation of the cell diameter no easy prediction can be made.

Table 4.9 summarizes the chosen objectives, parameters and their range for the optimization process.

Table 4.9: Objectives and parameters for optimization

Objectives	Goal	Parameters	Range
Absorber front surface temperature T_{surf}	Minimum	Cell diameter Φ	0.5 – 4mm
Pressure loss across the absorber Δp	Minimum	Porosity ε_p	50 – 95%
		Cavity height H	0.5 – 20 mm

The range of the cell diameter and the porosity was chosen because it corresponds to the most commonly used foams investigated in literature (i.a. [63]). Furthermore, porosities above 95 percent do not seem feasible from a manufacturing point of view.

4.1.4.b Optimization results

For a spatial resolution of 3x3 control volumes Figure 4.17 shows the results of the optimization for both SPU configurations.

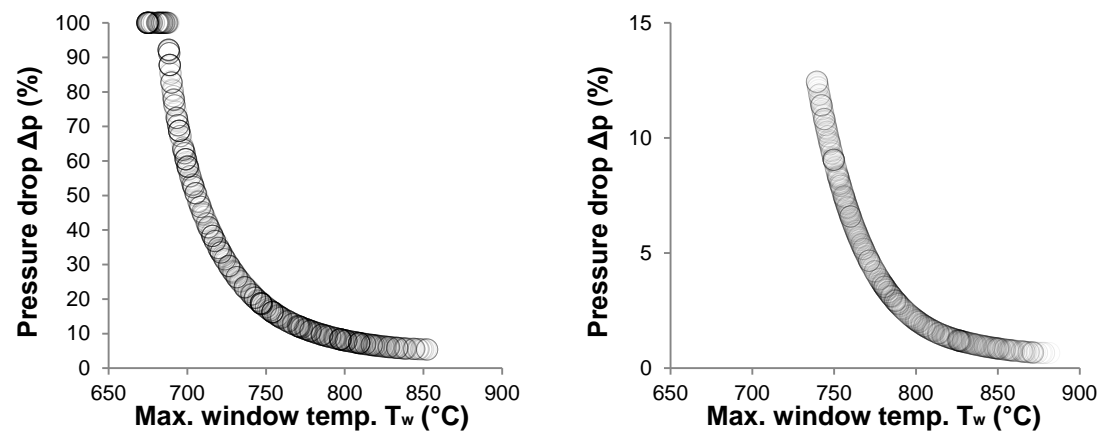


Figure 4.17: Receiver optimization objectives
pin = 1 bar (left), pin = 3bar (right)

The circles represent Pareto-optimal solutions i.e. within the given range of parameters no better solution for one objective can be found without impairing the other objective.

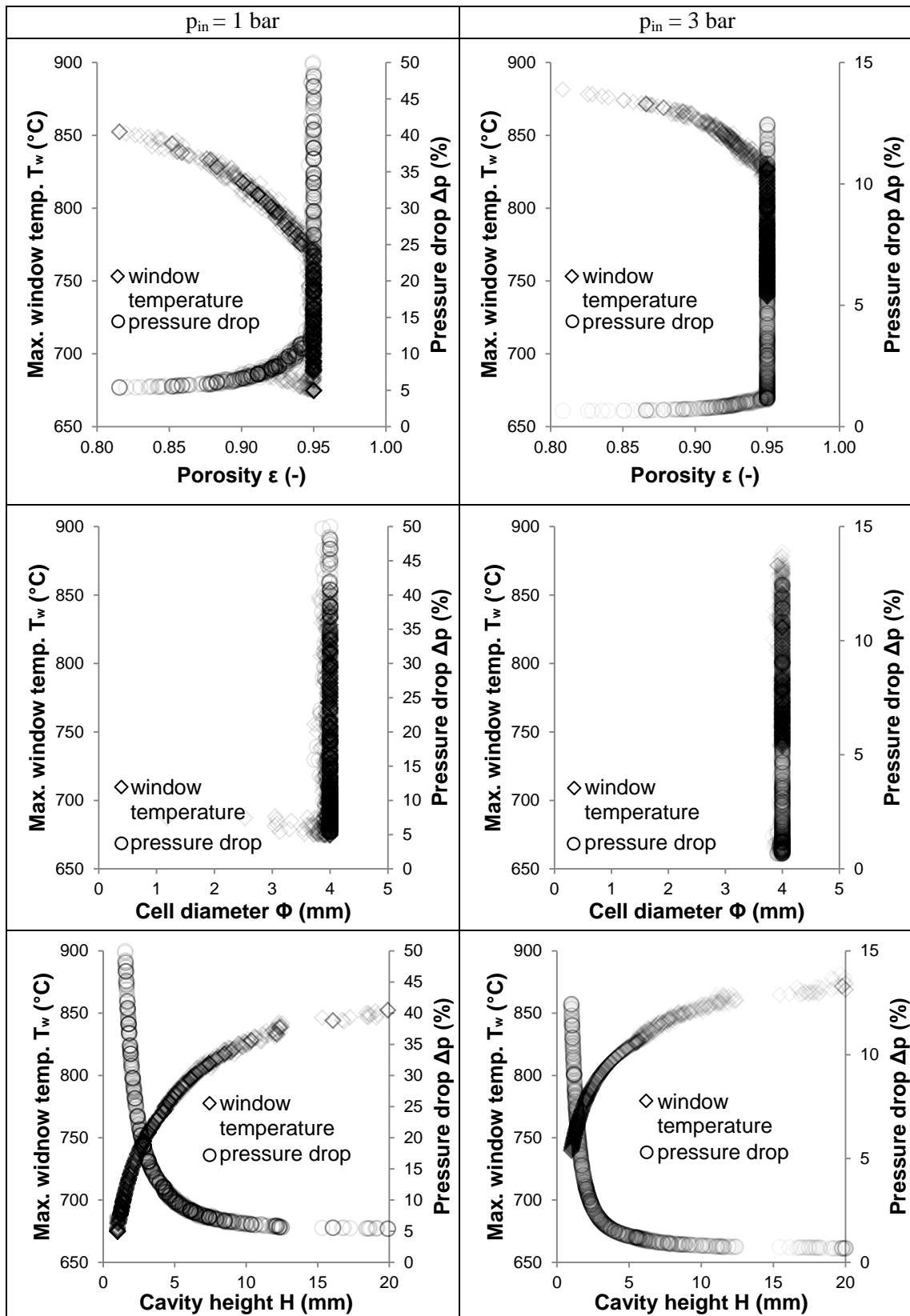


Figure 4.18: Receiver optimization parameters
 $p_{in} = 1 \text{ bar}$ (left), $p_{in} = 3 \text{ bar}$ (right)

Figure 4.18 shows the influence of the chosen parameters on the objectives. In the top row the objectives window temperature and pressure drop are presented as a function of the absorber porosity ϵ . For both configurations it can be seen that the porosity has a distinct influence on both objectives. The vertical lines of both objectives in these diagrams indicate that for better solutions porosities higher than 95 percent would be needed. However, the physical limit prevents the solver from going to higher porosities. The only way to find other Pareto-optimal solutions for the maximum porosity 95 percent is to vary the other two parameters.

The second row of Figure 4.18 shows the objectives as a function of the cell diameter. It can be seen that for the given range of cell diameters almost no optimal solution can be found with a cell diameter smaller than 4mm.

And finally, in the third row the influence of the cavity height, which is the distance between the absorber front surface and the inner surface of the window, on the window temperature is presented. For both configurations it can be seen that a decrease of the cavity height leads to a lower window temperature and a higher pressure drop as discussed before.

4.1.4.c Pareto-optimal design

Based on the results from the optimization a Pareto-optimal design can be chosen for both SPU configurations.

For the atmospheric configuration a compromise between the window temperature and the pressure drop has to be made. The maximal acceptable pressure drop has already been discussed in the preliminary study. It was found that a pressure drop of no more than 10 percent within the receiver is tolerable. A Pareto-optimal solution with a pressure drop of 10 corresponds to a window temperature of about 775 °C. The parameters for this solution are a porosity of 95 percent, a cell diameter of 4mm and a cavity height H of 5mm.

For the pressurized configuration the same decision has to be made. The main difference to the atmospheric configuration is that the pressure drop is generally smaller. This is due the fact that the fluid is pressurized and thus the flow velocities are smaller. Smaller flow velocities are favorable both for the free flow and the flow within the absorber. Because of simplicity the same specifications as for the atmospheric configuration are chosen. A porosity of 95 percent, a cell diameter of 4mm and a cavity height of 5mm lead to a pressure drop of about 2 percent and a maximal window temperature of 820°C.

4.1.5 **Situation analysis results**

This section presents the results of this situation analysis. The results were obtained by evaluating the previously chosen Pareto-optimal designs in the full COMSOL model. A detailed description of the model is given in the main study in section 4.4.1

4.1.5.a Heat transfer and pressure drop

The results of the heat transfer analysis as well as the pressure drop are outlined in Table 4.10 for both SPU configurations. As the designs used in the verification process are based on the optimization results Table 4.10 shows selected results from Table 4.6.

Table 4.10: Situation analysis results

	p_{in} = 1bar	p_{in} = 3bar
T _{f,out} (°C)	726.21	819.36
T _{w,max} (°C)	868.42	896.8
T _{abs,max} (°C)	1143.45	1196.23
$\Delta p = \frac{p_{in}-p_{out}}{p_{in}}$ (%)	11.77	1.85

4.1.5.b Stresses

The stresses within the absorber and the window are highly dependent on the connection to their neighboring parts. This is important because metallic component have a different coefficient of thermal expansion. With the assumption that the absorber is mechanically fully decoupled from its neighboring components the thermal stresses, permissible stresses and material utilization are shown for both configurations and both materials (ceramic and metal) in Table 4.11. The permissible stresses for the ceramic and the metal are calculated according to equation 4.37 and 4.35 respectively using material properties from Table 4.4.

Table 4.11: Absorber material stresses and material utilization

	Configuration			
	p_{in}=1bar		p_{in}=3bar	
	Ceramic	Metal	Ceramic	Metal
Comparison stress				
Max. principal stress $\sigma_{c,p}$ (MPa)	1.994		1.827	
Von Mises stress $\sigma_{c,v}$ (MPa)		2.581		2.388
Permissible stress σ_{per} (MPa)	1.386	0.275	1.386	0.275
Material utilization u (-)	1.439	9.385	1.318	8.684

The material utilization is defined as the fraction of the maximal stress and the permissible stress.

$$u = \frac{\sigma_{max}}{\sigma_{per}} \quad (-) \quad (4.94)$$

The inverse of the material utilization is factor of safety FoS or also called safety factor SF. Another way to relate the maximal stresses to the permissible stresses is the margin of safety MoS defined by the following equation.

$$MoS = \frac{\sigma_{per}}{\sigma_{max}} - 1 \quad (-) \quad (4.95)$$

As described in the physical modeling metallic and ceramic absorber require the calculation of different comparison stressed. For the ceramic absorber the maximal principal stress $\sigma_{c,p}$ is used whereas for the metallic absorber the comparison stress according to von Mises $\sigma_{c,v}$ is used.

Comparing the material utilizations of the two materials shows a clear trend. At elevated temperatures the metallic absorber is no longer able to withstand the internal thermal stresses

because its tensile strength decreases quite rapidly with increased temperatures. For the ceramic absorber the permissible stress is at least in the same order of magnitude.

Stresses within the window are presented in Figure 4.19. As glass is a brittle material the comparison stress according to Rankine (equation 4.40) needs to be used. Therefore, the stresses shown in Figure 4.19 are the maximum principal stresses.

The first row shows the stresses only due to pressure differences between the inside and outside of the window and the non-uniform spatial temperature distribution. This means the glass window is considered to be mechanically fully decoupled from its neighboring components. In the second row the stresses within the window are shown for the assumption that the window and the metallic tube on its left are fully coupled.

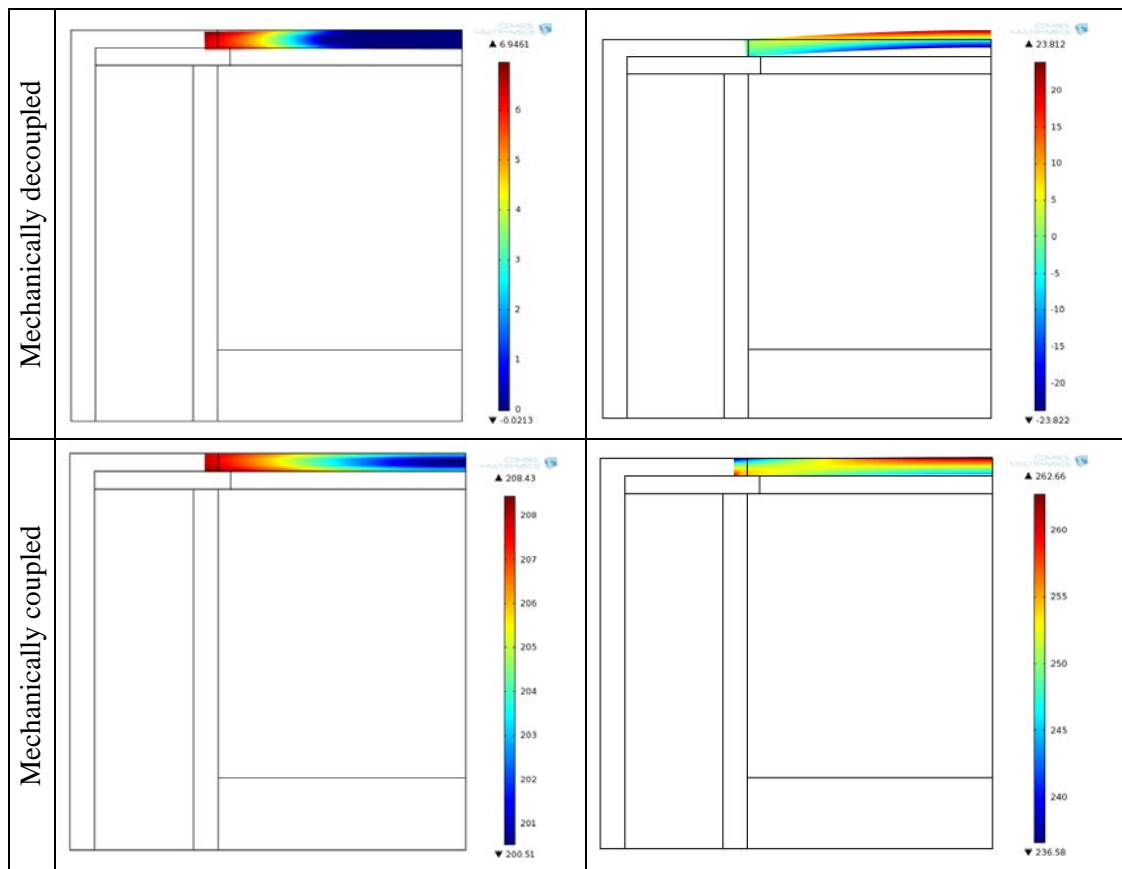


Figure 4.19: Stresses within the window
 $p_{in} = 1 \text{ bar}$ (left), $p_{in} = 3 \text{ bar}$ (right)

It can clearly be seen that the thermal stresses due to the non-uniform temperature distribution are not significant considering a rupture strength of 67 MPa as shown in Table 4.5. However, the stresses are significantly higher than the permissible stress if the window and the tube are coupled. That indicates the importance that the window and the neighboring parts are as much mechanically decoupled as possible.

4.2 Re-design objectives

The results of the situation analysis show that the maximum window temperature is in excess of the recommended 800°C even though the temperature was considered axially constant. In a more realistic analysis that also accounts for axial temperature variations window the maximal temperature will be even higher. Moreover, significant temperature differences within absorber were found leading to high thermal stresses.

The first objective of this main study is therefore finding ways to decrease the maximal window temperature as well as reducing temperature differences in the absorber in order to decrease thermal stresses. In other words improving and insuring the mechanical integrity of the receiver. Since the material utilization of metallic absorbers was almost 10 times worse than the material utilization of the ceramic absorber in this main study only ceramic absorbers are analyzed.

Furthermore, the thermal performance is of importance as well. That means the thermal efficiency of the receiver should not be decreased too much by trying to improve the mechanical integrity. Since the pressure drop is important for the whole system the designs should not increase the pressure drop to unacceptable limits.

And finally, the designs must be manufacturable at reasonable costs.

4.3 Synthesis of solutions

The approach to this synthesis of solutions is to find ways to alter the current design's parameter to meet the objectives. Figure 4.20 shows a variety of possible modifications for every receiver component.

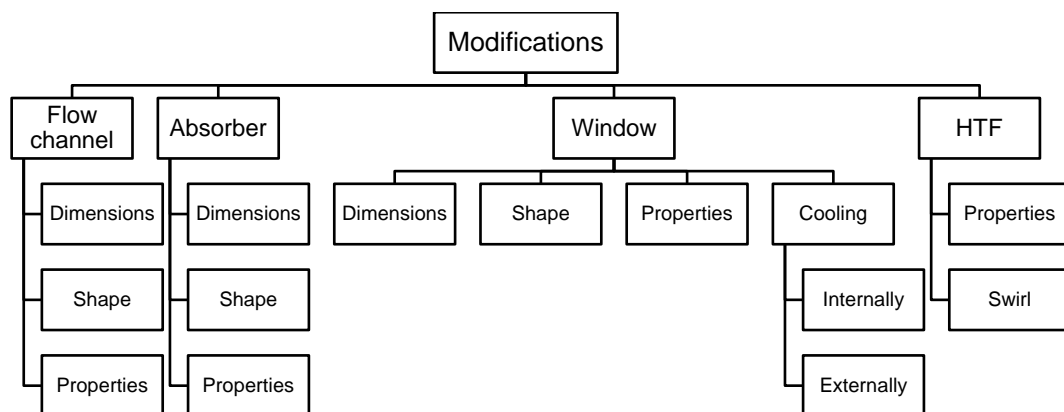


Figure 4.20: Receiver modifications

Basically, for almost every component of the receiver the dimensions, the shape and properties can be varied. Additionally, cooling can be introduced to in order to decrease the window temperature.

4.3.1 Flow channel

Concerning the flow channel all three modifications are viable. But since the dimensions and the shape of the flow channel are highly interconnected these modifications are analyzed in a single study.

The optimization in the situation analysis has already shown the distance H between the absorber and window surface has a significant impact. Therefore, the distance H , also called cavity height, is the dimension of interest to be analyzed in this main study.

When it comes to shape not all possible modifications can be analyzed because of limited time of this thesis. Therefore, three different designs are chosen and analyzed. The difference between the designs is the extent of how much the flow path is smoothed. The designs are shown in Figure 4.21 and range from an unmodified sharp-edged flow channel A0, a chamfered flow channel A1 to a very smooth flow channel A2.

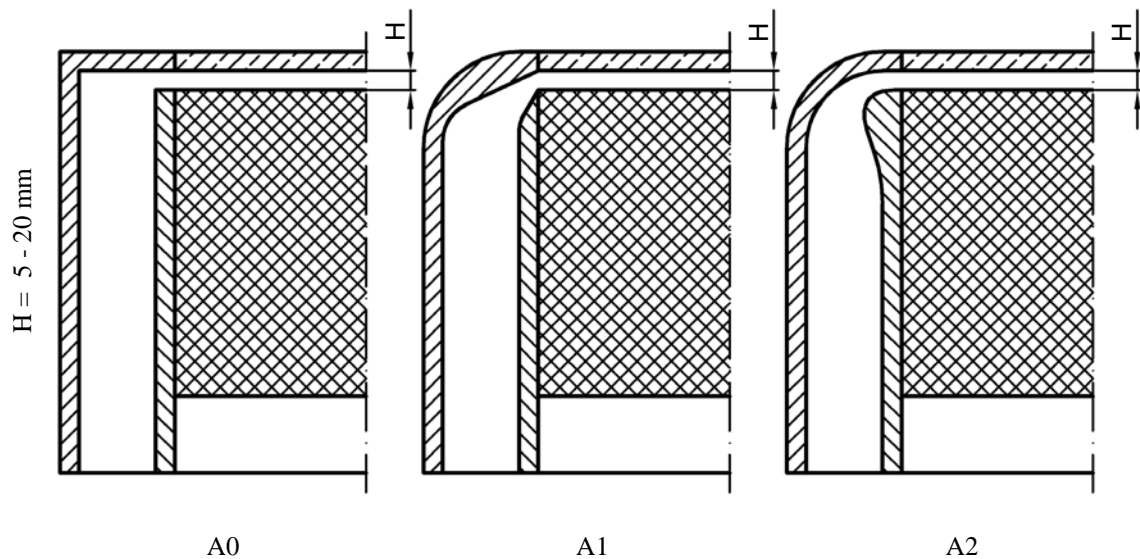


Figure 4.21: Flow channel modifications

Based on the optimization the cavity height H between the absorber and window surface will be varied from 5 mm to 20 mm. The analysis is conducted with an absorber that has a cell diameter of 4mm and a porosity of 95 percent as the situation analysis suggests.

The properties of the materials creating the flow channel have great influence on the manufacturability and subsequently the costs. Since the flow channel designs do not differ that much from a manufacturing point of view no detailed comparison of different materials will be done. The choice of an appropriate material will be discussed later in the detailed study.

4.3.2 Absorber

The part which allows the most modifications is the absorber. A variety of dimensions, shapes and properties can be tested.

The situation analysis already showed that there are significant temperature differences between the center and outer parts of the absorber creating significant thermal stresses. In order to reduce these temperature differences and hence the thermal stresses more power has to be removed from the center of the absorber. This can be done by increasing the flow velocity in the center compared to the outer regions by changing the shape and/or the properties of the absorber. These changes influence the flow resistance and consequently the flow velocity.

An increased flow velocity in the center of the absorber increases the convective heat transfer that is defined by the following equation in two ways.

$$\dot{Q}_{conv} = \dot{m} \cdot h_v \cdot (T_s - T_f) \quad (W) \quad (4.96)$$

First, an increased flow velocity means in turn increased mass flow \dot{m} . Second, the heat transfer coefficient h_v increases as well because it is dependent on the Reynolds number and thus the flow velocity as previously shown in Table 3.9. Moreover, a decrease of the absorber temperature at the surface also decreases the radiation losses.

4.3.2.a Absorber dimensions

Per se, the dimensions of the absorber cannot be altered randomly without compromising the functionality. First the absorber has to have a certain length in order to ensure that all impinging radiation is absorbed by the absorber itself and not by other parts. Second, the diameter of the absorber is defined by the focal spot determined by the SPU. That means, the absorber dimensions can only be changed by changing its properties.

4.3.2.b Absorber shape

The first study conducted focuses on changing the shape of the absorber rather than the properties. The basic idea is to change the shape in a way that the radial flow velocity distribution has the same shape as the impinging radiation. That means that as much power is removed from the absorber by convection as is transferred to it by absorbing radiation. Figure 4.22 shows a variety of ways to change the shape of the absorber.

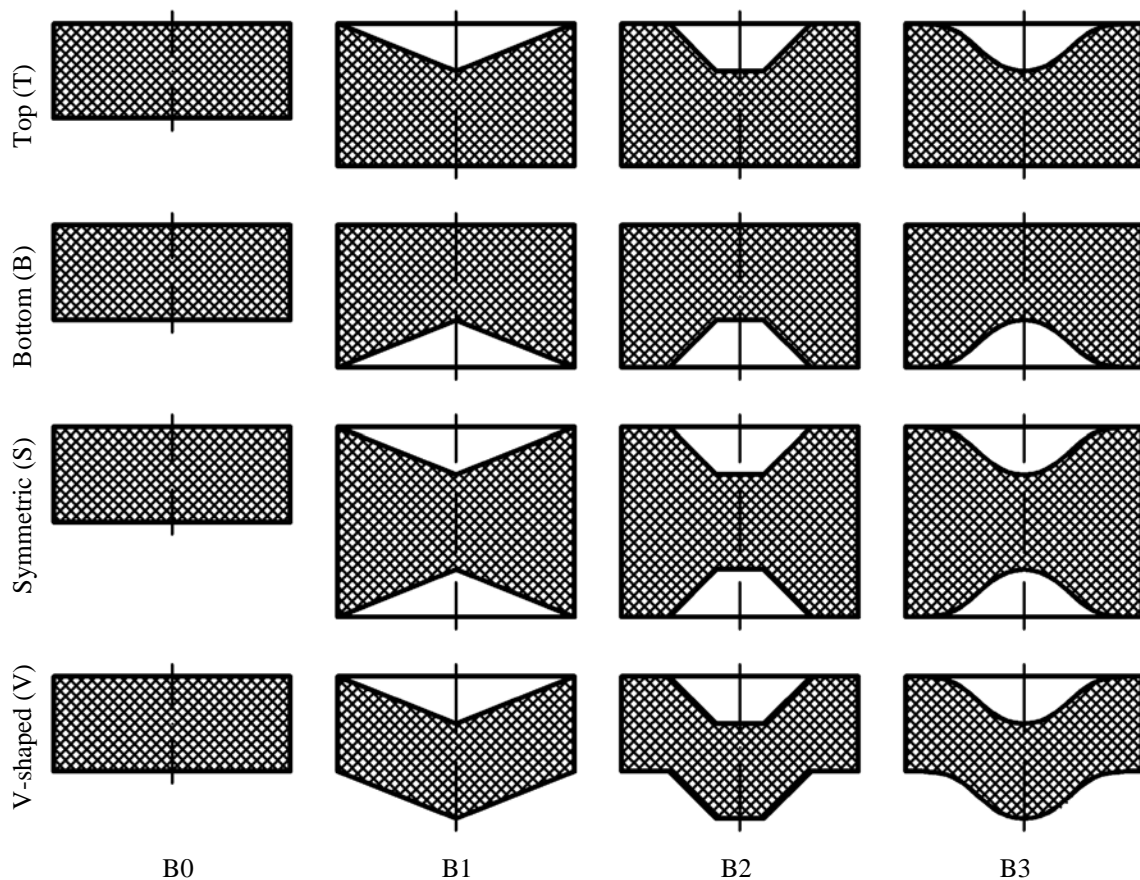


Figure 4.22: Absorber shape modifications

Design B3 is the attempt to shape the absorber surface in the same way as the impinging radiation distribution in order to achieve the above mentioned goal. The designs B2 and B1 are simplified versions of the design B3.

The surface of design B3 is defined as

$$z(r) = z_0 + \left(\Delta z^2 - \Delta z^{1 + \left(\frac{r}{R}\right)^2} \right) \quad (\text{m}) \quad (4.97)$$

where $z(r)$ is the surface as a function of the radius r , z_0 is the initial surface, Δz the depth of the cavity, r the radial index variable, and R the outer radius of the absorber. This function has the same form as the impinging radiation described previously in equation 3.3.

Additionally, to the shape of the surface is the placement of it is important as well. As shown in Figure 4.22 four different placements with different advantages and disadvantages are tested.

4.3.2.c Absorber properties

As described in the optimization the absorber properties have a quite big influence on the temperatures in both the absorber and window. Since the results of the situation analysis are based on a simplified model the influence of the absorber properties is analyzed again. Table 4.12 shows a discrete number of absorber properties chosen for the analysis which are based on previous results. The minimal absorber length is calculated according to equation 4.93 with the condition that 99 percent of the impinging radiation needs to be absorber. The results are rounded to the next whole number.

Table 4.12: Absorber properties modifications 1

#	Properties	C1	C2	C3
1	Cell diameter Φ (mm)	2	2	2
2		3	3	3
3		4	4	4
1,2,3	Porosity ε (-)	0.85	0.90	0.95
1	Minimal absorber length L (mm)	13	20	39
2		20	29	58
3		26	39	77

Furthermore to changing the properties of the whole absorber its properties can be changed locally. Figure 4.23 shows three different designs that are tested. Design D0 is the unmodified design with a constant porosity. Design D1 is divided into 2 zones with different porosities. Design D2 has a radially continuously changing porosity. In both designs the porosity in the center is higher than the porosity of the outer regions to increase the flow velocity in the center.

The reason why only the porosity is varied is based on the optimization in the situation analysis. A clear trend was visible that the cell diameter should be as big as possible. For the porosity on the other hand no clear trend was visible concerning both the temperatures and pressure drop.

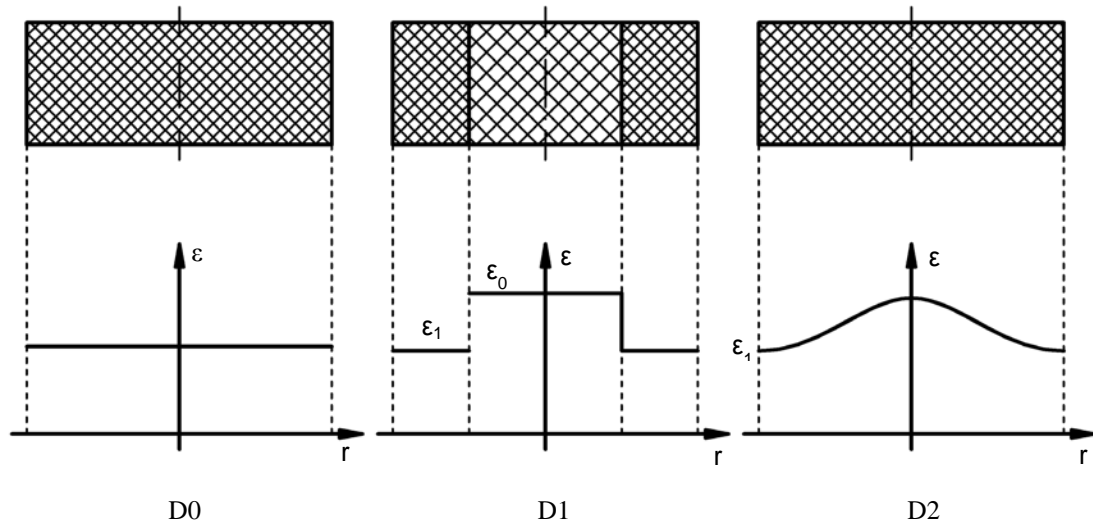


Figure 4.23: Absorber properties modifications 2

The porosity in design D2 changes radially in the same way as the impinging radiation. The local porosity $\varepsilon(r)$ can be calculated by

$$\varepsilon(r) = \varepsilon_1 - \left(\Delta\varepsilon^2 - \Delta\varepsilon^{1+\left(\frac{r}{R}\right)^2} \right) \quad (-) \quad (4.98)$$

where ε_0 is the porosity at the outer part of the absorber ($r=R$), $\Delta\varepsilon$ the porosity difference between the center ($r=0$) and the outer part ($r=R$), r the radial index variable, and R the outer radius of the absorber.

Table 4.13 shows the chosen absorber properties for this analysis. The minimal absorber length is rounded to the nearest tenth.

Table 4.13: Absorber properties modifications 2

#	Properties	D0	D1	D2
1,2,3	Cell diameter Φ (mm)	4	4	4
1	Porosity $\varepsilon_1 / \varepsilon_0$ (-)	0.85	0.85 / 0.90	0.85 / 0.90
2		0.90	0.85 / 0.95	0.85 / 0.95
3		0.95	0.90 / 0.95	0.90 / 0.95
1	Minimal absorber length L (mm)	30	40	40
2		40	80	80
3		80	80	80

4.3.3 Window

Additional to changing the dimensions, properties and shape the window can be cooled internally or externally to reduce the window temperatures.

4.3.3.a Window dimensions

As far as the dimensions are concerned there is little possibility of changes since the receiver needs to be designed to work in the SPU. That means that the minimal diameter of the window is determined by the focal spot of the system. Furthermore, the minimal thickness is limited due to the fact that the receiver is pressurized as well by the manufacturer (see Schott [95]). An increase in thickness on the other hand has no distinct advantage.

4.3.3.b Window properties

Changing the properties of the window would mean to change the material. Unfortunately, the two materials suitable for that high temperatures, fused silica and fused quartz, have very similar properties except the maximal working temperature. Thus an analysis of these two different materials does not provide additional information.

4.3.3.c Window shape

The main reason of changing the shape of the window is to transform bending stresses into compressive stresses. Since the pressure difference between the inside of the receiver and the outside is maximal 2 bar the bending stresses are relatively small as shown in Figure 4.19. However, changing the shape of the window might have positive effects on the temperature distribution due to increased convective cooling. Figure 4.24 shows different window and absorber shape combinations.

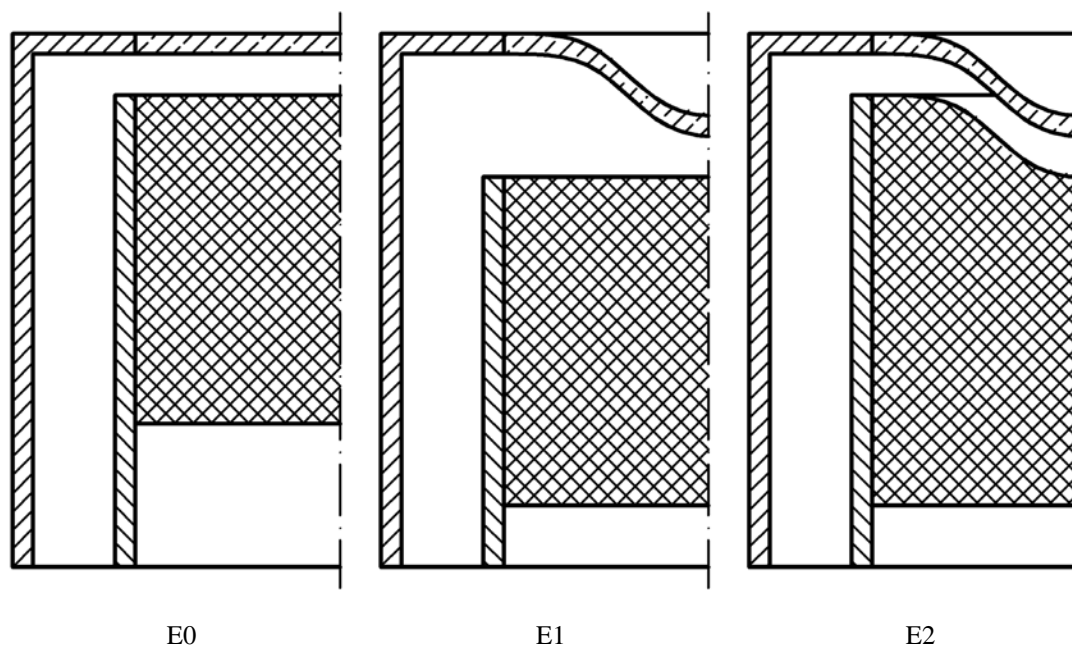


Figure 4.24: Window shape

The analysis is conducted with an absorber that has a cell diameter of 4mm and a porosity of 95 percent as the situation analysis suggests.

4.3.3.d Window cooling

If the window temperature exceeds the permissible temperature cooling is a possible way to decrease it to acceptable levels. Basically, the window can be cooled internally or externally with ambient air or air extracted the stream before entering the receiver.

Figure 4.25 shows the basic concept of window cooling both internally and externally. In reality most likely the cooling will be done by of nozzles around the perimeter. For this analysis the concept is simplified to a uniform flow around the perimeter.

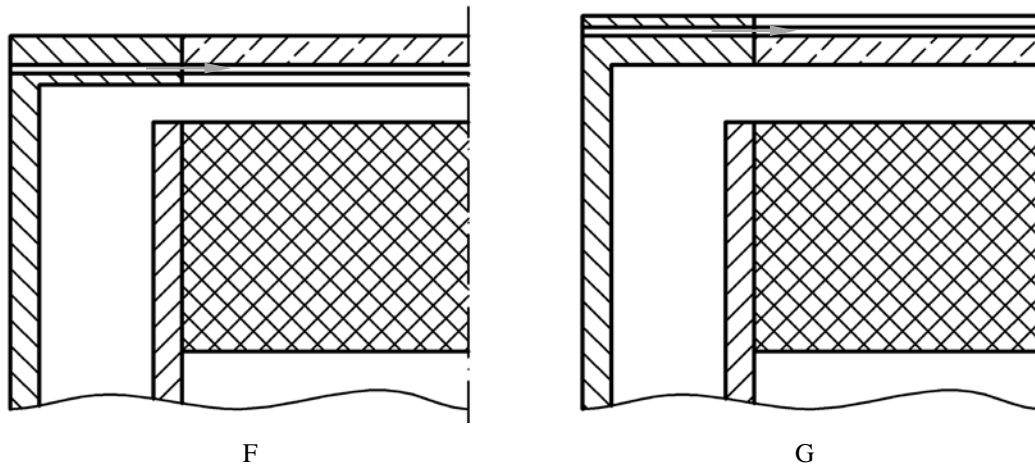


Figure 4.25: Window cooling

Table 4.14 shows the cooling mass flow and temperature that are used for the analysis for both SPU configurations. The designs F0 and G0 are used for comparison.

Table 4.14: Window cooling

Properties	F0 / G0	F1 / G1	F2 / G2
Porosity ε (-)	0.95	0.95	0.95
Cell diameter Φ (mm)	4	4	4
Cooling mass flow \dot{m}_c (g/s)	natural convection	5 10 15 20	5 10 15 20
Cooling air inlet temperature T_c ($^{\circ}\text{C}$)	$T_{\text{amb}} = 20^{\circ}\text{C}$	$T_{\text{amb}} = 20^{\circ}\text{C}$	$T_{\text{in}} = 400^{\circ}\text{C}$ (for $p_{\text{in}}=1\text{bar}$) $T_{\text{in}} = 500^{\circ}\text{C}$ (for $p_{\text{in}}=3\text{bar}$)

As Table 4.14 shows the analysis is conducted with an absorber having the highest cell diameter and porosity possible as the situation analysis suggests.

4.3.4 Heat transfer fluid

As far as the heat transfer fluid is concerned it is not possible to change neither its dimensions nor shape. The properties on the other hand can theoretically be changed by changing the HTF and/or adding additives in order to improve the convective heat transfer. Nevertheless, as the receiver is supposed to work in the SPU it is not possible to change the properties of the HTF either.

Another way of improving the heat transfer from the absorber to the HTF is by increasing the flow velocity. This could be done by placing inlet guide vanes in the inflow of the receiver creating angular momentum.

4.4 Analysis of solutions

In this section a variety of receiver solutions are analyzed. The results are the basis for the following evaluation and decision process.

4.4.1 Modeling

The analysis is conducted using the Multiphysics Modeling and Simulation Software COMSOL and a two dimensional rotation symmetric model. For the sake of simplicity a couple of assumptions and simplifications are made. The most important one is that the radiation absorber by the receiver is considered as a volumetric heat source. Similar to the self-made numerical model the absorber is treated as a continuum as described previously in section 4.1.1. Moreover, all analyses are conducted stationary. Furthermore, radiative heat exchange is only considered between the absorber and window surface. The fluid itself is considered as a radiative non-participating medium which is legitimate for air according to Incropera et al. [35]. As in the situation analysis, only heat losses from the window to the ambient are considered. That means that the outer tube is again considered to be perfectly insulated.

The analysis requires the use of the different physics models within COMSOL especially to be able to calculate both the solid and fluid temperatures inside the absorber. The fluid flow in the receiver including the absorber is model with the physic model “Free and Porous media flow”. To consider the heat transfer in the fluids and solids the models “Heat Transfer in Fluids” and “Heat Transfer in Solids” are used. Since thermal radiation is important especially between the absorber surface and window the model “Surface to Surface Radiation” is used. And finally, for the structural mechanics analysis the model “Solid Mechanics” is used.

4.4.1.a Heat transfer modeling

The fluid flow model is based on the standard Navier-Stokes equation for compressible Newtonian fluids. For the free flow i.e. outside of the absorber the momentum equation is defined as

$$\begin{aligned} \frac{\partial}{\partial t}(\rho \vec{u}) + \vec{\nabla} \cdot (\rho \vec{u} \vec{u}) \\ = \vec{\nabla} \cdot \left[-p \underline{I} + \mu (\vec{\nabla} \vec{u} + \vec{\nabla} \vec{u}^T) - \frac{2}{3} \mu \vec{\nabla} \cdot \vec{u} \underline{I} \right] + \rho \vec{g} + \vec{F} \end{aligned} \quad \left(\frac{N}{m^3} \right) \quad (4.99)$$

where t is the time, ρ the fluid density, \vec{u} the fluid velocity, p the static pressure, μ the dynamic viscosity, \vec{g} and \vec{F} gravitational body forces and external body forces respectively, and \underline{I} the identity matrix

For the fluid flow within the porous medium a source term is added to the momentum equation. For compressible Newtonian fluids the momentum equations can be expressed as

$$\begin{aligned} \frac{\partial}{\partial t}(\rho \vec{u}) + \vec{\nabla} \cdot (\rho \vec{u} \vec{u}) \\ = \vec{\nabla} \cdot \left[-p \underline{I} + \mu (\vec{\nabla} \vec{u} + \vec{\nabla} \vec{u}^T) - \frac{2}{3} \mu \vec{\nabla} \cdot \vec{u} \underline{I} \right] + \rho \vec{g} \\ - \left(\frac{\mu}{K} + \frac{\rho_f \cdot C_f}{\sqrt{K}} |\vec{u}| \right) \vec{u} + \vec{F} \end{aligned} \quad \left(\frac{N}{m^3} \right) \quad (4.100)$$

where K is the specific permeability and C_f the inertia coefficient that have been defined in equation 3.47 and equation 3.48 respectively.

The mass continuity equation is the same for both the free and porous media flow and defined as

$$\frac{\partial \rho}{\partial t} + \vec{\nabla} \cdot (\rho \vec{u}) \quad \left(\frac{kg}{m^3s} \right) \quad (4.101)$$

The heat transfer in the fluid is based on the following energy equation

$$\rho c_p \frac{\partial T}{\partial t} + \rho c_p \vec{u} \cdot \vec{\nabla} T = \vec{\nabla} \cdot (k_{fe} \cdot \vec{\nabla} T) + \dot{q}_f \quad \left(\frac{W}{m^3} \right) \quad (4.102)$$

where c_p is the specific heat capacity of the fluid at constant pressure, T the fluid temperature, \vec{u} the fluid velocity, k_{fe} the thermal conductivity according to equation 3.24, and \dot{q}_f the volumetric heat source. It is defined as

$$\dot{q}_f = h_v \cdot (T_2 - T) \quad \left(\frac{W}{m^3} \right) \quad (4.103)$$

where h_v is the volumetric heat transfer coefficient and T_2 the absorber temperature. The volumetric heat transfer coefficient is calculated according to equation 3.31 and 3.33. This heat source enables the coupling of the two heat transfer models of the fluid and solid inside the absorber.

The heat transfer in the absorber is based on the following equation

$$\rho c_p \frac{\partial T}{\partial t} = \vec{\nabla} \cdot (k_{abs} \cdot \vec{\nabla} T) + \dot{q}_{abs} \quad \left(\frac{W}{m^3} \right) \quad (4.104)$$

where c_p is the specific heat capacity of the solid at constant pressure, T the solid temperature, k_{abs} the thermal conductivity of the solid, and \dot{q}_{abs} the volumetric heat source. The heat source is based on equation 4.22 and defined by the following equation.

$$\dot{q}_{abs}(r, z) = \hat{E}_{00} \cdot \tau_w \cdot K \cdot e^{\left(\ln(\delta) \left(\frac{r}{R} \right)^2 - K(z-z_0) \right)} - h_v \cdot (T_2 - T) \quad \left(\frac{W}{m^3} \right) \quad (4.105)$$

The thermal conductivity accounts for both conduction and radiation heat transfer and is defined as

$$k_{abs} = k_{se} + k_r \quad \left(\frac{W}{m \cdot K} \right) \quad (4.106)$$

where k_{se} is the effective thermal conductivity according to equation 3.23 and k_r the radiative conductivity according to equation 4.28.

The heat transfer in the remaining solids is based on the following equation

$$\rho c_p \frac{\partial T}{\partial t} = \vec{\nabla} \cdot (k_s \cdot \vec{\nabla} T) + \dot{q}_s \quad \left(\frac{W}{m^3} \right) \quad (4.107)$$

where c_p is the specific heat capacity at constant pressure, T the solid temperature, k_s the thermal conductivity, and \dot{q}_s the volumetric heat source. The heat source within the window

is considered constant as in the self-made numerical model and according to equation 4.53. In the remaining solids i.e. the flow channel tubes the volumetric heat source is zero.

The surface to surface radiation model only considers radiation between surfaces and does not include absorption in the medium between the surfaces. It is based on the following two equations.

$$-\vec{n} \cdot (-k \cdot \vec{\nabla} T) = \varepsilon(E - \sigma T^4) \quad \left(\frac{W}{m^2}\right) \quad (4.108)$$

$$(1 - \varepsilon) \cdot E = J - \varepsilon \sigma T^4 \quad \left(\frac{W}{m^2}\right) \quad (4.109)$$

Here, the \vec{n} is the surface normal vector, k the thermal conductivity, T the temperature of the solid, ε the emissivity, δ the Stefan–Boltzmann constant, E the irradiation, and J the radiosity. Unfortunately, the model does not allow the simulation of semi-transparent materials. Therefore, the transmitted radiation through the window has to be accounted separately for as in the self-made numerical model. Furthermore, as equation 4.109 shows the reflectivity of the surfaces are calculated using the emissivity. Fortunately, the difference between the reflectivity of the window in the infrared spectrum according to Figure 4.9 ($\rho=12.5\%$) and the calculated one using the emissivity according to Table 4.5 ($\varepsilon=80\%$, $\rho=20\%$) is small enough.

The coupling of the radiation model and the fluid and solid heat transfer model is done by the following equations. The radiation exchange between the absorber and window surface is modeled as a boundary heat source. The boundary heat source at the inside of the window is defined as

$$-\vec{n} \cdot (-k \cdot \vec{\nabla} T) = -J - E \cdot \tau \quad \left(\frac{W}{m^2}\right) \quad (4.110)$$

where τ is the transmissivity of the window. The boundary heat source at the absorber surface can be expressed as

$$-\vec{n} \cdot (-k \cdot \vec{\nabla} T) = -J \quad \left(\frac{W}{m^2}\right) \quad (4.111)$$

At the outside of the window the radiation to the ambient and natural convective cooling are considered according to

$$-\vec{n} \cdot (-k \cdot \vec{\nabla} T) = -h_f \cdot (T - T_{amb}) - \varepsilon \sigma (T^4 - T_{amb}^4) \quad \left(\frac{W}{m^2}\right) \quad (4.112)$$

where T_{amb} is the temperature of the ambient and h_f the convective heat transfer coefficient as a function of the characteristic length L , the pressure p , and the ambient temperature.

Table 4.15 summarized the boundary conditions for the fluid flow and thermal models.

Table 4.15: Boundary conditions

	Fluid flow	Thermal
Inlet	Mass flow $\dot{m} = \dot{m}_{in}$ (4.113)	Entrance temperature $T = T_{in}$ (4.114)
Outlet	Outlet pressure $p = p_{out}$ (4.115)	Convective flow $\vec{n} \cdot (-k \cdot \vec{\nabla}T) = 0$ (4.116)
Other	Wall - no slip condition $u = 0$ (4.117)	Thermal insulation $\vec{n} \cdot (-k \cdot \vec{\nabla}T) = 0$ (4.118)

The boundary condition for the cooling nozzles is the inflow heat flux boundary conditions defined as

$$-\vec{n} \cdot (-k \cdot \vec{\nabla}T) = q_o + \rho(\Delta h_{in} - \Delta h_{\infty}) \vec{u} \cdot \vec{n} \quad \left(\frac{W}{m^2}\right) \quad (4.119)$$

where q_o is the inwards heat flux, ρ the fluid density at the boundary, Δh_{in} and Δh_{∞} the enthalpy at the inlet boundary and the exterior respectively, and \vec{u} the inflow velocity. The enthalpy difference between inlet and exterior is defined by

$$\Delta h_{in} - \Delta h_{\infty} = \int_{T_{\infty}}^{T_{in}} c_p dT + \int_{p_{\infty}}^{p_A} \frac{1}{\rho} \left[1 + \frac{T}{\rho} \left(\frac{\partial \rho}{\partial T} \right) \Big|_p \right] dp \quad \left(\frac{J}{kg}\right) \quad (4.120)$$

where T_{∞} and T_{in} are the fluid temperature at the exterior and the inlet boundary respectively, p_{∞} and p_A the pressure at the exterior and inlet boundary respectively.

4.4.1.b Solid mechanics modeling

The solid mechanics model is based on the Cauchy momentum equation

$$-\vec{\nabla} \cdot \underline{\underline{\sigma}} = \vec{F} \quad \left(\frac{N}{m^3}\right) \quad (4.121)$$

where $\underline{\underline{\sigma}}$ is the Cauchy stress tensor, and \vec{F} are the body forces. The stress and strain tensors are calculated according to equation 4.122 and equation 4.123 respectively.

The stresses within the materials can be calculated by superposing the stresses due to external forces and thermal stresses. According to Kienzler and Schröder [91] the stresses within the solids can be calculated using the Duhamel-Neumann formulation of Hooke's law.

$$\underline{\underline{\sigma}} = \mathbf{E} : (\underline{\underline{\varepsilon}} - \underline{\underline{\alpha}}\theta) \quad (Pa) \quad (4.122)$$

Here $\underline{\underline{\sigma}}$ is the Cauchy stress tensor, $\underline{\underline{\varepsilon}}$ the strain tensor, $\underline{\underline{\alpha}}$ the thermal expansion tensor, \mathbf{E} the fourth order elasticity tensor, and θ the temperature difference $\theta = T - T_{ref}$.

The strain tensor $\underline{\underline{\varepsilon}}$ can be written in terms of the displacement gradient

$$\underline{\underline{\varepsilon}} = \frac{1}{2}(\vec{\nabla}\vec{u} + \vec{\nabla}\vec{u}^T) \quad (-) \quad (4.123)$$

where \vec{u} is the displacement.

For isotropic materials the stresses can be expressed as

$$\sigma_{ij} = \frac{E}{1+\nu} \left(\varepsilon_{ij} + \frac{\nu}{1-2\nu} \varepsilon_{kk} \delta_{ij} \right) - \frac{E}{1-2\nu} \theta \delta_{ij} \quad (Pa) \quad (4.124)$$

where E is Young's modulus, ν is Poisson's ratio, and δ_{ij} Kronecker's delta. Written in full the stresses can be expressed by the following equations.

$$\sigma_{11} = \frac{E}{(1+\nu)(1-2\nu)} [(1-\nu)\varepsilon_{11} + \nu\varepsilon_{22} + \nu\varepsilon_{33}] - \frac{E}{1-2\nu} \alpha\theta \quad (Pa) \quad (4.125)$$

$$\sigma_{22} = \frac{E}{(1+\nu)(1-2\nu)} [\nu\varepsilon_{11} + (1-\nu)\varepsilon_{22} + \nu\varepsilon_{33}] - \frac{E}{1-2\nu} \alpha\theta \quad (Pa) \quad (4.126)$$

$$\sigma_{33} = \frac{E}{(1+\nu)(1-2\nu)} [\nu\varepsilon_{11} + \nu\varepsilon_{22} + (1-\nu)\varepsilon_{33}] - \frac{E}{1-2\nu} \alpha\theta \quad (Pa) \quad (4.127)$$

$$\sigma_{23} = \frac{E}{1+\nu} \varepsilon_{23} \quad (Pa) \quad (4.128)$$

$$\sigma_{31} = \frac{E}{1+\nu} \varepsilon_{31} \quad (Pa) \quad (4.129)$$

$$\sigma_{12} = \frac{E}{1+\nu} \varepsilon_{12} \quad (Pa) \quad (4.130)$$

4.4.1.c Meshing

The meshing is also done in the software COMSOL. Figure 4.26 shows two exemplary meshes one for a non-curved absorber and the other one for a curved absorber.

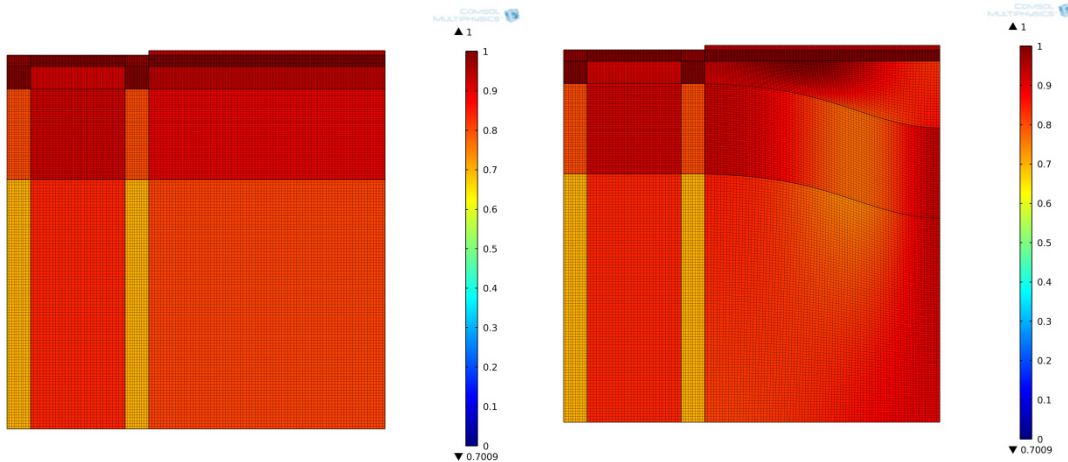


Figure 4.26: Mesh in COMSOL
Non-curved absorber (left), curved absorber (right)

For the completely non-curved design the mesh consists of perfectly rectangular elements. In the curved design the mesh consists of quadrangular elements. Since the geometry is relatively simple the mesh quality both designs is above 0.7.

4.4.2 Flow channel

This section presents the results of flow channels analysis based on the previously described model. Figure 4.27 summarized the main parameters of the analysis. It can be seen that for both configurations of the SPU the shape of the parameters are quite similar.

The first row of Figure 4.27 shows the material utilization of the absorber. It is not subject to a great change over the cavity height although there is a minimum for both configurations for a cavity height H of 5 mm. Moreover, the difference between the modified flow channels and the basic model is relatively small and always within ± 10 percent. However, from an absorber material utilization point of view the smooth model A2 seems to be favorable.

In the second row the pressure drop of the receiver is presented. The general shape for both configurations is very similar to the results of the optimization in the situation analysis shown in Figure 4.11. However, this more detailed study shows that the pressure loss was under predicted in the situation analysis. For both configurations the pressure loss significantly increases for cavity heights smaller than 7.5 mm. As far as the different flow channels are concerned both modifications improve the pressure losses of almost 10 percent.

The third row of Figure 4.27 shows the maximal window temperature. For cavity heights above 10 mm a clear trend can be seen that agrees with results of the situation analysis. The results suggest that the smaller the distance the smaller the window temperature. Nevertheless, below that limit the trend reverses and the window temperature rises again. It seems that the improved convective heat transfer is no longer enough to counteract the increased radiative heat transfer between the absorber and window surface. As far as the different flow channels are concerned the modifications do not improve the window temperature but increase it.

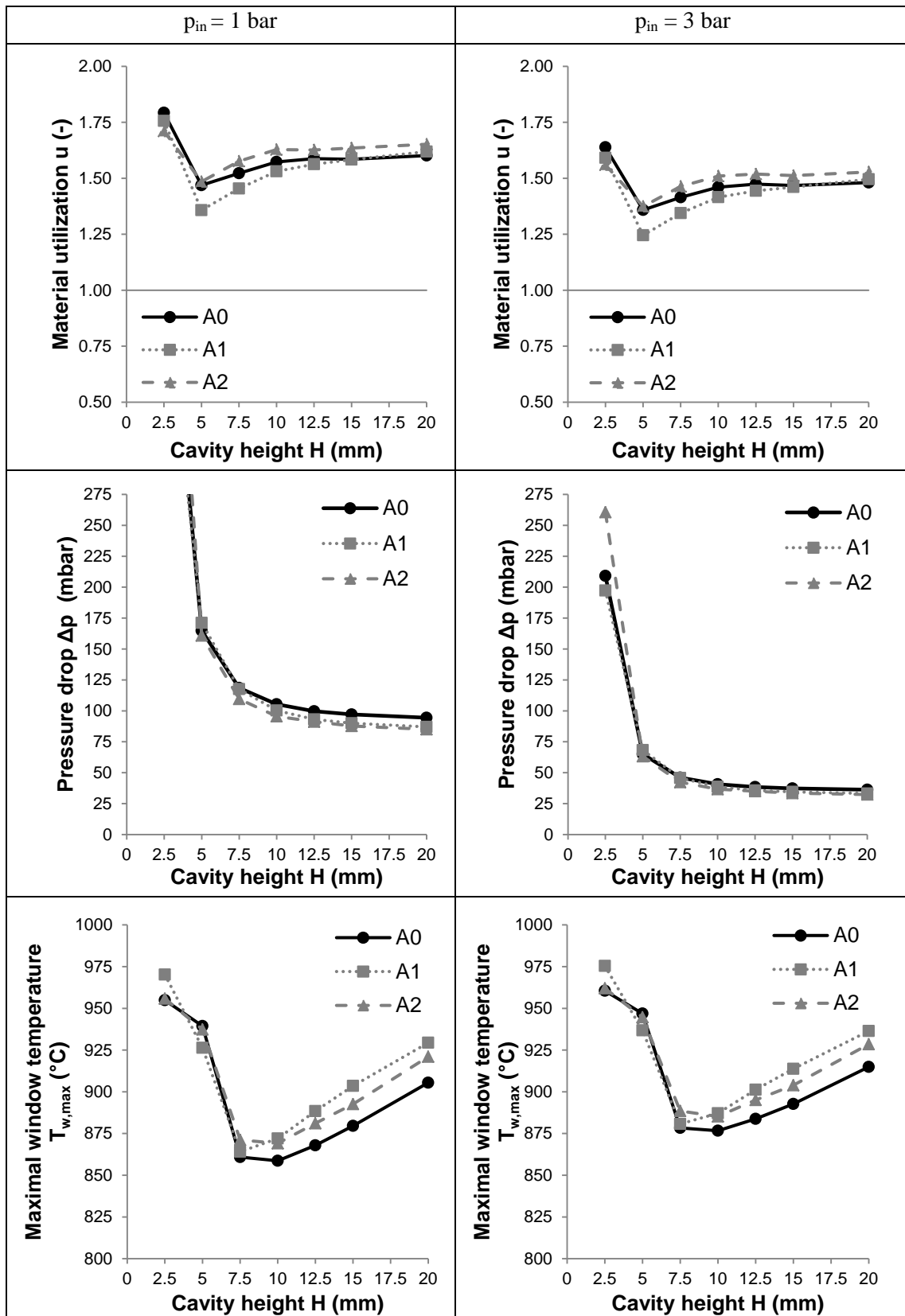


Figure 4.27: Flow channel modification (A) results
 $p_{in} = 1 \text{ bar}$ (left), $p_{in} = 3 \text{ bar}$ (right)

4.4.3 Absorber

This section presents the results of absorber modification analysis based on the previously described model.

4.4.3.a Absorber shape

First, the results of the shape modifications are presented in in Figure 4.28. It can be seen that for both configurations of the SPU the shape of the parameters are quite similar. In the diagrams the position of the modifications is specified by the capital letters T, B, S, and V according to Figure 4.22. T stands for top, B for bottom, S for symmetric, and V for V-shaped.

The first row shows the material utilization of the absorber. For both configurations the difference between the different modifications and position of the modifications is relatively big. One can clearly see that a modification of the absorber surface at the bottom of the receiver does not decrease the material utilization. Designs that include modifications at the top most of the time decrease the material utilization in the absorber. A smoother flow path in combination with a decreased flow resistance in the center of the absorber decreases the temperature differences in the absorber and thus the material utilization. The best results are obtained by V-shaped modifications that provide the lowest temperature differences and reduce the material utilization to acceptable values (<1) for every modification.

In the second row the pressure drop of the receiver is presented. The difference between the different modifications is relatively small. Nevertheless, the position of the modification has great influence on the pressure drop. From a pressure drop point of view absorber surface modification at the top and the bottom increase the pressure drop by about 15 percent for every modification. A symmetric modification increases the pressure drop for all modifications by more than 30 percent. A V-shaped modification on the other hand decreases the pressure drop for every modification compared to the simple design. The most important information of the pressure drop diagrams is that it is important to keep the absorber length at a minimum even though the shape changes.

The third row shows the maximal window temperature. For both configurations the maximal window temperature is highly affected by the position of the modification, too. All surface modifications that include a modification at the top surface decrease the window temperature. This is most likely due to the fact that the hot surface in the center the receiver is and the window surface are separated by a greater distance reducing the radiative heat transfer between the two parts. At the same time the convective cooling of the window by the HTF seems to be less affected. As far as the different modifications are concerned design B1 is favorable.

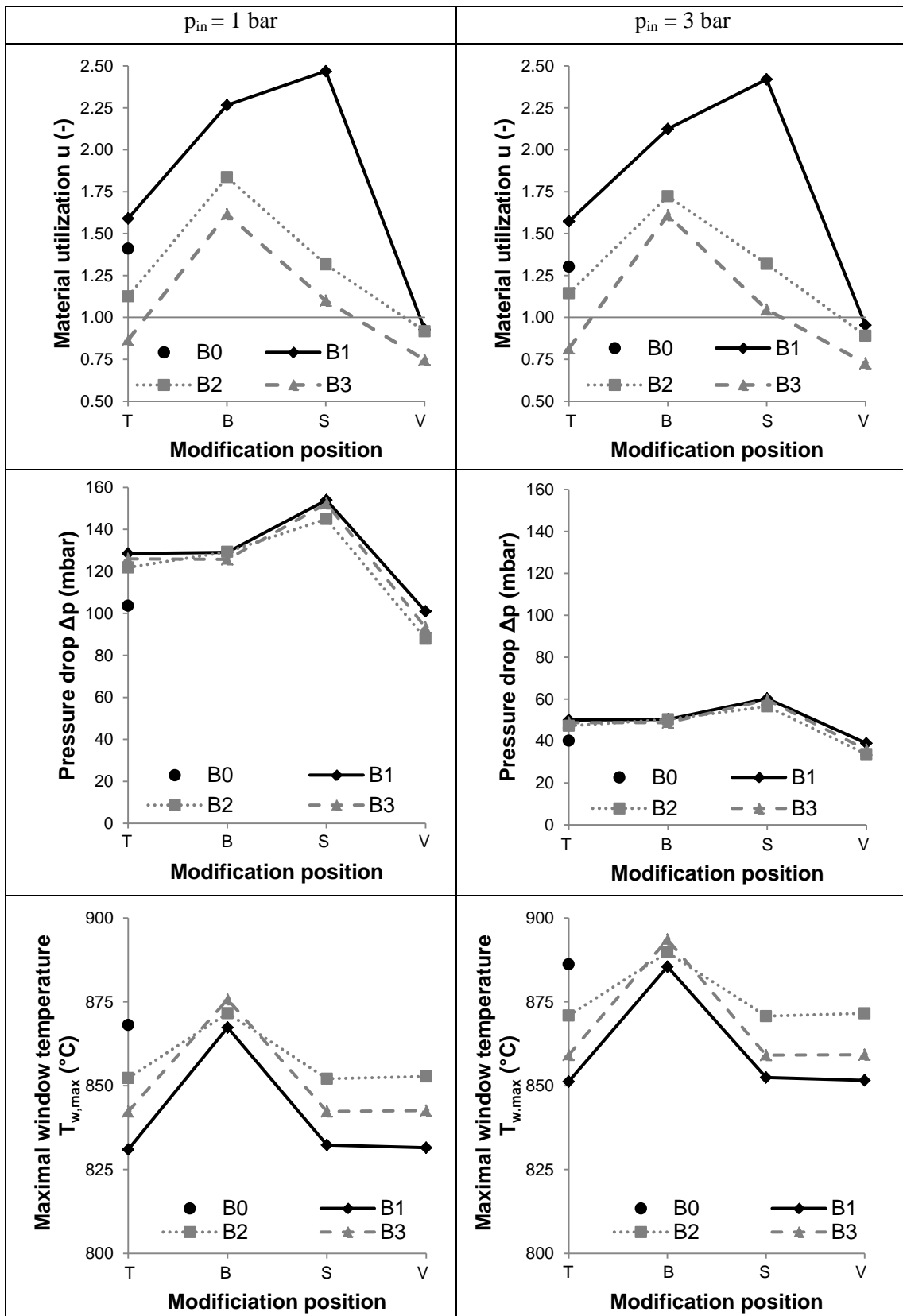


Figure 4.28: Absorber shape modification (B) results
 $p_{in} = 1 \text{ bar}$ (left), $p_{in} = 3 \text{ bar}$ (right)

4.4.3.b Absorber properties 1

Second, the results of the absorber properties modification analysis with spatially constant properties are summarized in Figure 4.29. Again, it can be seen that for both configurations of the SPU the shape of the parameters are quite similar.

The first row shows the material utilization of the absorber. The dependence of the material utilization of the cell diameter is relatively small for all three designs. That means it is mainly dependent on the porosity. From a material utilization point of view the higher the porosity the better. The main reason therefore is that a higher porosity decreases the extinction coefficient K_{ext} (cp. equation 4.22) which in turn decreases the axial gradient of the heat source and thus temperature differences in the absorber.

In the second row the pressure drop of the receiver is presented. Again, the dependence of the pressure drop on the cell diameter is relatively small. However, the difference between the three tested porosities is about 30 percent. This difference is based on two effects. First, an increase in porosity leads to a decrease in the flow resistance characterized by the specific permeability K and the inertia coefficient C_f (cp. equation 3.47 and equation 3.48). Second, an increase in porosity increases the needed length of the absorber in order to absorb all radiation (cp. equation 4.93). This analysis shows that the increase of the pressure drop due to the increase in length outweighs the reduction due to decreased flow resistance.

The third row shows the maximal window temperature. Again, the dependence of the pressure drop on the cell diameter is relatively small. The difference between the three tested porosities is less than 5 percent. However, it can be seen that an increased porosity leads to a decreased maximal window temperature. This is based on the fact that an increased porosity decreases the axial gradient of the heat source and thus decreasing the temperature at the absorber surface. This leads in turn to a decrease in the radiative heat transfer from the absorber to the window.

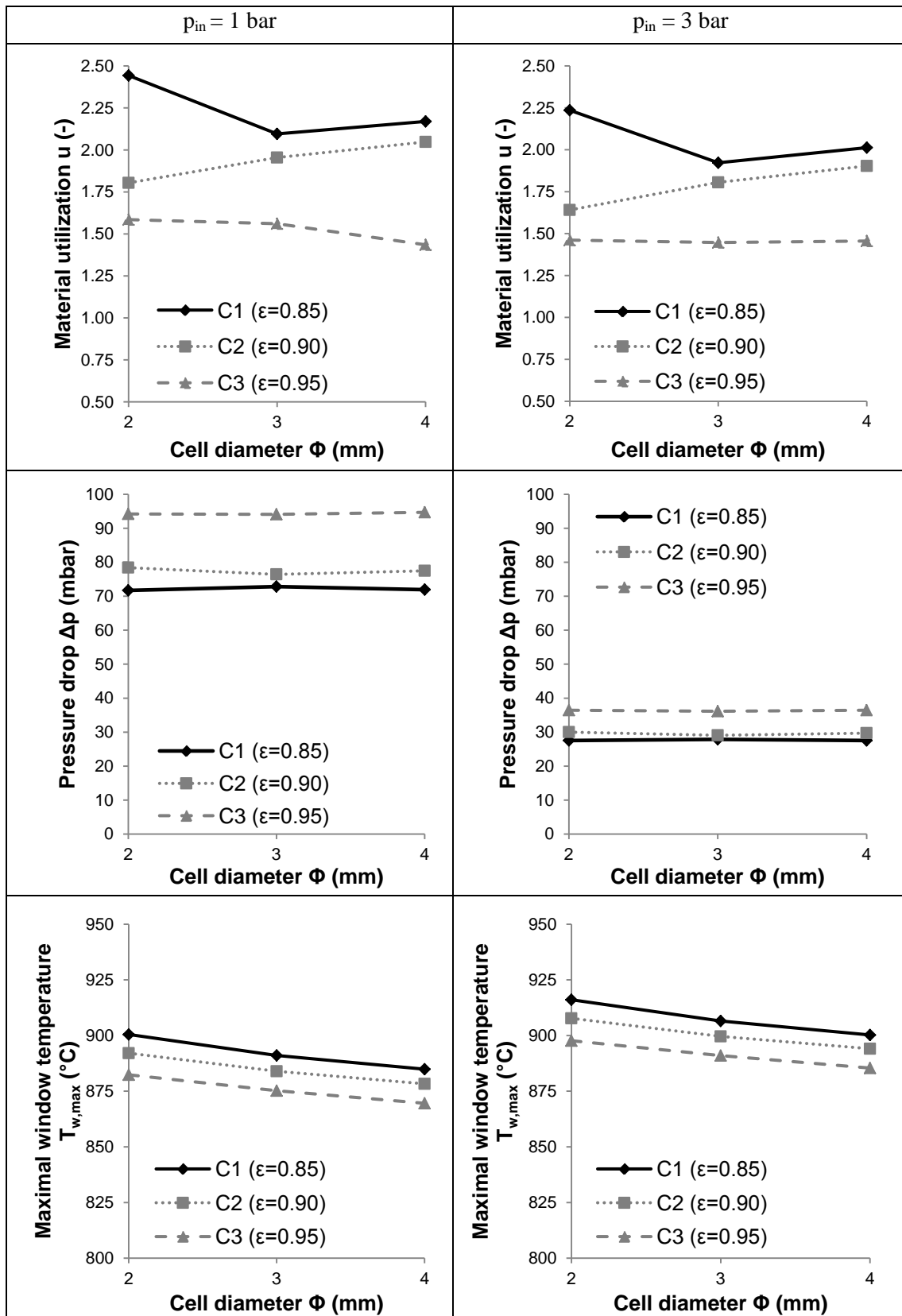


Figure 4.29: Absorber properties modification 1 (C) results
 $p_{in} = 1 \text{ bar}$ (left), $p_{in} = 3 \text{ bar}$ (right)

4.4.3.c Absorber properties 2

Finally, the results of the absorber properties modification analysis with spatially varying properties are summarized in Figure 4.30. And again, it can be seen that for both configurations of the SPU the shape of the parameters are quite similar.

The first row shows the material utilization of the absorber. Neither of the modifications provides any significant decrease in the material utilization. The lowest material utilization can even be achieved with the simple design D1 with a porosity of 95 percent (porosity configuration 3). This can be explained because a decrease of porosity over the radius causes two effects that work against each other. First, it has the advantage that the temperature difference between the center and the outer parts of the absorber decrease. That is based on the fact that the radial gradient of the heat source decreases because the extinction coefficient K_{ext} increases with increasing porosity (cp. equation 4.22). On the other hand a decrease of the porosity increases the Young's modulus (cp. equation 4.31) which makes the material less prone to deformation. For none of the tested configurations the decrease of temperature differences is big enough to counteract the increase of the Young's modulus in order to decrease the material utilization significantly.

In the second row the pressure drop of the receiver is presented. A clear trend can be seen. If the porosity changes over the radius the pressure drop increases significantly if the absorber length is kept constant to the length needed for the highest porosity.

The third row shows the maximal window temperature. Again, none of the modifications shows any improvement concerning the window temperature. The reason why the temperature peaks at the porosity configuration for the design D1 and D2 is the big difference in porosity. Since the flow resistance is significantly lower in the center than on the outer parts the flow velocity drops significantly in the outer parts. Thus these parts heat up to higher temperature levels and more energy is transferred to the window by radiative heat transfer. From a window temperature point of view a constant porosity seems favorable.

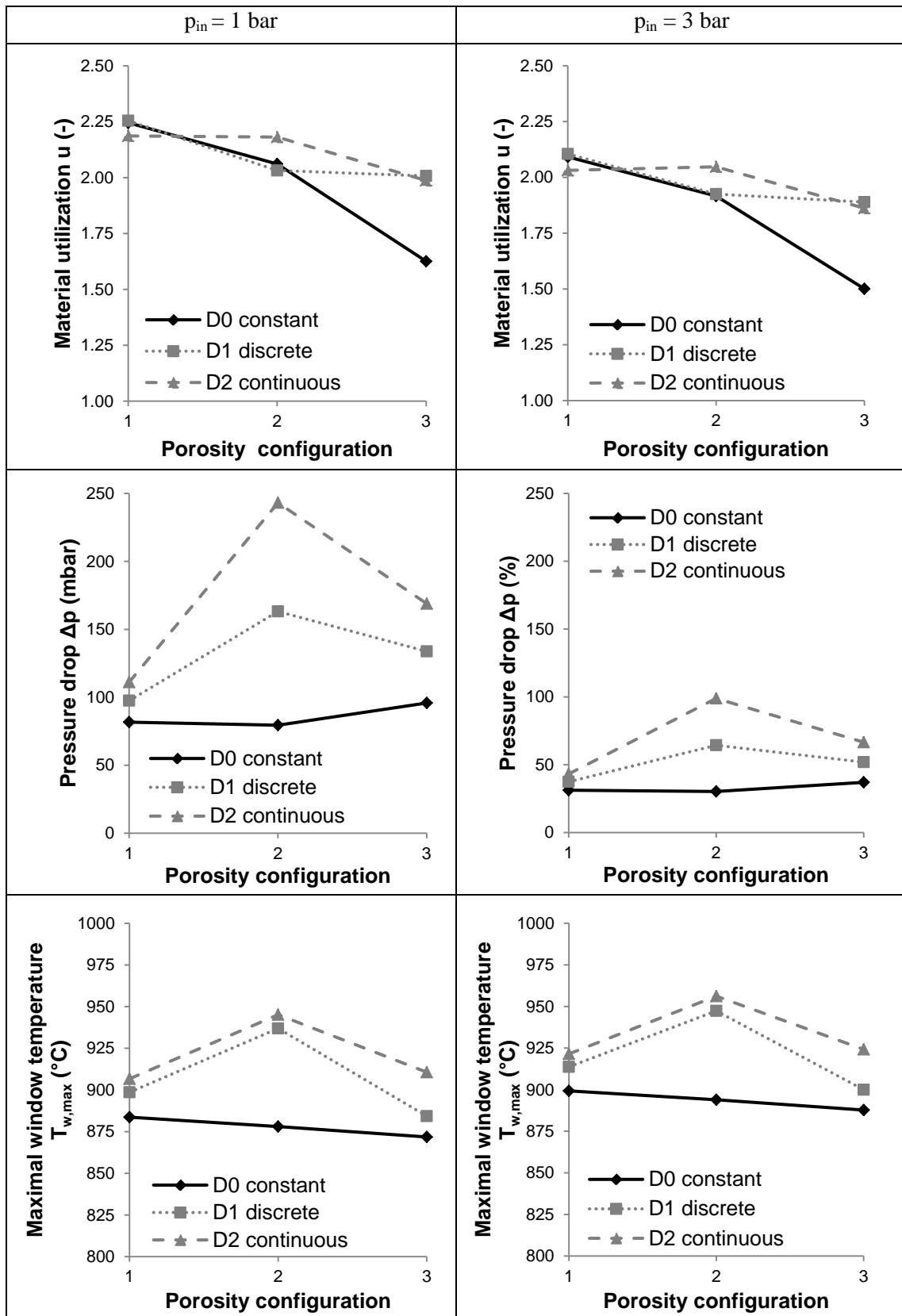


Figure 4.30: Absorber properties modification 2 (D) results
 $p_{in} = 1 \text{ bar}$ (left), $p_{in} = 3 \text{ bar}$ (right)

4.4.4 Window

This section presents the results of window modification analysis based on the previously described model.

4.4.4.a Window shape

First, the results of the window shape analysis are summarized in Figure 4.31. In the diagrams designs E0, E1 and E2 according to Figure 4.24 are specified by B, W, and W&A respectively. B stands for basis, W for window, and W&A for window and absorber. It can be seen that for both configurations of the SPU the shape of the parameters are quite similar.

The first row shows the material utilization of the absorber. For both SPU configurations a modification of only the window increases the material utilization compared to the unmodified basis. On the other hand, a modification of both the window and the absorber leads to a decreased material utilization. The reason for this is that a modification of the window alone reduces the flow speed entering the cavity between the absorber and window due to the bigger distance which in turn leads to a decreased flow velocity in the center of the absorber. That causes higher temperature differences and thus increased material utilization. The improvement due to a modification of both the window and the absorber is mainly based on the improvement by the absorber top surface. Comparing the material utilization of only the absorber top surface modification shown in in Figure 4.28 one can see that it provides an even lower material utilization than a modification of both the window and the absorber surface.

In the second row the pressure drop of the receiver is presented. A modification of only the window decreases the pressure drop insignificantly due to smaller flow velocities at inlet of the cavity between the absorber and window surface. A modification of both the window and the absorber increases the pressure drop for both SPU configurations by about 20 percent.

The third row shows the maximal window temperature. Both modifications provide higher window temperatures. For the configuration where only the window is modified the reason is the smaller flow velocity at the inlet to the cavity between the absorber and window surface which reduces the convective cooling. For the configuration where both the window and the absorber surface are modified the reason is not obvious.

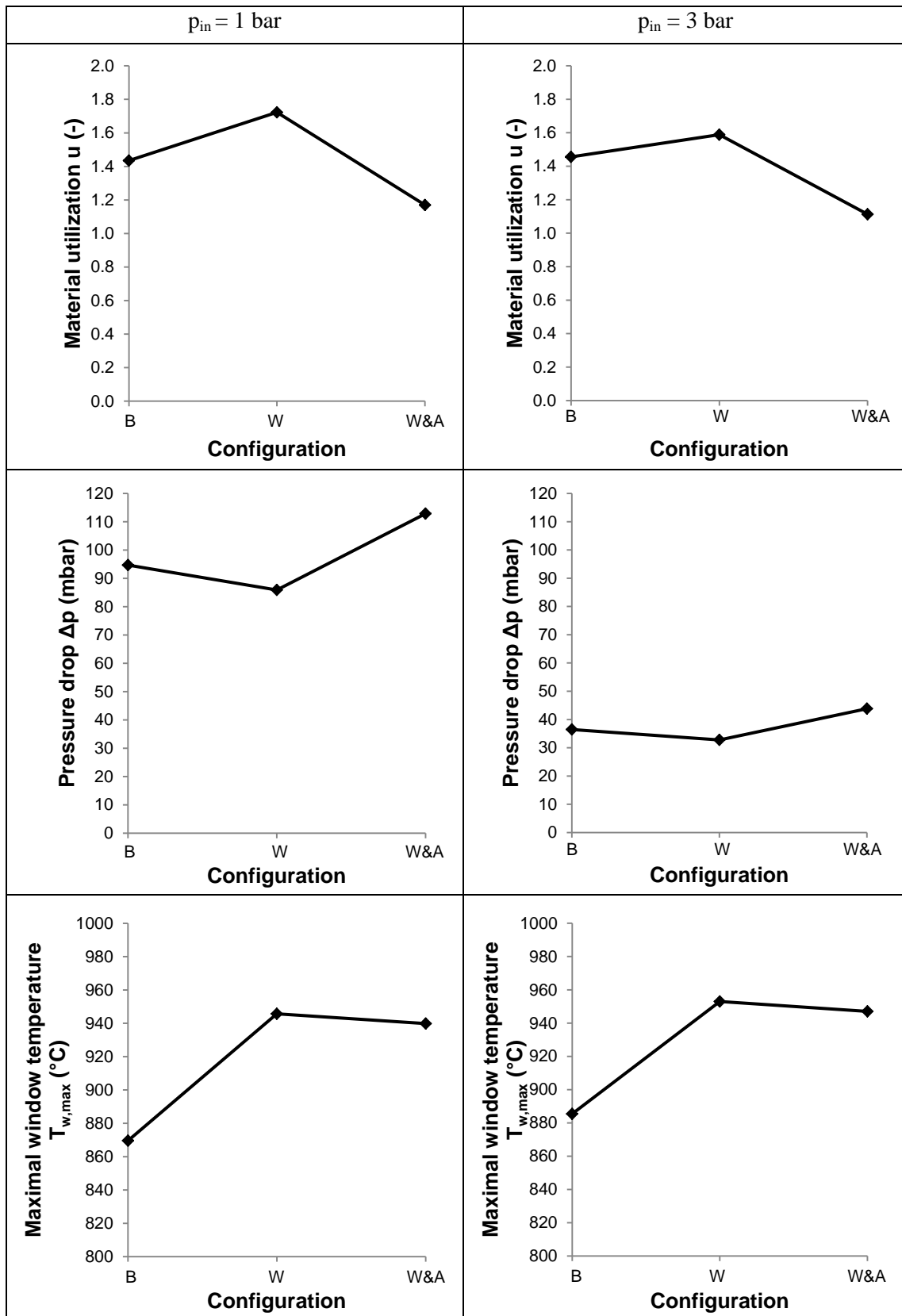


Figure 4.31: Window shape modification (E) results
 $p_{in} = 1 \text{ bar}$ (left), $p_{in} = 3 \text{ bar}$ (right)

4.4.4.b External window cooling

Figure 4.32 summarized the results of the external window cooling analysis. The difference between the point F0 and F1 with no cooling mass flow is that F0 includes natural convection on the outside of the window and F1 does not as described in section 4.3.3. Furthermore, the study F1 was conducted with ambient cooling air and study F2 with cooling air extracted at the receiver inlet and which reduces the mass flow inside the receiver. Again, it can be seen that for both configurations of the SPU the shape of the parameters are quite similar.

The first row shows the maximal window temperature. For both SPU configurations external window cooling with ambient air decreases the maximal window temperature significantly by about 60 K to the configuration with natural convection. The influence of the cooling mass flow above 5g/s is relatively small. External cooling of the window with air extracted at the receiver inlet does not decrease the maximal window temperature compared to the configuration without natural convection. Compared to the configuration that considers natural convection it even increases the temperature. The reason why the window temperature rises with increased cooling mass flow seems to be the decreased convective cooling on the inside because the mass flow is reduced.

In the second row the pressure drop of the receiver is presented. As expected the pressure drop remains almost constant for the external window cooling with ambient air since the mass flow inside the receiver is not changed. For the external window cooling with receiver inlet air the pressure drop decreases with an increase of the extracted air because the internal mass flow decreases.

The third row shows the material utilization of the absorber. For both SPU configurations an external window cooling with ambient air reduces the material utilization of the absorber. The reason for that can be seen in Figure 4.33. Since the window is significantly cooled the inflowing air to the absorber is not heated towards the center so much by the window but even slightly cooled by the relatively cold outer parts of the window. Hence more energy is transferred to the fluid at the center part of the absorber compared to the non-cooled configuration. This leads to smaller temperature differences and thus decreased material utilization of the absorber material. The difference between the fluid inflow temperatures to the absorber is relatively small for the different external cooling mass flows. Therefore, they are not shown. Concerning the efficiency the mean fluid inflow temperature to the absorber is only decreased by about 4 degrees for the atmospheric configuration and about 5 degrees for the pressurized configuration. Thus the receiver efficiency is not affected significantly. For the external window cooling with receiver inlet air the material utilization increases with an increase of the extracted air because the internal mass flow decreases resulting in higher material temperatures.

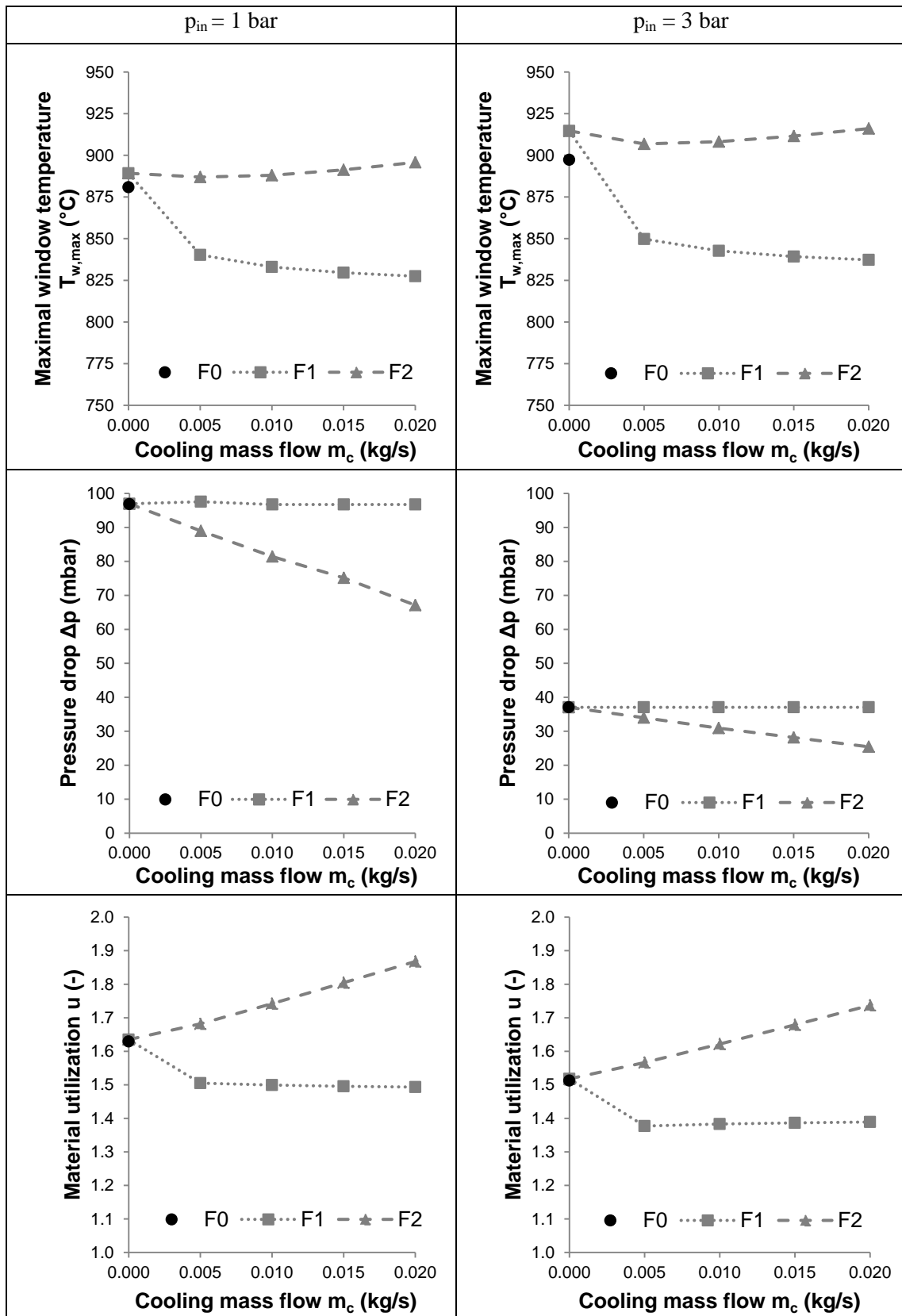


Figure 4.32: Window cooling outside (F) results
 $p_{in} = 1 \text{ bar}$ (left), $p_{in} = 3 \text{ bar}$ (right)

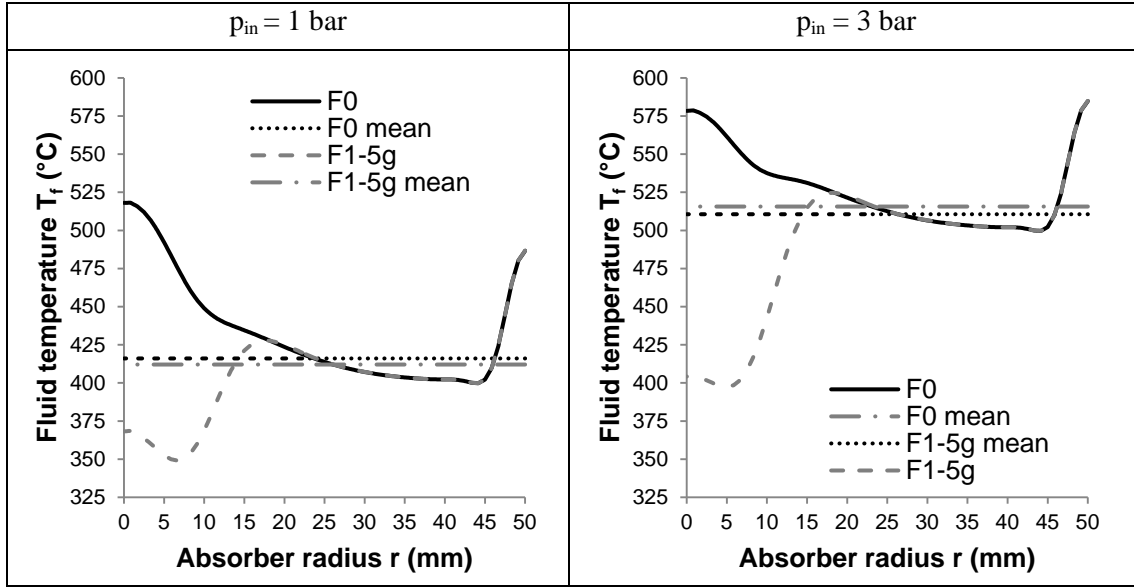


Figure 4.33: Fluid temperature before absorber (F)
 $p_{in} = 1\text{bar}$ (left), $p_{in} = 3\text{bar}$ (right)

The before mentioned thermal receiver efficiency can be calculated as

$$\eta_{\text{rec}} = \frac{\Delta \dot{Q}_{\text{fluid}}}{\dot{Q}_{\text{radiation}} + P_{\text{add}}} \quad (-) \quad (4.131)$$

$$= \frac{(\dot{m}_{f,\text{out}} \cdot h_{f0,\text{out}} - \dot{m}_{f,\text{in}} \cdot h_{f0,\text{in}})}{\dot{Q}_{\text{radiation}}}$$

where $\Delta \dot{Q}_{\text{fluid}}$ is the power gained in the fluid from the receiver inlet to outlet, $\dot{Q}_{\text{radiation}}$ the power input to the receiver due to radiation, P_{add} additional input power, $\dot{m}_{f,\text{out}}$ and $\dot{m}_{f,\text{in}}$ the air mass flow at the outlet and inlet respectively, and $h_{f0,\text{out}}$ and $h_{f0,\text{in}}$ the total enthalpy of the fluid at the outlet and inlet respectively. The total enthalpy is defined as

$$h_{f0} = h_f + \frac{c^2}{2} + gz \quad \left(\frac{J}{kg}\right) \quad (4.132)$$

where h_f is the fluid enthalpy, c the fluid flow velocity magnitude, g the gravitational acceleration, and z the potential height. Since the receiver is mounted horizontally there is not height difference between inlet and outlet. Furthermore, the kinetic energy of the fluid is almost the same for the inlet and the outlet and in both cases less than one percent of the enthalpy. Therefore, the potential and kinetic energy are neglected.

The additional energy that is needed to compress the cooling air is estimated by the kinetic energy and an overall compression efficiency as

$$P_{\text{add}} = \dot{m}_c \cdot \frac{c_c^2}{2} \cdot \eta_{\text{tot}} \quad (W) \quad (4.133)$$

where \dot{m}_c is the cooling mass flow, c_c^2 the cooling flow velocity magnitude at the outlet of the nozzle, and η_{tot} the overall compression efficiency. For the external cooling the maximal inflow velocity for a cooling mass flow of 20g/s is in the order of magnitude of 30 m/s. Even with a very low compressor efficiency and losses at the expansion the additional compression

power is less than one percent of the radiation power. Thus the compression power is neglected.

Figure 4.34 shows the thermal efficiency for the different designs. As expected the efficiency only decreases slightly for the external window cooling with ambient air. For the external cooling with receiver inlet air the efficiency drops dramatically with an increase of extracted air.

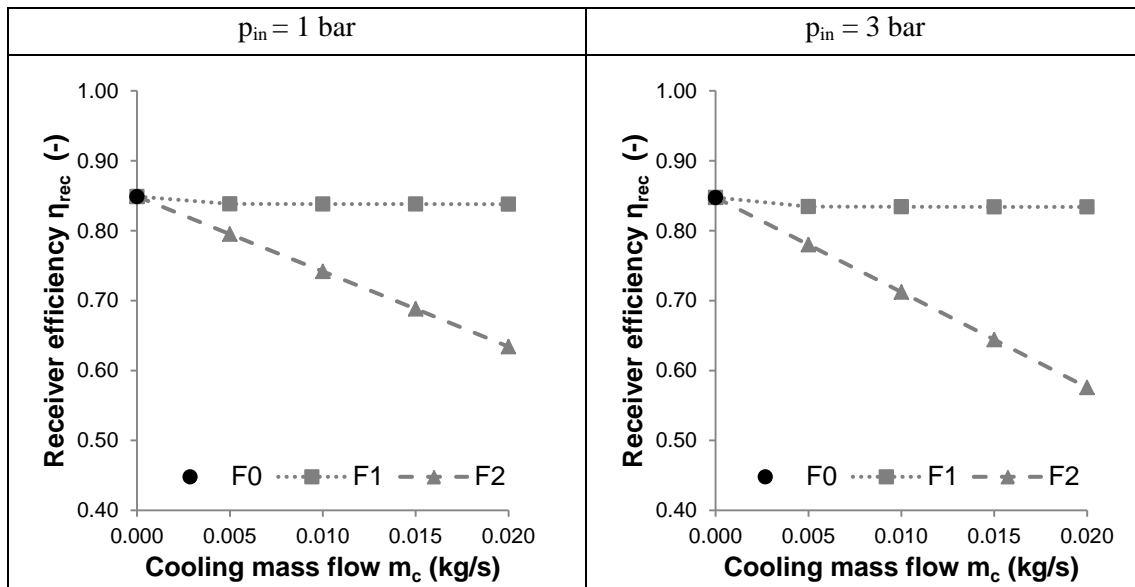


Figure 4.34: Window cooling outside (F) efficiency
 $p_{in} = 1 \text{ bar}$ (left), $p_{in} = 3 \text{ bar}$ (right)

4.4.4.c Internal window cooling

Finally, the results of the internal window cooling analysis are presented in Figure 4.35. Design G0 is the uncooled design used for comparison and is congruent with design G1 with a zero cooling mass flow. The study G1 was conducted with ambient cooling air which increased the mass flow inside the receiver. Study G2 was conducted with cooling air extracted at the receiver inlet which reduces the mass flow at the first part of the receiver. After the injection the mass flow reaches the initial level again which is especially important for the heat transfer in the absorber.

Again, for most parameters its shape is quite similar for both configurations of the SPU.

The first row shows the maximal window temperature. For the internal cooling with receiver inlet air the window temperature remains more or less constant for a cooling mass flow below 10 g/s. Above that limit it slowly starts to decrease for both SPU configurations. Internal cooling with ambient air decreases the window temperature significantly compared to the non-cooled design. However, the analysis gives inconsistent window temperatures for this design.

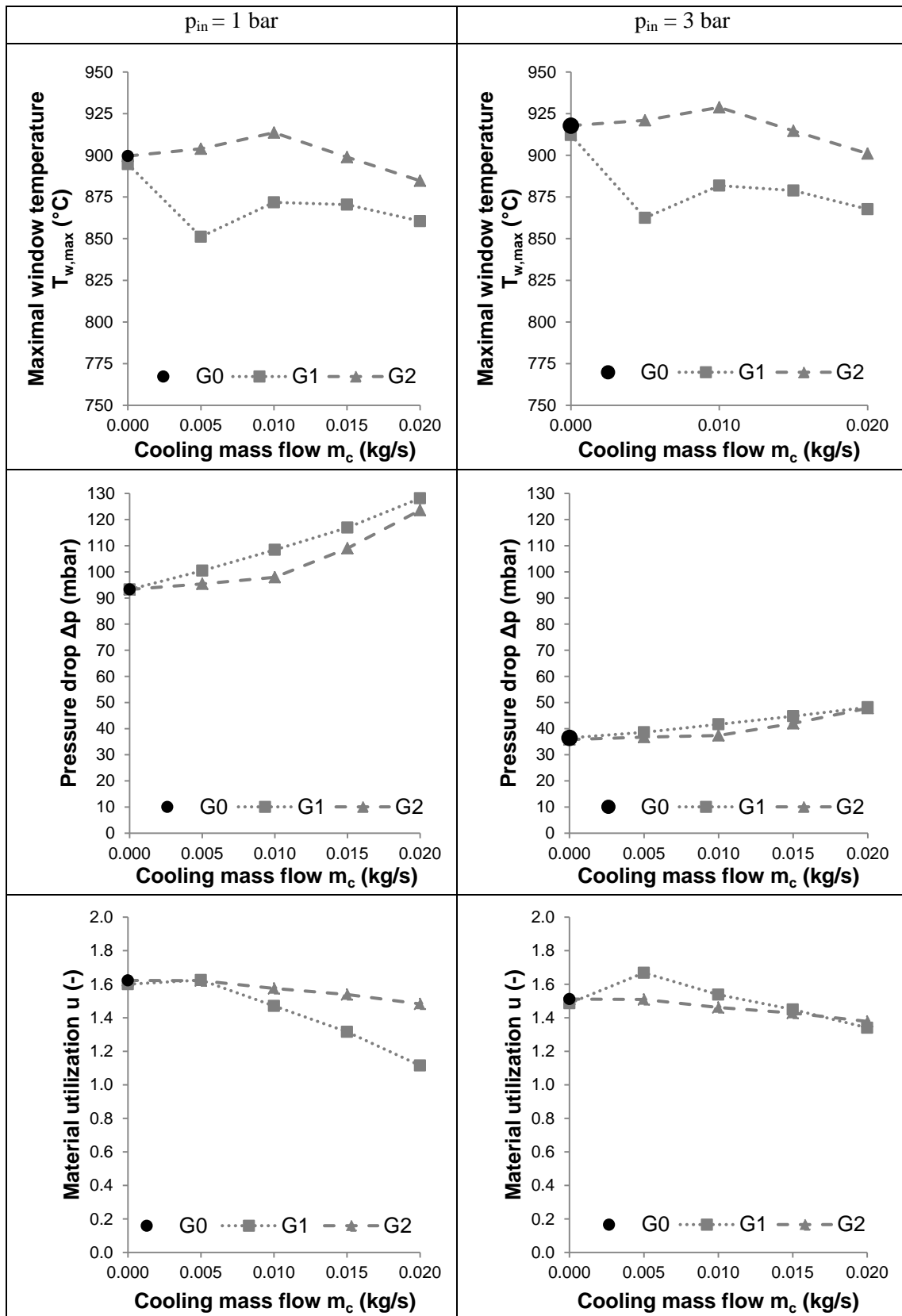


Figure 4.35: Window cooling inside (G) results
 $p_{in} = 1 \text{ bar}$ (left), $p_{in} = 3 \text{ bar}$ (right)

In the second row of Figure 4.35 the pressure drop of the receiver is presented. For the internal cooling with receiver inlet air the pressure drop was expected to decrease slightly with increasing cooling mass flow. This was expected because the more air is extracted before the receiver the lower the flow speed of the remaining air until the cooling air is injected. And that should cause a smaller pressure drop of the free flow until the absorber. However, for high cooling mass flows the accuracy of the models became poor. Especially the mass conservation from the inlet to the outlet was no longer valid with errors up to 20 percent. Reducing the mesh size helps to reduce the error. Unfortunately, at a certain point the available computers were no longer capable of handling an even finer mesh. The pressure drop for the internal cooling with ambient air looks like expected. It increases with increased cooling mass flow since the mass flow through the absorber increases.

The third row of Figure 4.35 shows the material utilization of the absorber. For the internal cooling with receiver air the material utilization for both SPU configurations is almost constant. It almost looks like expected since the mass flow and temperature of the fluid in front the absorber remains more or less constant. For the internal cooling with ambient air the material utilization decreases with increased cooling mass flow. The reason for that is most likely the fact that the relatively cool cooling air increased the heat transfer in the center of the absorber leading to smaller temperature differences. There is no obvious reason why the material utilization of the design with ambient cooling air for the pressurized configuration is generally higher than the one of the design with receiver inlet cooling air.

Figure 4.36 shows the thermal efficiency for both configurations. Since the analysis of the internal cooling with receiver inlet air gave inconsistent results the thermal efficiency is considered to be constant over the cooling mass flow.

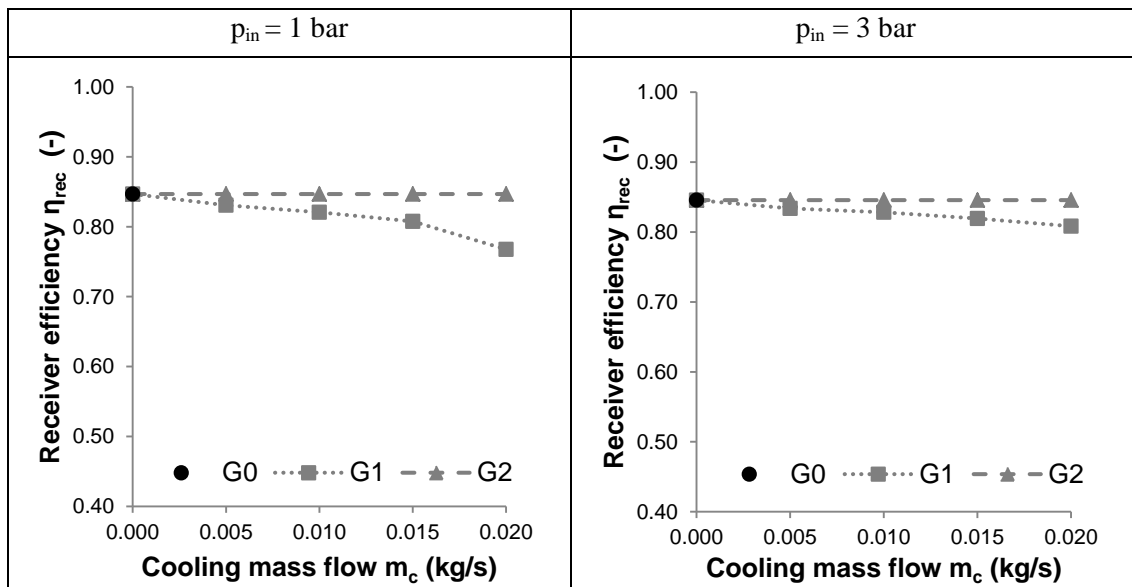


Figure 4.36: Window cooling inside (G) efficiency
 $p_{in} = 1$ bar (left), $p_{in} = 3$ bar (right)

Despite the mentioned inconsistencies the efficiency of the internal cooling with ambient air looks as expected as it decreases with increasing cooling mass flow.

4.4.5 Heat transfer fluid

It was already concluded in the synthesis of solutions that it is not possible to change the HTF to improve its heat transfer properties as the solar receiver needs to work within the SPU.

It was also mentioned that introducing angular momentum to the HTF by inlet guide vanes might be used to improve the heat transfer due to increased velocity. Considering constant mass flow for designs with and without inlet guide vanes, and thus constant axial inflow velocity, introducing a circumferential velocity component to the flow increases the velocity magnitude. However, the closer the flow gets to the axis of rotation the smaller the circumferential component and the smaller the increase of the velocity magnitude. As presented in the situation analysis it is not necessary to remove more energy by the HTF from the outer parts of the absorber but from the center. Thus, inlet guide vanes are not able to reduce temperature differences within the absorber. Therefore, no further analysis concerning inlet guide vanes is conducted.

4.5 Evaluation and decision

The evaluation and decision are based on the results of the main study presented in section 4.4. Since the objectives mechanical integrity, performance, manufacturability, and costs often conflict with each other a value of benefit analysis can be applied. It allows weighting the different criteria and comparing the different designs. The value of benefit analysis is done according to Haberfellner et al. [24].

4.5.1 Value of benefit analysis

First of all, a matrix of criteria needs to be set up to assess the importance of the different parameters. Table 4.16 shows the matrix with the criteria performance, mechanical integrity, manufacturability, and costs according to the objectives.

Table 4.16: Matrix of criteria

		1	2	3	4	Preference frequency	Weighting	Real weighting
1	Performance	1	1	1	1	3	30	30
		1	2	3	4			
2	Mechanical integrity		2	2	2	4	40	40
			2	3	4			
3	Manufacturability			3	3	2	20	20
				3	4			
4	Costs				4	1	10	10
					4			

Due to the fact that the receiver is supposed to be a prototype for the laboratory manufacturability and costs are not that essential as if it was for mass production. Therefore, the performance and mechanical integrity outweigh the manufacturability and costs. However, the most important thing remains the functionality. That means that the designed receiver does not break the first time it is tested. Therefore, the mechanical integrity is favored over the performance.

These four main criteria need to be subdivided again to sub criteria and weighted again. Table 4.17 shows the division and the corresponding weighting. As far as the performance is concerned both the thermal efficiency and the pressure drop are of the same importance. The same is valid for the mechanical integrity. The integrity of the absorber and the window are equally important because if one of the two components fails the whole receiver fails. Regarding the manufacturability and the costs the weighting is a bit different because a third component the flow channel is considered as well. Nevertheless, since the absorber and the window are more crucial for the whole system they are weighted higher than the flow channel.

Table 4.17: Weighting of sub criteria

	Main criteria	Sub criteria	Sub weighting (%)
1	Performance	Thermal efficiency	50
		Pressure drop	50
2	Mechanical integrity	Absorber utilization factor	50
		Window temperature	50
3	Manufacturability	Absorber	40
		Window	40
		Flow channel	20
4	Costs	Absorber	40
		Window	40
		Flow channel	20

For the assessment of the result a target scale needs to be specified. The criteria thermal efficiency, pressure drop, absorber utilization factor, and window temperature are continuous function and therefore can be assessed using a continuous utility function. The manufacturability on the other hand is rather difficult to assess with a specific number. The same applies to the costs if no more detailed analysis is conducted. Thus these two criteria are qualitatively assessed using a nominal scale. Table 4.18 shows the target scale for the different criteria.

In order for the above mentioned utility functions to provide meaningful results they need to cover the range of interest of the different criteria. The pressure drop is very different for the two SPU configurations. Therefore, different upper limits for the pressure drop for the utility functions need to be specified. As mentioned in the preliminary study a pressure drop of less than 10 percent is acceptable for the laboratory setup. Since most of the pressure drop for the atmospheric configuration of the previous analysis is below 10 percent that is a suitable upper limit. For the pressurized configuration the average pressure drop is way lower. Furthermore, a more realistic scenario would require a pressure drop that is smaller than 4 percent. Thus, for the pressurized configuration a pressure drop of 4 percent is chosen as the upper limit.

For the thermal efficiency, the mechanical integrity, and the window temperature the difference between the configurations is not significant. Thus the same upper and lower limits can be used for both SPU configurations. However, these values need to be chosen wisely. As far as the thermal efficiency is concerned the choice is relatively simple. For both

configurations the statement the higher the efficiency the better is valid. Thus the minimal and maximal value are zero and one hundred percent respectively.

The limits for the absorber material utilization are a bit more complicated. Basically, a material utilization below one is needed ensuring the absorber does not break. A very low material utilization on the other hand means that the component is oversized. That means at some point a smaller material utilization does not provide any additional value. Thus, the lower limit is chosen to be 0.5. In order to be able to compare the different designs the upper limit is chosen to be 2 although designs with a material utilization above one will fail.

The lower and upper limits for the window temperature are chosen on the following considerations. According to Schott [87] the maximal operating temperature for their fused silica glass is 930°C. Therefore, this value is chosen as the upper limit. The lower limit is based on Röger et al. [88]. They claim that an operating temperature of 800°C of the glass window in a pressurized receiver is acceptable. That means a lower window temperature does not provide any obvious additional value.

Table 4.18: Target scale for value of benefit analysis

Criteria	Scale					
	0	1	2	3	4	5
Performance						
Thermal efficiency η_{th} (-)	$5 \cdot \eta_{th}$					
Pressure drop Δp (-)	$\frac{5}{\Delta p_{max}} \cdot \max\{(\Delta p_{max} - \Delta p), 0\}$					
Mechanical integrity						
Absorber material utilization factor u_{abs} (-)	$\frac{5}{u_{max} - u_{min}} \cdot \min\{\max[(u_{max} - u), 0], u_{max} - u_{min}\}$					
Maximal window temperature T_w (°C)	$5 \cdot \min\left\{\max\left[\frac{(T_{w,max} - T_w)}{(T_{w,max} - T_{w,min})}, 0\right], 1\right\}$					
Manufacturability						
Absorber	impossible	bad	medium	good	very good	excellent
Window	impossible	bad	medium	good	very good	excellent
Flow channel	impossible	bad	medium	good	very good	excellent
Costs						
Absorber	very high	high	medium	low	very low	negligible
Window	very high	high	medium	low	very low	negligible
Flow channel	very high	high	medium	low	very low	negligible

Table 4.19 summarizes the upper and lower limits for the different criteria of the value of benefit analysis.

Table 4.19: Limits for target scale

Criteria	Configuration	
	$p_{in} = 1\text{bar}$	$p_{in} = 1\text{bar}$
$\Delta p_{min}, \Delta p_{max}$ (%)	0, 10	0, 4
u_{min}, u_{max} (%)	50, 200	
$T_{w,min}, T_{w,max}$ (°C)	800, 930	

Figure 4.37 shows the utility functions for the pressure drop, the material utilization, and the maximal window temperature graphically.

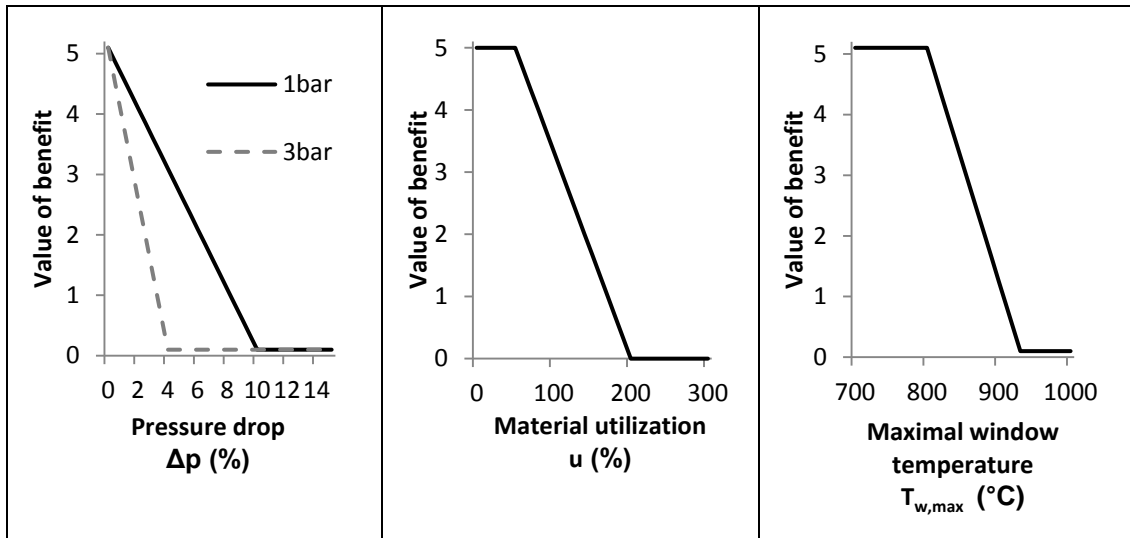


Figure 4.37: Utility functions for value of benefit analysis

4.5.2 Values of benefit

In this section the values of benefit of the different designs are presented. First, Figure 4.38 presents the results of the value of benefit analysis of the flow channel modification.

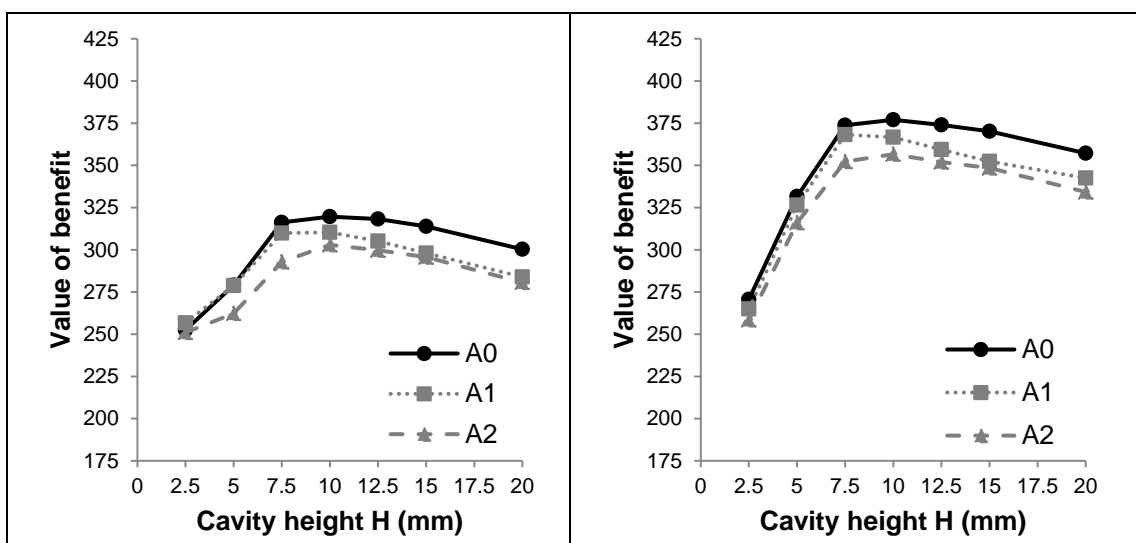


Figure 4.38: Value of benefit flow channel (A)
 $p_{in} = 1\text{bar}$ (left), $p_{in} = 3\text{bar}$ (right)

Considering all parameters the basic design A0 gives the highest value of benefit for both SPU configurations at a cavity height of 10mm. Apparently, the decrease of pressure drop of both modified flow channels A1 and A2 did not outweigh the increased window temperature, the slightly worse manufacturability, and slightly higher cost of these designs.

Figure 4.39 summarizes the results of the absorber shape and both absorber properties modification.

In the first row the values of benefit of the absorber shape modification are shown. All three designs give very similar results. However, regarding the position of the modification the V-shaped design is clearly favorable. Even though the values of benefit of the different designs are very similar for the V-shaped position the design B3 gives the highest value of benefit for both SPU configurations.

The second row presents the values of benefit of the first absorber properties modification. In general an increase cell diameter gives a slightly higher value of benefit. However, the difference between the different designs and their porosities is more significant. For both SPU configurations the design with the highest porosity is favorable.

In the third row the values of benefit of the second absorber properties modification are shown. Not surprisingly the basic design D0 is favorable. It is the design that is favorable concerning all three parameters discussed before. Additionally, it is the simplest one.

Figure 4.40 summarizes the results of the value of benefit analysis for the window shape and cooling modifications. In the first row the results of the window shape analysis are presented. According to the value of benefit analysis there is no good reason for a special shape of the window.

The second row presents the values of benefit of the external window cooling. For both SPU configurations external cooling of the window with ambient air increases the value of benefit by about 20 percent to the uncooled design. The dependence on the cooling mass flow above 5 g/s is almost negligible. External cooling with receiver inlet air on the other hand does not provide any significant additional value of benefit.

In the third row the values of benefit of the internal window cooling are shown. Again, cooling with ambient air provides additional value of benefit compared to the uncooled design. However, the increase is smaller than the increase due to external cooling. Moreover, the results are based on partly inconsistent data. Internal cooling with receiver inlet air on the other hand does not provide any significant additional value of benefit.

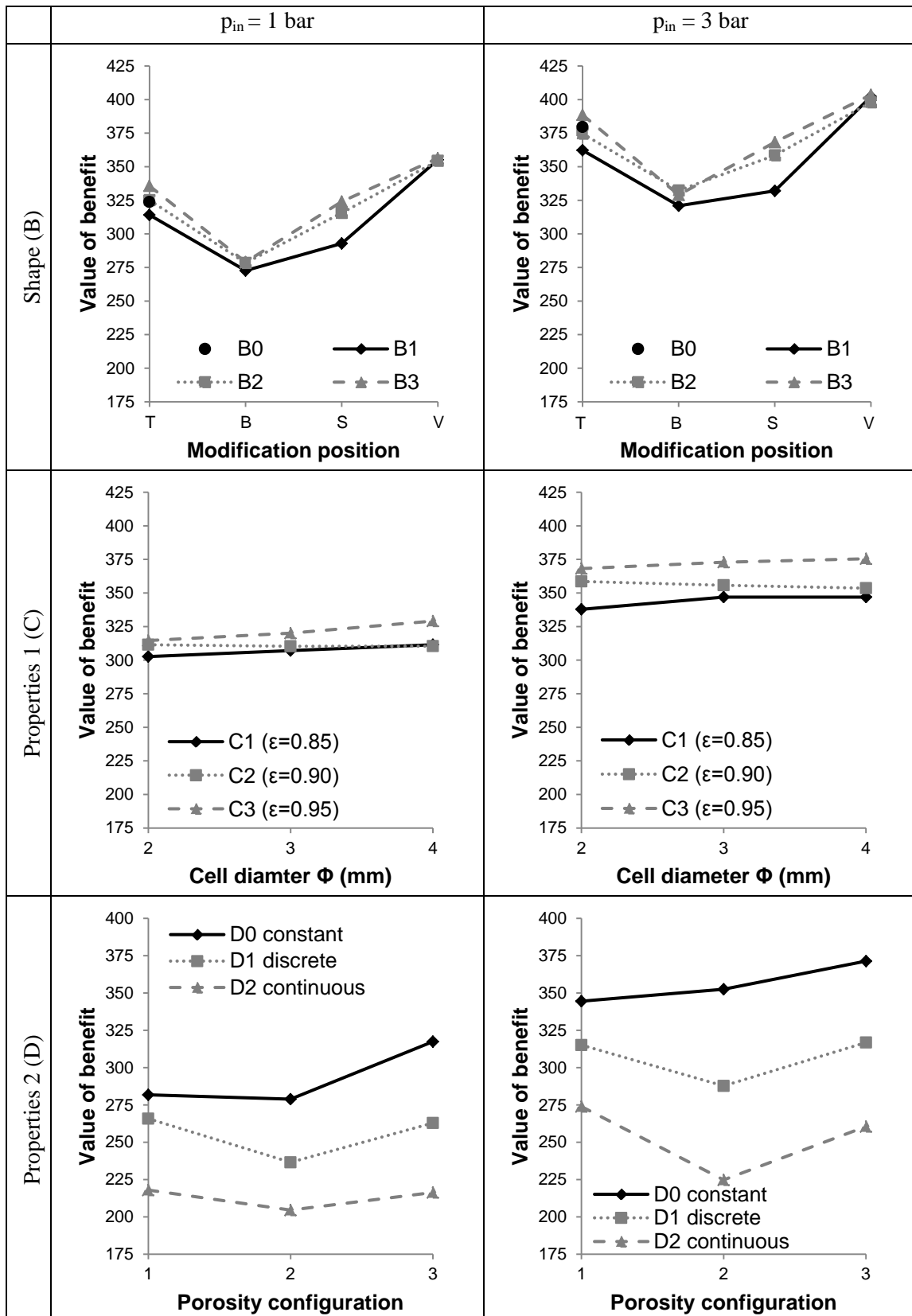


Figure 4.39: Value of benefit absorber modifications (B), (C), and (D)
 $p_{in} = 1 \text{ bar}$ (left), $p_{in} = 3 \text{ bar}$ (right)

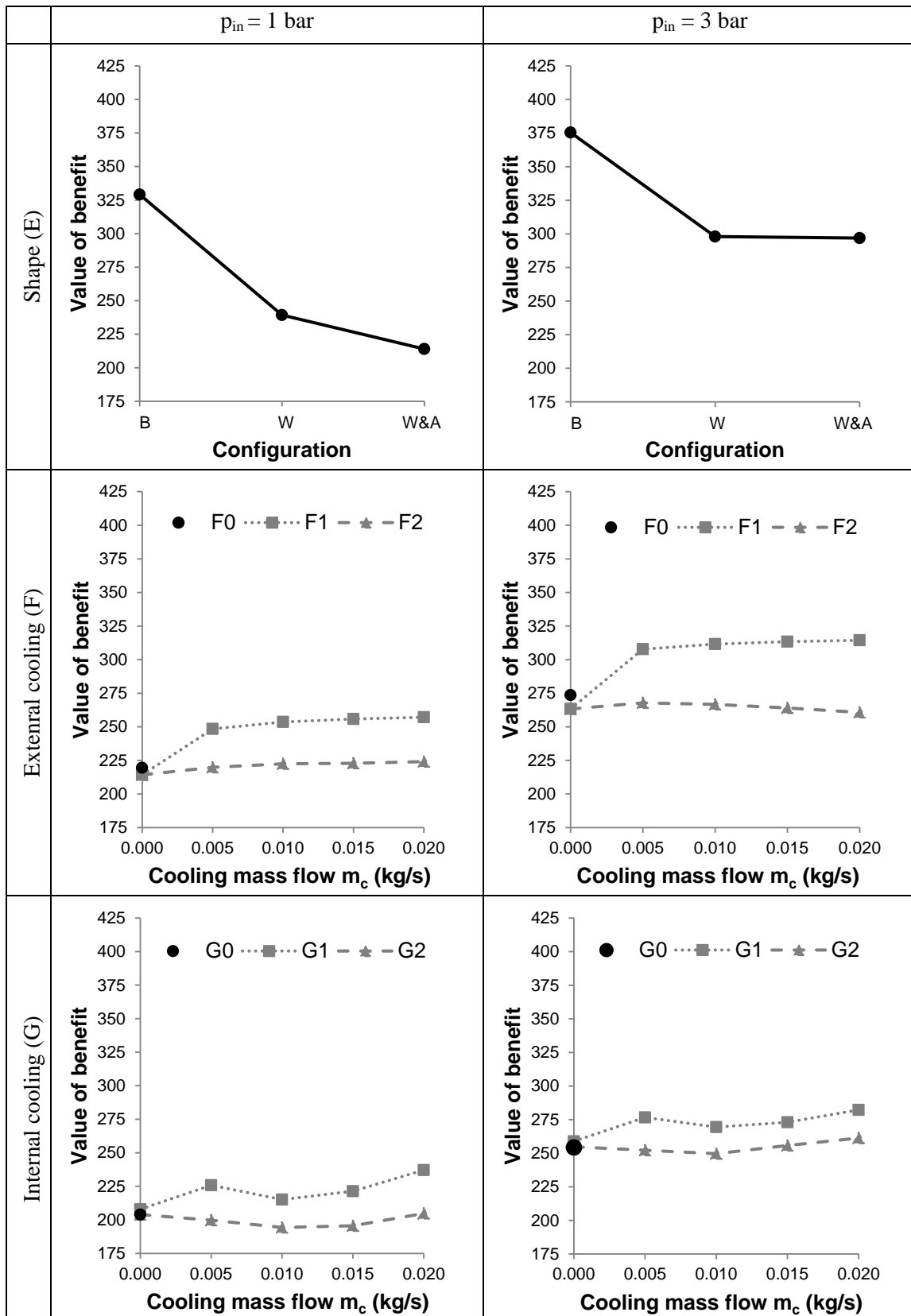


Figure 4.40: Value of benefit window modifications (E), (F), and (G)
 $p_{in} = 1 \text{ bar}$ (left), $p_{in} = 3 \text{ bar}$ (right)

4.5.3 Decision

Combining the designs with the highest values of benefit should give the best design for both SPU configurations. For the studies A through E this is pretty much straight forward. The combination of the basic flow channel A0 with a cavity height of 10mm, a V-shaped absorber B3, with the porosity of the design C3 ($\epsilon=0.95$) and a cell diameter of 4mm that are spatially constant (cp. design C1), and an unmodified window shape should give the best result.

As far as the cooling is concerned external cooling has distinct advantage over internal cooling. However, the analyses showed that a working receiver can be built without cooling as well. In order to make the solar receiver for the SPU as simple as possible it will be designed without window cooling at all. Nevertheless, if tests show that the window temperature gets to high it is recommended to implement external cooling with ambient air.

5. DETAILED STUDY

In this section the receiver design that was chosen on basis of the main study is analyzed and a prototype is designed. Furthermore, the COMSOL model is verified using the Flow Modeling Simulation Software ANSYS FLUENT. The analysis is done in three dimensions so that the model can be used for a CFD analysis of the whole receiver including inflow and outflow from and to adjacent components in a future work.

5.1 Design analysis

Based on the main study Figure 5.1 shows the chosen receiver design.

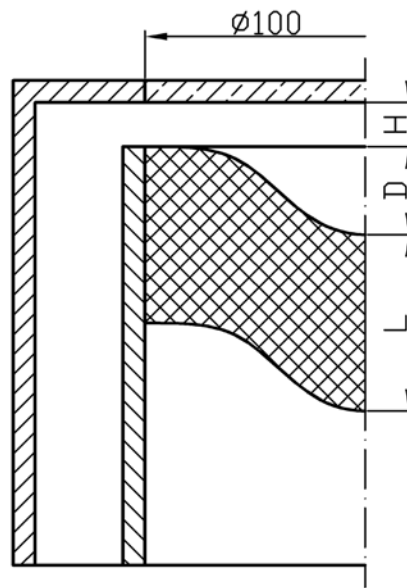


Figure 5.1: Receiver design

According to the value of benefit analysis the optimal cavity height H is 10 mm, the optimal porosity of the absorber 95 percent, and the optimal cell diameter Φ is 4 mm. As described earlier the minimal absorber length L is a function of the porosity and the cell diameter. However, the absorber depth D was not investigated in the main study.

5.1.1 Parameter study

Therefore, a final parameter study on the cavity depth D is done. At the same time the cell diameter is varied as well because the main study showed almost no dependence of the investigated criteria on the cell diameter. One study is done with a cell diameter Φ of 4 mm and one with 2 mm. The cavity depth on the other hand is varied between zero and 40 mm.

The results of this final parameter study are summarized in Figure 5.2. The first row shows the material utilization. The trends are quite similar for both SPU configurations. For both configurations and both cell diameters a clear trend is visible. Apparently, a cavity depth D of 20 to 25 mm gives the lowest material utilization. Surprisingly, the smaller cell diameter gives lower material utilization resulting in a margin of safety of about 40 percent for both configurations.

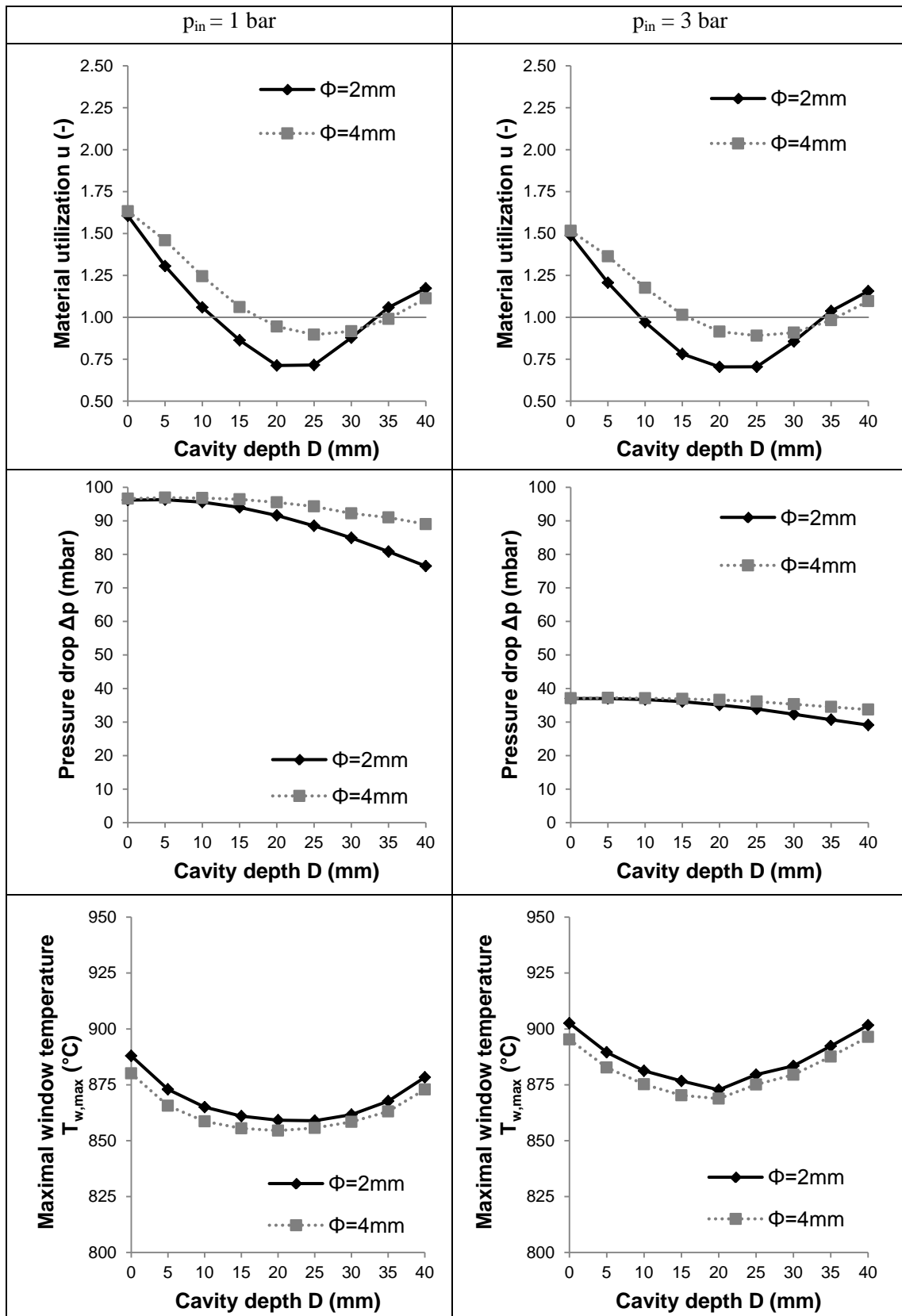


Figure 5.2: Chosen receiver design cell diameter variation
 $p_{in} = 1 \text{ bar}$ (left), $p_{in} = 3 \text{ bar}$ (right)

The reason for this can be seen in Figure 5.3. For both cell diameters the temperature distribution is relatively similar. Moreover, the maximal absorber temperature only differs about 45°C. The absorber with the bigger cell diameter experiences higher compressive stresses compared to the absorber with the smaller cell diameter because of its greater length.

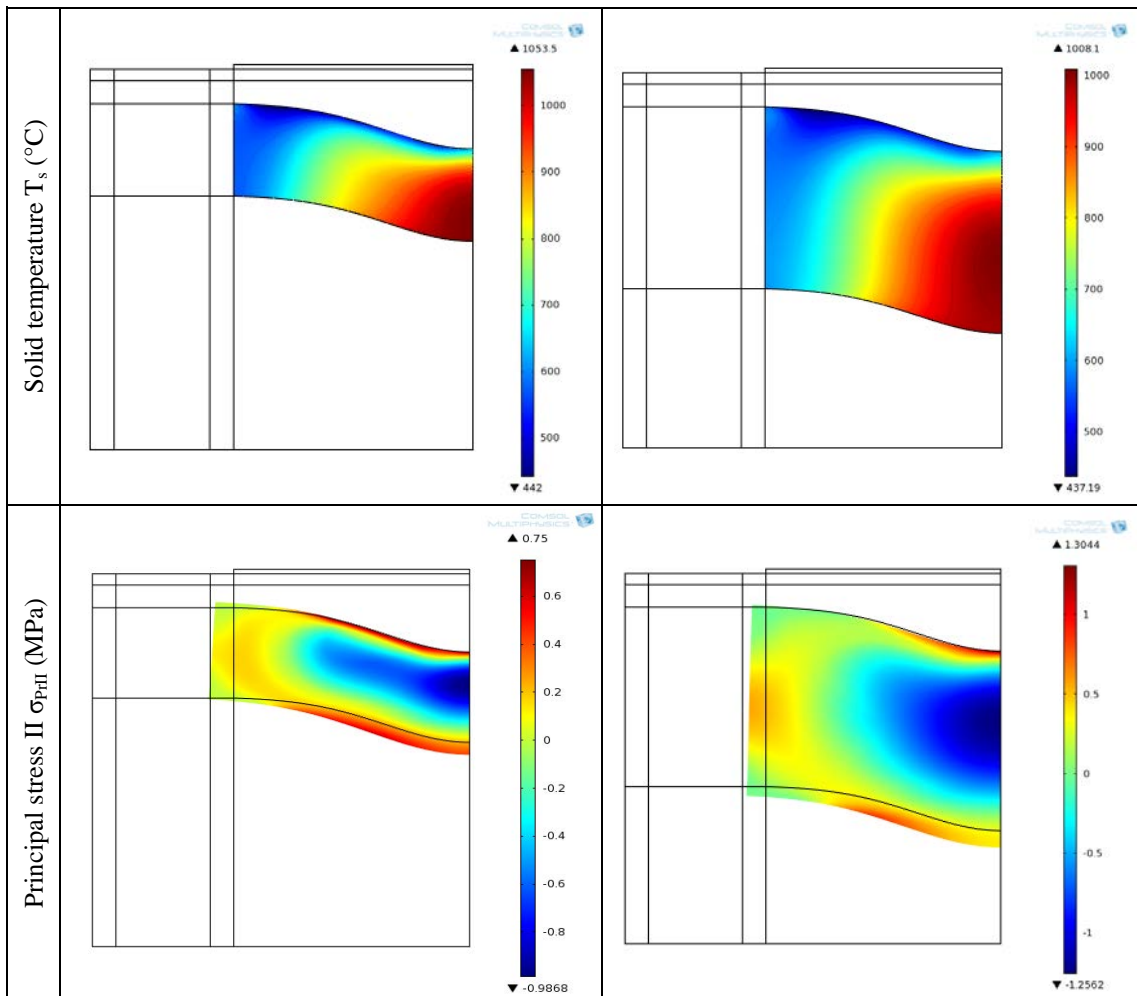


Figure 5.3: Temperature distribution and material stresses inside the absorber $\Phi=2\text{mm}$ (left), $\Phi=4\text{mm}$ (right)

The results shown in Figure 5.3 are both designs operating at atmospheric conditions.

In the second row of Figure 5.2 the pressure drop is presented. For both configurations a higher cavity depth D results in a lower pressure drop. The reasons for that are not obvious. The most likely reason is that path length of some fluid decreases because the thickness of the absorber at some points decreases with increasing cavity depth.

The third row of Figure 5.2 shows the maximal window temperature. As expected the higher cell diameter results in smaller window temperatures. However, the difference between the two different cell diameters is relatively small. It is worth mentioning that the minimal window temperature appears at same depth as the minimal material utilization. As far as the dependence of the window temperature of the cavity depth is concerned the same trend as for the cavity height H in the main study can be seen. If the cavity depth is decreased the window temperature increases because the increase in radiative heat transfer between the absorber surface and the window is bigger than the increase in convective cooling. On the other hand if

the cavity depth is increased too much the decrease in radiative heat transfer is lower than the decrease in convective cooling due to lower velocities.

5.1.2 Evaluation and decision

In order to evaluate the conflicting parameters in Figure 5.2 the same value of benefit analysis as in the main study analysis is done. Figure 5.4 shows the results for said analysis.

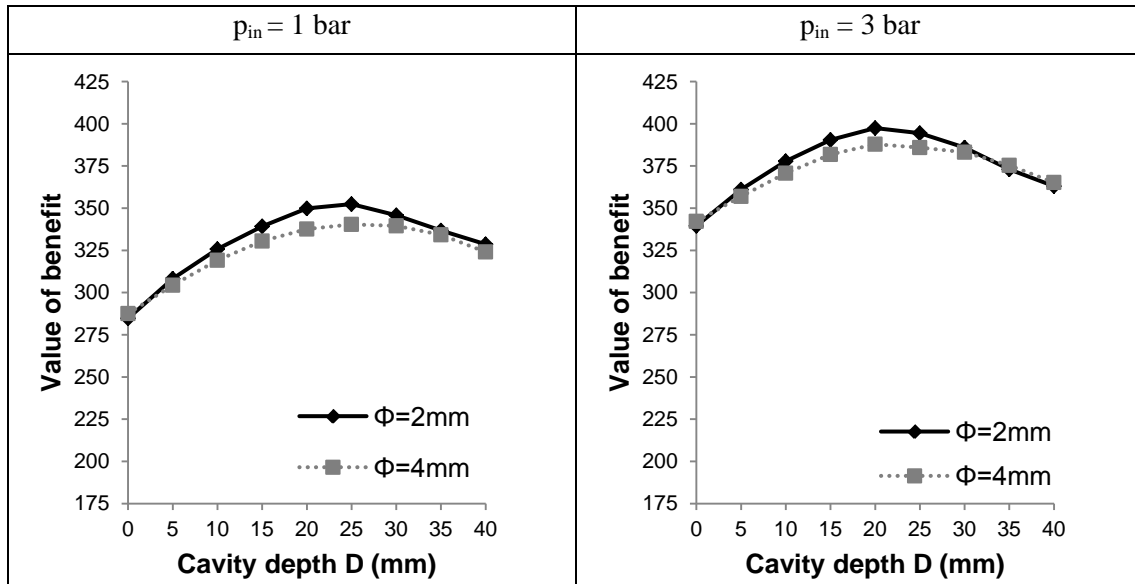


Figure 5.4: Value of benefit
pin = 1bar (left), pin = 3bar (right)

The trend for both SPU configurations is similar. In most cases the decrease in material utilization outweighs the increase of the window temperature.

For the atmospheric configuration and the pressurized configuration a cavity depth of 25 and 20 mm gives the highest value of benefit. Due to the fact that the pressurized configuration is generally preferable and due to simplicity reasons a cavity depth of 20 mm for both configurations is chosen.

Based on the main study and the previous final parameter study Table 5.1 summarizes the final design parameters.

Table 5.1: Final design parameters

Parameter	Configuration	
	pin = 1bar	pin = 3bar
Cavity height H (mm)	10	10
Cavity depth D (mm)	20	20
Absorber porosity ϵ (%)	95	95
Absorber cell diameter Φ (mm)	2	2

5.1.3 Results and discussion

Table 5.2 summarizes the main results for the chosen designs based on Table 5.1 for both SPU configurations.

Table 5.2: Main results

Results	Configuration	
	$p_{in} = 1\text{bar}$	$p_{in} = 3\text{bar}$
Outlet temperature T_{out} (°C)	722.54	822.17
Mass flow difference $\Delta\dot{m}$ (%)	< 1	< 1
Thermal efficiency η_{th} (%)	83.32	84.83
Pressure drop Δp (%)	8.39	1.16
Maximal window temperature $T_{w,max}$ (°C)	859.17	872.74
Maximal material utilization window $u_{w,max}$ (%)		
Decoupled	11.47	55.86
Coupled	309.02	392.89
Maximal absorber temperature $T_{abs,max}$ (°C)	1053.50	1120.20
Maximal material utilization absorber $u_{abs,max}$ (%)		
Ceramics absorber	71.3	70.4
Metal absorber	435.6	428.3
Maximal tube temperature T_{tube} (°C)	561.97	659.08

In Table 5.2 it can be seen that the thermal efficiency for the pressurized configuration is higher than for the atmospheric configuration despite the fact that the window temperature for the pressurized configuration is higher than in the atmospheric configuration. However, it has to be considered that the mass flow in both configurations is subjected to a numerical error of ± 1 percent from inlet to outlet. Moreover, the mass averaging technique used to calculate the equivalent outlet temperature according to equation 4.92 is subject to inaccuracies as well. Considering these two inaccuracies it is not obvious which configuration gives the best thermal efficiency. However, it can be said that the difference in thermal efficiency between the two configurations is relatively small.

The pressure drop on the other hand is quite different for the two configurations. It can be concluded with high certainty that from a pressure drop point of view the pressurized configuration is preferable.

As far as the window temperature is concerned the atmospheric configuration has a slight advantage compared to the pressurized configuration. Nevertheless, the difference is not as high as expected considering that the difference in inlet temperature is 100°C. The material utilization for both the atmospheric and pressurized configurations is within acceptable limits. However, it has to be mentioned that it is very important to design the window mounting in a way that the tubes and the window are can move radially more or less independent. This is important because the thermal expansion of the steel tubes is about 30 times higher than the one of silica glass.

From an absorber material utilization point of view the two configurations are almost equivalent. However, it can clearly be seen that a ceramic absorber is able to withstand the stresses whereas a metallic absorber is not even though the maximal temperature is below the

maximal operating temperature for both materials. The main reason for the poor performance of the metal receiver is due to the fact that its tensile strength decreases quite rapidly with increased temperatures as well as its higher thermal expansion factor.

And finally, the maximal temperatures in the metallic tubes of the receiver are similar for both configurations as well. Furthermore, they are lower than expected.

5.2 Verification

In order to verify the COMSOL model the chosen receiver design is modeled in the computational fluid dynamics program ANSYS FLUENT.

5.2.1 Modeling

The fluid flow model is based on the Reynolds-Averaged Navier-Stokes (RANS) equations. For the fluid flow within the absorber an additional source term is added to the momentum equation to account for the porous medium. This source term is the same term added to the momentum equation used in the COMSOL model as described in equation 4.100.

In order to close the RANS equations the Reynolds stresses representing the effects of turbulence need to be modeled. Here, the effects of turbulence are modeled using the Boussinesq hypothesis and the standard k- ϵ model [97]. The k- ϵ model is based on following transport equations for the turbulence kinetic energy k and the dissipation rate ϵ .

$$\begin{aligned} \frac{\partial}{\partial t}(\rho k) + \frac{\partial}{\partial x_i}(\rho k u_i) \\ = \frac{\partial}{\partial x_j} \left[\left(\mu + \frac{\mu_t}{\sigma_k} \right) \frac{\partial k}{\partial x_j} \right] + G_k + G_b - \rho \epsilon - Y_M + S_k \end{aligned} \quad \left(\frac{N}{m^3} \right) \quad (5.1)$$

$$\begin{aligned} \frac{\partial}{\partial t}(\rho \epsilon) + \frac{\partial}{\partial x_i}(\rho \epsilon u_i) \\ = \frac{\partial}{\partial x_j} \left[\left(\mu + \frac{\mu_t}{\sigma_\epsilon} \right) \frac{\partial \epsilon}{\partial x_j} \right] + C_{1\epsilon} \frac{\epsilon}{k} (G_k + C_{3\epsilon} G_b) \\ - C_{2\epsilon} \rho \frac{\epsilon^2}{k} + S_\epsilon \end{aligned} \quad \left(\frac{N}{m^3} \right) \quad (5.2)$$

“Here G_k denotes the generation of turbulence kinetic energy due to mean velocity gradients, G_b the generation of turbulence kinetic energy due to buoyancy, Y_M the contribution of the fluctuating dilatation in compressible turbulence to the overall dissipation rate, $C_{1\epsilon}$, $C_{2\epsilon}$, and $C_{3\epsilon}$ are constant. σ_k and σ_ϵ are the turbulent Prandtl numbers for k and ϵ respectively. S_k and S_ϵ are user-defined source terms.” [97]

The heat transfer in fluid is based on the energy equation

$$\begin{aligned} \frac{\partial}{\partial t}(\rho e) + \vec{\nabla} \cdot (\vec{u}(\rho e + p)) \\ = \vec{\nabla} \cdot (k_{eff} \cdot \vec{\nabla} T + \underline{\underline{\tau}}_{eff} \cdot \vec{u}) + S_h \end{aligned} \quad \left(\frac{W}{m^3} \right) \quad (5.3)$$

where ρ is the fluid density, c_p is specific heat capacity at constant pressure, e the specific total energy, p the pressure, k_{eff} the thermal effective conductivity, $\underline{\underline{\tau}}_{eff}$ the deviatoric stress tensor, \vec{u} the velocity, and S_h a volumetric heat source.

The effective conductivity is defined as

$$k_{eff} = k + k_t \quad \left(\frac{W}{mK} \right) \quad (5.4)$$

where k is the laminar conductivity and k_t the turbulent conductivity defined according to the turbulence model used. For the standard k - ϵ model the turbulent thermal conductivity is defined as

$$k_t = \frac{c_p \mu_t}{Pr_t} \quad \left(\frac{W}{mK} \right) \quad (5.5)$$

where μ_t is the turbulent dynamic viscosity and Pr_t the turbulent Prandtl number.

The specific total energy is calculated as

$$e = h - \frac{p}{\rho} + \frac{u^2}{2} \quad \left(\frac{J}{kg} \right) \quad (5.6)$$

where h is sensible enthalpy h .

In the fluid flow model a couple of material properties had to be specified. The following two models are based on FLUENT theory guide [97]. The dynamic viscosity μ of the fluid is calculates according to Sutherland's law

$$\mu = \mu_{ref} \cdot \left(\frac{T}{T_0} \right)^{3/2} \frac{T_{ref} + S}{T + S} \quad (Pa \cdot s) \quad (5.7)$$

where μ_{ref} is the reference viscosity, T the static temperature, T_{ref} the reference temperature, S the Sutherland constant. Furthermore, the thermal conductivity k of the fluid is calculates the kinetic theory law

$$k = \frac{15}{4} \frac{R}{M_w} \mu \left[\frac{4}{15} \frac{c_p M_w}{R} + \frac{1}{3} \right] \quad \left(\frac{W}{mK} \right) \quad (5.8)$$

where R is the universal gas constant, M_w the molecular weight, dynamic viscosity μ , and c_p the specific heat capacity at constant pressure.

The heat transfer in the solid regions is based on the following energy equation

$$\begin{aligned} \frac{\partial}{\partial t} (\rho h) + \vec{\nabla} \cdot (\vec{u} \rho h) \\ = \vec{\nabla} \cdot (k \cdot \vec{\nabla} T) + S_h \end{aligned} \quad \left(\frac{W}{m^3} \right) \quad (5.9)$$

where ρ is the solid density, h the sensible enthalpy, \vec{u} the velocity of the solid, k the thermal conductivity, and S_h a volumetric heat source. The sensible enthalpy is defined as

$$h = \int_{T_{ref}}^T c_p dT \quad \left(\frac{J}{kg} \right) \quad (5.10)$$

where T_{ref} and T are the and actual temperature, and c_p the specific heat capacity at constant pressure.

Unfortunately, FLUENT does not support the non-thermal equilibrium calculation within porous media either. Therefore, the solid of the absorber is modeled using a user-defined-scalar (UDS) and user-defined-functions (UDF). The code can be found in Appendix B: User defined function in FLUENT. The coupling between the solid and fluid is done the same way as in the COMSOL model using a volumetric heat source in order to account for the convective heat transfer according to equation 4.103. Inside the solid of the absorber the thermal conductivity accounts for the effective thermal conductivity and the radiative thermal conductivity according to equation 4.106.

The absorption of solar radiation within the window is again modeled as a spatially constant heat source according to equation 4.53. In the remaining solids i.e. the flow channel tubes the volumetric heat source is zero.

Since the radiation between the absorber surface and the window is important is taken into account as well. The radiative heat transfer is calculated using the discrete ordinate method (DOM) that is based on the radiative transfer equation (RTE) specified in equation 4.16 and equation 4.18. On the front surface the absorber the emission term of the RTE is modified so that the emission is based on the solid temperature instead of the fluid temperature (see Appendix B: User defined function in FLUENT, DEFINE_DOM_SOURCE). Due to the fact that the solid of the absorber does not exist physically in the model the absorption of thermal radiation on the absorber front surface has to be accounted for specially. The most practical way is to set the absorption of the fluid at the absorber surface to the absorption value of the solid. Thus the emitted thermal radiation of the solid is absorbed by the fluid in the same way as it would be by the solid. This approach does not reflect reality but is the closest that can be done in FLUENT. Outside the absorber the fluid is again considered as a radiative non-participation gas.

The main boundary conditions for this model are the same as for the COMSOL model as shown in Table 4.15. Additionally, turbulence parameters need to be specified at the inlet.

As in the COMSOL model the window does not participates in thermal radiation process. The boundary between the fluid and the window is considered to be opaque. The thermal radiation passing through the window is considered in the same way as in the COMSOL model. That means that the irradiation at the boundary is reduced by the transmitted amount as described in equation 4.110 (see Appendix B: User defined function in FLUENT, DEFINE_DOM_FLUX). Furthermore, on the outside of the window radiation to the ambient and natural convective cooling is considered according to equation 4.112.

5.2.2 Meshing

The meshing for the FLUENT model is done in ANSYS ICEM. Figure 5.5 shows the surface mesh for one quarter of the absorber. As said before the reason to model the receiver in three dimensions is that in a future analyses the whole receiver including inflow and outflow from and to adjacent components has to be analyzed. The surface mesh consists of quadrangular elements and the volume mesh of hexahedral elements.

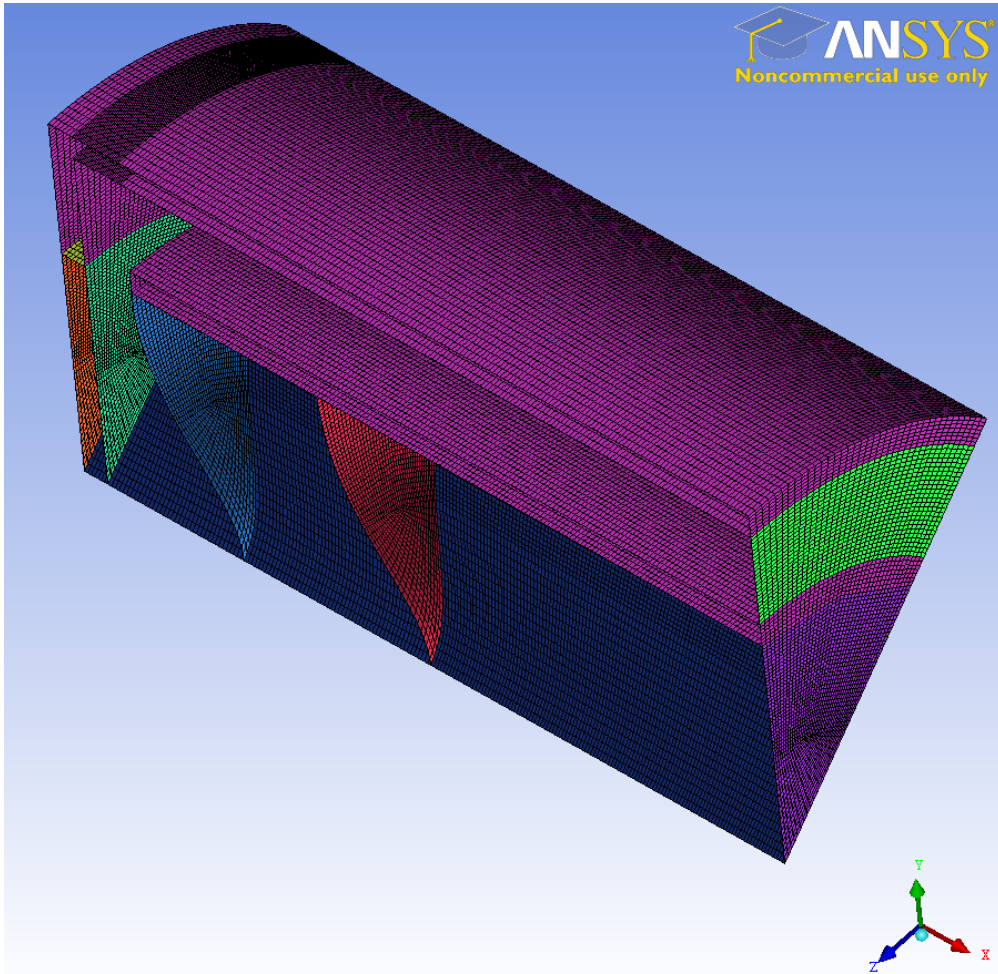


Figure 5.5: Mesh in ANSYS ICEM

Figure 5.6 shows the overall mesh quality for the above shown mesh. Since the geometry is relatively simple the worst element quality is 0.6. Moreover, almost 90 percent of the elements have a quality above 0.9.

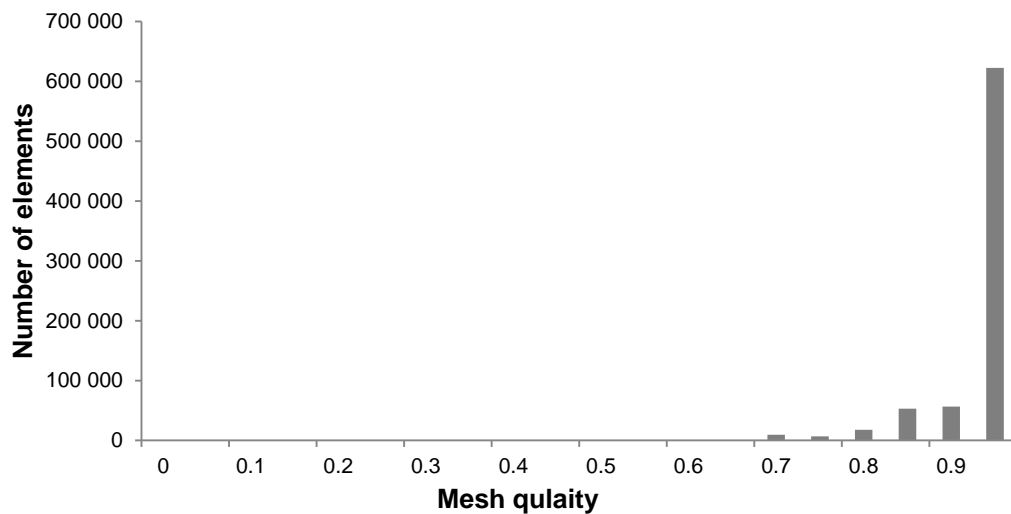


Figure 5.6: Mesh quality

5.2.3 Results and discussion

The main results of the computational fluid dynamics simulation in ANSYS FLUENT are summarized in Table 5.3.

Table 5.3: Main FLUENT results

Results	Configuration	
	$p_{in} = 1\text{bar}$	$p_{in} = 3\text{bar}$
Outlet temperature T_{out} (°C)	726.72	820.61
Mass flow difference $\Delta \dot{m}$ (%)	< 0.006	< 0.0008
Thermal efficiency η_{th} (%)	84.43	84.41
Pressure drop Δp (%)	6.09	0.83
Maximal window temperature $T_{w,max}$ (°C)	898.64	915.85
Maximal material utilization window $u_{w,max}$ (%)		
Decoupled	-	-
Coupled	-	-
Maximal absorber temperature $T_{abs,max}$ (°C)	1060.55	1141.36
Maximal material utilization absorber $u_{abs,max}$ (%)		
Ceramics absorber	-	-
Metal absorber	-	-
Maximal tube temperature T_{tube} (°C)	569.55	664.88

Since FLUENT is a pure CFD program solid mechanics calculations are not possible. Thus the results do neither include material utilization of the window nor the absorber. However, the material temperature within the solid of the absorber was modeled. The difference of the material temperature for both configurations is less than 2 percent.

In Table 5.3 in the first row the fluid outlet temperature is presented. The difference between the FLUENT and COMSOL calculations presented in Table 5.2 are within 5°C. Fortunately, the numerical error concerning the mass flow is negligible. Therefore, the calculated thermal efficiencies are more trustworthy especially because the efficiency of the pressurized configuration is slightly smaller than the one of the atmospheric configuration. As described at the beginning of section 5.2 the only losses to the ambient are losses at the window. Thus these efficiencies makes sense because the window temperature of the pressurized configuration is higher than the atmospheric one.

As far as the pressure drop is concerned the same trend as in the COMSOL model can be seen. It is obvious that the pressurized configuration is preferable. However, for both configurations the difference to the COMSOL model is almost 30 percent.

From a window temperature point of view the simulation shows the same trend as the COMSOL model. Apparently, the window temperature for the pressurized configuration is only about 15°C higher than of the atmospheric one despite the fact the inlet temperature is 100°C higher. Nevertheless, the general temperature level is about 40°C higher the in the previous analysis. Unfortunately, the reason for this deviation cannot be explained.

And finally, in the last row of Table 5.3 the maximal temperatures of the metallic tubes are presented. Again, the temperatures are relatively low and the difference to the COMSOL model is almost negligible.

5.2.4 Conclusion

Depending on the considered parameter the results of the two analyses agree more or less well. Regarding the fluid outlet temperature, the thermal efficiency, and the tube temperatures the agreement is relatively good. As far as the pressure drop and the window temperature are concerned the deviation is quite significant. Nevertheless, the FLUENT simulation shows that the general trends in the COMSOL analysis are viable. Moreover, both analyses are based on numerous simplifications and assumption. Thus the results of both analyses need to be experimentally validated.

5.3 Prototype

Based on the results of the design analysis and the verification a prototype is design. First of all, the materials for the key components need to be determined.

5.3.1 Materials

One of the key components is undoubtedly the glass window. Basically, three different materials that can withstand the high expected temperatures are available. Their temperature stability and properties have already been presented in Table 4.3 and Table 4.5 respectively. Both the design analysis and the verification showed that glass temperatures below the maximal continuous working temperature of all three glasses can be expected. The decisions can therefore be based on availability and costs of the material. This has to be done when the prototype is actually built. As far as the sealing of the glass against the window is concerned the most suitable material are high temperature gaskets.

The second key component is the absorber. As shown in Table 5.2 metallic absorbers are not suitable for this application because of the high material utilization. Ceramic absorbers on the other hand are able to withstand the high solar fluxes and the thermal stresses are below permissible limits. As discussed earlier in section 4.1.1 silicon carbide is a commonly used material in solar receivers. All analyses were conducted using this material and the results are promising. Therefore, silicon carbide should be used as an absorber material for this prototype.

The last key components are the metallic tubes building the body of the receiver. Both the design analysis and the verification showed that the temperature levels inside the tubes do not exceed 700°C. Numerous austenitic steel alloys are suitable for these temperatures. Table 5.4 show suitable materials.

Table 5.4: Austenitic steel alloys

Material	Reference
INCONELL Alloy 718	Bibus Metals [98]
INCOLOY Alloy 800H/HT	Bibus Metals [99]
INCOLOY Alloy 825	Bibus Metals [100]
WASPALLOY	Special Metals [101]
HASTELLOX Alloy	Haynes [102]
Outokumpu 252 MA	Outokumpu [62]

All above mentioned materials are able to withstand the expected temperature levels. However, there are differences in the machinability and weldability. For this prototype Outokumpu's 252 MA is chosen. This is based on its relatively good machinability and its very good weldability. Furthermore, KTH has experience with this material.

5.3.2 Drawings

Based on the design analysis drawings for the prototype are issued. The assembly of the prototype can be seen in Appendix C: Receiver assembly.

5.3.3 Description

In the prototype design a couple of components need to be described. The most important thing to mention is that the prototype is designed in a very modular way allowing the change and modification of most parts with little effort.

The first component of interest is the secondary CPC which is optional. The first test will be done without a secondary CPC. However, the prototype is designed in a way that a secondary CPC can easily be added.

As mentioned in the objectives of the preliminary study in section 3.2 the prototype needs to be designed in a way that different absorbers and configurations can be tested. Therefore, the inner tube that supports the absorber can easily be removed in order to change the absorber. Furthermore, the axial position of the absorber in relation to the glass window can easily be adjusted by distance plates.

In order to test different flow channel shapes the front part of the other flow channel is changeable without big efforts.

Finally, to ensure a uniform fluid inflow a mixing box is added. The air enters the box from a single inflow tube. From there it passes through six holes around the perimeter into the outer tube of the receiver.

6. CONCLUSIONS

This chapter summarizes and presents the main results are summarized. Furthermore, an analysis and interpretation of the results as well as remarks are presented. Finally, possible future work is presented.

6.1 Summary of results

Four basic solar receiver types were identified in section 2: tubular, volumetric, heat pipe and solid particle receiver. Of these, the solid particle receiver type was deemed unsuitable for integration into the SPU. The remaining tubular, volumetric and heat pipe designs were evaluated in section 3. The heat transfer analysis revealed that tubular designs were unable to operate at the high solar irradiance levels that are expected in the solar polygeneration unit. In theory heat pipe receivers are able to withstand these high irradiance levels. However, a thorough review of the literature revealed that for practical applications the heat pipe receiver irradiance limits are well below what is theoretically expected. Volumetric receivers were found to be the only type capable of withstanding the high irradiance levels expected. In addition, as one of the configurations within the solar polygeneration unit is to be pressurized the most suitable receiver type was found to be the closed volumetric receiver.

Considering closed volumetric receivers, the preliminary study showed that the metallic and ceramic foam and metallic and ceramic honeycomb structures were the most suitable absorbers. Further review of the literature revealed identified that honeycomb structures have a problem concerning flow stability which can lead to local hot spots and overheating of the absorber. Therefore these were eliminated from consideration and additional analyses of closed volumetric receivers were conducted with metallic and ceramic foam absorbers.

Major design challenges were identified by a situation analysis. Using a multi-objective optimization tool and a relatively simple numerical heat transfer model a set of Pareto-optimal solutions was obtained showing the tradeoff between pressure drop and material temperatures especially the window temperature. This demonstrated already that from a pressure drop point of view the pressurized configuration is clearly favorable.

A parameter study was conducted based on the situation analysis to improve specific aspects of the initial design. This incorporated a value of benefit analysis of the different designs with the objective of selecting a design which best satisfied the objectives discussed in section 4.2. The study showed that the parameters with the most positive impact on the objectives were the absorber properties and the absorber shape. Variation in flow channel shape also demonstrated positive effects on the objectives although not as significant. External window cooling with ambient air improved the window temperature quite significantly without decreasing the thermal efficiency too much. Due decreases of the value of benefit or insignificant improvements, internal window cooling, external window cooling with receiver inlet air and modification of the window shape are not recommended.

In a final detailed study the chosen design was analyzed and the model verified using a more complex computational fluid dynamics software. While the results of the two models had some differences, overall the main trends and results were found to be valid.

Overall, it was found that by applying the suggested modifications a receiver could be designed that was able to operate under the specific expected conditions of the solar polygeneration unit. For both the atmospheric and pressurized configurations material temperatures and stresses are expected to be below the permissible limits. Mechanically decoupling of both the window and the absorber from their surrounding parts was found to be very important; enabling them to expand more or less independently with changing temperatures. Ceramic was found to be the only feasible absorber material. Although the maximum material temperatures were below the maximum operating temperature, thermal stresses inside the material were much higher than the permissible stresses. The pressurized configuration was found to be much more preferable than the atmospheric configuration. Depending on the tool used, the pressure drop for the pressurized design was shown to be between 0.83 and 1.15 percent whereas for the atmospheric design it was found to be between 6.09 and 8.39 percent. The achieved thermal efficiencies were about 84 percent for both configurations.

6.2 Analysis and interpretation

One of the most important conclusions that can be drawn from this study concerns the operating pressure of closed volumetric receivers. Each analysis clearly showed that the pressurized configuration outperformed the atmospheric configuration assuming the same mass flow. This is based on two facts. First, the pressure drop within a foam absorber has a quadratic dependency on the velocity as shown in equation 2.1. Additionally, the velocity is proportional to the operating pressure. Thus the pressure drop is dependent on the operating pressure. Second, high velocities at low operating pressures lead to higher pressure losses due to the contraction of the flow channel before the window. This means that the higher the operating pressure the better. However, material stresses due to the pressure difference between the inside and outside of the window, limit the maximum operating pressure. Depending on the design of the glass window the maximum operating pressure is about 30 to 50 bar [26].

There are two reasons why ceramic materials are more suitable than metallic materials for solar receivers with high irradiance levels. First, the linear thermal expansion coefficient of metal is about four times higher than that of ceramic resulting in higher thermal stresses. Second, the strength of metals decreases rapidly with increased temperature whereas the strength of ceramics remains more or less constant. These properties highlight that ceramic materials are much more suitable than metallic materials for absorbers.

Absorber properties and shape had the most positive influence on the objectives of all investigated parameters. In particular, the absorber porosity had a strong influence on the radiation absorption within the absorber and thus the temperature of the solid. A higher porosity resulted in a more even distribution of absorption and decreased temperature differences and thus thermal stresses. Therefore, higher porosities were beneficial even though they resulted in a slightly higher pressure drop.

The absorber shape also influenced the objectives quite significantly. At the highest irradiation levels, a well-chosen absorber surface shape was found to increase the fluid flow velocity in the center of the absorber without significantly increasing the pressure drop. This increased heat transfer from the center of the absorber resulted in decreased material stresses. However, no generalized shape can be recommended and each design requires separate

analysis. This is mainly because a tradeoff was observed between the convective heat cooling of the window and the radiative heat transfer to the window by decreasing the distance between absorber and window surface.

It can be concluded, that when properly designed, volumetric solar receivers for small scale solar polygeneration units are feasible.

6.3 Remarks

This work was based on a couple of assumptions and simplifications. First of all, the irradiance and its distribution at the receiver front surface are subject to significant uncertainty. For more accurate results this has to be evaluated in more detail using ray tracing techniques.

The relatively high thermal efficiencies of the receiver might be explained by the relatively closed system view during this work. Only reflection losses of the impinging radiation, natural convection losses and radiation losses at the window front surface were considered. In order to gain more significant results concerning the thermal efficiency losses of the receiver body both to the ambient and adjacent parts need to be considered. However, even though the absolute efficiency might not be accurate the comparison between the different designs is still valid because the error for each design remains almost constant.

Most of the thermal and radiative properties of the receiver components have been considered constant regarding the temperature and/or the radiation spectrum. Especially, the consideration of the spectral dependence of the absorber extinction coefficient will improve these results. The conditions for the radiative conduction model inside the absorber were also not fulfilled.

6.4 Future work

A couple of challenges could be addresses for the continuation of this work. Firstly, the boundary conditions could be experimentally verified especially the irradiation and its distribution at the focal plane. Second, a more suitable heat transfer model accounting for the thermal radiation exchange in the absorber material could be applied to improve the results.

Aside from flow stability problems honeycomb structures were found to be promising absorber materials. Future work could include a more detailed analysis of these structures.

Before building the receiver to be tested in the solar polygeneration unit an analysis of the whole receiver could be beneficial. This should include in and outflow from and to adjacent components as well as heat transfer to and from adjacent components. Heat transfer due to radiation that is not focused onto the focal spot should also be accounted for. Subsequently, the final receiver design should be built and tested within the solar polygeneration unit to verify the results of this work.

The greatest challenge will be in considering the function of the receiver under non-steady state conditions. This work is not able to make any statements about the behavior of the receiver if the solar load and/or the inlet conditions to the receiver change. In this worst case scenario this could lead to local overheating and failure of receiver components. This reinforces the importance of conducting tests on the built system.

7. REFERENCES

- [1] Bass M., Van Styrland E.W., Williams D.R., Wolfe W.L., 1995: Handbook of Optics, Volume I: Fundamentals, techniques and design, second edition, McGraw-Hill Inc., New York, USA [et al.]
- [2] Solomon S., Qin D., Manning M., Chen Z., Marquis M., Averyt K.B., Tignor M. and Miller H.L. (eds.), 2007: Climate Change 2007: The Physical Science Basis, Cambridge University Press, New York, USA
- [3] IPCC, 2007: Climate Change 2007: Synthesis Report. Contribution of Working Groups I, II and III to the Fourth Assessment Report of the Intergovernmental Panel on Climate Change [Core Writing Team, Pachauri, R.K and Reisinger, A. (eds.)], IPCC, Geneva, Switzerland
- [4] UNFCCC, 2009: Copenhagen Accord. The Conference of the Parties to the United Nations Framework Convention on Climate Change (UNFCCC), document FCCC/CP/2009/11/Add.1, available at <http://unfccc.int/documentation/items/2643.php>, as accessed 30.08.2011
- [5] IEA, 2010: World Energy Outlook 2010: Executive Summary, available at http://www.worldenergyoutlook.com/docs/weo2010/WEO2010ES_English.pdf, as accessed 30.08.2011
- [6] Müller-Steinhagen H., Trieb Freng, Trieb Franz, 2004: Concentrating solar power - A review of the technology, in: ingenia, Royal Academy of Engineering, issue 18, pp. 43-50
- [7] Fernández-García A., Zarza E., Valenzuela L., Pérez M., 2010: Parabolic-trough solar collectors and their applications, Renewable and Sustainable Energy Reviews 14 (7), pp. 1695-1721
- [8] Pitz-Paal R., Dersch J., Milow B., 2005: European Concentrated Solar Thermal Road Mapping (ECOSTAR), DLR Project – EC contract SES6-CT-2003-50257
- [9] Sunpower Corporation, 2008: The Drivers of The Levelized Cost of electricity for Utility-Scale Photovoltaics, available at: http://fr.sunpowercorp.be/downloads/SunPower_levelized_cost_of_electricity.pdf, as accessed 01.09.2011
- [10] Gary J., 2011: CSP and the SunShot Initiative, United States Department of Energy (U.S. DOE), available at: www1.eere.energy.gov/solar/pdfs, as accessed 30.08.2011
- [11] Richter C., Teske S., Nebrera, J., 2009: Concentrating solar power global outlook 09 – why renewable energy is hot, Greenpeace International, SolarPACES and ESTELA
- [12] Trieb F., Schillings C., O'Sullivan M., Pregger T., Hoyer-Klick C., 2009: Global Potential of Concentrating Solar Power, SolarPACES Conference, 15-18 September 2009, Berlin, Germany
- [13] Bennett S., 2007: The Encyclopedia of Energy, Global Media, Delhi, India
- [14] SolarPACES, 2011: Technology Characterization Solar Parabolic Trough, available at: http://www.solarpaces.org/CSP_Technology/docs/solar_trough.pdf, as accessed 31.08.2011

- [15] Geyer M., Lüpfert E., Osuna R., Esteban A., Schiel W., Schweitzer A., Zarza E., Nava P., Langenkamp J., Mandelberg E., 2002: EUROTROUGH - Parabolic Trough Collector Developed for Cost Efficient Solar Power Generation, 11th Int. Symposium on Concentrating Solar Power and Chemical Energy Technologies, 4-6 September 2002, Zurich, Switzerland
- [16] Kennedy C.E., Price H., 2005: Progress in development of high-temperature solar selective coating, International Solar Energy Conference, 6-12 August 2005, Orlando, USA
- [17] Häberle A., Zahler C., Lerchenmüller H., Mertins M., Wittwer C., Trieb F., Dresch J., 2011: The Solarmundo line focussing Fresnel collector: Optical and thermal performance and cost calculations, available at: http://www.solarpaces.org/CSP_Technology/docs/solarpaces_fresnel_9_2002.pdf, as accessed 01.09.2011
- [18] DLR, 2007: WP 1: Review of CSP and Desalination Technology, available at http://www.dlr.de/tt/Portaldata/41/Resources/dokumente/institut/system/projects/aqua-csp/WP01_AQUA-CSP-Technologies-Final.pdf, as accessed 01.09.2011
- [19] SolarPACES, 2011a: Technology Characterization Solar Dish Systems, available at: http://www.solarpaces.org/CSP_Technology/docs/solar_dish.pdf, as accessed 31.08.2011
- [20] Pitz-Paal R., 2011: High temperature solar concentrators, Encyclopedia of life support systems (EOLSS), available at: www.eolss.net/ebooks/Sample%20Chapters/C08/E6-106-06-00.pdf, as accessed 02.09.2011
- [21] Lovegrove K., Burgess G., Pye J., 2011: A new 500 m² paraboloidal dish solar concentrator, *Solar Energy* 85 (4), pp. 620–626
- [22] SolarPACES, 2011b: Technology Characterization Solar Power Tower, available at: http://www.solarpaces.org/CSP_Technology/docs/solar_tower.pdf, as accessed 31.08.2011
- [23] SolarPACES, 2000: Catalog of Solar Heliostats, IEA-Solar Power and Chemical Energy Systems, Technical Report No. III - 1/00 2000
- [24] Haberfellner R., Nagel P., Becker M., Büchel A., von Massow H., 2002: *Systems Engineering: Methodik und Praxis*, 11. Auflage, Verlag Industrielle Organisation, Zürich, Switzerland, as cited in: Haberfellner R., 2009: *Projekt-Management auf der Basis des Systems Engineering*, Lecture Notes Project Management, Institute of General Management and Organization, Graz University of Technology
- [25] The Association of German Engineers, 1993: VDI-Richtlinie 2221 - Methodik zum Entwickeln und Konstruieren technischer Systeme und Produkte
- [26] Ávila-Marín A. L., 2011: Volumetric receivers in Solar Thermal Power Plants with Central Receiver System technology: A review, *Solar Energy* 85 (5), pp. 891-910
- [27] Stine W.B., Harrigan R.W., 1986: *Solar Energy Systems Design*, John Wiley and Sons Inc., Hoboken, USA
- [28] Reddy K.S., Sendhil Kumar N., 2009: An improved model for natural convection

- heat loss from modified cavity receiver of solar dish concentrator, *Solar Energy* 83 (10), pp. 1884-1892
- [29] Karni J., Kribus A., Doron P., Rubin R., Fiterman A., Sagie D., 1997: The DIAPR: A High-Pressure, High-Temperature Solar Receiver, *Journal of Solar Energy Engineering* 119 (1), pp. 74-78
 - [30] Romero M., Buck R., Pacheco J.E., 2002: An Update on Solar Central Receiver Systems, Projects, and Technologies, *Journal of Solar Energy Engineering* 124 (2), pp. 98-108
 - [31] European Commission (EC), 2002: SOLGATE Solar hybrid gas turbine electric power system – final publishable report, Publication office, European commission contract ENK5-CT-2000-00333
 - [32] Ctein, 2011: Ctein homepage, available at www.ctein.com, as accessed 06.09.2011
 - [33] SOLHYCO, 2011: SOLHYCO homepage, available at: www.solhyco.com, as accessed 06.09.2011
 - [34] SOLUGAS, 2011: SOLUGAS homepage, available at: www.solugas.com, as accessed 06.09.2011
 - [35] Incropera F.P., DeWitt D.P., Bergmann T.L., Lavine A.S., 2007: *Fundamentals of heat and mass transfer*, Wiley and Sons Inc., Hoboken, USA
 - [36] Becker M., Fend T., Hoffschmidt B., Pitz-Paal R., Reutter O., Stamatov V., Steven M., Trimis D., 2006: Theoretical and numerical investigation of flow stability in porous materials applied as volumetric solar receivers, *Solar Energy* 80 (10), pp. 1241-1248
 - [37] Kribus A., Ries H., Spirkel W., 1996: Inherent Limitations of Volumetric Solar Receivers, *Journal of Solar Energy Engineering* 118 (3), pp. 151-156
 - [38] Hoffschmidt, B., Pitz-Paal, R., Böhmer, M., Fend, T., Rietbrock, P., 1999: 200 kWth open volumetric air receiver (HiTRec) of DLR reached 1000°C average outlet temperature at PSA, *Journal of Physics IV France* 9 (PR3), pp. Pr3-551–Pr3-556
 - [39] Kribus A., Doron P., Rubin R., Reuven R., Taragan E., Duchan S., Karni J., 2001: Performance of the Directly-Irradiated Annular Pressurized Receiver (DIAPR) Operating at 20 Bar and 1,200°C, *Journal of Solar Energy Engineering* 123 (1), pp. 10-17
 - [40] Augsten, E., 2009: Make the desert bloom, *Sun and Wind Energy* 9, pp. 2052– 2055
 - [41] Buck R., Bräuning T., Denk T., Pfänder M., Schwarzbözl, P. Téllez F., 2002: Solar-Hybrid Gas Turbine-based Power Tower Systems (REFOS), *Journal of Solar Energy Engineering* 124 (1), pp. 2-9
 - [42] Hofmann A., Schenk C., Uhlig R., 2009: Optical quartz glass windows for high concentrated thermal power plants, *SolarPACES Conference*, 15-18 September 2009, Berlin, Germany
 - [43] Röger M., Pfänder M., Buck R., 2006: Multiple Air-Jet Window Cooling for High-Temperature Pressurized Volumetric Receivers: Testing, Evaluation, and Modeling, *Journal of Solar Energy Engineering* 128 (3), pp. 265-274

- [44] Petrasch J., Coray P., Meier A., Brack M., Häberling P., Wüllemmin D., Steinfeld A., 2007: A Novel 50 kW 11,000 suns High-Flux Solar Simulator Based on an Array of Xenon Arc Lamps, *Journal of Solar Energy Engineering*, 129 (4), pp. 405-411
- [45] NOYEchina 2011: E-mail communication with technical support, 20.08.2011
- [46] Rottman G., 2006: Measurement of Total and Spectral Solar Irradiance, *Space Science Reviews* 125 (1), pp. 39-51
- [47] The Association of German Engineers, 2006: VDI-Wärmeatlas, zehnte bearbeitete und erweiterte Auflage, Springer, Berlin, Germany [et al.]
- [48] Lauriat G. and Ghafir R., 2000: Forced Convective Heat Transfer in Porous Media, in: Vafai K., 2000: Handbook of porous media, Marcel Dekker Inc., New York, USA
- [49] Bienert W., 1980: The heat pipe and its application to solar receivers, *Electric Power Systems Research* 3 (1-2), pp. 111-123
- [50] Cui H., Wang Z., Guo Y., Xu W., Yuan X. 2006: Thermal performance analysis on unit tube for heat pipe receiver, *Solar Energy* 80 (7), pp. 875-882
- [51] Hall C.A., Glakpe E.K., Cannon J.N., 1999: Thermodynamic analysis of space solar dynamic heat receivers with cyclic phase change, *Journal of Solar Energy Engineering* 121 (3), pp. 133–144, as cited in: Cui H., Wang Z., Guo Y., Xu W., Yuan X. 2006: Thermal performance analysis on unit tube for heat pipe receiver, *Solar Energy* 80 (7), pp. 875-882
- [52] Adkins D., 1990: Design Considerations for Heat-Pipe Solar Receivers, *Journal of Solar Energy Engineering* 112 (3), pp. 169-176
- [53] Evans G., Houf W., Greif R., Crowe C., 1987: Gas-Particle Flow Within a High Temperature Solar Cavity Receiver Including Radiation Heat Transfer, *Journal of Solar Energy Engineering* 109 (2), pp. 134-142
- [54] Ho C.K., Khalsa S.S., Siegel N.P., 2009: Modeling on-sun tests of a prototype solid particle receiver for concentrating solar power processes and storage, *Energy Sustainability Conference*, 19-23 July 2009, San Francisco, USA
- [55] Kibum K., Siegel N., Kolb G., Rangaswamy V., Moujaes S.F., 2009: A study of solid particle flow characterization in solar particle receiver, *Solar Energy* 83 (10), 1784-1793
- [56] Siegel N., 2008: 2008 Solar Annual Review Meeting, Session: CSP Advanced Systems, Company or Organization: Sandia National Laboratories, Funding Opportunity: Thermochemical Hydrogen Project, United States Department of Energy (U.S. DOE), available at: www1.eere.energy.gov/solar/review_meeting/pdfs/prm2008_siegel_sandia.pdf, as accessed 14.09.2011
- [57] Giuliano S., Buck R., Eguiguren S., 2011: Analysis of Solar-Thermal Power Plants With Thermal Energy Storage and Solar-Hybrid Operation Strategy, *Journal of Solar Energy Engineering* 133 (3), pp. 031007-1-031007-7
- [58] Tan T., Chen Y., Chen Z., Siegel N., Kolb G., 2009: Wind effect on the performance of solid particle solar receivers with and without the protection of an aerowindow, *Solar Energy* 83 (10), pp. 1815-1827

- [59] Chen H., Chen Y., Hsieh H.-T., Siegel N., 2007: Computational Fluid Dynamics Modeling of Gas-Particle Flow Within a Solid-Particle Solar Receiver, *Journal of Solar Energy Engineering* 129 (2), pp. 160-170
- [60] Wohinz J.W., Plankenauer E., Premm G., 2010: Creativity Techniques, English and German Edition, Lecture Notes Creativity Techniques, Institute of Industrial Management and Innovation Research, Graz University of Technology
- [61] Ritchey T., 1998: Fritz Zwicky, Morphologie and Policy Analysis, Defence Research Establishment, Swedish Defence Research Agency, available at: www.foi.se/ma/morphology.pdf, as accessed 19.09.2011
- [62] Outokumpu, 2011: High Temperature Austenitic Stainless Steel data sheet, available at: www.outokumpu.com/20259.epibrw, as accessed 20.09.2011
- [63] Lacroix M., Nguyen P., Schweich D., Huu C.P., Savin-Poncet S., Eduard D., 2007: Pressure drop measurements and modeling on SiC foams, *Chemical Engineering Science* 62 (12), pp. 3259-3267
- [64] Xu C., Song Z., Chen L., Zhen Y., 2011: Numerical investigation on porous media heat transfer in a solar tower receiver, *Renewable Energy* 36 (5), pp. 1138-1144
- [65] Alazmi B., Vafai K., 2000: Analysis of Variants Within the Porous Media Transport Models, *Journal of Heat Transfer* 122 (2), pp. 300-326
- [66] Hwang, G. J., Wu, C. C., and Chao, C. H., 1995: Investigation of Non-Darcian Forced Convection in an Asymmetrically Heated Sintered Porous Channel, *Journal Heat Transfer* 117 (3), pp. 725–732, as cited in: Alazmi B., Vafai K., 2000: Analysis of Variants Within the Porous Media Transport Models, *Journal of Heat Transfer* 122 (2), pp. 300-326
- [67] Dixon, A. G., and Cresswell, D. L., 1979: Theoretical Prediction of Effective Heat Transfer Parameters in Packed Beds, *AIChE Journal* 25 (4), pp. 663–676, as cited in: Alazmi B., Vafai K., 2000: Analysis of Variants Within the Porous Media Transport Models, *Journal of Heat Transfer* 122 (2), pp. 300-326
- [68] Achenbach E., 1995: Heat and flow characteristics of packed beds, *Experimental Thermal and Fluid Science* 10 (1), pp. 17-27
- [69] Fend T., Hoffschmidt B., Pitz-Paal R., Reutter O., Rietbrock P., 2004: Porous materials as open volumetric solar receivers: Experimental determination of thermophysical and heat transfer properties, *Energy* 29 (5) pp. 823-833
- [70] Chinajintai, 2011: Chinajintai homepage, available at: www.ceramic-honeycombs.com, as accessed 22.09.2011
- [71] Bai F., 2010: One dimensional thermal analysis of silicon carbide ceramic foam used for solar air receiver, *International Journal of Thermal Sciences* 49 (12), pp. 2400-2404
- [72] Asako Y., Nakamura H., Faghri M., 1988: Developing laminar flow and heat transfer in the entrance region of regular polygonal ducts, *International Journal of Heat and Mass Transfer* 31 (12), pp. 2590-2593
- [73] Fend T., Pitz-Paal R., Reutter O., Bauer J., Hoffschmidt B., 2004: Two novel high-porosity materials as volumetric receivers for concentrated solar radiation, *Solar*

- [74] Howell J.R., 2000: Radiative Transfer in Porous Media, in: Vafai K., 2000: Handbook of porous media, Marcel Dekker Inc., New York, USA
- [75] Kaviany M., 1995: Principles of heat transfer in porous media, Springer, New York, USA
- [76] Hsu P.F. and Howell J.R., 1992: Measurements of thermal conductivity and optical properties of porous partial stabilized zirconia, *Experimental Heat Transfer* 5 (4), pp. 293–313, as cited in: Howell J.R., 2000: Radiative Transfer in Porous Media, in: Vafai K., 2000: Handbook of porous media, Marcel Dekker Inc., New York, USA
- [77] Hendricks T.J. and Howell J.R., 1996: Absorption Scattering Coefficients and Scattering Phase Functions in Reticulated Porous Ceramics, *Journal of Heat Transfer*, 118 (1), pp. 79-87
- [78] Mital R., Gore J.P. and Viskanta R., 1996: Measurements of radiative properties of cellular ceramics at high temperatures, *Journal of Thermophysics and Heat Transfer*, 10 (1), pp. 33-38, as cited in: Howell J.R., 2000: Radiative Transfer in Porous Media, in: Vafai K., 2000: Handbook of porous media, Marcel Dekker Inc., New York, USA
- [79] Fu X., Viskanta R. and Gore J.P., 1997: A model for the volumetric radiation characteristics of cellular ceramics, *International Communications in Heat and Mass Transfer* 24 (8), pp. 1069-1082
- [80] Somiya S. and Inomata Y., 1991: Silicon Carbide Ceramics: Fundamental and solid reaction, Elsevier Applied Science, London, UK [et al.]
- [81] Fend T., Pitz-Paal R., Hoffschmidt B., Reutter O., 2005: Solar Radiation Conversion, in: Scheffler M. and Colombo B., 2005: Cellular Ceramics-Structure - Manufacturing, Properties and Applications, WILEY-VCH, Weinheim, Germany
- [82] Bach H. and Neuroth N., 1995: The Properties of Optical glass, Springer, Berlin, Germany
- [83] Bennet J.M., 1995: Polarization, in: Bass M., Van Styrland E.W., Williams D.R., Wolfe W.L., 1995: Handbook of Optics, Volume I: Fundamentals, techniques and design, second edition, McGraw-Hill Inc., New York, USA [et al.]
- [84] Philipp H.R., 1997: Silicon Dioxide (SiO₂) (Glass), in: Palik E.D., 1997: Handbook of Optical Constants of Solids, Academic Press, San Diego, USA
- [85] Kitamura R., Laurent P. and Jonasz M., 2007: Optical constants of silica glass from extreme ultraviolet to far infrared at near room temperature, *Applied Optics* 46 (33), pp. 8118-8133
- [86] Heraeus, 2011: Heraeus homepage, available at www.heraeus-quarzglas.de/en/quarzglas/opticalproperties/Optical_properties.aspx, as accessed 21.03.2011
- [87] Schott, 2011: Fused silica brochure, available at: www.schott.com/advanced_optics/english/download/schott_fused_silica_jan_2010_en_brochure.pdf, as accessed 21.03.2011
- [88] Röger M., Rickers C., Uhlig R., Neumann F., Polenky C., 2007: Infrared-reflective

- coating on fused silica for a solar high-temperature receiver, ASME Energy Sustainability Conference, 27-30 June 2007, Long Beach, USA
- [89] Tanaka H., Sawai S., Morimoto K., Hisano K., 2000: Evaluation of Hemispherical Total Emissivity for Thermal Radiation Calorimetry, *International Journal of Thermophysics* 21 (4), pp. 927-940
 - [90] Smith C.M.. 2006: Silica, Vitreous, Kirk-Othmer Encyclopedia of Chemical Technology, John Wiley and Sons Inc., Hoboken, USA
 - [91] Kienzler R. and Schröder R., 2009: Einführung in die Höhere Festigkeitslehre, Springer, Berlin and Heidelberg, Germany
 - [92] Ashby M.F., 2005: Cellular Solids – Scaling of Properties, in: Scheffler M. and Colombo B., 2005: Cellular Ceramics-Structure - Manufacturing, Properties and Applications, WILEY-VCH, Weinheim, Germany
 - [93] Gibson L.J. and Ashby M.F., 1997: Cellular solids : structure and properties, Cambridge University Press, Cambridge, UK
 - [94] Molyneaux A., Leyland G. and Favrat D. 2010: Environomic multi-objective optimisation of a district heating network considering centralized and decentralized heat pumps, *Energy* 35 (2), pp. 751-758
 - [95] Schott, 2011a: Pressed blanks brochure, available at: www.schott.com/advanced_optics/german/download/schott_pressed_blanks_may_2011_en.pdf, as accessed 21.06.2011
 - [96] Baehr H.D. and Kabelac S. 2009: Thermodynamik: Grundlagen und technische Anwendungen, Springer, Berlin, Germany [et al.]
 - [97] ANSYS, 2010: ANSYS FLUENT Theory Guide
 - [98] Bibus Metals, 2011: Bibus Metals homepage, available at: www.bibusmetals.ch/pdf/datasheets/Inconel%20718.pdf, as accessed: 03.03.2011
 - [99] Bibus Metals, 2011a: Bibus Metals homepage, INCOLOY 800H/HT data, sheet, available at: www.bibusmetals.ch/pdf/datasheets/Incoloy%20800H_800HT.pdf, as accessed: 03.03.2011
 - [100] Bibus Metals, 2011b: INCOLOY Alloy 825 data sheet, www.bibusmetals.ch/pdf/datasheets/Inconel%20825.pdf, access date 03.03.2011
 - [101] Special Metals, 2011: Waspaloy data sheet, www.specialmetals.com/documents/Waspaloy.pdf, access date: 03.03.2011
 - [102] Haynes International 2011: HASTELLOY X Alloy data sheet: www.haynesintl.com/pdf/h3009.pdf, access date: 03.03.2011

8. APPENDIXES

Appendix A: Numerical model in MATLAB

Appendix B: User defined functions in FLUENT

Appendix C: Receiver assembly

8.1 Appendix A: Numerical model in MATLAB

8.1.1 Receiver specifications

```

%-----RECEIVER SPECIFICATIONS-----%
%
%-----LIGHT SOURCE-----%
o = struct; % variable containing all specifications %

%-----LIGHT SOURCE-----%
o.light.flux=in.n*5.355*10^3; % [W] ... radiant power before win. %
% n = number of lamps %
o.light.focalspot.D=0.100; % [m] ... diameter of focal spot %
o.light.focalspot.A=pi/4*o.light.focalspot.D^2; % [m^2] ... area of focal spot %
o.light.irradiance.mean= % [W/m^2] ... mean irradiance %
    o.light.flux/o.light.focalspot.A;
o.light.irradiance.distribution=0.1; % [-] ... irradiance distribution fact. %
% delta=I0(r=R)/I0(r=0) %
o.light.irradiance.peak= % [W/m^2] ... peak irradiance %
    o.light.irradiance.mean*
    log(o.light.irradiance.distribution)/(exp(log(o.light.irradiance.distribution))-1);

%-----HEAT EXCHANGER-----%
%-----dimensions-----%
o.tube.inner.d=0.100; % [m] ... diameter inner tube %
o.tube.outer.d=0.150; % [m] ... diameter outer tube %
o.tube.inner.s=0.005; % [m] ... wall thickness inner tube %
o.tube.outer.s=0.005; % [m] ... wall thickness outer tube %
o.tube.inner.L=0.100; % [m] ... length heat exchanger %
o.tube.outer.L=0.100;
o.tube.inner.D=o.tube.inner.d+o.tube.inner.s; % [m] ... outer diameter inner tube %
o.tube.outer.D=o.tube.outer.d+o.tube.outer.s; % [m] ... outer diameter outer tube %
o.tube.inner.A=pi/4*o.tube.inner.d^2; % [m^2] ... area inner tube %
o.tube.outer.A= % [m^2] ... area outer tube %
    pi/4*(o.tube.outer.d^2-o.tube.inner.D^2);
o.tube.inner.Dh=o.tube.inner.d; % [m] ... hydraulic diam. inner tube %
o.tube.outer.Dh=4*o.tube.outer.A/(pi*o.tube.outer.D+pi*o.tube.inner.d); % [m] ... hydraulic diam. outer tube %

%-----thermal properties-----%
o.tube.inner.k=24; % [W/(m*K)] ... therm. conduct. %
o.tube.outer.k=22; % [W/(m*K)] ... therm. conduct. %

%-----fluid mechanics properties-----%
o.tube.inner.K=0.2*10^-3; % [m] ... absolute roughness %
o.tube.outer.K=0.2*10^-3; % [m] ... absolute roughness %

%-----ABSORBER-----%
%-----dimensions-----%
o.absorber.inner.d=0; % [m] ... inner diameter absorber %
o.absorber.inner.D=o.tube.inner.d; % [m] ... outer diameter absorber %
o.absorber.inner.R=o.absorber.inner.D/2; % [m] ... outer radius absorber %
o.absorber.inner.A=pi/4*o.absorber.inner.D^2; % [m^2] ... area absorber %

%-----thermal properties-----%

```

```

o.absorber.inner.porosity=Xspec(2);           % [-] ... porosity (0-1)           %
o.absorber.inner.phi=Xspec(3);               % [m] ... cell diameter           %
o.absorber.inner.dp=                         % [m] ... average particle diameter %
    (1.5/2.3)*o.absorber.inner.phi*(4/(3*pi)*
    (1-o.absorber.inner.porosity))^(1/2)/(1-(4/(3*pi)*(1-o.absorber.inner.porosity))^(1/2));
o.absorber.inner.conductivity=120;           % [W/(mK)] ... conductivity solid %
o.absorber.inner.keff=                       % [W/(mK)] ... eff. cond. solid   %
    o.absorber.inner.conductivity*(1-o.absorber.inner.porosity);
%----- optical properties ----- %
o.absorber.inner.emissivity=0.8;             % [-] ... emissivity (0-1)       %
o.absorber.inner.Kcoefficient=4.8;           % [-] ... coeff. for extinction coeff. %
o.absorber.inner.extinctioncoefficient=      % [1/m] ... extinction coefficient %
    o.absorber.inner.Kcoefficient/o.absorber.inner.phi*(1-o.absorber.inner.porosity);
%----- fluid mechanics properties ----- %
o.absorber.inner.E1=150;                     % [-] ... Ergun constant 1       %
o.absorber.inner.E2=1.75;                   % [-] ... Ergun constant 2       %
o.absorber.inner.permeability=              % [m^2] specific permeability     %
    (o.absorber.inner.dp^2/o.absorber.inner.E1)*
    (o.absorber.inner.porosity^3/((1-o.absorber.inner.porosity)^2));
o.absorber.inner.inertiacoefficient=        % [-] ... inertia coefficient     %
    o.absorber.inner.E2/(o.absorber.inner.E1^0.5*o.absorber.inner.porosity^1.5);
%----- dimensions continued ----- %
o.absorber.inner.absorption = 0.99;          % [-] ... absorption of radiation %
o.absorber.inner.L =                        % [m] ... minimal absorber length %
    -1/o.absorber.inner.extinctioncoefficient * log (1-o.absorber.inner.absorption);
o.absorber.inner.V=                         % [m^3] ... absorber volume      %
    o.absorber.inner.A*o.absorber.inner.L;
%----- finite volume method parameters ----- %
% [-] ... number of nodes incl. boundary CV inlet/outlet in axial direction %
o.absorber.inner.n=20;
o.absorber.inner.deltax=                    % [m] ... axial spatial resolution %
    o.absorber.inner.L/o.absorber.inner.n;
% [-] ... number of nodes incl. boundary CV inlet/outlet in radial direction %
o.absorber.inner.p=15;
o.absorber.inner.deltar=                   % [m] ... radial spatial resolution %
    o.absorber.inner.R/o.absorber.inner.p;
[o.absorber.inner.grid.R, o.absorber.inner.grid.X]= % meshgrid for plotting %
    meshgrid(0.5:1:o.absorber.inner.p-0.5, 0.5:1:o.absorber.inner.n-0.5);

%-----WINDOW----- %
%----- dimensions ----- %
o.window.D=0.100;                           % [m] ... diameter of glass window %
o.window.s=0.005;                           % [m]... thickness of glass window %
o.window.A=pi/4*o.window.D^2;               % [m^2] ... window area          %
%----- thermal properties ----- %
o.window.emissivity=0.8;                     % [-] ... emissivity (0-1)       %
o.window.emissivityIR=0.8;                  % [-] ... emissivity (0-1)       %
o.window.k=2;                               % [W/(m*K)] ... thermal conductivity %
%----- optical properties UV ----- %
o.window.absorptivity=0.013;                % [-] ... absorptivity (0-1)     %
o.window.reflectivity=0.136;                % [-] ... reflectivity (0-1)     %
o.window.transmissivity=0.851;              % [-] ... transmissivity (0-1)   %

```

```

%----- optical properties IR----- %
o.window. absorptivityIR=0.326;          % [-] ... absorptivity (0-1)      %
o.window. reflectivityIR=0.125;         % [-] ... reflectivity (0-1)       %
o.window. transmissivityIR=0.549;       % [-] ... transmissivity (0-1)     %
%----- finite volume method parameters ----- %
o.window.grid.R=0.5:1:o.absorber.inner.p-0.5; % grid for plotting                %

%-----CAVITY ----- %
%----- dimensions ----- %
o.cavity.L=Xspec(1);                    % [m] ... cavity height            %

%-----CHECKS ----- %
if (o.absorber.inner.n < 2)
    error('The inner absorber has to be divided in at least 3 CV in axial direction. n >= 3');
end

if (o.absorber.inner.p < 2)
    error('The inner absorber has to be divided in at least 3 CV in radial direction. p >= 3');
end

```

8.1.2 Numerical system solver

```

%----- %
%          SOLVING THE NUMERICAL SYSTEM          %
%----- %
function [Tw, Tabs, T, T4i exitflag] = calculate_temperatures (Tfsolve0, m, o, in, g, T, Tcomponents)
%----- constants ----- %
sigma=g.sigma;
alphasf= % specific surface area per unit volume %
    20.346*(1-o.absorber.inner.porosity)*o.absorber.inner.porosity^2/o.absorber.inner.dp;
K = o.absorber.inner.extinctioncoefficient; % extinction coefficient %

deltax=o.absorber.inner.deltax; % length of finite volume elements %
n=o.absorber.inner.n; % number of CV including boundary CV at inlet and outlet %

deltar=o.absorber.inner.deltar; % radius of finite volume elements %
p=o.absorber.inner.p; % number of CV including boundary CV at inlet and outlet %
R=o.absorber.inner.R;

% Options to display output %
options=optimset('Display','iter', 'MaxFunEvals', 8000, 'MaxIter', 4000);

% set names for solution vector indices %
c=1;
Ts_w = c; c=c+p;
%internal window temperatures
Ts11 = c; Ts00=Ts11-p-1; c=c+(n*p);
% internal solid temperatures
T2=c; c=c+1;
T3=c; c=c+1;
T4=c; c=c+1;
Tf11=c; Tf00=Tf11-p-1; c=c+n*p;
%internal fluid temperatures
T5=c; c=c+1;
T6=c;

% Call solver %

```

```

[Tfsolve,fval, exitflag] = fsolve(@nestedfun, Tfsolve0, options);
function y=nestedfun(x)
%heat exchanger: 1-2, 5-6 %
    [UA, cp_o, cp_i] = UA_HX (m, o, in, [T(1), x(T2), x(T3), x(T4), x(T5), x(T6)]);
    UA_HX_in_out=UA;
    cph=cp_i;      cpmx=cph;
    cpc=cp_o;      cpmin=cpc;

    Cr=cpmin/cpmx;
    NTU=UA_HX_in_out/(m*cpmin);
    epsilon_NTU=(1-exp((-NTU)*(1-Cr)))/(1-Cr*exp((-NTU)*(1-Cr)));
    Q_max=m*cpmin*(x(T5)-T(1));
    Q=epsilon_NTU*Q_max;

% UA values %
    Tcomponents.window=x(Ts_w);
    Tcomponents.absorber.inner(1)=x(Ts11);
    [h, hf, hv_i_temp] =
        UA_front (m, o, in, g, [T(1), x(T2), x(T3), x(T4), x(T5), x(T6)], Tcomponents);

% HTCs %
    hv_i = zeros(1, n);    %pre-allocation to increase speed
    for i=1:n
        for j=1:p
            hv_i(i,j) = UA_abs_i (m, o, in, g, x(Tf00+i*p+j));
        end
    end

% Radiative heat transfer %
    Rad_coeff=zeros(p,1);
    for j=1:p
        Fabs_glass = 1;
        Rad_coeff(j) =
            sigma / ( ((1-o.absorber.inner.emissivity)/(o.absorber.inner.emissivity*((j*deltar)^2-((j-1)*
            deltar)^2)*pi()) + 1/(((j*deltar)^2-((j-1)*deltar)^2)*pi()*Fabs_glass)
            + (1-o.window.emissivity)/(o.window.emissivity*((j*deltar)^2-((j-1)*deltar)^2)*pi() );
    end

% mean glass window temperature %
    Tw_mean = 0;
    for j=1:p
        Tw_mean =
            Tw_mean + x(Ts_w+(j-1)) * ((j*deltar)^2-((j-1)*deltar)^2)*pi() / o.absorber.inner.A;
    end

% SYSTEM OF NON-LINEAR EQUATIONS (requirement: y(x)=0 (y,x,0 = vectors))
i=1;
% SOLID phase
% (2) Ts_w window
    Q = Rad_coeff(0+1)*(x(Ts11))^4 -
        - o.window.emissivityIR/(1-o.window.reflectivityIR)*x(Ts_w)^4);
    Ew = ( Q/(deltar^2*pi()) +
        o.window.emissivityIR*sigma*x(Ts_w)^4 ) / (1-o.window.reflectivityIR);
    e=1;
    y(e) = get_irradiation_w(0,o)*deltar^2*pi()*o.window.absorptivity % Srcce
        - o.window.k*(2*pi()*deltar*o.window.s)*(x(Ts_w)-x(Ts_w+1))/deltar % Cd-
        - h*deltar^2*pi()*x(Ts_w)-x(T3) % Cv
        - sigma*o.window.emissivity*deltar^2*pi()*x(Ts_w)^4-g.Tamb^4 % Rad
        - hf*deltar^2*pi()*x(Ts_w)-g.Tamb % Cvf
        + Q - (deltar^2*pi()*Ew*o.window.transmissivityIR; % Rs

```

```

for j=1:(p-2)
    Q = Rad_coeff(j+1)*(x(Ts11+j))^4
        - o.window.emissivityIR/(1-o.window.reflectivityIR)*x(Ts_w+j)^4;
    Ew = ( Q/(((j+1)*deltar)^2-(j*deltar)^2)*pi()
        + o.window.emissivityIR*sigma*x(Ts_w+j)^4 ) / (1-o.window.reflectivityIR);
    e=e+1;
    y(e) = get_irradiation_w(j,o)*(((j+1)*deltar)^2-(j*deltar)^2)*pi()*o.window.absorptivity % Srce
        + o.window.k*(2*pi()*(j*deltar)*o.window.s)*(x(Ts_w+(j-1))-x(Ts_w+j))/deltar % Cdr+
        - o.window.k*(2*pi()*(j+1)*deltar)*o.window.s*(x(Ts11+j)-x(Ts11+(j+1)))/deltar % Cdr-
        - h*(((j+1)*deltar)^2-(j*deltar)^2)*pi()*(x(Ts_w+j)-x(T3)) % Cv
        - sigma*o.window.emissivity*(((j+1)*deltar)^2-(j*deltar)^2)*pi()*(x(Ts_w+j)^4- % Rad
            g.Tamb^4)
        - hf*(((j+1)*deltar)^2-(j*deltar)^2)*pi()*(x(Ts_w+j)-g.Tamb) % Cvf
        + Q - (((j+1)*deltar)^2-(j*deltar)^2)*pi()*Ew*o.window.transmissivityIR; % Rs
end

Q = Rad_coeff((p-1)+1)*(x(Ts11+(p-1)))^4
    - o.window.emissivityIR/(1-o.window.reflectivityIR)*x(Ts_w+(p-1))^4;
Ew = ( Q/(((p-1)+1)*deltar)^2-((p-1)*deltar)^2)*pi()
    + o.window.emissivityIR*sigma*x(Ts_w+(p-1))^4 ) / (1-o.window.reflectivityIR);
e=e+1;
y(e) = get_irradiation_w((p-1),o) % Srce
    (((p-1)+1)*deltar)^2-((p-1)*deltar)^2)*pi()*o.window.absorptivity
    + o.window.k* % Cdr+
        (2*pi()*((p-1)*deltar)*o.window.s)*(x(Ts_w+(p-1)-1)-x(Ts_w+(p-1)))/deltar
    - h*(((p-1)+1)*deltar)^2-((p-1)*deltar)^2)*pi()*(x(Ts_w+(p-1))-x(T3)) % Cv
    - sigma*o.window.emissivity*(((p-1)+1)*deltar)^2-((p-1)*deltar)^2)*pi()* % Rad
        (x(Ts_w+(p-1))^4-g.Tamb^4)
    - hf*(((p-1)+1)*deltar)^2-((p-1)*deltar)^2)*pi()*(x(Ts_w+(p-1))-g.Tamb) % Cvf
    + Q - (((p-1)+1)*deltar)^2-((p-1)*deltar)^2)*pi()*Ew*o.window.transmissivityIR; % Rs

% (3) inner absorber: CV inlet i=0
e=e+1;
y(e) = get_heat_source_2(0,0,o)*deltar^2*pi()*deltax % Srce
    - (o.absorber.inner.keff + 16*sigma/(3*K)*x(Ts11))^3)* % Cdr-
        (2*pi()*deltar*deltax)*(x(Ts11)-x(Ts11+1))/deltar
    - o.absorber.inner.keff*(deltar^2*pi()*(x(Ts11)-x(Ts11+1*p)))/deltax % Cdx-
    - hv_i(1,1)*(deltar^2*pi()*deltax*(x(Ts11)-x(Tf11))) % Cv
    - Rad_coeff(0+1)* % Rs
        (x(Ts11)^4 - o.window.emissivityIR/(1-o.window.reflectivityIR)*x(Ts_w)^4);

for j=1:(p-2)
    e=e+1;
    y(e) = get_heat_source_2(0,j,o)*(((j+1)*deltar)^2-(j*deltar)^2)*pi()*deltax % Srce
        + o.absorber.inner.keff*(2*pi()*(j*deltar)*deltax)*(x(Ts11+(j-1))-x(Ts11+j))/deltar % Cdr+
        - (o.absorber.inner.keff + 16*sigma/(3*K)*x(Ts11+j))^3)* % Cdr-
            (2*pi()*(j+1)*deltar)*deltax*(x(Ts11+j)-x(Ts11+(j+1)))/deltar
        - (o.absorber.inner.keff + 16*sigma/(3*K)*x(Ts11+j))^3)* % Cdx-
            (((j+1)*deltar)^2-(j*deltar)^2)*pi()*(x(Ts11+j)-x(Ts11+1*p+j))/deltar
        - hv_i(1,(j+1))*(((j+1)*deltar)^2-(j*deltar)^2)*pi()*deltax*(x(Ts11+j)-x(Tf11+j)) % Cv
        - Rad_coeff(j+1)* % Rs
            (x(Ts11+j)^4 - o.window.emissivityIR/(1-o.window.reflectivityIR)*x(Ts_w+j)^4);
end

e=e+1;
y(e) = get_heat_source_2(0,(p-1),o)*(((p-1)+1)*deltar)^2-((p-1)*deltar)^2)*pi()*deltax % Srce
    + (o.absorber.inner.keff + 16*sigma/(3*K)*x(Ts11+(p-1)))^3)* % Cdr+
        (2*pi()*((p-1)*deltar)*deltax)*(x(Ts11+(p-1)-1)-x(Ts11+(p-1)))/deltar
    - (o.absorber.inner.keff + 16*sigma/(3*K)*x(Ts11+(p-1)))^3)* % Cdx-
end

```

```

        (((p-1)+1)*deltar)^2-((p-1)*deltar)^2)*pi()*x(Ts11+(p-1))-x(Ts11+1*p+(p-1)))/deltax
    - hv_i(1,(p-1)+1)* % Cv
        (((p-1)+1)*deltar)^2-((p-1)*deltar)^2)*pi()*deltax*(x(Ts11+(p-1))-x(Tf11+(p-1)))
    - Rad_coeff((p-1)+1)* % Rs
        (x(Ts11+(p-1))^4 - o.window.emissivityIR/(1-o.window.reflectivityIR)*x(Ts_w+(p-1))^4);

j=1;
% (4) inner absorber: CV i
for i=1:(n-2)
    e=e+1;
    y(e) = get_heat_source_2(i,0,o)*deltar^2*pi()*deltax % Srce
        - (o.absorber.inner.keff + 16*sigma/(3*K)*x(Ts11+i*p)^3)* % Cdr-
            (2*pi()*deltar*deltax)*(x(Ts11+i*p)-x(Ts11+i*p+1))/deltar
        + (o.absorber.inner.keff + 16*sigma/(3*K)*x(Ts11+i*p)^3)* % Cdx+
            (deltar^2*pi()*x(Ts11+i*p-1*p)-x(Ts11+i*p))/deltax
        - (o.absorber.inner.keff + 16*sigma/(3*K)*x(Ts11+i*p)^3)* % Cdx-
            (deltar^2*pi()*x(Ts11+i*p)-x(Ts11+i*p+1*p))/deltax
        - hv_i(i+1,1)*(deltar^2*pi()*deltax*(x(Ts11+i*p)-x(Tf11+i*p))); % Cv
    for j=1:(p-2)
        e=e+1;
        y(e) = get_heat_source_2(i,j,o)*(((j+1)*deltar)^2-(j*deltar)^2)*pi()*deltax % Srce
            + (o.absorber.inner.keff + 16*sigma/(3*K)*x(Ts11+i*p+j)^3)* % Cdr+
                (2*pi()*j*deltar*deltax)*(x(Ts11+i*p+(j-1))-x(Ts11+i*p+j))/deltar
            - (o.absorber.inner.keff + 16*sigma/(3*K)*x(Ts11+i*p+j)^3)* % Cdr-
                (2*pi()*((j+1)*deltar)*deltax*(x(Ts11+i*p+j)-x(Ts11+i*p+(j+1))))/deltar
            + (o.absorber.inner.keff + 16*sigma/(3*K)*x(Ts11+i*p+j)^3)* % Cdx+
                (((j+1)*deltar)^2-(j*deltar)^2)*pi()*x(Ts11+i*p-1*p+j)-x(Ts11+i*p+j))/deltax
            - (o.absorber.inner.keff + 16*sigma/(3*K)*x(Ts11+i*p+j)^3)* % Cdx-
                (((j+1)*deltar)^2-(j*deltar)^2)*pi()*x(Ts11+i*p+j)-x(Ts11+i*p+1*p+j))/deltax
            - hv_i(i+1,j+1)* % Cv
                (((j+1)*deltar)^2-(j*deltar)^2)*pi()*deltax*(x(Ts11+i*p+j)-x(Tf11+i*p+j));
    end
    e=e+1;
    y(e) = get_heat_source_2(i,(p-1),o)*(((p-1)+1)*deltar)^2-((p-1)*deltar)^2)*pi()*deltax % Srce
        + (o.absorber.inner.keff + 16*sigma/(3*K)*x(Ts11+i*p+(p-1))^3)* % Cdr+
            (2*pi()*((p-1)*deltar)*deltax)*(x(Ts11+i*p+(p-1)-1))-x(Ts11+i*p+(p-1)))/deltar
        + (o.absorber.inner.keff + 16*sigma/(3*K)*x(Ts11+i*p+(p-1))^3)* % Cdx+
            (((p-1)+1)*deltar)^2-((p-1)*deltar)^2)*pi()*
            (x(Ts11+i*p-1*p+(p-1))-x(Ts11+i*p+(p-1)))/deltax
        - (o.absorber.inner.keff + 16*sigma/(3*K)*x(Ts11+i*p+(p-1))^3)* % Cdx-
            (((p-1)+1)*deltar)^2-((p-1)*deltar)^2)*pi()*
            (x(Ts11+i*p+(p-1))-x(Ts11+i*p+1*p+(p-1)))/deltax
        - hv_i(i+1,(p-1)+1)* % Cv
            (((p-1)+1)*deltar)^2-((p-1)*deltar)^2)*pi()*deltax*(x(Ts11+i*p+(p-1))-x(Tf11+i*p+(p-1)));
end % of nested function

% (5) inner absorber: CV outlet
e=e+1;
y(e) = get_heat_source_2(n-1,0,o)*deltar^2*pi()*deltax % Srce
        - (o.absorber.inner.keff + 16*sigma/(3*K)*x(Ts11+(n-1)*p)^3)* % Cdr-
            (2*pi()*deltar*deltax)*(x(Ts11+(n-1)*p)-x(Ts11+(n-1)*p+1))/deltar
        + (o.absorber.inner.keff + 16*sigma/(3*K)*x(Ts11+(n-1)*p)^3)* % Cdx+
            (deltar^2*pi()*x(Ts11+(n-2)*p)-x(Ts11+(n-1)*p))/deltax
        - hv_i((n-1)+1,1)*(deltar^2*pi()*deltax*(x(Ts11+(n-1)*p)-x(Tf11+(n-1)*p))); % Cv
for j=1:(p-2)
    e=e+1;
    y(e) = get_heat_source_2(n-1,j,o)*(((j+1)*deltar)^2-(j*deltar)^2)*pi()*deltax % Srce
        + (o.absorber.inner.keff + 16*sigma/(3*K)*x(Ts11+(n-1)*p+j)^3)* % Cdr+
            (2*pi()*j*deltar*deltax)*(x(Ts11+(n-1)*p+(j-1))-x(Ts11+(n-1)*p+j))/deltar
        - (o.absorber.inner.keff + 16*sigma/(3*K)*x(Ts11+(n-1)*p+j)^3)* % Cdr-

```

```

    (2*pi()*((j+1)*deltar)*deltax)*(x(Ts11+(n-1)*p+j)-x(Ts11+(n-1)*p+(j+1)))/deltar
+ (o. absorber.inner.keff + 16*sigma/(3*K)*x(Ts11+(n-1)*p+j)^3)* % Cdx+
    (((j+1)*deltar)^2-(j*deltar)^2)*pi()*x(Ts11+(n-2)*p+j)-x(Ts11+(n-1)*p+j))/deltax
- hv_i((n-1)+1,j+1)* % Cv
    (((j+1)*deltar)^2-(j*deltar)^2)*pi()*deltax*(x(Ts11+(n-1)*p+j)-x(Tf11+(n-1)*p+j));
end
e=e+1;
y(e) = get_heat_source_2(n-1,(p-1),o)*(((p-1)+1)*deltar)^2-((p-1)*deltar)^2)*pi()*deltax % Ssrc
+ (o. absorber.inner.keff + 16*sigma/(3*K)*x(Ts11+(n-1)*p+(p-1))^3)* % Cdr+
    (2*pi()*((p-1)*deltar)*deltax)*(x(Ts11+(n-1)*p+(p-1)-1)-x(Ts11+(n-1)*p+(p-1)))/deltar
+ (o. absorber.inner.keff + 16*sigma/(3*K)*x(Ts11+(n-1)*p+(p-1))^3)* % Cdx+
    (((p-1)+1)*deltar)^2-((p-1)*deltar)^2)*pi()*
    (x(Ts11+(n-2)*p+(p-1))-x(Ts11+(n-1)*p+(p-1)))/deltax
- hv_i((n-1)+1,(p-1)+1)* % Cv
    (((p-1)+1)*deltar)^2-((p-1)*deltar)^2)*pi()*deltax*
    (x(Ts11+(n-1)*p+(p-1))-x(Tf11+(n-1)*p+(p-1)));

% FLUID phase
% (6) outer absorber (does not exist)
e=e+1; y(e) = x(T2) - x(T3);
% (7) cavity
Qconv = 0;
Qconv = Qconv + h*deltar^2*pi()*x(Ts_w)-x(T3));
for j=1:(p-2)
    Qconv = Qconv + h*(((j+1)*deltar)^2-(j*deltar)^2)*pi()*x(Ts_w+j)-x(T3));
end
Qconv = Qconv + h*(((p-1)+1)*deltar)^2-((p-1)*deltar)^2)*pi()*x(Ts_w+(p-1))-x(T3));
e=e+1;
y(e) = m*get_h(x(T3)) - m*get_h(x(T4)) + Qconv;

% (8) inner absorber: CV inlet
e=e+1;
y(e) = m*(deltar^2/R^2)*( get_h(x(T4)) - get_h(x(Tf11+0)) )
+ hv_i(1,1)*(deltar^2*pi())*deltax*(x(Ts11)-x(Tf11));
for j=1:(p-2)
e=e+1;
y(e) = m*(((j+1)*deltar)^2-(j*deltar)^2)/R^2*( get_h(x(T4)) - get_h(x(Tf11+j)) )
+ hv_i(1,j+1)*(((j+1)*deltar)^2-(j*deltar)^2)*pi()*deltax*(x(Ts11+j)-x(Tf11+j));
end
e=e+1;
y(e) = m*(((p-1)+1)*deltar)^2-((p-1)*deltar)^2)/R^2*( get_h(x(T4)) - get_h(x(Tf11+(p-1))))
+ hv_i(1,(p-1)+1)*
    (((p-1)+1)*deltar)^2-((p-1)*deltar)^2)*pi()*deltax*(x(Ts11+(p-1))-x(Tf11+(p-1)));

% (9) inner absorber: CV i
for i=1:(n-2)
e=e+1;
y(e) = m*(deltar^2/R^2)*( get_h(x(Tf11+(i-1)*p)) - get_h(x(Tf11+i*p)) )
+ hv_i(i+1,1)*(deltar^2*pi())*deltax*(x(Ts11+i*p)-x(Tf11+i*p));
for j=1:(p-2)
e=e+1;
y(e) = m*(((j+1)*deltar)^2-(j*deltar)^2)/R^2*
    ( get_h(x(Tf11+(i-1)*p+j)) - get_h(x(Tf11+i*p+j)) )
+ hv_i(i+1,j+1)*
    (((j+1)*deltar)^2-(j*deltar)^2)*pi()*deltax*(x(Ts11+i*p+j)-x(Tf11+i*p+j));
end
e=e+1;
y(e) = m*(((p-1)+1)*deltar)^2-((p-1)*deltar)^2)/R^2*
    ( get_h(x(Tf11+(i-1)*p+(p-1))) - get_h(x(Tf11+i*p+(p-1)))) )

```



```

+ hv_i(i+1,(p-1)+1)*
  (((p-1)+1)*deltar)^2-((p-1)*deltar)^2)*pi()*deltax*
  (x(Ts11+i*p+(p-1))-x(Tf11+i*p+(p-1)));
end

% (10) inner absorber: CV outlet
e=e+1;
y(e) = m*(deltar^2/R^2) *( get_h(x(Tf11+(n-2)*p)) - get_h(x(Tf11+(n-1)*p)) )
  + hv_i((n-1)+1,1)*(deltar^2*pi())*deltax*(x(Ts11+(n-1)*p)-x(Tf11+(n-1)*p));
for j=1:(p-2)
  e=e+1;
  y(e) = m*(((j+1)*deltar)^2-(j*deltar)^2)/R^2*
    ( get_h(x(Tf11+(n-2)*p+j)) - get_h(x(Tf11+(n-1)*p+j)) )
    + hv_i((n-1)+1,j+1)*
      (((j+1)*deltar)^2-(j*deltar)^2)*pi()*deltax*(x(Ts11+(n-1)*p+j)-x(Tf11+(n-1)*p+j));
end
e=e+1;
y(e) = m*(((p-1)+1)*deltar)^2-((p-1)*deltar)^2)/R^2 *
  ( get_h(x(Tf11+(n-2)*p+(p-1)))- get_h(x(Tf11+(n-1)*p+(p-1))))
  + hv_i((n-1)+1,(p-1)+1)*
    (((p-1)+1)*deltar)^2-((p-1)*deltar)^2)*pi()*deltax*
    (x(Ts11+(n-1)*p+(p-1))-x(Tf11+(n-1)*p+(p-1)));

% (11) heat exchanger hot
e=e+1;    y(e) = x(T5) - x(T6) - Q/(m*cph);

% (12) heat exchanger cold
e=e+1;    y(e) = T(1) - x(T2) + Q/(m*cpc);

% (13) outlet temperature T5
Qout=0;
for j=0:(p-1)
  Qout = Qout + m*(((j+1)*deltar)^2-(j*deltar)^2)/R^2 * get_h(x(Tf11+(n-1)*p+j));
end
e=e+1;    y(e) = Qout - m*get_h(x(T5));

end

%SOLID temperatures
%pre-allocation for improved performance
Tw = zeros(p);
Tabs = zeros(n*p);
%glass window
for j=1:p
  Tw(j) = Tfsolve(Ts_w+(j-1));
end
%inner absorber (n*p finite volumen elements)
for i=1:(n*p)
  Tabs(i)=Tfsolve(Ts11+(i-1));
end

%FLUID temperatures
%pre-allocation for improved performance
T4i = zeros(n*p);
%fluid 2-4
T(2)=Tfsolve(T2);          %fluid temperature 2
T(3)=Tfsolve(T3);          %fluid temperature 3
T(4)=Tfsolve(T4);          %fluid temperature 4
%fluid within inner absorber T(4)=Tf11
for i=1:(n*p)

```



```
T4i(i)=Tfsolve(Tf11+(i-1));           %fluid temperature Tf11-T_(in+n)
end
%fluid 5-6
T(5)=Tfsolve(T5);                     %fluid temperature 5
T(6)=Tfsolve(T6);                     %fluid temperature 6
end % of function calculate_temperatures
```

8.2 Appendix B: User defined function in FLUENT

```

/*****
/*      User defined functions (UDFs) for Receiver      */
*****/

#include "udf.h"
#include "mem.h"
#include "prop.h"

/*****
/* Global definitions                                     */
*****/
/*****
/* ***** constants *****                             */
#define SIGMA 5.670373e-8          /* [W/(m^2*K^4)] ... Stefan Boltzmann constant */
#define GRAVITY 9.81              /* [m/s^2] ... gravitational acceleration      */
/*****
/* ***** ambient *****                               */
#define TAMB 273.15              /* [K] ... ambient temperature                */
/*****
/* ***** porous media: constants/functions for solid diffusivity ***** */
#define SOLID_DENSITY(T) 3100.0   /* [kg/m^3]... density                        */
#define SOLID_THERMAL_COND(T) 120.0 /* [W/m-K] ... thermal conductivity          */
#define SOLID_CP(T) 750.0        /* [J/kg-K] ... specific heat                 */
/*****
/* ***** porous media: constants/functions for fluid flow calculations ***** */
#define POROSITY 0.95            /* [-] ... porosity                           */
#define CELL_DIAMETER 0.002     /* [m] ... cell diameter                      */
#define E1 150.0                 /* [-] ... factor for Ergun equation          */
#define E2 1.75                  /* [-] ... factor for Ergun equation          */
/*****
/* ***** porous media: radiation properties ***** */
#define ABS_EMISSIVITY 0.8       /* [-] ... emissivity of absorber surface     */
#define ABS_REFRACTIVE_INDEX 1  /* [-] ... refractive index of absorber*/
/*****
/* ***** porous media: absorber boundaries ***** */
#define ABS_X0 0.015            /* [m] ... x-boundary                        */
#define ABS_Y0 0.0              /* [m] ... y-boundary                        */
#define ABS_Z0 0.0              /* [m] ... z-boundary                        */
/*****
/* ***** porous media: dimensions ***** */
#define RABS 0.050              /* [m] ... outer radius of absorber          */
#define DELTA_L 0.020           /* [m] ... absorber cavity depth             */
/*****
/* ***** glass window: optical properties ***** */
#define TRANSMISSIVITY 0.851     /* [-] ... transmissivity                    */
#define ABSORPTIVITY 0.013      /* [-] ... absorptivity                      */
#define REFLECTIVITY 0.136      /* [-] ... reflectivity                      */
#define TRANSMISSIVITY_UV 0.549 /* [-] ... transmissivity for thermal rad.   */
/*****
/* ***** glass window: dimensions ***** */
#define SW 0.005                /* [m] ... thicknes of glass window          */
#define RW 0.05                 /* [m] ... outer radius of glass window      */
/*****
/* ***** light source properties ***** */
/*****
#define N 8.0                    /* [-] ... number of lamps                   */
#define DFS 0.1                  /* [m] ... focal spot diameter               */
#define LDF 0.1                  /* [-] ... light distribution factor         */
/*                               ldf = I(r=r0)/I(r=0) */
#define FLUX 5.355e3             /* [W] .... radiant power at boundary       */
/*                               window-ambient for one lamp */

/*****
/* Hard coded cell-IDs and boundary-IDs                 */
*****/
/*****
#define FLUID_ABSORBER          22      /* [int]                                     */
#define FLUID_OUTFLOW           23      /* [int]                                     */
#define FLUID_INFLOW            21      /* [int]                                     */
#define SOLID_TUBES              20      /* [int]                                     */
#define SOLID_WINDOW             24      /* [int]                                     */

```

```

#define INTERFACE_DUCT_ABSORBER      32      /* [int] */
#define SYMMETRY_ABSORBER           3       /* [int] */
#define OUTLET                       36     /* [int] */
#define WINDOW                       38     /* [int] ... surface inside */

/*****
/* Definition of user defined scalars (UDS) */
/*****
enum
{
    /*0*/  SOLID_TEMP,           /* UDS for absorber solid temperature */
    /*1*/  UDS_POROSITY,        /* UDS for variable porosity */
    /*2*/  UDS_PR,              /* Prandtl number within absorber */
    /*3*/  UDS_KF,              /* fluid thermal conductivity within absorber */
    /*4*/  UDS_MU,              /* fluid dynamic viscosity within absorber */
    /*5*/  UDS_RE,              /* Reynold's number within absorber */
    /*6*/  UDS_VOL_HTC,         /* volumetric HTC within absorber */
    /*7*/  ABS_SURFACE,         /* absorber surface coordinates */
    /*8*/  SURFACE_S0,          /* 1 if surface of absorber, else 0 */
    N_REQUIRED_UDS              /* max. number of UDS */
};

/*****
/* Initialization */
/*****
DEFINE_INIT(INIT_receiver, domain)
{
    int c_ID, f_ID;
    face_t f;
    cell_t c, C0;
    Thread *c_thread, *c_thread_abs, f_thread;
    real S0[3], Xc[3], Xf[3, x, y, z, r, rs, s, delta_r, delta_r_new;

    /*** Initialize the absorber solid temperatures *****/
    for(i=1; i<=3; i++)
    {
        if (i==1) c_ID=FLUID_INFLOW;           /* cells of fluid inflow */
        if (i==2) c_ID=FLUID_ABSORBER;        /* cells of absorber */
        if (i==3) c_ID=FLUID_OUTFLOW;         /* cells of fluid outflow */
        c_thread = Lookup_Thread(domain, c_ID); /* get cell thread */
        begin_c_loop(c, c_thread)
        {
            C_UDSI(c,c_thread,SOLID_TEMP) = 773;
        }
        end_c_loop(c, c_thread)
    }

    /*** Initialize the absorber porosity *****/
    c_ID=FLUID_ABSORBER;                       /* cells of absorber */
    c_thread = Lookup_Thread(domain, c_ID);     /* get cell thread */
    begin_c_loop(c, c_thread)
    {
        C_UDSI(c,c_thread,UDS_POROSITY) = POROSITY;
    }
    end_c_loop(c, c_thread)

    /*** Initialize the window temperature *****/
    c_ID=SOLID_WINDOW;                          /* cells of window */
    c_thread = Lookup_Thread(domain, c_ID);     /* get cell thread */

    begin_c_loop(c, c_thread)

```

```

    {
        C_T(c,c_thread) = 773;
    }
end_c_loop(c, c_thread)

/** Calculate the UDS containing the surface coordinates of the absorber *****/
for(i=1; i<=3 ;i++)
{
    if (i==1) c_ID=FLUID_INFLOW;           /* cells of fluid inflow */
    if (i==2) c_ID=FLUID_ABSORBER;        /* cells of absorber */
    if (i==3) c_ID=FLUID_OUTFLOW;         /* cells of fluid outflow */
    c_thread = Lookup_Thread(domain, c_ID); /* get cell thread */
    begin_c_loop(c, c_thread)
    {
        C_CENTROID(Xc, c, c_thread);      /* get cell coordinate Xc */
        /* calculate current radius */
        x=Xc[0];
        y=Xc[1];
        z=Xc[2];
        r = sqrt(pow(y,2.0)+pow(z,2.0));

        f_ID=INTERFACE_DUCT_ABSORBER; /* face of absorber in x */
        f_thread = Lookup_Thread(domain, f_ID); /*get face thread for x */
        delta_r=RABS;
        begin_f_loop(f, f_thread)          /* loop over the absorber surface */
        {
            F_CENTROID(Xf, f, f_thread);
            rs = sqrt(pow(Xf[1],2.0)+pow(Xf[2],2.0));
            delta_r_new = sqrt(pow((rs-r),2.0));
            if (delta_r_new < delta_r)
            {
                delta_r = delta_r_new;
                s = Xf[0];
                C_UDSI(c,c_thread,ABS_SURFACE) = s;
            }
        }
        end_f_loop(f, f_thread)
    }
    end_c_loop(c, c_thread)
}

/** Initialize the UDS that states if the cell is at surface of the absorber *****/
for(i=1; i<=3 ;i++)
{
    if (i==1) c_ID=FLUID_INFLOW;           /* cells of fluid inflow */
    if (i==2) c_ID=FLUID_ABSORBER;        /* cells of absorber */
    if (i==3) c_ID=FLUID_OUTFLOW;         /* cells of fluid outflow */
    c_thread = Lookup_Thread(domain, c_ID); /* get cell thread */
    begin_c_loop(c, c_thread)
    {
        C_UDSI(c,c_thread,SURFACE_S0)=0;
    }
    end_c_loop(c, c_thread)
}
f_thread = Lookup_Thread(domain, INTERFACE_DUCT_ABSORBER);
begin_f_loop(f, f_thread) /* loop over the absorber surface */
{
    C0 = F_C1(f,f_thread); /* get adjacent cell inside volume */
    c_thread = THREAD_T1(f_thread); /* get adjacent cell thread inside vol.*/
    C_UDSI(C0,c_thread,SURFACE_S0)=1;
}

```

```

    }
    end_f_loop(f, f_thread)
}

/*****
/* Absorber properties */
*****/

/** Porosity profile *****/
DEFINE_PROFILE(PROFILE_porosity, thread, i)
{
    cell_t c;
    begin_c_loop(c,thread)
    {
        F_PROFILE(c,thread,i) = C_UDSI(c,thread,UDS_POROSITY);
    }
    end_c_loop(c,thread)
}

/** Material properties *****/
void PROP_absorber(cell_t cell, Thread *thread, real *DP, real *VRC, real *IRC, real *Kext)
{
    real porosity, dp, K, C, kext;

    porosity = C_UDSI(cell,thread,UDS_POROSITY);
    dp = 1.5/2.3*CELL_DIAMETER*sqrt(4.0/(3.0*M_PI)*(1.0-porosity))/(1-
sqrt(4.0/(3.0*M_PI)*(1-porosity)));
    K = pow(dp,2.0)/E1*pow(porosity,3.0)/pow((1-porosity),2.0);
    C = E2/(sqrt(E1)*pow(porosity,1.5));
    kext = 4.8/CELL_DIAMETER*(1-porosity);
    *DP=dp;
    *VRC=1/K;
    *IRC=2*C/pow(K,0.5);
    *Kext=kext;
}

/** Diffusivity for UDS (SOLID_TEMP) *****/
DEFINE_DIFFUSIVITY(UDS_diff, cell, thread, i)
{
    real source,Ts, k, kr, rho, cp, porosity, DP, VRC, IRC, Kext;
    Thread *c_thread_abs;
    Domain *domain;

    if (i==SOLID_TEMP)
    {
        domain=Get_Domain(1); /* fluid domain pointer */
        c_thread_abs = Lookup_Thread(domain, FLUID_ABSORBER);
        if (thread == c_thread_abs)
        {
            Ts=C_UDSI(cell,thread,SOLID_TEMP);
            porosity = C_UDSI(cell,thread,UDS_POROSITY);
            PROP_absorber(cell, thread, &DP, &VRC, &IRC, &Kext);
            k = SOLID_THERMAL_COND(Ts) * (1-porosity);
            rho = SOLID_DENSITY(Ts) * (1-porosity);
            cp = SOLID_CP(Ts);
            kr = 16*SIGMA*pow(Ts,3.0)/(3*Kext);
            source = (k+kr)/(rho*cp);
        }
        else source = 0;
    }
}

```

```

else source = 0;
return source;
}

/** Viscous resistance coefficient (VRC) profile*****
DEFINE_PROFILE(PROFILE_VRC, thread, i)
{
    real DP, VRC, IRC, Kext, source;
    cell_t c;

    begin_c_loop(c,thread)
    {
        PROP_absorber(c, thread, &DP, &VRC, &IRC, &Kext);
        F_PROFILE(c,thread,i) = VRC;
    }
    end_c_loop(c,thread)
}

/** Inertial resistance coefficient (IRC) profile*****
DEFINE_PROFILE(PROFILE_IRC, thread, i)
{
    real DP, VRC, IRC, Kext, source;
    cell_t c;

    begin_c_loop(c,thread)
    {
        PROP_absorber(c, thread, &DP, &VRC, &IRC, &Kext);
        F_PROFILE(c,thread,i) = IRC;
    }
    end_c_loop(c,thread)
}

*****
/* Air properties */
*****

/** Dynamic viscosity according to the Sutherland law *****
/* flu_ug.pdf, page 410, eq. 8-18 */
DEFINE_PROPERTY(PROP_air_mu, cell, thread)
{
    real mu, T, mu_ref, T_ref, S_const;

    S_const=110.56; /* [K] Sutherland constant */
    T_ref=273.11; /* [K] reference temperature */
    mu_ref=1.716e-5; /* [Pa*s] reference viscosity */
    T=C_T(cell, thread); /* get cell temperature */
    mu = mu_ref * pow((T/T_ref), 1.5) * (T_ref+S)/(T+S);
    return mu;
}

/** Thermal conductivity of air using the kinetic theory law *****
/* flu_ug.pfd, page 420, eq. 8-41 */
DEFINE_PROPERTY(PROP_air_kf, cell, thread)
{
    real R, Mw, mu, cp, kf;
    R=8314.34; /* [J/kmol-K] universal gas constant */
    Mw=28.966; /* [kg/kmol] molecular weight */
    mu = PROP_air_mu(cell, thread); /* get dynamic viscosity */
    cp = C_CP(cell, thread); /* get specific heat capacity */
}

```

```

kf = 15.0/4.0 * R/Mw * mu * (4.0/15.0*cp*Mw/R+1/3);
C_UDSI(cell,thread,UDS_KF) = kf;
return kf;
}

/** Absorption coefficient inside the absorber *****/
/* emitted energy by the solid is absorbed by the fluid */
DEFINE_PROPERTY(PROP_air_alpha, cell, thread)
{
    Domain *domain_abs;
    Thread *c_thread_abs;
    int c_ID_abs;
    real DP, VRC, IRC, Kext, alpha, surface;

    PROP_absorber(cell, thread, &DP, &VRC, &IRC, &Kext
    domain_abs=Get_Domain(1); /* fluid domain pointer */
    c_ID_abs=FLUID_ABSORBER; /* cells of absorber */
    c_thread_abs = Lookup_Thread(domain_abs, c_ID_abs);
    if (thread == c_thread_abs)
    {
        /* 1 if cell is adjacent to absorber surface, else 0*/
        if (C_UDSI(cell,thread,SURFACE_S0) > 0) surface = 1;
        else surface = 0;
        Kext = 10e3;
        alpha=surface*Kext;
    }
    else alpha = 0; /* no absorption of radiation by air outside the absorber */
    return alpha;
}

/** Light source properties */
void PROP_light_source(real *I0mean, real *I0peak)
{
    real i0mean, i0peak;

    i0mean = N*FLUX/(pow(DFS,2.0)*M_PI/4); /* calculate mean irradiation */
    i0peak = i0mean*log(LDF)/(exp(log(LDF))-1); /* calculate peak irrad. at r=0 */
    *I0mean = i0mean;
    *I0peak = i0peak;
}

/** Heat Transfer */
/** Heat transfer coefficient between Solid and Gas within absorber */
real HTC_solid_gas(cell_t cell, Thread *thread)
{
    real DP, VRC, IRC, Kext, Us, Re, Pr, Pr0,
    real kf, hsf, hsf1, hsf2, hv, alphasf, dv, porosity;

    porosity = C_UDSI(cell,thread,UDS_POROSITY);
    /* calculate superficial velocity */
    Us = sqrt( pow(C_U(cell,thread),2.0) + pow(C_V(cell, thread),2.0) +
    pow(C_W(cell,thread),2.0));

    /* calculate Reynolds number */

```

```

PROP_absorber(cell, thread, &DP, &VRC, &IRC, &Kext);
Re = Us*DP*C_R(cell,thread)/PROP_air_mu(cell,thread);
/* calculate Prandtl number */
Pr = C_CP(cell,thread)*PROP_air_mu(cell,thread)/PROP_air_kf(cell,thread);
/* calculate HTC */
alphasf = 20.346*(1-porosity)*pow(porosity,2.0)/DP;
dv = 4*porosity/alphasf;
kf = PROP_air_kf(cell,thread);
if (Re <= 75.0)
    hsf = 0.004 * dv/DP * kf/DP * pow(Pr,0.33) * pow(Re,1.35);
else if (Re >= 350.0)
    hsf = 1.064 * kf/DP * pow(Pr,0.33) * pow(Re,0.59);
else
{
    hsf1 = 0.004 * dv/DP * kf/DP * pow(Pr,0.33) * pow(Re,1.35);
    hsf2 = 1.064 * kf/DP * pow(Pr,0.33) * pow(Re,0.59);
    hsf = hsf1 + (hsf2-hsf1)/(350.0-75.0)*(Re-75.0);
}

hv = hsf*alphasf;
/* UDS for control/debuggin purposes */
/*SOLID_TEMP*/
/*UDS_POROSITY*/
C_UDSI(cell,thread,UDS_PR) = Pr;
C_UDSI(cell,thread,UDS_KF) = kf;
C_UDSI(cell,thread,UDS_MU) = PROP_air_mu(cell, thread);
C_UDSI(cell,thread,UDS_RE) = Re;
C_UDSI(cell,thread,UDS_VOL_HTC) = hv;
return hv;
}
/** Heat transfer coefficient between glass window and ambient *****/
DEFINE_PROFILE(PROFILE_window_hfree, thread, i)
{
    real L, beta, GrL, g_of_Pr, nu, Pr, kf, Tw, hfree;
    cell_t c;

    nu = 153.2e-7;          /* [m^2/s] ... kinematic viscosity of air at p=1 bar          */
                          /* and T=TAMB=273.15K                                          */
    Pr = 0.7081;          /* [-] ... Pr number of air at p=1 bar and T=TAMB          */
    kf = 25.373e-3;      /* [W/m-K] ...conductivity of air at p=1bar and T=TAMB*/
    begin_c_loop(c,thread)
    {
        L = RW*2;          /* characteristic length L=D          */
        beta = 1/TAMB;     /* expansion coefficient, for ideal gases beta=1/T          */
        Tw = C_T(c,thread); /* get cell temperature of window          */
        GrL = GRAVITY*beta*(Tw-TAMB)*pow(L,3.0)/pow(nu,2.0); /*Grashof n.          */
        g_of_Pr = 0.75*pow(Pr,0.5)/(0.609+1.221*pow(Pr,0.5)+1.238*pow(Pr,0.25));
        hfree = kf/L * 4.0/3.0*pow((GrL/4.0),0.25) * g_of_Pr; /*HTC          */
        F_PROFILE(c,thread,i) = hfree;
    }
    end_c_loop(c,thread)
}

/** Heat sources/sinks *****/
/** Solar heat source within absorber *****/
real SRCE_absorber_solar(cell_t cell, Thread *thread)
{

```



```

real source, DP, VRC, IRC, Kext, I0mean, I0peak, Xc[3], x, y, z, r, s, p;

PROP_absorber(cell, thread, &DP, &VRC, &IRC, &Kext); / * get extinction coeff. */
PROP_light_source(&I0mean, &I0peak); / * get irradiation */
C_CENTROID(Xc, cell, thread); / * get cell coordinate Xc */
    x=Xc[0];
    y=Xc[1];
    z=Xc[2];
    r = sqrt(pow(y,2.0)+pow(z,2.0));
    s = C_UDSI(cell,thread,ABS_SURFACE); / * get absorber surface */
p = Xc[0] - s; / * calculate penetration depth p */
/ * calculate solar radiation heat source dependence of penetration depth p */
    source = TRANSMISSIVITY * I0peak*Kext*exp(log(LDF)*pow((r/RABS),2.0) -
        Kext*p);
return source;
}

/ ** Heat source fluid within absorber **** */
DEFINE_SOURCE(SRCE_fluid_heat, cell, thread, dS, eqn)
{
    real V, hv, Ts, T, convection_source, solar_radiation_source, source;

    hv = HTC_solid_gas(cell,thread); / * get volumetric convective HTC */
    Ts = C_UDSI(cell,thread,SOLID_TEMP); / * get cell temperature of solid */
    T = C_T(cell,thread); / * get cell temperature of fluid */
    convection_source = hv*(Ts-T); / * convection heat source */
    solar_radiation_source = 0; / * solar radiation heat source = 0 */
    / * assuming absorption and scattering coefficient of air = 0 */
    source = convection_source + solar_radiation_source;
    dS[eqn] = -hv;
return source;
}

/ ** Heat source solid within absorber **** */
DEFINE_SOURCE(SRCE_solid_heat, cell, thread, dS, eqn)
{
    real Ts, T, hv, convection_source, solar_radiation_source, radiation_source, source;
    real n, porosity, DP, VRC, IRC, Kext;
    Domain *domain;
    Thread *c_thread_abs;

    domain=Get_Domain(1); / * fluid domain pointer */
    c_thread_abs = Lookup_Thread(domain, FLUID_ABSORBER);
    if (thread == c_thread_abs)
    {
        porosity = C_UDSI(cell,thread,UDS_POROSITY); / * get porosity */
        PROP_absorber(cell, thread, &DP, &VRC, &IRC, &Kext
        hv = HTC_solid_gas(cell,thread); / * get volumetric conv. HTC */
        Ts = C_UDSI(cell,thread,SOLID_TEMP); / * get cell temperature of solid */
        T = C_T(cell,thread); / * get cell temperature of fluid */
        convection_source = -hv*(Ts-T); / * convection heat source */
        / * solar radiation heat source */
        solar_radiation_source = SRCE_absorber_solar(cell,thread);
        / * radiation heat source (sink) */
        radiation_source = 0; / *-ABS_EMISSIVITY*SIGMA*pow(Ts,4.0);
        source = convection_source + solar_radiation_source + radiation_source;
        dS[eqn] = -hv; / *-4*ABS_EMISSIVITY*SIGMA*(pow(Ts,3.0));*/
    }
    else
    {

```

```

        dS[eqn] = 0;
        source = 0;
    }
    return source;
}

/** Heat source
window*****/
DEFINE_SOURCE(SRCE_window_heat, cell, thread, dS, eqn)
{
    real source, Xc[3], x, y, z, r, I0mean, I0peak;

    C_CENTROID(Xc, cell, thread);          /* get cell coordinate      */
    x=Xc[0];
    y=Xc[1];
    z=Xc[2];
    r = sqrt(pow(y,2.0)+pow(z,2.0));
    PROP_light_source(&I0mean, &I0peak);  /* get irradiation          */
    source = I0peak*exp(log(LDF)*pow((r/RABS),2.0))/SW * ABSORPTIVITY;
    dS[eqn] = 0.0;
    return source;
}

/*****
/* Radiation */
*****/

/** Discrete Ordinates Model (DOM) Source *****/
DEFINE_DOM_SOURCE(SRCE_DOM, cell, thread, ni, nb, emission, in_scattering, abs_coeff,
scat_coeff)
{
    real porosity, absorption_coeff, Ts, Tf, surface;
    Domain *domain_abs;
    Thread *c_thread_abs, *f_thread;
    int c_ID_abs, f_ID;
    cell_t C0, C1;

    Tf = C_T(cell,thread);                  /* get cell temperature of fluid */
    Ts = C_UDSI(cell,thread,SOLID_TEMP);    /* get cell temperature of solid */
    /* 1 if cell is adjacent to absorber surface, else 0*/
    if (C_UDSI(cell,thread,SURFACE_S0) > 0) surface = 1;
    else surface = 0;

    *emission *= surface * 1/pow(Tf,4.0) * pow(Ts,4.0);
}

/** Definition of the radiative boundary heat source window *****/
DEFINE_HEAT_FLUX(FLUX_DOM, face, f_thread, c0, t0, cid, cir)
{
    Domain *domain;
    Thread *f_thread_win;
    int f_ID;

    domain=Get_Domain(1);                  /* fluid domain pointer      */
    f_ID=WINDOW;                           /* face of window inside     */
    f_thread_win = Lookup_Thread(domain, f_ID); /* get cell thread          */
    if (f_thread == f_thread_win)
    {
        cir[0] *= (1-TRANSMISSIVITY_UV);
    }
}

```

```

    }
}

/*****
/* Outlet temperature */
/*****
/** Calculate equivalent outlet temperature *****/
void CALC_outlet_temperature()
{
    Domain *domain;
    Thread *f_thread, *c_thread;
    face_t f;
    cell_t c0;
    int f_ID, c_ID, i;
    real T, cp, dm, m, Qout, Tout;

    domain=Get_Domain(1);          /* fluid domain pointer */
    f_ID=OUTLET;                   /* face ID of outlet */
    f_thread = Lookup_Thread(domain, f_ID); /* get face thread */
    c_ID=FLUID_OUTFLOW;           /* ID of cell zone inner duct */
    c_thread = Lookup_Thread(domain, c_ID); /* get cell thread */
    Qout = 0;                       /* intilizing of Qout */
    m = 0;
    begin_f_loop(f, f_thread)
    {
        c0 = F_C0(f, f_thread);     /* get adjacent cell C0 */
        T = C_T(c0, c_thread);     /* get cell temperature of fluid */
        dm = F_FLUX(f, f_thread);  /* get mass flux through face */
        m += dm;                   /* calculate total mass flux */
        Qout += T*dm;              /* calculate outlet temperature flux */
        /* for mass averaging */
    }
    end_f_loop(f, f_thread_x)
    Tout = Qout/m;
    printf("m: %e\n", m);
    printf("Tout: %e\n", Tout);
}

/** Display inlet and outlet pressure *****/
{
    Domain *domain;
    face_t f;
    cell_t c;
    Thread *f_thread_inlet, *f_thread_outlet;
    real p_in, p_out, p_op;

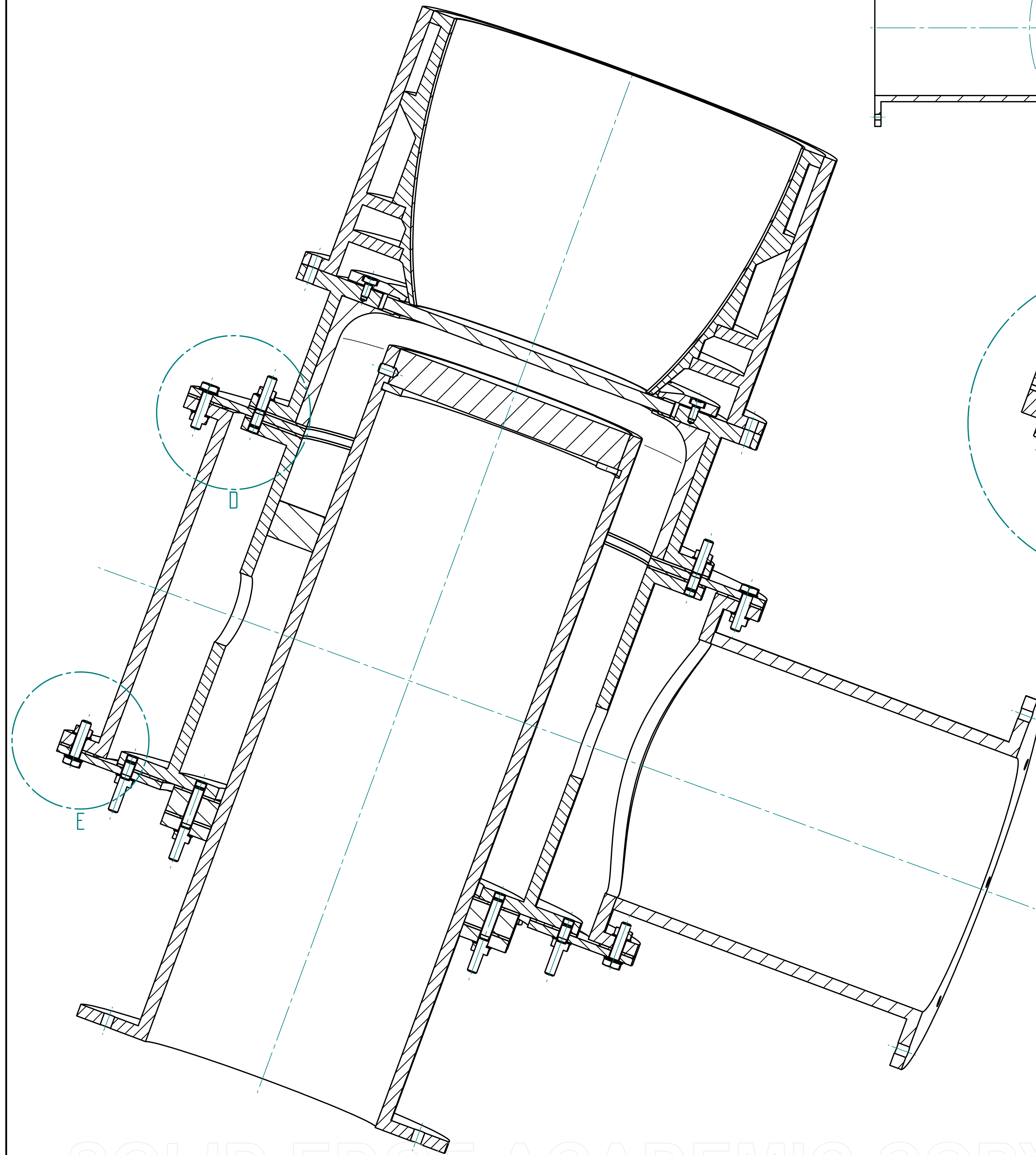
    domain=Get_Domain(1);          /* fluid domain pointer */
    f_thread_inlet = Lookup_Thread(domain, INLET); /* get face thread */
    f_thread_outlet = Lookup_Thread(domain, OUTLET); /* get face thread */
    p_op = RP_Get_Float("operating-pressure"); /* get operation pressure*/
    begin_f_loop(f, f_thread_inlet)
    {
        p_in = F_P(f, f_thread_inlet)+p_op;
    }
    end_f_loop(f, f_thread_inlet)
    begin_f_loop(f, f_thread_outlet)
    {
        p_out = F_P(f, f_thread_inlet)+p_op;
    }
    end_f_loop(f, f_thread_outlet)
}

```

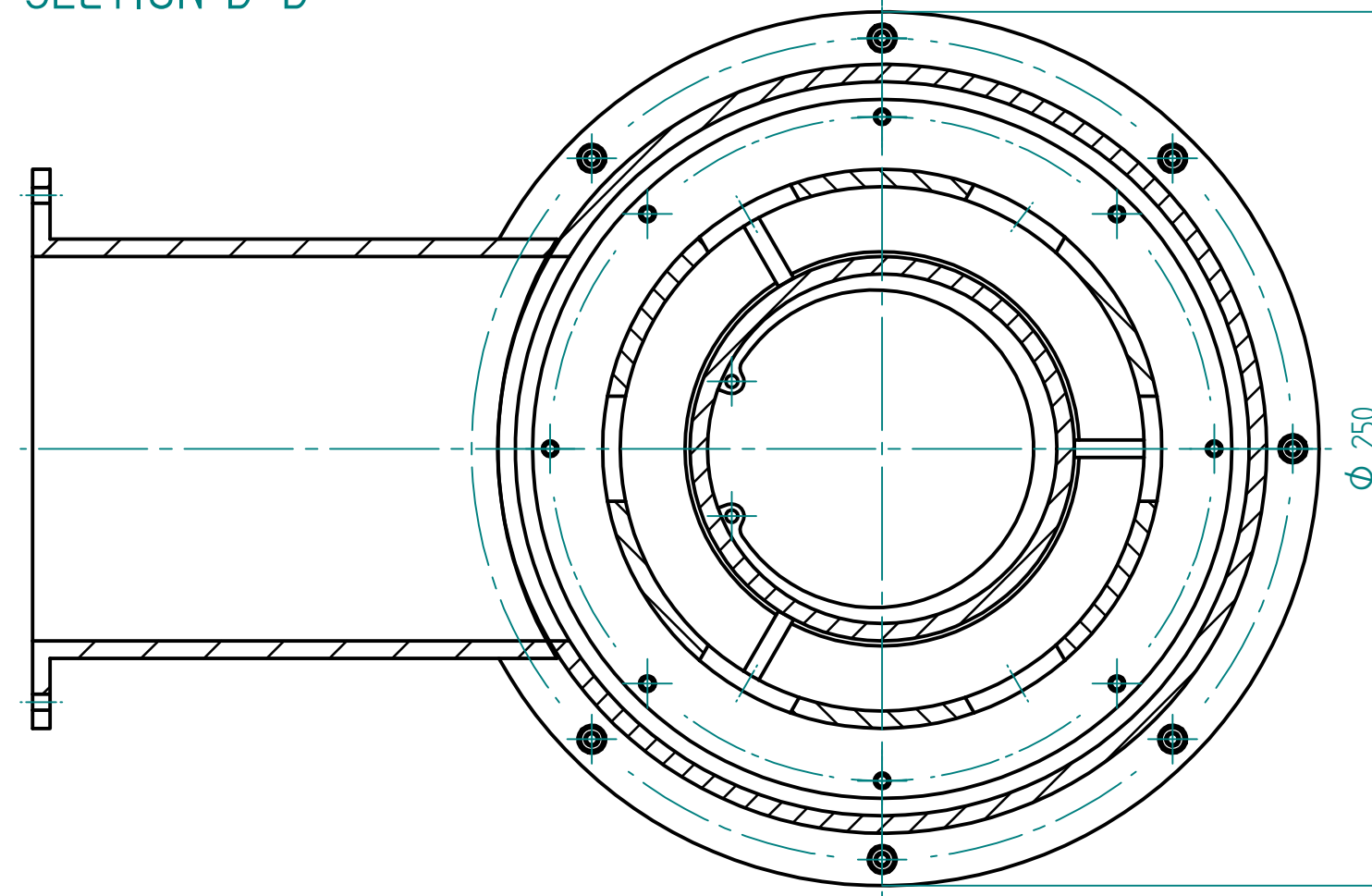
```
    printf("p_in: %e\n", p_in);  
    printf("p_out: %e\n", p_out);  
}
```

8.3 Appendix C: Receiver assembly

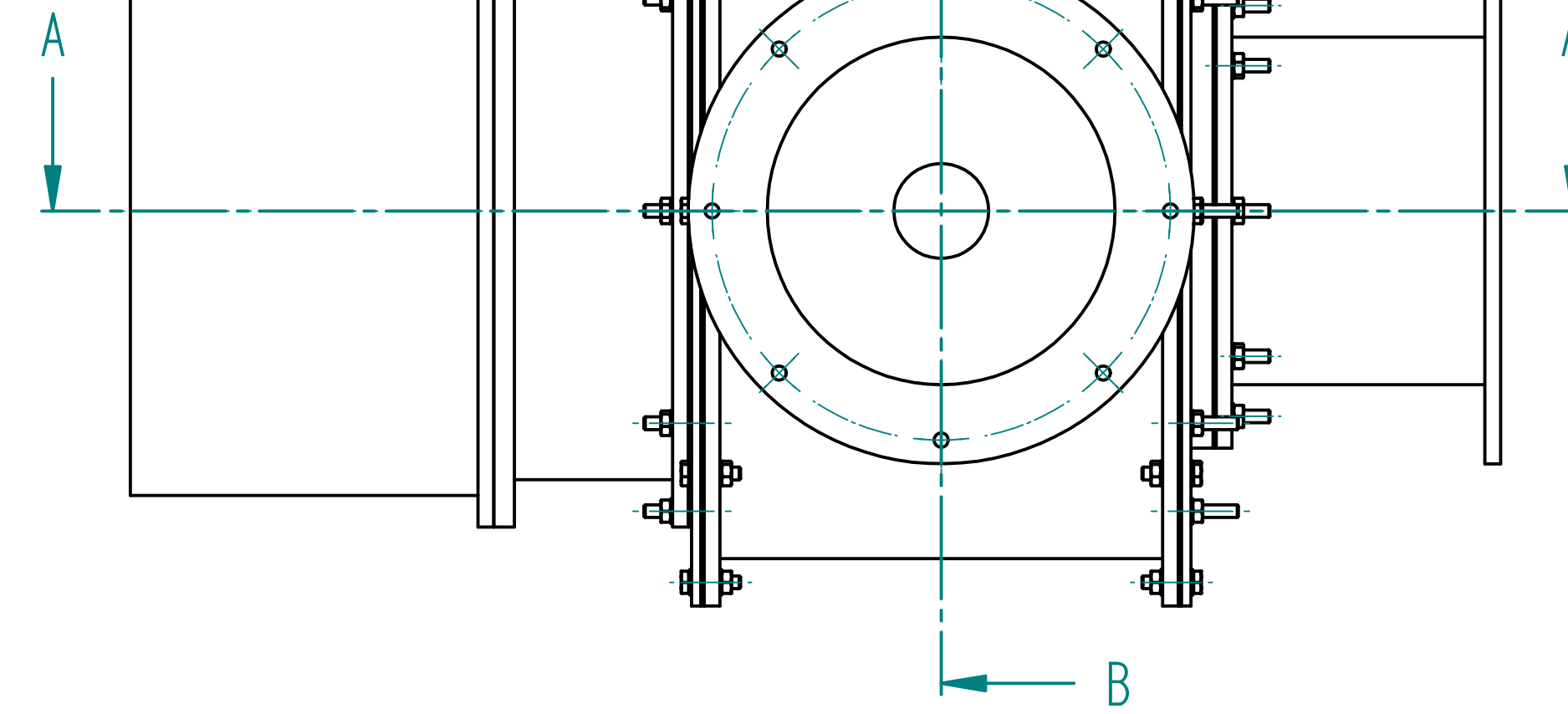
See next page.



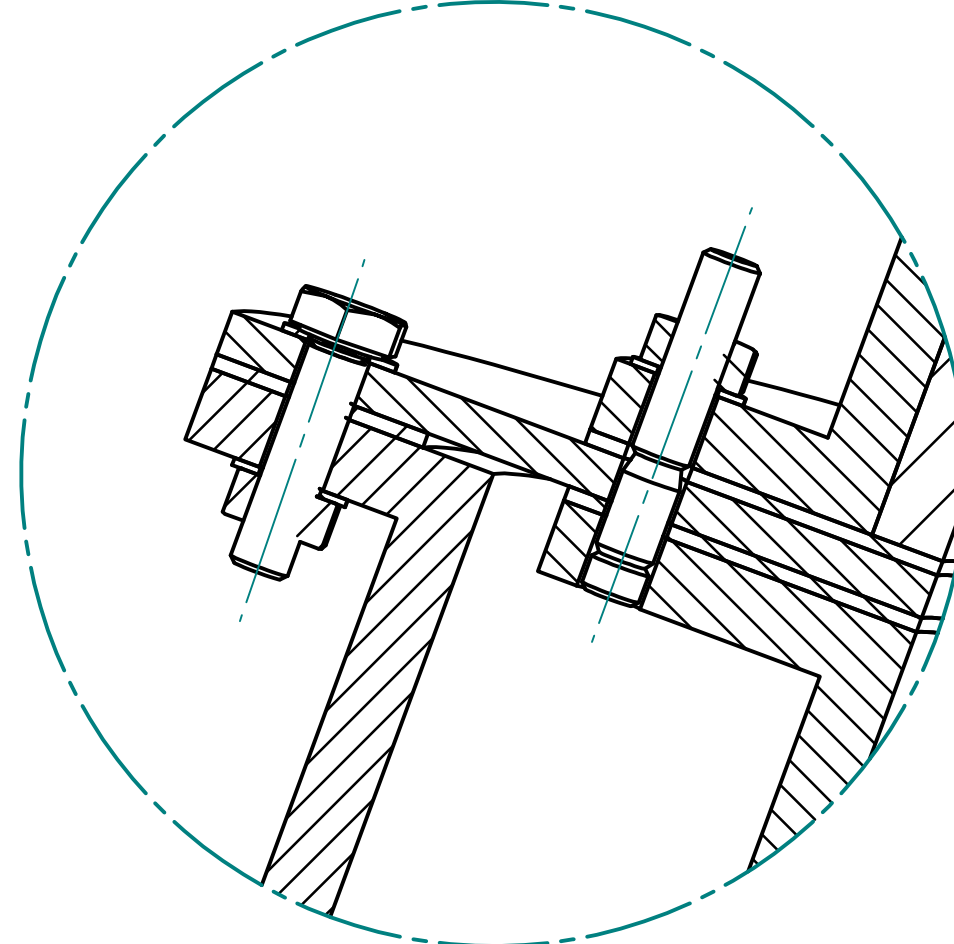
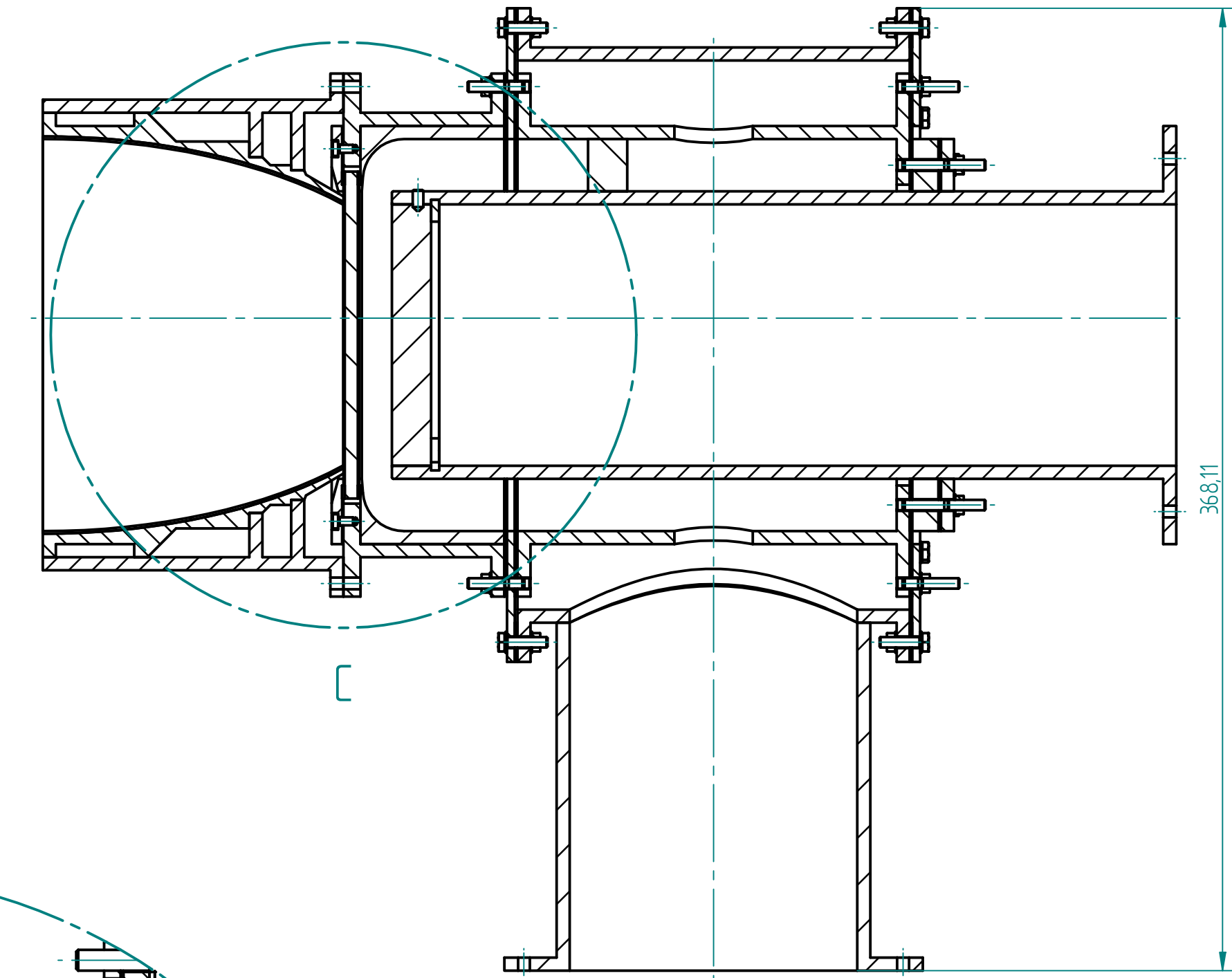
SECTION B-B



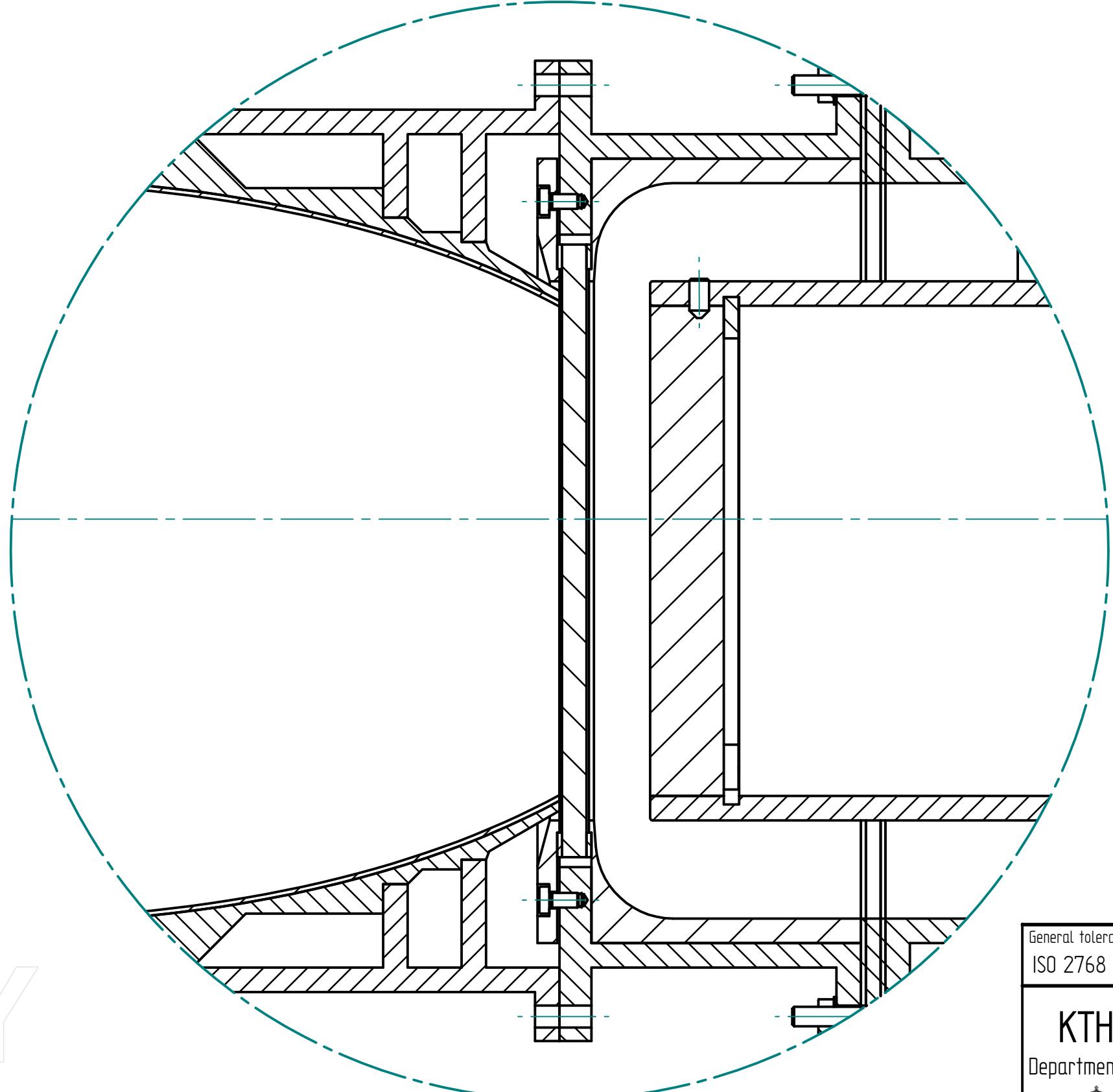
A



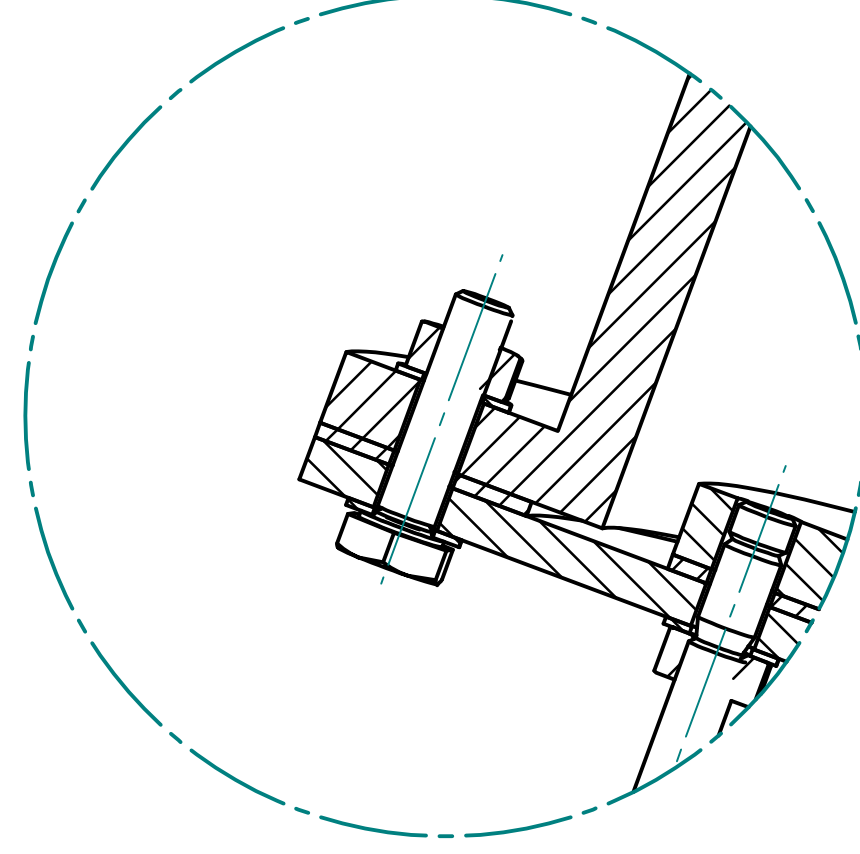
SECTION A-A



DETAIL D



DETAIL C



DETAIL E

SOLID EDGE ACADEMIC COPY

General tolerance ISO 2768	Surface finishing EN ISO 1302	Tolerancing ISO 8015
KTH Stockholm Department of Energy Technology	Created by Lukas Aichmayer	Approved by Document type Assembly
Title, Supplementary title Assembly Receiver		MSc-00-00
Scale 1:2 1:1	Rev. 12 13	Date of issue 2011-11-07
Lang en		Sheet 1/1